



UNIVERSITÀ DEGLI STUDI DELL'AQUILA
DIPARTIMENTO DI INGEGNERIA INDUSTRIALE
E DELL'INFORMAZIONE E DI ECONOMIA

Dottorato di Ricerca in Ingegneria Industriale e dell'Informazione e di Economia

Curriculum Ingegneria Chimica e Materiali

XXXVI ciclo

Titolo della tesi

Treatment and recovery of precious and base metals from industrial waste through sustainable hydrometallurgical processes and with a circular economy approach

SSD: ING-IND/26

Dottorando

Pietro Romano

Coordinatore del corso

Prof.ssa Katia Gallucci

Tutor

Prof. Francesco Vegliò

a.a. 2022/2023

A chi c'è sempre stato.

A chi avrebbe voluto esserci.

A Ida.

A te, papà.

Abstract

The recovery of material and energy from end-of-life products is increasingly fundamental for sustainable development. The most significant challenge for research in this sector is to find increasingly cutting-edge technologies that allow us to help the environment while generating profitable economic activities. Through the union of these two aspects, which until now may have seemed antithetical, we can talk about progress.

From this standpoint, materials such as spent catalysts or electrical and electronic equipment are not seen as waste but as sources of supply, in many cases even better than natural ones.

This thesis reports the studies conducted to develop and optimize several processes for recovering raw materials from different types of waste, such as Oil&Gas catalysts, printed circuit boards, photovoltaic panels, and permanent magnets.

Through laboratory-scale experimental tests, process simulations, and the creation of mathematical models, it has been possible to have innovative and internationally competitive process solutions compared to those currently on the market.

In this sense, a new process for the valorization of Oil&Gas catalysts has been developed and patented: the ORIM-CAT2 process. A process for recovering silver and silicon from end-of-life photovoltaic panels has been developed and is being patented. Two processes have been optimized for recovering precious and base metals from waste electrical and electronic equipment (Gold-REC1 and Gold-REC2) and a process for recovering rare earths from end-of-life permanent magnets.

Preface

This work summarizes the experimental activity and results obtained during the three years of the PhD course in Industrial Engineering and Information and Economics. Thanks to participation during these three years in various research projects, getting in touch with a consortium of important European companies has been possible. In this context, it was possible to come up against several important problems concerning the world of recovery of metals and critical raw materials.

The activity involved the application of numerous engineering, chemical, physical, statistical, and economic techniques and methods to solve various technical and theoretical problems. The final aim of this work is to summarize all these concepts to illustrate the solutions found and the process that led to the identification of the optimal solutions.

In developing new sustainable processes and with an approach to the concept of circular economy, various types of studies have been carried out on industrial waste of various and different natures. The materials were kindly provided by the partners of the various projects and the companies we collaborate with. The complete list of projects and companies involved is reported at the end of this work.

This activity's ultimate goal is to formulate results that can be exploited through technology transfer. The two most sought-after results were creating turnkey plants or specific recipes that could be transferred to potential investors. To reach this goal, we started from the laboratory scale and evaluated the possibility of scale-up towards a pilot scale. Industrial scale applications were evaluated for successful pilot scale processes.

ABOUT THE THESIS

The thesis has been set up with a schematic structure. Chapter 1 presents a general introduction to the problem of recovering materials and energy from end-of-life products or their components. This introduction explains the importance of recovery processes within a cultural paradigm increasingly based on a circular economy.

Each of the following chapters is related to a different type of material. In Chapter 2, spent catalysts from Oil&Gas sector are considered. In Chapter 3, we talk about the problem related to electronic equipment, particularly the treatment of printed circuit boards. Chapter 4 illustrates the analyses made for photovoltaic panels. Finally, in Chapter 5, the treatment of permanent magnets from different types of equipment is examined.

The structure of each chapter has been designed on the classic structure found in research articles. Each chapter introduces the problem of dealing with that specific material. The Materials and Methods section follows, where the materials used and the different procedures are described. Subsequently, there is a section of Results and Discussions where the most important results of the analyses described in Materials and Methods are reported, with comments relating to interpreting the results obtained. Each

chapter closes with the Conclusions section, briefly summarizing the main conclusions. At the end of the thesis, there is a chapter with the conclusions and appendices with market analyses.

THESIS OBJECTIVES

The work presented in this thesis is focused on developing and optimizing sustainable processes with an approach to circular economy for the recovery of precious and base metals from different types of industrial waste. In particular, this research has been aimed at:

- Development of a new hydrometallurgical process, sustainable from a technological, economic, and environmental point of view for the recovery of vanadium and molybdenum from spent Oil&Gas catalysts.
- Study and optimization some steps of the Gold-REC1 and Gold-REC2 processes for recovering precious and base metals from end-of-life printed circuit boards.
- Development of a new hydrometallurgical process, sustainable from a technological, economic, and environmental point of view for the recovery of silver and silicon from end-of-life photovoltaic panels.
- Optimization of some steps of the Hydro-Nd process for the recovery of rare-earth elements from end-of-life permanent magnets..

ACKNOWLEDGMENTS

I express my appreciation to the many students, instructors, and colleagues who have dedicated their time to help me during my research activities in the last three years. In particular, I would like to thank Prof. Francesco Vegliò for allowing me to join his research group and to be able to grow professionally thanks to his teachings and advice.

I would like to thank Prof. Ionela Birloaga for carefully following my first steps in this beautiful world of research and for giving me good foundations to carry out any experimental activity. The contributions of Prof. Ida De Michelis, Prof. Francesco Ferella, Prof. Valentina Innocenzi, Dr. Nicolò Maria Ippolito, Dr. Svetlana Borisovna Zueva, Dr. Valentina Corradini, Dr. Marco Passadoro and Mr. Marcello Centofanti with whom I have worked have been invaluable. They have provided an intellectually stimulating environment in which to work.

Dr. Vittorio Ricci and Dr. Nicola Stampone also significantly contributed to this research activity with their suggestions. A special thanks goes to Ms. Fabiola Ferrante for her support in the various activities.

I thank the University of L'Aquila and its staff for supporting this research.

Contents

Chapter 1 - Abstract	3
Chapter 1 - Preface	4
Chapter 1 - Introduction	10
1.1 Critical Raw Materials	13
1.1.1 Silver.....	16
1.1.2 PGMs.....	19
1.1.3 REEs.....	23
1.1.4 Vanadium.....	30
1.1.5 Molybdenum.....	32
Chapter 2 – Oil&Gas Catalysts	35
2.1 Introduction.....	35
2.1.1 Oil&Gas sector	35
2.1.2 LCF Catalysts	37
2.1.3 Recovery processes.....	38
2.2 Materials	40
2.2.1 Sample	40
2.3 Methods.....	41
2.3.1 GULF Process.....	41
2.3.2 Citric acid Process	47
2.3.3 ORIM-CAT2 Process.....	47
2.4 Results and Discussions	51
2.4.1 GULF Process.....	52
2.4.2 Citric acid process.....	71
2.4.3 ORIM-CAT2 Process.....	72
2.4.4 Rotary Kiln Optimization	95
2.5 Conclusions.....	101

Chapter 3 - Printed Circuit Boards.....	104
3.1 Introduction.....	104
3.2 Materials	106
3.2.1 Arduino Board	106
3.2.2 EuroLCDs Board	106
3.3 Methods.....	107
3.3.1 Arduino disassembly.....	107
3.3.2 EuroLCDs Board Treatments.....	108
3.3.3 ASPEN PLUS Simulation.....	110
3.4 Results and Discussions	112
3.4.1 Arduino Characterization.....	112
3.4.2 EuroLCDs Board Results.....	115
3.4.3 ASPEN PLUS Simulation Results.....	116
3.5 Conclusions.....	119
Chapter 4 - Photovoltaic panels.....	121
4.1 Introduction.....	121
4.1.1 PV Panel Market Share.....	123
4.1.2 PV Panel Components	123
4.1.3 PV Panel Composition.....	125
4.1.4 Recycling Processes.....	126
4.2 Materials	126
4.3 Methods.....	128
4.3.1 Process optimization.....	128
4.3.2 Kinetic Analysis.....	131
4.4 Results and Discussions	134
4.4.1 Process optimization.....	134
4.4.2 Kinetic results	138
4.5 Conclusions.....	143
Chapter 5 - Permanent magnets.....	145
5.1 Introduction.....	145
5.1.1 Recycling processes.....	148
5.2 Materials	149
5.3 Methods.....	150
5.3.1 Process optimization.....	150
5.3.2 Kinetic Analysis.....	153
5.4 Results and Discussions	153
5.4.1 Process optimization.....	153
5.4.2 Kinetic results	172

5.4 Conclusions.....	178
Chapter 5 - Conclusions.....	180
Bibliography.....	182
Appendix A.....	186
Figures.....	196
Tables.....	200
Projects & Companies.....	202

1

Introduction

Many define progress as the elimination of compromises. Indeed, progress often involves the removal of old compromises, that is, temporary solutions that were necessary to solve problems in the past but now prove obsolete or limiting. Eliminating these trade-offs paves the way for new solutions, leading to further progress. Reflecting on human history, infinite examples can be observed to support this definition. To date, one of the most significant compromises concerns the contrast between development and pollution.

In recent decades, the world has witnessed enormous economic growth and technological development, leading to unimaginable benefits in many sectors. However, this progress has come at a significant cost to our planet. Environmental pollution has become a serious global problem that threatens our health, biodiversity, and the balance of ecosystems. Faced with this challenge, a crucial debate has opened on the contrast between development and pollution. While the desire for economic growth and human well-being drives progress, negative environmental impacts threaten our future and require urgent solutions.

In the modern sense, the concept of development is often associated with the increase in industrial production, the expansion of infrastructure, and economic growth. Technological progress and innovation have made it possible to improve people's quality of life by increasing productivity, creating new jobs, and providing essential services such as energy, transport, and communications. However, this development model has also led to increased pollution in various forms: the emission of greenhouse gases, deforestation, water and air pollution, the accumulation of waste, and the loss of natural habitat.

Pollution has become a serious problem that endangers both ecosystems and human health. The emission of greenhouse gases, such as carbon dioxide, is the leading cause of climate change, which results in extreme weather events, droughts, and rising sea levels and threatens food and water security. Air pollution is responsible for millions of premature deaths every year due to the increase in respiratory and cardiovascular diseases. Water pollution, caused by industrial and agricultural discharges, threatens water security and the survival of aquatic ecosystems, putting biodiversity at risk. Furthermore, plastic waste accumulation in our oceans is a massive threat to marine wildlife and the food chain.

The issue of the contrast between development and pollution presents itself as a crucial challenge for humanity. How can we balance the desire for economic progress with the need to protect the environment and ensure a sustainable future for future generations? This question has led to debates between governments, international organizations, companies, and environmental activists. On the one hand, some argue that economic progress and technological development are necessary to improve people's quality of life and address global challenges such as poverty, hunger, and disease. These supporters of industrialization believe that it is possible to reduce environmental impact and find sustainable solutions through innovation and technological efficiency. They highlight the importance of

economic growth to fund scientific research, promote education, and improve infrastructure, which can help reduce pollution.

On the other hand, some warn about the risks of an unsustainable development model. These critics argue that the irrational exploitation of natural resources and environmental pollution resulting from human activity is destroying the ecosystems that support life on Earth. They call for a transition towards a green economy based on renewable energy, sustainable agricultural practices, and responsible production and consumption models.

To successfully address the conflict between development and pollution, adopting an integrated approach involving governments, the private sector, non-governmental organizations, and civil society is necessary. Investments are needed in the research and development of clean and sustainable technologies, in the promotion of energy efficiency, in the conservation of ecosystems, and in raising public awareness of environmental issues. Furthermore, effective policies and regulations are essential to encourage businesses to adopt sustainable and environmentally responsible practices.

In addition to promoting sustainable practices and reducing pollution resulting from human activities, another crucial aspect to consider in the contrast between development and pollution is the recovery of raw materials from secondary sources. This concept refers to recovering and recycling materials from slag, industrial waste, and discarded products to reduce dependence on mining and minimize the associated environmental impact. We find metals among the raw materials of particular economic and strategic importance.

Metals and minerals are an integral part of our daily lives. These raw materials are essential to the functioning and integrity of a wide range of industrial ecosystems. Tungsten makes phones vibrate, gallium and indium are integral parts of light-emitting diode (LED) technology found in lamps, semiconductors require silicon metal, and hydrogen cells require platinum group metals. The need for large quantities of these raw materials harms our planet through greenhouse gas emissions, water stress, and biodiversity loss.¹

Suppose looking at the geographical distribution of the different mineral deposits on Earth. In that case, it is possible to immediately notice that no country can produce all the mineral resources modern society requires. This aspect means that international trade plays a very critical role in the supply of these raw materials. Many countries depend on metal trade for their economies, so the ability to export or import metals can influence their economic growth and the well-being of their communities. Furthermore, metal trading contributes to the creation of jobs, the transferability of technological and scientific knowledge, and the development of sustainable economies. International metals trade also has the potential to promote international cooperation and peace between nations.

From this perspective, a complex global network links production, export, import, and use together. This network must continually adapt to national and international scientific, technological, political, and economic developments.

The recent crisis has highlighted this network's fragility, particularly regarding the supply chain. This factor has highlighted many countries' need for national resilience to potential supply disruptions and market changes. One of these areas is the European Union (EU). The distribution of mineral deposits on Earth is undoubtedly at a clear disadvantage compared to other large global political entities such as China and the United States.

From this perspective, starting a real transition towards a circular economy is even more necessary. In it, a product is not used, thrown away, and sent to landfill but undergoes various recovery processes. This concept allows us not only to partially stem the problems related to the supply of raw materials but also to significantly reduce the impact of our human activities on the planet's health.

New life is given to all those products that can have value once recovered. In this way, the life cycle of a product/object is made longer, and the quantity of waste is reduced. Once the product has completed its life cycle, it is reintroduced into a production cycle, which generates further value. Adopting a circular approach means reviewing all production phases and paying attention to the entire supply chain involved in the production cycle. This attention passes through respect for some basic principles, which the Ellen Mc Arthur Foundation has identified in 5 fundamental criteria:

- **Eco-Design:** Designing the products thinking about their use at the end of their life, therefore with characteristics that will allow them to be dismantled or renovated;

- Modularity and versatility: Give priority to the modularity, versatility, and adaptability of the product so that its use can adapt to changing external conditions;
- Renewable energy: relying on energy produced from renewable sources, encouraging the rapid abandonment of the energy model based on fossil fuels
- Ecosystem approach: think holistically, paying attention to the entire system and considering the cause-effect relationships between the different components
- Recovery of materials: Encourage replacing virgin raw materials with secondary raw materials from recovery chains that preserve their qualities.²

Currently, much of metal recycling relies on traditional processes such as smelting. However, these methods can be energy inefficient and result in the production of harmful waste and by-products. To overcome these limitations, new approaches and more advanced technologies are needed.

One of the areas in which notable progress is being made is the application of technologies for the selective extraction and recovery of metals from aqueous solutions, known as "hydrometallurgy". These processes use specific reagents to extract and separate desired metals from solutions containing different types of metals. Hydrometallurgy offers numerous advantages, including excellent selectivity in metal separation and reduced waste generated during recovery.

Another promising approach is the application of biotechnology in metal extraction and recovery. Some microorganisms, such as bacteria and fungi, can bind and accumulate certain metals in their cellular structures. These microorganisms can recover metals from secondary sources, such as industrial waste and wastewater.

Some researchers are exploring using porous materials, such as coordinated organic metals (MOFs) and zeolites, which can capture and concentrate metals from aqueous or gaseous solutions. These materials can then be processed to recover the precious metals and reduce dependence on mining.

This text presents in detail some innovative processes, some of which are patented, for recovering various precious or critical raw materials. Most of these processes fall into the category of hydrometallurgical processes.

Hydrometallurgy is based on several fundamental principles that guide extracting and separating metals. First, hydrometallurgy exploits the ability of aqueous solutions to solubilize metal compounds. Through controlled chemical reactions, metals in waste materials or industrial waste are dissolved in aqueous solutions, forming soluble metal complexes. These complexes can then be separated and recovered through subsequent processes.

A second fundamental principle of hydrometallurgy is selectivity in the separation of metals. Since many aqueous solutions contain different types of metals, it is necessary to develop specific chemical strategies and agents to extract and separate the desired metals. This aspect is crucial to ensure adequate recovery and minimize the use of chemical reagents.

Another essential principle is the management of by-products and waste generated during the hydrometallurgy process. While hydrometallurgy reduces environmental impact compared to traditional methods, properly managing by-products and waste is still necessary. Developing strategies for recycling and treating waste is crucial to minimize the overall environmental impact.

Hydrometallurgy finds wide applications in the recovery of metals from various secondary sources. One of the areas where it is widely used is the recovery of precious and critical metals from electronic waste, spent catalysts, and industrial waste.

Another critical application of hydrometallurgy is recovering metals from inactive or abandoned mines. Many mines still contain significant metals, but traditional mining may no longer be economical or sustainable. Hydrometallurgy offers a promising alternative where metals can be extracted in situ. This approach reduces the need to move large quantities of material and can reduce the environmental impact of traditional mining.

Despite the advantages of hydrometallurgy, there are still significant challenges to its full development and use. One of the main challenges concerns optimizing metal extraction and separation processes. It is necessary to discover more selective and efficient chemical agents to extract desired metals and minimize the formation of unwanted by-products. Furthermore, hydrometallurgy requires accurate control of process parameters, such as temperature, pH, and reagent concentration. Optimization of these parameters is essential to ensure effective metal recovery and minimize the use of energy and chemical reagents. Further research and development are needed to improve the

understanding of metal extraction and separation mechanisms and develop predictive models to optimize processes.

Implementing new metal recovery processes requires significant investments in equipment and infrastructure, which could represent a barrier to large-scale adoption. However, the numerous ongoing research is bringing to light increasingly high-performance and economically sustainable processes.

1.1 CRITICAL RAW MATERIALS

Critical Raw materials (CRMs) are raw materials of fundamental economic and strategic importance for the European economy and present a high risk associated with their supply source.³ They constitute the basis of the European economy as they guarantee to create jobs and competitiveness; furthermore, they are essential for maintaining and improving the quality of life. Although all of them are important, some are of more significant concern due to the points seen initially, given the high risk of interruption of supplies.

In order to be classified as CRMs, some important relationships and parameters have been introduced. The two main parameters used to determine criticality for the EU are economic importance (EI) and supply risk (SR). The list of CRMs will be established based on exceeding both threshold limits defined by the European Commission. The data used, based on an average of the various values measured over the last five years, take into account their priority, quality, and availability; it is no coincidence that priority is given, in decreasing order, to official EU sources, official sources of individual member states and finally those of states outside the EU.^{4,5}

ECONOMIC IMPORTANCE (EI)

This parameter aims to provide an idea of the importance of the material for the EU economy in terms of its final application use and the value added to the corresponding manufacturing sectors classified according to NACE Rev.2. The parameter is calculated using the relationship:

$$EI = \sum_S (A_S \cdot Q_S) \cdot SI_{EI}$$

Where A_S is the quantity of a raw material in the end use relating to the NACE Rev. 2 sector (2-digit level), Q_S is the added value (AV) of the S sector to which we refer (always in relation to NACE Rev. 2 (2-digit level)), SI_{EI} is a correction factor described below and the subscript S denotes the corresponding sector of NACE Rev. 2.

The economic importance is corrected by the substitution index SI_{EI} , which will evaluate the possible replacement of the raw material with a second one available on the market, which depends on the technical performance and cost-effectiveness of the substitutes considered.⁶ It will, therefore, measure the difficulty of substitution, calculated and weighted on all final applications, with values between 0 and 1, where 1 indicates the least replaceable raw material. The substitution index is calculated with the following relationship.⁵

$$SI_{EI} = \sum_i \sum_a (SCP_{i,a} \cdot Sub - share_{i,a} \cdot share_a)$$

Where i denotes the single substitute material, a denotes the single application of the substitute material, SCP (substitute cost performance parameter) is the parameter that quantifies the ability to replace the raw material analyzed with another in our application, based on technical and performance economics of the materials considered; it is calculated thanks to **Table 1**. Sub – Share represents the sub-part of each replacement material within each application; Share is the share of raw materials in the final application.

Table 1. Matrix for evaluating the SCP parameter.⁵

Substitute material cost	Substitute material technical performance		
	Similar performance	Reduced performance	Performance in case of no substitute
Very high costs (more than 2 times)	0.9	1	1
Slightly higher costs (up to 2 times)	0.8	0.9	1
Similar or lower costs	0.7	0.8	1

SUPPLY RISK (SR)

This parameter aims to explain the risk of possible supply disruptions to the EU. It is based on the concentration of primary supply from raw material-producing countries. It is calculated in the so-called "bottleneck" phase (typically extraction or processing), where the greatest supply risk is present. It is calculated as below:

$$SR = \left[(HHI_{WGI,t})_{GS} \cdot \frac{IR}{2} + (HHI_{WGI,t})_{EU\ sourcing} \cdot \left(1 - \frac{IR}{2}\right) \right] \cdot (1 - EoL_{RIR}) \cdot SI_{SR}$$

Where *HHI* is Herfindahl-Hirschman index; *IR* is import resilience; *GS* indicates global supply; *EU sourcing* indicates European supply; *WGI* is the scaled global governance index; *t* is the commercial parameter that regulates the *WGI*; *EoL_{RIR}* is the input rate of end-of-life recycling; *SI_{SR}* is a corrective factor described below. The supply risk is corrected by the substitution index *SI_{SR}*, which will evaluate the physical availability of a candidate material to replace the main raw material in various applications. To calculate the individual items listed previously, please refer to the bibliographic source analyzed.^{5,6}

In light of these parameters, the various materials are evaluated, defining whether or not they belong to the list of CRMs. **Figure 1** shows all the raw materials updated to 2023 in the SR versus EI graph. From the analysis, the following list of CRMs is obtained:


Table 2. 2023 Critical Raw Materials (new CRMs in italics).⁷

aluminum/bauxite	coking coal	lithium	phosphorus
antimony	<i>feldspar</i>	LREE	scandium
<i>arsenic</i>	fluorspar	magnesium	silicon metal
baryte	gallium	<i>manganese</i>	strontium
beryllium	germanium	natural graphite	tantalum
bismuth	hafnium	niobium	titanium metal
boron/borate	<i>helium</i>	PGM	tungsten
cobalt	HREE	phosphate rock	vanadium
		<i>copper*</i>	<i>nickel*</i>

1.1.1 Silver

1.1.1.1 Overview

Silver is a chemical element with atomic number 47. Silver is one of eight precious or noble metals resistant to corrosion. This metal is soft, very malleable and ductile and has all metals' highest electrical and thermal conductivity values.



H																	He	
Li	Be											B	C	N	O	F	Ne	
Na	Mg											Al	Si	P	S	Cl	Ar	
K	Ca	Sc	Ti	V	Cr	Mn	Fe	Co	Ni	Cu	Zn	Ga	Ge	As	Se	Br	Kr	
Rb	Sr	Y	Zr	Nb	Mo	Tc	Ru	Rh	Pd	Ag	Cd	In	Sn	Sb	Te	I	Xe	
Cs	Ba	La	Hf	Ta	W	Re	Os	Ir	Pt	Au	Hg	Tl	Pb	Bi	Po	At	Rn	
Fr	Ra	Ac																
			Ce	Pr	Nd	Pm	Sm	Eu	Gd	Tb	Dy	Ho	Er	Tm	Yb	Lu		
			Th	Pa	U	Np	Pu	Am	Cm	Bk	Cf	Es	Fm	Md	No	Lr		

Figure 3. Photographic aspect of silver and position in the periodic table.

The concentration of silver in the Earth's crust is relatively low, with 53 ppm in the upper crust. Silver is almost always monovalent in its compounds; it is not a chemically active metal but reacts with nitric acid (which forms nitrate) and hot, concentrated sulfuric acid. It does not oxidize in the air but reacts with the hydrogen sulfide to form silver sulfide (oxidation). It is stable in water.⁸

1.1.1.2 Uses

These properties make it one of the metals found in electronic components such as wires and electrical contacts in printed circuit boards, switches, relays, electrical connectors, and chips. It is also used in high-frequency electronic components such as antennas and radars. Silver is also present in medical devices such as pacemakers and defibrillators, EEC, and ECG.^{9,10}

Furthermore, thanks to its properties, silver is also used in welding or brazing. Adding silver to the soldering or brazing process helps produce smooth, watertight, electrically conductive, and corrosion-resistant joints. Silver brazing alloys are used in everything from air conditioning and refrigeration to electrical power distribution. Silver brazing and soldering combine high tensile strength, ductility, and thermal conductivity. Silver-tin solders are used to bond copper pipes in homes, where they not only eliminate the use of previously used harmful lead-based solders but also provide pipes with the natural antibacterial action of silver.

Refrigerator manufacturers use silver-based binding materials to provide the flexibility for constant temperature changes in cooling tubes. Due to health concerns, the traditional 63% tin and 37% lead solder used to build electronic equipment is rapidly replaced by a combination of silver, tin, and copper.^{9,10}

A recent article from June 2023 published by the Silver Institute deals with different and innovative applications of silver thanks to its numerous properties.⁹ Some researchers from Duke, University of Durham in North Carolina, have experimented with replacing lithium in batteries with argyrodite, a silver, selenium, and tin mineral. The research group still uses "machine learning", a branch of artificial intelligence capable of simulating such combinations to find the optimal combination of chemical substances. The main advantage of using argyrodite is that it allows the battery to be in a "solid-state" meaning that there are no electrolyte liquids in the battery, as is the case with lithium cells, as liquids

make batteries sensitive to high temperatures causing gradual degradation and producing what engineers classify as "thermal catastrophes": fires and explosions. Furthermore, acid-rod batteries would allow cars to recharge faster, be safer, and last longer.^{9,10}

Another interesting application of silver is silver nanoparticles for membranes capable of separating oil from water. Some Chinese scientists have managed to produce a membrane by electrospinning, a process in which drops of a liquid polymer are found which, when hit by an electric current, can stretch its fibers. The result was a membrane that was 99% effective at separating oil from water. The addition of silver nanoparticles increases the membrane's ability to better separate water from the oil and the duration of the membrane itself, which becomes more resistant and rough. Furthermore, the silver nanoparticles make the membrane antibacterial, delaying the growth of the microbial film that causes clogging. A team led by the University of Houston has discovered that silver nanoparticles can be used as welds by connecting the hot and cold sides of thermoelectrics over a wide temperature range without diminishing the electrical power of the silver or melting it. The researchers tested different silver nanoparticles on widely used thermoelectric materials, each producing electricity at a different temperature. As long as the heat does not exceed approximately 960°C (the melting point of pure silver), the silver nanoparticles for soldering will remain stable. For example, a lead-tellurium-based module, operating between approximately 300°C and 550°C, produced a heat-to-electricity conversion efficiency of approximately 11% and remained stable after 50 thermal cycles.^{9,10}

Scientists at the University of California at Los Angeles have taken a cue from nature to develop a process to produce soft, electrically conductive materials, such as fibers at room temperature, that resemble how spiders spin their webs. The fibers are made of a synthetic polymer and silver ions that conduct electricity. The combination is then dissolved in a solvent used to produce synthetic fibers. The resulting fiber exhibits rubber-like elasticity with a strength equal to that of cotton and is used to make a sensing smart glove and face mask that is durable, stretchable, and conductive of electricity. The glove can detect hand movements, and the mask can monitor the wearer's breathing patterns, among other abilities.^{9,10}

Silver has even greater germ-fighting properties when infused with so-called "bioglass," biomaterials made of silicone often used for bone grafts. Researchers at the University of Birmingham (UK) tested these materials on a biofilm of *Pseudomonas Aeruginosa*, a bacterium that usually spreads in hospitals through contaminated hands, equipment, and surfaces. The bacterium is resistant to many antibiotics and often causes infections in chronic wounds. The researchers found that the silver-bioglass combination was five times more effective against the spread of this particular microbe than silver alone.^{9,10}

Additionally, silver is a crucial component in producing synthetic gas or "syngas," which helps eliminate carbon dioxide pollution from production facilities. Another interesting application of silver is as a key part of an "artificial leaf" produced by scientists at the University of Cambridge (UK), which uses sunlight to convert water and carbon dioxide directly into ethanol and propanol. This process produces so-called "drop-in" fuels, which provide energy directly to internal combustion engines by mimicking the photosynthesis process of plants. The artificial leaf is composed of layers of silver, glass, copper, and graphite, while the catalyst that initiates the chemical reaction is composed of copper and palladium. According to Virgil Andrei, co-lead author of the research paper from the team at Cambridge's Yusuf Hamied chemistry department, artificial leaves could substantially reduce the fuel cost of sustainable production, but because they are heavy and fragile, they are challenging to produce and transport on a large scale. While the technology still requires some development, researchers will continue the study to produce light absorbers and catalysts that can help convert sunlight into fuel.^{9,10}

1.1.1.3 EU Supply Chain

Silver prices increased significantly in 2011, reaching an all-time high of 35 US\$/troy ounce in 2022. Silver prices are more volatile than gold because silver markets are smaller than those of other metals (such as gold).⁸

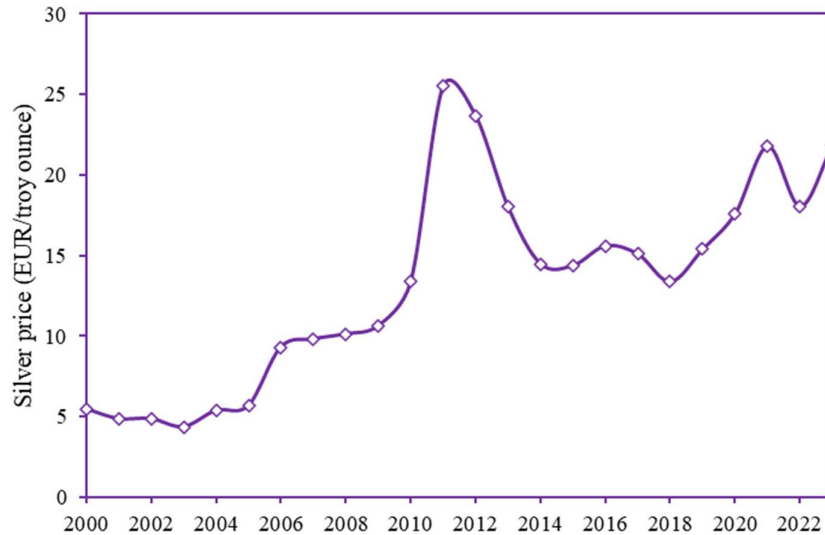


Figure 4. Annual average price of silver in the period 2000-2023.

PRIMARY SUPPLY

According to the Silver Institute, in 2021, the global supply of silver (from primary and secondary sources) reached 31 kton, an increase of 5% compared to 2020. Demand for silver was slightly higher at around 33 kton (an increase of 19% compared to 2020). In 2020, national silver mining within the EU produced approximately 2 kton of silver (Eurostat, 2022). This quantity mainly flows into European supply chains, reducing dependence on imports, albeit to a very limited extent.⁸

Mexico is the world's largest producer of silver ore, contributing approximately 24% of the total global supply. This country is by far the largest producer of silver ore, while most other countries produce silver as a byproduct of mining other metals. In fact, in 2021, 72% of mined silver production came from lead-zinc, copper and gold mines.⁸

Table 3. Silver supply and demand in metric ton, 2016-2020 average.⁸

Global production (<i>kton</i>)	Global producers	EU Consumption (<i>kton</i>)	EU Share	EU Suppliers	Import Reliance
27.5	Mexico 24%	19.5	71%	Mexico 41%	54%
	Peru 14%			Argentina 27%	
	China 13%			Peru 15%	
	Chile 5%			Bolivia 11%	
	Russia 5%			Canada 2%	

SECONDARY SUPPLY

The global end-of-life silver recycling input rate is estimated to be around 19% in 2020. It should be mentioned that several other end-of-life recycling input rate (EoL-RIR) percentages are reported, ranging between 20-80%. At the European level, the EoL-RIR is 4.23%, the highest rate recorded due to the high price of silver. For applications where the use of silver is less dissipative, for example, in vehicle electrical and electronic parts and electronics, losses occur during metallurgical collection, shredding, and recovery operations.⁸

especially metal oxides, for the electronics industry. Examples are YAG crystals for lasers, LSO and GSO crystals for medical scanners, and X-ray scanners for baggage and container screening.

In the electrochemical field, iridium and ruthenium oxides coat the anodes of chlor-alkali industry equipment for producing chlorine. Iridium is also used in the coatings of anodes used in electro-galvanization electrolytic extraction and electrodes used in the electrolytic chlorination of water process (along with ruthenium).

In the chemical field, the catalytic properties of iridium allow the manufacture of catalysts that promote hydrogenation, acetic acid synthesis, and hydroformylation for the production of aldehydes, as well as use together with platinum in some applications such as reforming in petroleum refining. Other uses concern the automotive sector, where they participate in components to control exhaust gas emissions.⁵

OSMIUM

Due to the high toxicity of Osmium oxide, this element is rarely used pure but combined with other metals in applications that require high wear resistance. An example of application is Osmium alloys, in which the presence of this metal aims to increase the hardness of the alloy. It is used to make fountain pen nibs, record player needles, pins, electrical contacts, and other platinum group metals. Other applications include tissue staining, microscopy slide preparation, surgical implants, and fingerprinting.⁵

PALLADIUM

Among the main applications of palladium, we find catalysts in the automotive sector, electronics, and the production of chemical products.

The catalyst market covers palladium demand by up to around 80%. In this application, palladium is used as the dominant active ingredient (often with rhodium) to control emissions of pollutants in combustion gases, mainly in petrol engine vehicles (in diesel engine vehicles, the use is reduced).

As regards the electrical sector, palladium is widely used to create effective and long-lasting coatings for electronic components. These palladium coatings (in addition to guaranteeing durability thanks to the resistance of this element to corrosion) allow for high conductivity. Its most important use is in multilayer ceramic capacitors (MLCCs).

In the chemical industry, palladium is used as a catalyst for numerous reactions that require hydrogen exchange between two reagents, such as in the production of butadiene and cyclohexane. This element catalyzes other reactions to produce terephthalic acid, hydrogen peroxide, and high-purity hydrogen. Furthermore, it is also used for the catalysis of hydrocracking processes.⁵

PLATINUM

The main application of this element is in the automotive sector. In this context, platinum is the main active component in catalytic converters and filters mounted on diesel engines, reducing toxic exhaust emissions by up to 98%.

In the industrial chemical field, many processes involve using platinum-based catalysts. A significant application is the conversion of ammonia to nitric oxide, corresponding to the first step in the nitric acid production process. Platinum-based catalysts are also important in the oil industry, where they are used for refining crude oil. In particular, they are used in the catalytic reforming process of high-octane naphtha.

Other critical applications are the production of specific silicones, the production of paraxylene, an intermediate in the production of PET, and finally, the use as a selective hydrogenation agent in the pharmaceutical industry.

Platinum is also used in the medical field as an active ingredient in anti-cancer drugs, and thanks to its excellent biocompatibility, it is ideal for the electrodes of temporary or permanent biomedical implants such as pacemakers and cardiac defibrillators.

In the electronic field, it is a critical component in the magnetic coating of hard disks, allowing the data storage capacity to increase. It is also used in high-temperature thermocouples, fuel cells as a catalyst, and multilayer ceramic capacitors (MLCCs), although to a lesser extent than palladium. Other secondary applications include its use as a coating for turbine blades and a precious metal for making jewelry.⁵

RHODIUM

As with platinum, the main application for rhodium concerns catalysis in the automotive sector to eliminate harmful emissions from exhaust gases. The demand for rhodium for this application is up to 80% of the total rhodium demand.

Another important use is that of catalysis in the chemical industry, where it acts in an alloy with platinum (Rh 10%) to produce nitric oxide or numerous aldehydes, acetic acid, and hydrogenation reactions.

Other secondary uses concern the manufacture of tools for the glass industry and electroplating surface treatments, which make the mirrors used in optical instruments hard and reflective.⁵

RUTHENIUM

The main applications of ruthenium globally concern catalysis and the electronics industry. In the chemical field, ruthenium-based compounds are used in specific catalytic applications to produce numerous organic and inorganic chemical products. They are used in petroleum refining for the removal of H₂S or the production of caprolactam and adipic acid.

In the electrical sector, platinum-ruthenium alloys play an essential role in the complex structure of the layered materials of hard disks, increasing their data storage capacity per unit of surface area. Furthermore, ruthenium is an alloying element with palladium in thermostats and relays, increasing the abrasion resistance of the electrical contact surfaces.

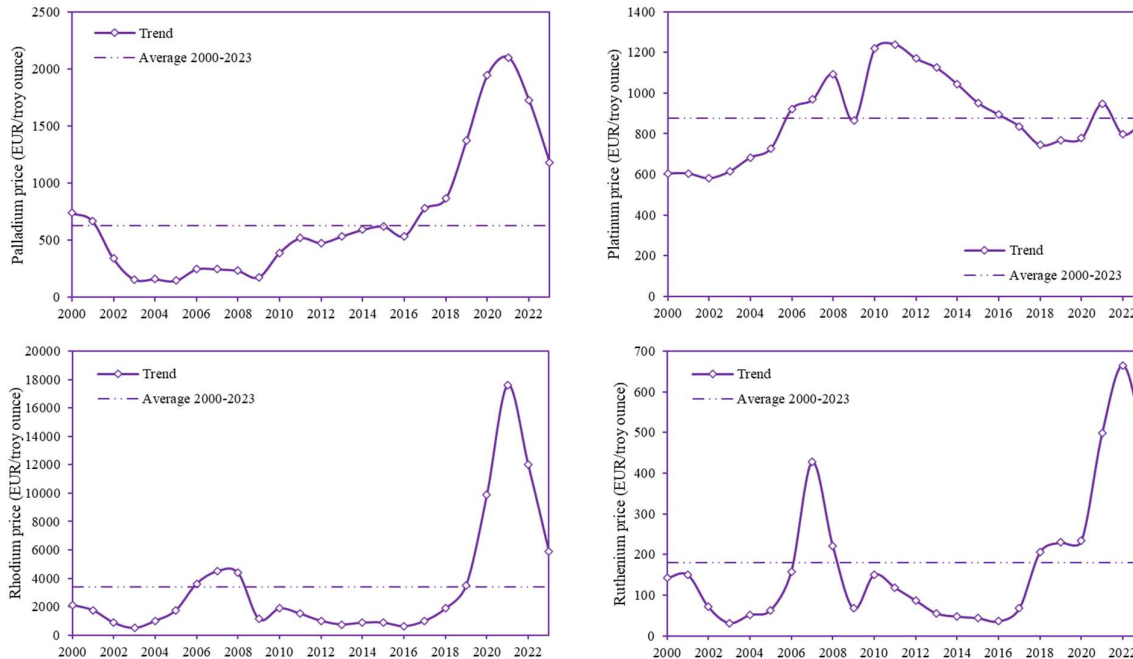
In the electrochemical field, ruthenium oxides are used as coatings for titanium anodes in the chlor-alkaline process to produce chlorine and sodium hydroxide.

A minor use, in combination with iridium, is in the coatings of the electrodes used by devices for the electrolytic chlorination of swimming pools. Other uses in minor quantities concern jewelry, dental applications, and the production of particular blades for turbines (more excellent resistance to creep) in which it is used as an alloying element.⁵

1.1.2.3 EU Supply Chain

PGMs are extremely rare metals in the Earth's crust. For example, iridium is one of the most deficient metals, with an abundance of about 1 part per billion (ppb) in the Earth's crust.

Prices of PGMs are high and generally volatile due to limited availability in nature and their low level of flexibility to accommodate rapid changes in demand.



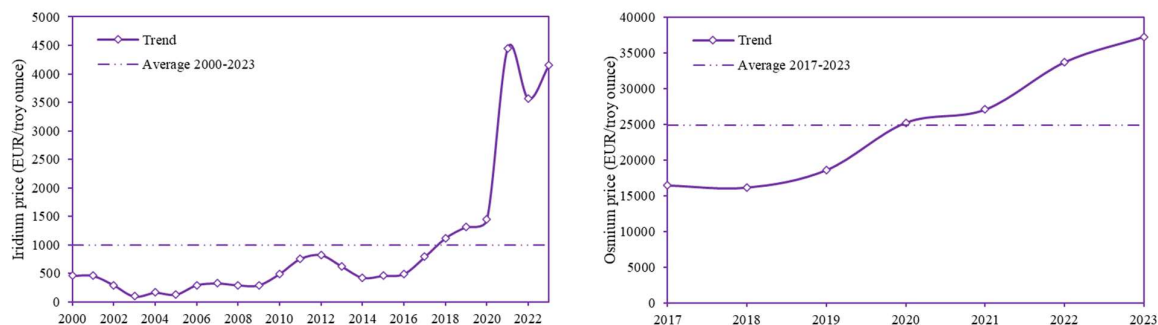


Figure 7. Annual average price of PGMs.

PRIMARY SUPPLY

Due to the geographical location of PGM reserves, mining activities are concentrated in very few countries. The smaller number of mines and the high degree of specialization required translate into fewer companies extracting and refining PGMs. In the short term, introducing more stringent emissions standards for vehicle engines is expected to significantly impact demand for platinum, palladium, and rhodium used in manufacturing car catalysts. Furthermore, an increase in the adoption of fuel cell technology is expected to benefit platinum demand.⁸

SECONDARY SUPPLY

PGMs are highly technically recyclable due to their noble characteristics and durability in use. Very high recovery yields of metal content can be achieved once end-of-life devices containing PGMs reach a modern refining plant.

In this case, the recovery rates for platinum and palladium are even higher than 95%. The metallurgical yields are slightly lower but still high regarding rhodium, iridium, and ruthenium.

In addition to the technical feasibility of recovery from secondary sources, the product is interesting from an economic point of view as PGMs, like all precious metals, have a high intrinsic value. Therefore, the potential for effective recycling is generally excellent, except in some applications and/or when used in minimal quantities.⁸

Table 4. PGMs supply and demand in metric ton, 2016-2020 average.⁸

	Global production (Mine production)	Global Producers	EU Consumption	EU Share	EU suppliers
Iridium	35.1 ton	South Africa	17.3 ton	49%	South Africa
Ruthenium		Zimbabwe			USA
Osmium					Japan
					Switzerland
Palladium	213 ton	Russia	20 ton	9%	USA
		South Africa			Russia
		Canada			UK
					South Africa
					Switzerland
Platinum	185 ton	South Africa	72 ton	39%	UK
		Russia			South Africa
		Zimbabwe			Switzerland
					Russia
Rhodium	23 ton	South Africa	Negative value...		South Africa
		Russia			UK
		Zimbabwe			Russia
					USA
					Mexico

1.1.3 REEs


1.1.3.1 Overview

The term rare earths (Rare Earth Elements, REEs) identifies a group of 17 chemical elements, comprising the lanthanide group, Scandium (Sc), and Yttrium (Y). Despite the name, these elements are relatively abundant on Earth, so much so that the International Union of Pure and Applied Chemistry (IUPAC) advises against using the term "rare earths".¹¹

In the earth's crust, these elements can be present mainly in three states:

- Primary building blocks in the crystal lattice of some minerals, in the form of ionic compounds. Such minerals are typically called "rare earth minerals" (for example, monazite, bastnaesite, and xenotime).
- As impurities, through isomorphous substitution, within other minerals, which may be rock or rare metals. These are referred to as "REE-containing minerals".
- Some minerals contain mica and clay. In these cases, the REEs are easily extractable.¹²

Based on atomic weight, REEs are typically divided into light rare earth elements (Light Rare Earth Elements, LREEs) and heavy rare earth elements (Heavy Rare Earth Elements, HREEs). The two subgroups have different properties and, consequently, different market dynamics. HREEs are more "rare" and, therefore, more expensive.¹³



The image shows several small piles of different colored powders representing various rare earth elements. The colors include shades of yellow, black, grey, and white.

H																	He	
Li	Be											B	C	N	O	F	Ne	
Na	Mg											Al	Si	P	S	Cl	Ar	
K	Ca	Sc	Ti	V	Cr	Mn	Fe	Co	Ni	Cu	Zn	Ga	Ge	As	Se	Br	Kr	
Rb	Sr	Y	Zr	Nb	Mo	Tc	Ru	Rh	Pd	Ag	Cd	In	Sn	Sb	Te	I	Xe	
Cs	Ba	La	Hf	Ta	W	Re	Os	Ir	Pt	Au	Hg	Tl	Pb	Bi	Po	At	Rn	
Fr	Ra	Ac																
			Ce	Pr	Nd	Pm	Sm	Eu	Gd	Tb	Dy	Ho	Er	Tm	Yb	Lu		
			Th	Pa	U	Np	Pu	Am	Cm	Bk	Cf	Es	Fm	Md	No	Lr		

Figure 8. Photographic aspect of REEs and position in the periodic table.

1.1.3.2 Uses

Due to their unique properties, rare earths are used for various military, energy, and industrial applications, ranging from permanent magnets to batteries. Although REEs are often discussed as a group, their properties and applications differ significantly.

SCANDIUM

Scandium is mainly used for research purposes. It has, however, significant potential because it has a density almost as low as aluminum and a much higher melting point. For this reason, a very important application of scandium is in producing lightweight aluminum-scandium alloys for aerospace components¹⁴, in producing high-end bicycle frames and baseball bats.

Scandium iodide is added to mercury vapor lamps to produce a highly efficient light source similar to sunlight. These lamps help cameras reproduce colors well when shooting indoors or at night.

The radioactive isotope scandium-46 is used as a tracer in petroleum refining to monitor the movement of various fractions. It can also be used in underground pipes to detect any leaks.¹⁵

YTTRIUM

Yttrium is used in a wide range of applications.

It is often used as an additive in alloys as its presence increases the strength of aluminum and magnesium alloys.

It is also used in making microwave radar filters and has been used as a catalyst in the polymerization of ethene. Yttrium aluminum garnet (YAG) is used in lasers that can cut metals and in white LED lights.

Instead, if in the form of yttrium oxide, it is added to the glass used to make camera lenses to increase resistance to heat and shock. It is also used to make superconductors.

Yttrium oxysulfide was widely used to make red phosphors for old-style color television tubes. The radioactive isotope yttrium-90 has medical uses and can be used to treat some cancers, such as liver cancer.¹⁵

LANTHANUM

Lanthanum metal has no commercial uses. However, its alloys have a wide range of applications. One of the lanthanum-nickel alloys is used to store H₂ in hydrogen-powered vehicles.

Another application is as an additive in the anodes of nickel-metal hydride batteries used in hybrid cars. Furthermore, lanthanum is an essential component of the mischmetal alloy (in which it is present for approximately 20%). The best-known use of this alloy is in "flints" for lighters.

Lanthanum-containing "rare earth" compounds are widely used in carbon lighting applications, such as studio lighting and film projection. They increase brightness and give an emission spectrum similar to that of sunlight.

Lanthanum(III) oxide is used in producing special optical glasses, as it improves the glass's optical properties and alkali resistance. Lanthanum salts are used in catalysts for petroleum refining.

The La³⁺ ion is used as a biological tracer for Ca²⁺.

Studies are underway for the use of radioactive lanthanum in the treatment of cancer.¹⁵

CERIUM

Cerium is the main component of the mischmetal alloy (where it is present for approximately 50%). As previously mentioned, the best-known use of this alloy is in "flints" for lighters. This application is due to cerium's ability to produce sparks when struck. The only other element that has this ability is iron.

Cerium (III) oxide is used as a catalyst for various chemical reactions in the internal walls of self-cleaning ovens to avoid the accumulation of cooking residues or is used in catalytic converters. Cerium (III) oxide nanoparticles are being studied as an additive for diesel fuel to have more complete combustion and reduce exhaust emissions.

In sulfide, cerium is a deep red, non-toxic compound used as a pigment. In addition, cerium is also used in flat-screen televisions, energy-efficient light bulbs, and projectors.¹⁵

PRASEODYMIUM

The main application of Praseodymium is in the making of alloys. Praseodymium is used in a wide variety of alloys. The high-strength alloy it forms with magnesium is used in aircraft engines. Mischmetal is an alloy containing approximately 5% praseodymium and is used to produce lighter flints. However, the most important alloy from a strategic point of view is undoubtedly the one for manufacturing permanent magnets.

Along with other lanthanide elements, it is used in carbon arc electrodes for lighting.

Praseodymium salts are used to color glass and enamel intense yellow. Praseodymium oxide is a component of didymium glass (along with neodymium). This glass is used in glasses used by welders and glaziers because it filters yellow light and infrared radiation.¹⁵

NEODYMIUM

The most important use of neodymium is making an alloy with iron and boron to make powerful permanent magnets. This discovery, in 1983, made it possible to miniaturize many electronic devices, including cell phones, microphones, speakers, and electronic musical instruments. These magnets are also used in car windshield wipers and wind turbines.

Neodymium is a component, together with praseodymium, of didymium glass. As previously reported, this glass has unique properties that make it essential for making glasses for glass blowing and welding. Neodymium colors the glass with delicate purple, wine, and gray shades. Neodymium is also used in the glass of tanning booths, as it transmits tanning UV rays but not heating infrared rays. Neodymium glass is also used to make lasers. These are used as laser pointers, in eye surgery, in cosmetic surgery, and for treating skin tumors.

Furthermore, neodymium oxide and nitrate are used as catalysts in polymerization reactions. Instead, neodymium versatate is used as a catalyst in butadiene synthesis in the tire manufacturing industry.¹⁵

PROMETHIUM

The application of promethium is linked almost exclusively to research purposes.

However, a small amount of promethium is used in specialized atomic batteries. The latter are about the size of a thumbtack and are used for pacemakers, guided missiles, and radios. Their functioning is due to the decay of promethium. The radioactive decay of promethium is used to make a phosphor emit light, which is converted into electricity by a solar cell.

Promethium can also be used as a source of X-rays and radioactivity in measuring instruments.¹⁵

SAMARIUM

The most important use of samarium is in the production of permanent magnets. Samarium-cobalt magnets are much more powerful than iron magnets, remain magnetic at high temperatures, and are therefore used in microwave applications. These magnets have enabled the miniaturization of electronic devices such as headphones and the development of personal stereos. However, neodymium magnets are now more commonly used.

Samarium is used to dope calcium chloride crystals for use in optical lasers. It is also used in infrared-absorbing glass and as a neutron absorber in nuclear reactors. In the form of an oxide, samarium finds specialized application in glass and ceramics. Similar to other lanthanides, samarium is used in carbon arc lighting for studio lighting and projection.¹⁵

EUROPIUM

Europium is used in the printing of euro banknotes. This application is related to the property of this element to glow red under UV light; as a result, it is possible to recognize fake banknotes by the lack of this red glow.

Some energy-efficient light bulbs use a little europium to provide more natural light, balancing the blue (cool) light with a small quantity of red (warm) light.

Another important property of europium is that it can absorb neutrons excellently, making it valuable in the control rods of nuclear reactors.¹⁵

GADOLINIUM

Gadolinium has useful properties in alloys. Just 1% gadolinium can improve the workability of iron and chromium alloys and their resistance to high temperatures and oxidation. It is also used in alloys to make magnets, electronic components, and data storage disks.

Its compounds are useful in magnetic resonance imaging (MRI), particularly in diagnosing cancerous tumors.

An important property of europium is that it can excellently absorb neutrons, becoming a fundamental element in the control rods of nuclear reactors.¹⁵

TERBIUM

Terbium is used to dope calcium fluoride, calcium tungstate, and strontium molybdate, all used in solid-state devices. It is also used in low-energy light bulbs and mercury lamps. It has been used to

improve the safety of medical X-rays by allowing the same quality image to be produced with a much shorter exposure time. Terbium salts are used in laser devices.

An alloy of terbium, dysprosium, and iron stretches and shortens in a magnetic field. This effect forms the basis of speakers placed on a flat surface, such as window glass, which then acts as a loudspeaker.¹⁵

DYSPROSIUM

Dysprosium is rarely used as a pure metal, as it reacts readily with water and air. The primary use of dysprosium is in neodymium-based magnet alloys. This application is due to the high resistance to demagnetization at high temperatures. This aspect is crucial for magnets used in motors or generators used in wind turbines and electric vehicles.

Dysprosium iodide is used in halide discharge lamps. This salt allows the lamps to emit a very intense white light.

A cermet (ceramic-metal composite material) of dysprosium-nickel oxide is used in nuclear reactor control rods. It readily absorbs neutrons and does not swell or contract when bombarded by neutrons for long periods.¹⁵

HOLMIUM

The main application of holmium is in the nuclear energy sector. Holmium can absorb neutrons, so it is used in nuclear reactors to keep fission chain reactions under control. Furthermore, although in very few applications, its alloys are used in some magnets.¹⁵

ERBIUM

Erbium finds little use as a metal because it oxidizes in contact with air and is easily corroded by water.

When alloyed with metals such as vanadium, erbium reduces their hardness and improves workability.

Erbium oxide is occasionally used in glass that absorbs infrared, for example, in safety glasses for welders and metalworkers. When added to glass, erbium gives the glass a pink tint. It is used to give color to some sunglasses and fake gems.

Another important application is in the production of glass fiber. Including erbium in this material makes it possible to amplify broadband signals carried by fiber optic cables.¹⁵

THULIUM

The only applications of this element are in the medical field. When irradiated, thulium produces an isotope that emits X-rays. This isotope makes a lightweight, portable X-ray machine for medical use. Additionally, thulium is used in lasers with surgical applications.¹⁵

YTTERBIUM

Until recently, this element did not have many applications. However, ytterbium is starting to find an ever-wider variety of uses. To date, it is used in making memory devices and tunable lasers. It can also be used as an industrial catalyst and is increasingly chosen to replace other catalysts considered too toxic and polluting.¹⁵

LUTETIUM

Lutetium is little used outside of research. One of its few commercial uses is as a catalyst for cracking hydrocarbons in oil refineries.¹⁵

1.1.3.3 EU Supply Chain

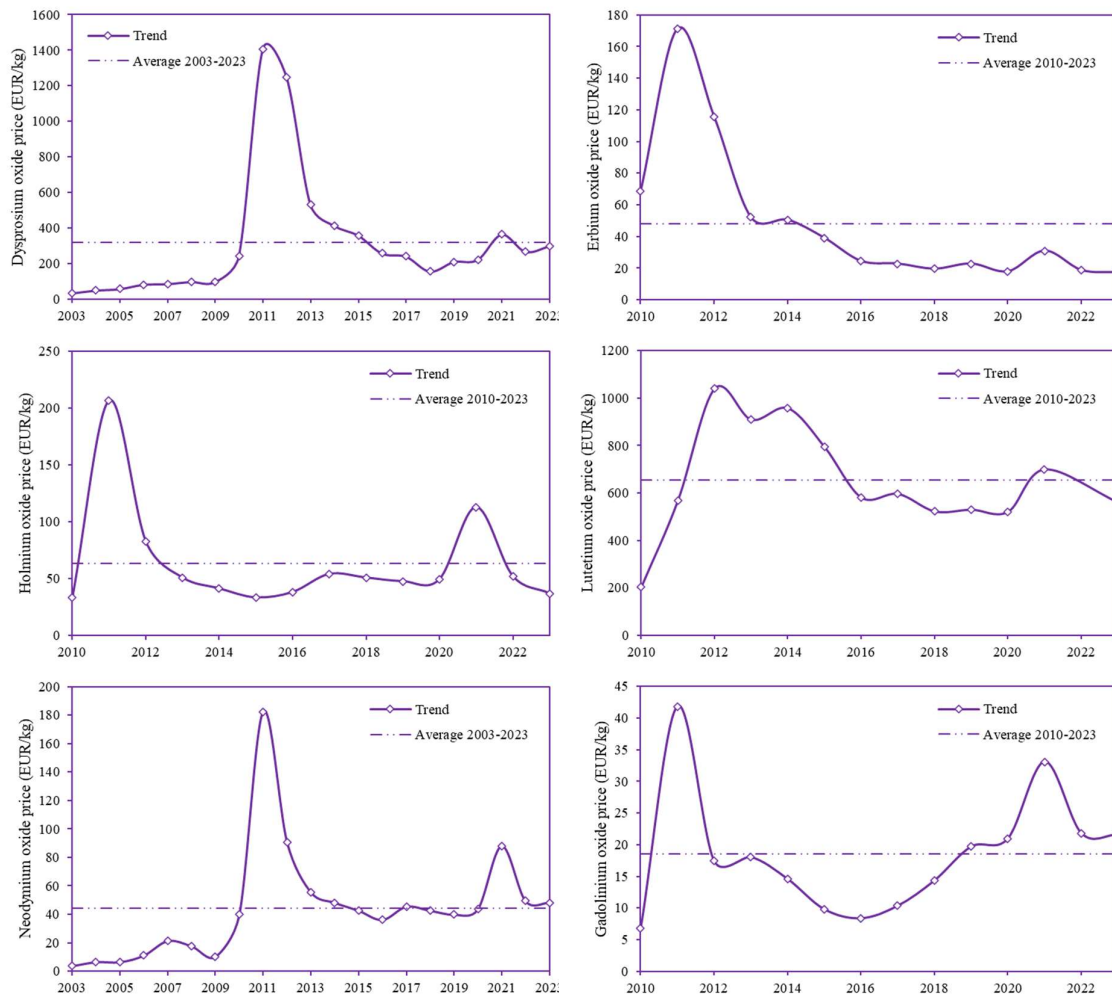
Global mine production of rare earth oxides (REOs) is estimated at approximately 280 kton in 2021, a significant increase compared to 2020 (240 kton). The production of REOs in China was estimated to

be approximately 168 kton in 2022. In 2020, China supplied approximately 62% of the world's primary production of REEs.⁸

The EU imports 100% of its REEs, although some European players are at different stages of the REE value chain. Some can separate individual REOs (Estonia and France) and produce REOs-based products for various industries (phosphors, catalysts, polishing powders, etc.). Some alloy and magnet makers (in Germany and Slovenia) operate with machined materials imported mainly from China. Just outside the EU, there is metal and alloy production capacity in the UK.⁸

Consumption within the EU of rare earths is approximately 4,734 ton/year of compounds (expressed in rare earth oxide) and approximately 683 ton/year of metals of REEs and interalloys in 2016-2018 and is entirely based on imports.⁸

REE prices have undergone significant changes over the last decade. In 2010-2011, the increase was approximately 12 times the initial value, triggered mainly by a misinterpretation by the global market of a significant reduction in China's export quotas in 2010 (not actual exports). This aspect has caused geopolitical tension at a time of strong demand for permanent magnet devices, driven by the expected growth of the renewable energy and electric vehicle markets. By the beginning of 2012, prices had fallen by half and almost continuously until 2019, proving relatively volatile in the short term. **Figure 9** shows the graph with the performance of the main REOs in recent years.⁸



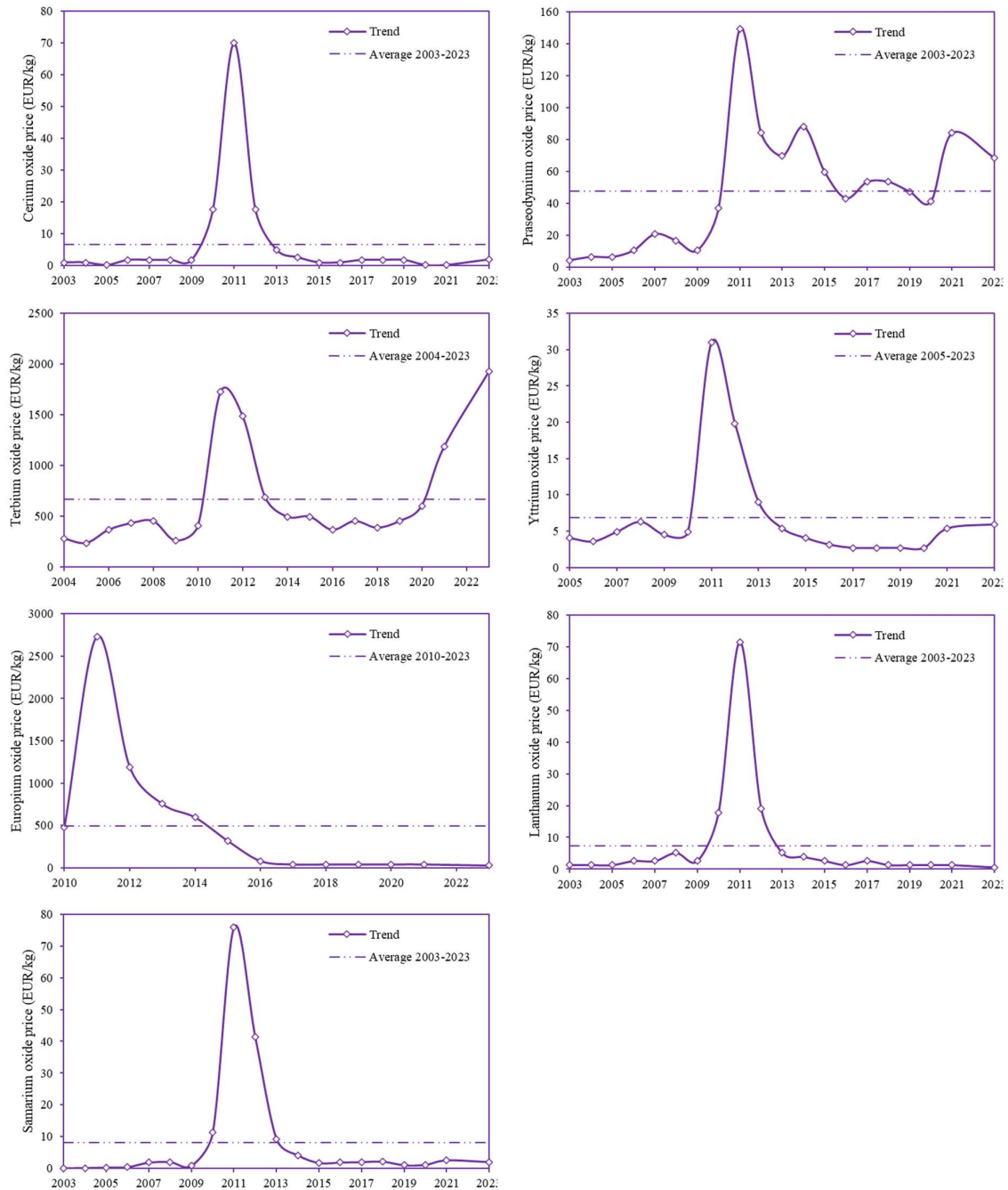


Figure 9. Annual average price of REEs oxides.

PRIMARY SUPPLY

Before the 1990s, less than 10% of rare earth production comprised separated rare earths. In 2011, this percentage was already at 60%, and, to date, the production of lanthanum and cerium oxides represents approximately 70%, praseodymium and neodymium oxides approximately 20%, and other elements represent approximately 10%.

In recent years, the Chinese fraction of global REEs mine production has decreased slightly as some new mines outside China have been activated or reactivated (albeit to a minimal extent).

However, China has steadily expanded its share of downstream value-added production from oxides, metals, alloys, and magnets.⁸

Table 5. REE supply and demand in metric tonnes, 2016-2020 average (in metal content).⁸

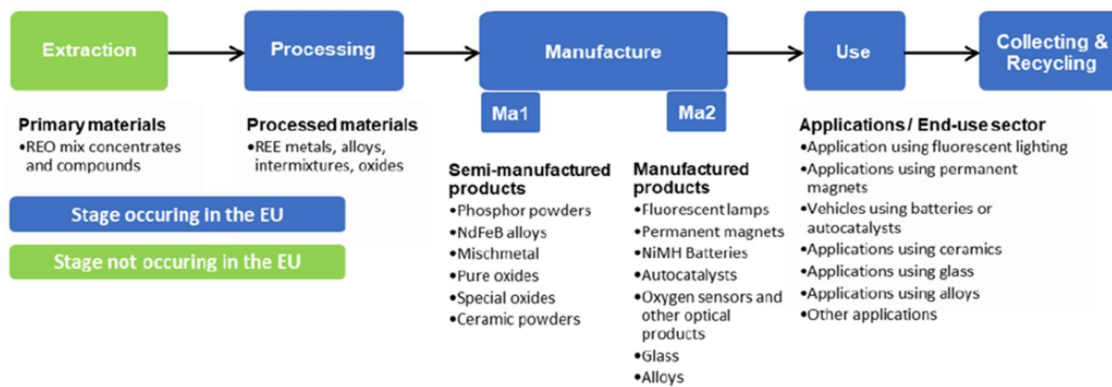
REE	Global production (ton)	Global Producers	EU Consumption (ton)	EU Suppliers	Import Reliance
Ce	57740	China Australia USA Myanmar Russia	4086	Russia 64% China 18% Other countries 7% UK 4%	100
Nd	26845		119	China 80%	100
La	42823		2234	Other countries 11%	
Pr	6860		107	UK 3%	
Sm	3343		265	USA 2%	
Eu	381		386	China 64% Japan 17% UK 8% Russia 5% SouthKorea 3%	100
Tb	182		59		
Gd	1974		170		
Er	478		111		
Y	5133		224		
Ho	12311		23		
Lu	1549		205		
Tm	1544		74		
Yb	186		27		
Dy	708		113		

SECONDARY SUPPLY

Today, the recycling input rate still needs to be higher, usually less than 1%, especially in Europe, due to the lack of efficient collection systems and the prohibitive costs of creating REE recycling capacity.

Higher recycling input rates for europium, yttrium, and terbium are only reported due to the recycling of fluorescent lamps.


Permanent magnets are the main secondary resources for recovering neodymium, praseodymium, dysprosium, and samarium. Chips from shaping and cutting the final magnet represent a potential source of secondary materials, although some issues hamper its large-scale exploitation.⁸

**Figure 10.** Simplified value chain for REE in the EU.⁸

1.1.4 Vanadium

1.1.4.1 Overview

Vanadium is a steel gray metal with atomic number 23. However, the color of its compounds varies greatly depending on the element's oxidation state. Although minerals containing vanadium exist, it is most commonly produced as a byproduct of iron. It has a high melting point and resists corrosion well.



H																	He	
Li	Be											B	C	N	O	F	Ne	
Na	Mg											Al	Si	P	S	Cl	Ar	
K	Ca	Sc	Ti	V	Cr	Mn	Fe	Co	Ni	Cu	Zn	Ga	Ge	As	Se	Br	Kr	
Rb	Sr	Y	Zr	Nb	Mo	Tc	Ru	Rh	Pd	Ag	Cd	In	Sn	Sb	Te	I	Xe	
Cs	Ba	La	Hf	Ta	W	Re	Os	Ir	Pt	Au	Hg	Tl	Pb	Bi	Po	At	Rn	
Fr	Ra	Ac																
			Ce	Pr	Nd	Pm	Sm	Eu	Gd	Tb	Dy	Ho	Er	Tm	Yb	Lu		
			Th	Pa	U	Np	Pu	Am	Cm	Bk	Cf	Es	Fm	Md	No	Lr		

Figure 11. Photographic aspect of Vanadium as a mineral and position in the periodic table.

1.1.4.2 Uses

Vanadium is used in a wide range of applications. Its primary use is in producing strength low alloy steels (HSLA), special steels, special alloys, and catalysts.

In metallurgy, vanadium is an essential alloying element in HSLA steels. The formation of vanadium-rich carbides and nitrides strengthens steel, even by adding a few kilograms per ton of steel. Furthermore, it protects the final product from corrosion and oxidation; most of the vanadium produced (about 80%) is used as ferrovanadium.

Other uses include it combined with titanium to produce a stronger, more stable alloy suitable for critical tools, crankshafts, and gears, and aluminum in titanium alloys to produce materials suitable for high-speed aircraft jet engines.

Another interesting use concerns nuclear reactors since vanadium has low neutron absorption capabilities and does not deform at high temperatures.

In the catalytic field, vanadium-based catalysts are used to process hydrocarbons to remove nickel. Think of vanadine (pentavalent vanadium, V_2O_5) used as a catalyst in the production of sulfuric acid and maleic anhydride or in the manufacture of ceramics, where it is added to glass to produce a green or blue tint.

Another important use concerns the production of vanadium redox batteries, a rapidly growing sector where they are mainly used for the mass storage of solar energy.⁵

1.1.4.3 EU supply chain

Over 2018-2019, vanadium showed the highest price volatility (around 60%) among all materials tracked by DERA, with an upward trend.¹⁶ However, prices remained very stable over the period 2019-2021.¹⁶ The average price in 2020 was around 14 EUR/kg.⁸

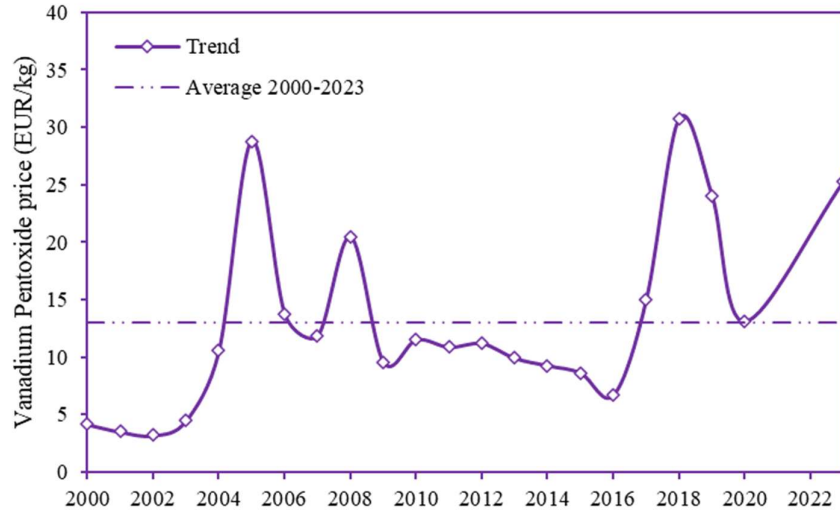


Figure 12. Annual average price of vanadium pentoxide.

PRIMARY SUPPLY

The EU only has small vanadium reserves located in Finland and Sweden. For this reason, the EU does not extract significant quantities of vanadium from ore. Vanadium is imported mainly in the form of oxides (molten flakes powder of V_2O_5 and powder of V_2O_3) and hydroxides.

The second main intermediate product is ferrovandium, with a total import of around 5700 ton in 2021.⁸

Table 6. Vanadium supply and demand in metric tonnes, 2016-2020 average.⁸

Global production (kton)	Global Producers	EU Consumption (kton)	EU Share	EU Suppliers	Important Reliance
91.4	China	61%	12.9	Netherlands	22%
	Russia	20%		Austria	16%
	South Africa	10%		Russia	15%
	Brazil	8%		Germany	7%
			15%		94%

SECONDARY SUPPLY

The primary input for recycling is steel scrap, recycled with vanadium contents and catalysts of exhausted chemical processes. Some tools containing vanadium can also be recycled. The EOL RIR is estimated at 6%.¹⁷

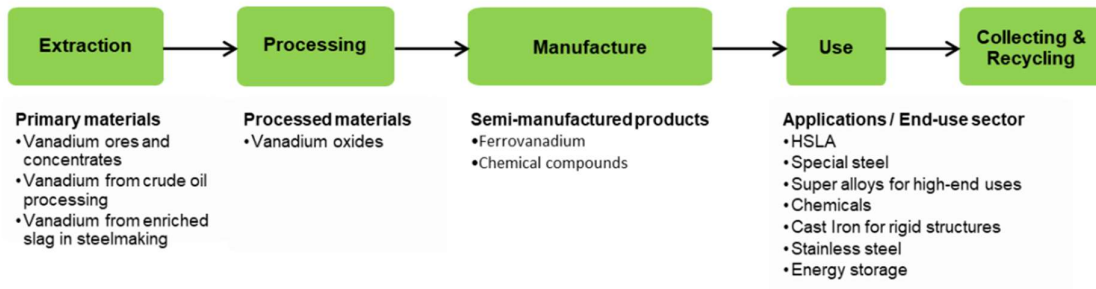



Figure 13. Simplified value chain for vanadium in the EU.⁸

1.1.5 Molybdenum

1.1.5.1 Overview

Molybdenum is a shiny, silvery refractory metal with a very high melting point (2623°C). It has the lowest thermal expansion coefficient of all technical materials; furthermore, it has a high resistance to corrosion and a relatively high thermal conductivity. Its density (10.22 g/cm³) is lower than most other high-melting-point metals.⁸



A photograph of a piece of molybdenum metal, showing its characteristic silvery, lustrous appearance and crystalline structure. The metal is broken into several sharp, angular fragments, highlighting its brittle nature.

H																	He	
Li	Be											B	C	N	O	F	Ne	
Na	Mg											Al	Si	P	S	Cl	Ar	
K	Ca	Sc	Ti	V	Cr	Mn	Fe	Co	Ni	Cu	Zn	Ga	Ge	As	Se	Br	Kr	
Rb	Sr	Y	Zr	Nb	Mo	Tc	Ru	Rh	Pd	Ag	Cd	In	Sn	Sb	Te	I	Xe	
Cs	Ba	La	Hf	Ta	W	Re	Os	Ir	Pt	Au	Hg	Tl	Pb	Bi	Po	At	Rn	
Fr	Ra	Ac																
			Ce	Pr	Nd	Pm	Sm	Eu	Gd	Tb	Dy	Ho	Er	Tm	Yb	Lu		
			Th	Pa	U	Np	Pu	Am	Cm	Bk	Cf	Es	Fm	Md	No	Lr		

Figure 14. Photographic aspect of Molybdenum and position in the periodic table.

1.1.5.2 Uses

Molybdenum is used for multiple applications. Due to its very high melting point, it is produced and sold as a gray powder. In this sense, many molybdenum items are formed by compressing the powder under very high pressure.

The main application of molybdenum is related to the production of alloys. It is used in steel alloys to increase strength, hardness, electrical conductivity, and resistance to corrosion and wear. These "moly steel" alloys are used in engine parts. Other alloys are used in heating elements, drills, and saw blades.

Molybdenum disulfide is used as a lubricant additive. Other uses of molybdenum include catalysts for the oil industry, printed circuit inks, pigments and electrodes.⁸

1.1.5.3 EU supply chain

Oil prices, gas prices, and stainless steel market dynamics strongly influence molybdenum prices. The oversupply pushed molybdenum prices down from an annual average of 28 USD/kg in 2012 to 14 USD/kg in 2016. Between August 2014 and November 2015, molybdenum prices fell below 10 USD/kg, with the collapse of oil prices. Oil prices began to recover in late 2016, and molybdenum prices stabilized around 2017. Minor changes in molybdenum prices were recorded between 2018 and 2020.⁸

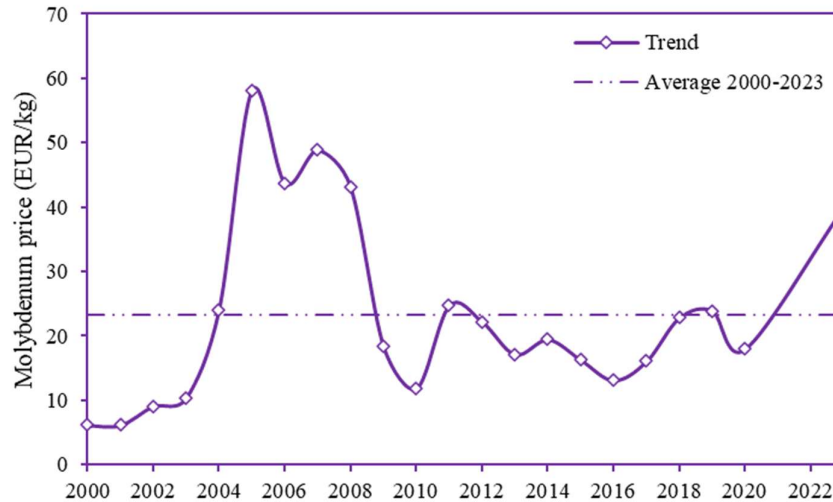


Figure 15. Annual average price of molybdenum between 2000 and 2023.

PRIMARY SUPPLY

About 60% of the global supply of molybdenum comes from a byproduct of copper smelting copper-molybdenum porphyry minerals. After extraction, molybdenum concentrate is produced using a flotation technique separating the gangue from the minerals. Most molybdenum concentrate contains 85-93% molybdenite.

China, Chile, and the United States are the leading molybdenum ore producers. There is no molybdenum mine production in the EU; therefore, needs across the Union depend on imports.⁸

Table 7. Molybdenum supply (extraction stage) and demand in metric ton, 2016-2020 average.⁸

Global production (kton)	Global Producers	EU Consumption (kton)	EU Share	Eu Suppliers	Import reliance
276	China	38%	10.5%	USA	64%
	Chile	21%		Chile	18%
	USA	15%		Peru	9%
	Peru	10%		Canada	6%
	Mexico	6%			
	Armenia	3%			
		9			96%

SECONDARY SUPPLY

According to the International Mo Association¹⁸, of the 330 kton of molybdenum used in all applications worldwide in 2013, approximately 86 kton (or 26%) came from recycled materials. In the same year, the share of recycled molybdenum in stainless steel production was 39%, increasing to 50% in tool and high-speed steels.

Approximately two-thirds of secondary molybdenum comes from waste produced during steelmaking and scrap recycling. Recycling scrap to produce new materials requires less energy than producing new metals, resulting in fewer emissions. Furthermore, it is often purchased locally, so transportation routes are short.⁸

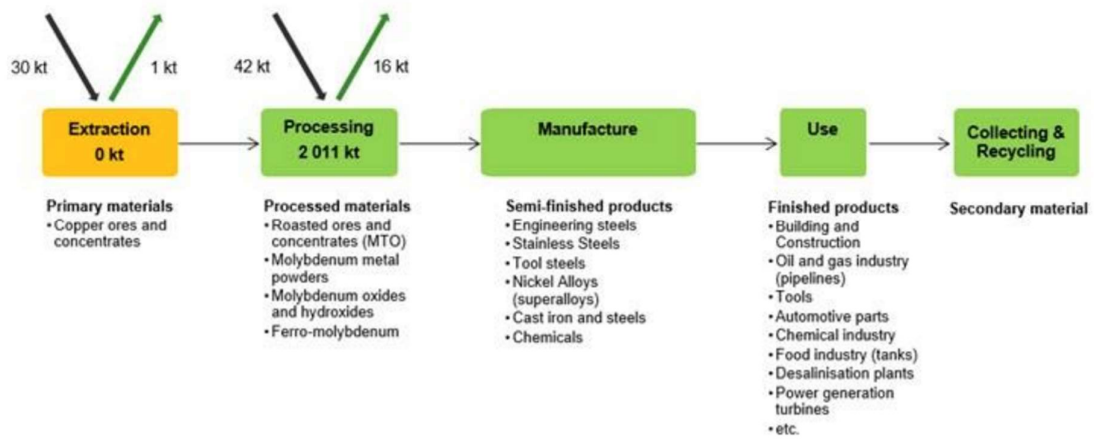


Figure 16. Simplified value chain for molybdenum in the EU.⁸

2

Oil&Gas Catalysts

2.1 INTRODUCTION

2.1.1 Oil&Gas sector

The petrochemical sector is essential to the global energy industry and is vital in producing a wide range of petroleum-derived chemicals and fuels. This sector plays a crucial role in the world economy, influencing numerous industrial sectors and contributing to nations' economic and technological development.

The petrochemical sector is closely linked to the extraction and refining of crude oil, a non-renewable natural resource. After extraction, the oil is refined to separate its main components, including gasoline, kerosene, and diesel fuel. A significant portion of oil is used for the production of petrochemicals. Petrochemical products are chemical substances that derive from transforming components of crude oil or its derivatives. These products include polymers, plastics, synthetic fibers, solvents, fertilizers, detergents, dyes, lubricants, and more. They are used in various industrial sectors such as automotive, construction, electronics, agriculture, packaging, and energy production.



Figure 17. Crude oil reserves in million barrels (Gbbl).¹⁹

The growing demand for petrochemical products is driven by the constant development of the global economy and the need to meet consumer needs. This sector is a primary source of income for many countries, especially those with significant oil reserves. **Figure 17** shows the main countries and their oil reserves.

One of the critical factors for the success of the petrochemical sector is its capacity for innovation. Petrochemical companies invest considerable resources in research and development to improve production processes, discover new applications, and reduce the environmental impact of their activities. Sustainability has become a priority in the petrochemical sector, with an increasing focus on reducing greenhouse gas emissions, energy efficiency, and using renewable or alternative feedstocks.

Catalysts play a fundamental role within this sector. Catalysts are chemicals that accelerate the rate of a chemical reaction without being consumed. They work by reducing the activation energy needed for the chemical reaction to occur, thus allowing the reaction to proceed more rapidly.

The use of catalysts has several advantages. First, it saves energy, reducing the temperature and pressure required for a chemical reaction to occur. Second, catalysts can improve the selectivity of a reaction, promoting the formation of desired products and limiting the formation of unwanted byproducts. These aspects can help improve the efficiency of chemical processes and reduce raw material waste. It is essential to underline that the catalysts do not undergo permanent changes during the chemical reaction. At the end of the process, they can be recovered and reused, which makes them even more economically and environmentally advantageous. However, it is critical to carefully choose the appropriate catalyst for a specific chemical reaction, as the chemical and physical properties of the catalyst can influence the reactivity and selectivity of the reaction. Additionally, some catalysts may be sensitive to specific operating conditions, such as temperature, pH, or the presence of pollutants, and may require specific operating conditions to maintain their catalytic activity.

Chemical catalysts play a vital role in the Oil&Gas industry, enabling a variety of chemical and catalytic processes that improve the efficiency and effectiveness of hydrocarbon refining and production operations.

In the Oil&Gas sector, catalysts are mainly used in oil refining and natural gas conversion processes. **Figure 18** shows the block diagram of the classic oil refining process. These catalysts are designed to promote specific chemical reactions and improve the efficiency of manufacturing processes. Among the various types of catalysts we find:

- Fluid Catalytic Cracking (FCC) Catalysts: These catalysts are used in the fluid catalytic cracking process, one of the main steps in petroleum refining. FCC catalyzes the breakdown of heavy hydrocarbon molecules into lighter molecules such as gasoline, diesel, and diesel fuel. This process helps to increase the yield of high-value-added products.
- Hydrodesulfurization (HDS) catalysts: These are used to remove sulfur content from petroleum products, such as gasoline, diesel, and aircraft fuel. HDS is a desulfurization process that reduces sulfur content to acceptable levels to ensure compliance with environmental regulations and improve the quality of petroleum products.
- Hydrodeoxygenation (HDO) catalysts: These are used in refining biofuels and the production process of low-sulfur fuels. HDO catalyzes the removal of oxygen from biomass, vegetable oils, or other renewable sources to obtain cleaner fuels suitable for emissions standards.

One of the characteristics that determine the quality of crude oil is the concentration of sulfur present in it, which can produce, following combustion, sulfur dioxide SO_2 and sulfur dioxide SO_3 , which are highly polluting and corrosive agents in the presence of water.

The great demand for crude oil means that it is also extracted from deposits where the quality of the product is very low. Therefore, treatment is necessary to allow its use in conventional engines. Precisely in this HDS phase, Ni-Mo catalysts (belonging to the LC-Finer family) are used, which have the function of promoting fundamental operations such as the removal of sulfur, heavy metals such as Nickel and Vanadium and nitrogen compounds and of increasing cracking efficiency. With the progress of technology, these catalysts have become very efficient and with high selectivity.

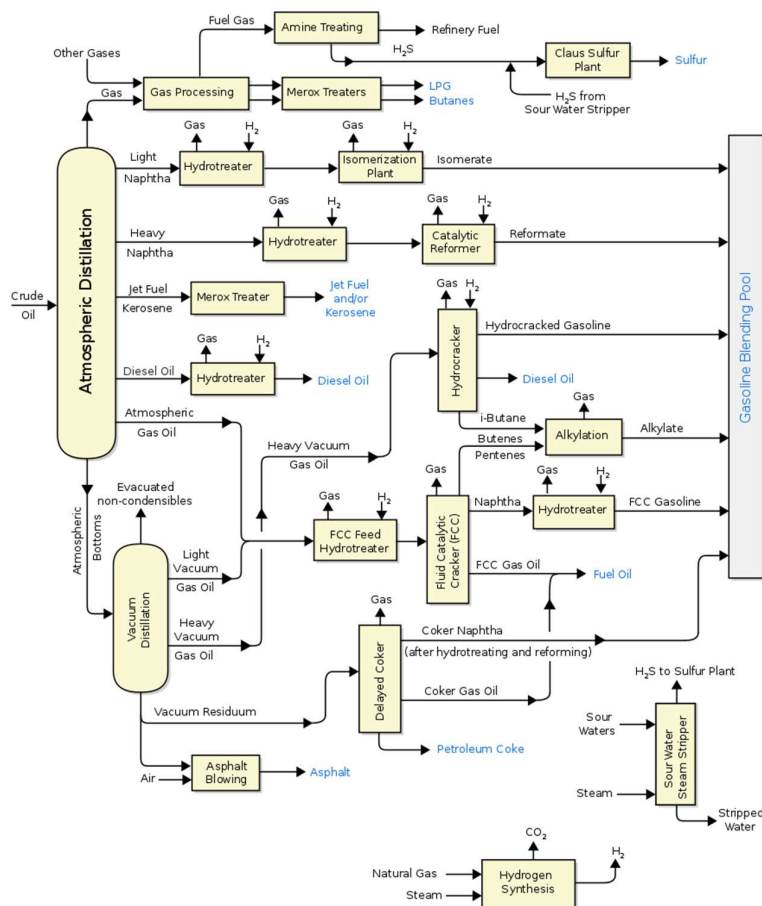


Figure 18. Simplified block diagram of the oil refining process.²⁰

The market for spent catalysts has been experiencing an ever-increasing growth in recent years. The quantities of this waste generated by the Oil&Gas sector are in the order of thousands and thousands of ton per year. For further details, see [Appendix A](#).

2.1.2 LCF Catalysts

Ni-Mo catalysts, generally all LC-Finers (LCFs), are composed of cylinders of approximately 10 mm in length ([Figure 19](#)), mainly made up of porous alumina on which the active metals give the catalytic properties.

Based on the metals present, a distinction is made between Ni-Mo (Nickel - Molybdenum) or Co-Mo (Cobalt - Molybdenum) type catalysts. The characteristics that influence a catalyst's catalytic capacity are the active sites' nature and the active sites' dispersion and distribution of the activators and promoters. Particular attention must also be paid to the porosity of the support (alumina in our case). The size of the pores can influence the diffusion of the high molecular weight molecules we want to convert (if the pores are too small) or on the poor active surface (if they are too large).

During use, the pores of the catalyst gradually become clogged due to deposits of nickel, molybdenum, vanadium, and carbon sulfides. Depending on the process conditions, the latter deposits can range from 10% to over 40% by weight. This phenomenon leads to a loss of efficiency of the catalysts up to complete deactivation.

Ni-Mo catalysts are high-tech products and, therefore, of high value. It is preferable to regenerate, use them as raw materials, or recover the metals within them.



Figure 19. Photographic aspect of LCF catalysts.

The regeneration is a process in which carbon deposits in the pores are removed through thermal oxidation. However, this process can be carried out a limited number of times (max 3-4 times) until the catalytic activity of the catalyst is irreversibly compromised.²¹ The life cycle of alumina-based catalysts is approximately 1-3 years, and for those dealing with heavy crude oils, it ranges from 0.5-1 year.²² Every time this procedure is carried out, we cannot remove deposits that reduce the catalytic activity by decreasing the activity surface. Once regeneration is no longer possible, we proceed with reuse in other applications or by recovering raw materials. For example, these spent catalysts can be shredded and used as a small percentage of fine aggregates in cement constituents or in refractory and ceramic materials.

The path to recovering raw materials is certainly much more promising. In the metal recovery process, spent catalysts are usually subjected to a roasting process (650-900°C) in which the metal sulfides are converted into oxides and the deposited carbon is burned. Subsequently, a hydrometallurgical extraction process can be envisaged.

2.1.3 Recovery processes

Chemical processes based on high-temperature operations represent the most used technologies for treating these wastes. Pyrometallurgical processes, in particular, require temperatures reaching up to 1600°C, with related costs and pollution problems.

Table 8 summarizes the main processes developed in the art for the industrial treatment of V- and Mo-based catalysts.

Table 8. Main important processes for the recovery of metals from Oil&Gas catalysts.

Process/Patent/ Year/Type	Description
Gulf Chemical & Metallurgical Corporation (GCMC) USA Year:1997 Type: Hydro	The process consists of roasting the spent catalysts with sodium carbonate and melting them in an electric arc furnace. Their technology allows all metals and alumina to be recovered. The catalyst is roasted to remove the sulfur residues and hydrocarbons present, and to transform Mo, V and the other metals present into water-soluble complexes. After a stage of grinding the product coming from pre-treatment, there follows the stage of solubilization of Mo and V in water and filtration of the solid residue containing alumina, Co and Ni. The solid residue is melted to produce pure alumina for abrasive applications, and Ni and Co alloys for Ni-Co refineries. The solution is purified in a first step to remove phosphorus and aluminum and then, in a second step, is purified with ammonium sulfate and chloride to produce ammonium metavanadate. Finally, the ammonium metavanadate is calcined to produce vanadium pentoxide. The ammonia is recovered by washing with a dilute solution of sulfuric acid and hydrochloric acid; the resulting solution is recycled to the precipitation of ammonium metavanadate. The granular vanadium pentoxide is further melted and cooled to obtain flakes with a V ₂ O content of more than 99%. The residual solution is further subjected to a

third purification step with a reducing agent to produce molybdic acid; this is then calcined to produce high-quality molybdenum trioxide.²³

EURECAT Inc. Year 2011 Type: Pyro	The technology initially adopted by EURECAT Inc. is a combination of pyro-hydrometallurgical technology. However, according to Dufresne, the current technology adopted is based on the pyrometallurgical process that allows the separation of metals (V, Mo, Ni and Co) as special alloys and alumina or inert silica for the production of insulation material. ²⁴
CRI-MET Year 1987 Type: Hydro	The process consists of using two-stage pressure leaching with NaOH for the treatment of spent HPR. In the first leaching stage Mo and V are solubilized and then recovered as oxides. The second leaching stage enables aluminum to be completely recovered and the solid residue enriched in Ni and Co is roasted and sent to a nickel-cobalt refinery. ²⁵
Taiyo Koko Company Process Year 1987 Type: Hydro	The process is focused on the recovery of Mo and V. Initially, there is a roasting step at 850°C to transform Mo and V into soluble complexes. The resulting material is then ground, leached with water and the solid residue is removed from the solution by filtration. The leaching liquid obtained is first treated to remove aluminum and phosphorus using magnesium chloride and ammonium chloride. Once these impurities have been removed, ammonium chloride is added to the solution to recover ammonium vanadate. This precipitate is further calcined to remove the ammonia. The resulting vanadium oxide is then melted to form flakes with a resulting purity of about 98% with Fe and Mo as minor impurities. The resulting solution is then acidified with hydrochloric acid to precipitate Mo as molybdic acid. This is further calcined to obtain MoO ₃ . ²⁶
Full Yield Industry Process Year 1985 Type: Hydro	The process calcines the HPR catalyst with NaOH for further dissolution of Mo, Ni, Co and V. Selective recovery of the elements from the leaching solution takes place by precipitation, solvent extraction or ion exchange methods. V and Mo are recovered as oxides and Ni and Co as salts. ²⁷
Moxba-Metrex Type: Hydro	This is a thermal-hydrometallurgical process that enables the recovery of all elements from the spent catalyst. The HPR catalyst first undergoes heat treatment to remove the carbon and the resulting solid is leached with sulfuric acid. This process allows Co, Ni, Mo and V to be dissolved. The solid residue consists mainly of alumina, which is further used for refractories. The multi-stage solvent extraction process is used to recover the metals from solution. The products of the process are molybdenum trioxide, ammonium molybdate, ammonium vanadate and nickel and cobalt salts. ²⁸
Quanzhou Jing-Tai Year 2000 Type: Hydro	The process uses hydrogen peroxide to leach the spent catalyst, which is first calcined at low temperature and then ground. During the leaching process all four metal elements (Mo, Ni, V and Co) are dissolved, leaving more than 95% of the alumina and silica present in the initial material in the solid residue. The pH of the leaching solution is first acidified with sulfuric acid to precipitate Mo and V. Subsequently the solution pH is neutralized with sodium hydroxide to recover Ni and Co. The waste solution is then subjected to an ion exchange step to remove residual elements. After a subsequent treatment step, the solution is discharged as it possesses all the properties required by environmental regulations. The solid residue of the leaching process is used for the production of masonry bricks. ²⁹
AMG Vanadium Company Type: Pyro	This is a pyrometallurgical process that transforms the spent HPR catalyst into alloys (ferro-vanadium and other ferroalloys) that are further sold to steel companies. ³⁰
Nippon Catalyst Cycle Co. Ltd Type: Pyro	The process treats the HPR catalyst for the recovery of vanadium and molybdenum in the form of alloys (Fe-V, Fe-Mo), oxides (V ₂ O ₅ , MoO ₃) and separated metals (metal with a high V content). ³¹
GfE Metalle and Materialien GMBH, AURA Metallurgie GMBH Year 2007 Type: Hydro & Pyro	GMBH uses both hydrometallurgical and pyrometallurgical processes to recover metals from spent HPR catalyst. First they obtain molybdenum chemicals, Ni or Co solutions and aluminium oxides. The product of AURA Metallurgie GMBH consists of molybdenum and aluminium oxides, molybdenum concentrate, ammonium molybdate, cobalt-nickel sulfate and gypsum. ³²⁻³⁴
US82897B2 Year 2012 Type: Hydro	This process enables boehmite and gamma-alumina to be recovered from spent HPR catalyst. The first step is removal of the oil by washing with naphtha. Then the catalyst is dried, ground and roasted at about 500°C to remove the carbon. Calcination at 750°C in the presence of sodium carbonate is carried out. The resulting product is then leached with water at high temperature to solubilise Mo and V. The residue is separated from the solution by filtration and then leached in a sodium hydroxide solution at about 200°C under pressure. This second step produces a sodium

aluminate-rich solution and a solid containing the oxides of nickel and cobalt. The sodium aluminate solution is then neutralised with carbon monoxide to precipitate the aluminium as boehmite. Since this product is a powder, an autoclave hydrothermal process is then applied. The well-crystallised boehmite is finally calcined at 500°C to obtain γ -Al₂O₃, which can be further used in the production of a new catalyst. No further information is given regarding the recovery of Mo, V, Ni or Co or the treatment of waste solutions.³⁵

US8287618B2
Year 2012
Type: Hydro

The process recovers Ni, Mo, V, Co and Al using a combination of heat treatment and a hydrometallurgical process. The process starts with de-oiling of the catalyst in toluene or naphtha solution. This is followed by grinding to a particle size of less than 500 μ m. The resulting powder is subjected to removal of coke and sulfur species by means of a thermal process carried out at around 500°C. Subsequently, the process is continued with all solid leaching into EDTA solution using an ultrasound bath. In this process Ni, V, Co and Mo are almost completely dissolved and the solid residue is a pure alumina product. The resulting solution is subjected to EDTA precipitation with nitric acid. Once the EDTA has been recovered from the solution, the solvent extraction process is performed to recover V, Mo, Ni and Cu. The process was performed at different pH values using Cyanex 272 diluted in paraffin. Complete extraction of Mo was obtained at pH=0. Then, by neutralising the solution at pH=2, over 99% extraction of V from the solution was achieved. With a third neutralisation step at pH=5.1, almost complete extraction of Ni was also achieved.³⁶

US 2007/025899
Year 2007
Type: Hydro

The process begins with a de-oiling step using an organic solvent. The catalyst is then washed with water and leached with ammonia and oxygen in an autoclave at a temperature of around 200°C. Mo and Ni form soluble complexes of ammonium molybdate and nickel ammonium sulfate. By contrast, ammonium metavanadate is insoluble and is further removed from the solution with the other insoluble part by filtration. This solid is again leached in an autoclave with ammonia to achieve dissolution of the ammonium metavanadate. At the end of the reaction the residual solid is removed by filtration and the solution is subjected to recovery of vanadium. The process is carried out by neutralising the solution to a certain pH level with sulfuric acid and then subjecting it to a crystallisation process. This results in crystallised ammonium metavanadate as the end product. The Ni and Mo solution undergoes a solvent extraction process. In this step Ni is recovered from the solution and then separated from the organic phase using a solution of sulfuric acid. The residual Mo solution is further neutralised with sulfuric acid and subjected to a crystallisation process to remove other impurities. Once the solid impurities have been removed from the solution by filtration, the solution undergoes precipitation with sodium sulfide. The resulting molybdenum disulfide is again leached in ammonia and oxygen, resulting in pure ammonium molybdate.³⁷

CN105274344A
Year 2016
Type: Hydro

In this process the catalyst undergoes two roasting steps. The first is performed to remove carbon and oil at a temperature of 500-600°C. The second is performed in the presence of sodium carbonate at 600-850°C. The treated catalyst is then ground and leached with water at high temperature to recover soluble molybdenum and vanadium salts. Since the solution contains a small amount of aluminium, it is first acidified to remove this element. The vanadium is then precipitated by a second stage of acidification and the addition of ammonium chloride. After concentration (probably by evaporation) and the ion exchange process (probably to remove other impurities), an ammonium molybdate-enriched solution is obtained.³⁸

KR 10-1189183
Year 2012
Type: Pyro

This pyrometallurgical process enables V, Ni and Mo to be recovered from spent HPR catalysts as ferroalloys. The reductive melting process by carbo-thermal reaction in an electric arc furnace is first carried out at a temperature of 1600°C. The Fe-V-Ni-Mo alloy obtained is then treated at about 1200°C in the presence of oxygen and iron oxide for the selective oxidation of V. The sludge obtained is then subjected to an alumina-thermal reduction process to produce Fe-V alloy.³⁹

HyVent Process

This process involves a single hydrothermal step for both the removal of carbon and sulfur from spent catalysts and the extraction of base metals. The hydrothermal process is followed by the recovery of base metals by selective precipitation and subsequent filtration.⁴⁰

2.2 MATERIALS

2.2.1 Sample

The sample used in the laboratory-scale experimentation is of the LC-Finer type and was supplied by the company ORIM S.p.A (see **Projects & Companies** section). This type of catalyst is generally made up of an alumina matrix on which the active sites of metals such as Ni and Mo are located. During

hydrodesulfurization processes, these catalysts undergo chemical deactivation due to the deposition of carbon residues on the solid particles and poisoning by V and sulfides (present in variable concentrations in the treated crude oil).

The received sample was subjected to chemical attack via Aqua Regia (HCl to HNO₃ of 3:1), and the resulting solutions were analyzed via inductively coupled plasma optical emission spectroscopy (ICP-OES) to characterize the metallic fraction present. **Table 9** shows the results of two analyses, with the mean value and the standard deviation.

Table 9. Results of chemical composition analysis of LCF sample.

Element	Ni (wt.%)	V (wt.%)	Al (wt.%)	Mo (wt.%)	As (ppm)
I	3.34	9.35	13.30	4.60	56.52
II	3.19	8.66	13.59	4.49	49.41
Average	3.27	9.01	13.44	4.55	52.97
St.DEV	0.11	0.48	0.20	0.07	5.03

The metals present in the catalyst are in the form of sulfides. In order to proceed with easy solubilization in a leaching process, they must be converted into oxides or sodium salts. This conversion is usually carried out by heat treatment at around 800 °C in the presence or absence of sodium (usually as carbonate or bicarbonate). The thermal oxidation of these catalysts and calcination are characterized by high temperatures due to the various highly exothermic reactions. In this context, it is essential to keep the temperature below approximately 850 °C to avoid the alumina's sintering. This phenomenon is highly undesirable due to lowering the total extraction yields of the metals of interest.

The sample was also subjected to chemical analysis using CHNS to determine the percentage of carbon deposited following oil refining processes. The results obtained from this analysis are reported in **Table 10**.

Table 10. Results of CHNS analysis of LCF sample.

C (wt.%)	H (wt.%)	S (wt.%)	N (wt.%)
22.67	2.65	11.45	-2.76

2.3 METHODS

Various experimental tests were carried out to identify a recovery process for the metals present that was as sustainable as possible from an economic and environmental point of view. Among the different paths that can be taken, the most advantageous ones studied, developed, and optimized are listed below.

2.3.1 GULF Process

The GULF process takes its name from the company that first patented this series of operations to recover vanadium and molybdenum from spent LCF catalysts. The process is hydrometallurgical, with some thermal steps. Initially, the material will be roasted inside a rotary kiln to eliminate the residual organic component from the oil refining processes. After this operation, a calcination step follows, always inside a calciner in the presence of sodium carbonate to form the sodium salts of the metals of interest. The latter, being soluble in water, were sent to leaching reactors which used water after grinding.

The reactors were designed to perform a dual function: allowing the leaching of vanadium and molybdenum and promoting the sedimentation of the solid residue. GULF achieved high extraction yields through a counter-current configuration of two or more reactors.

The leaching solution was sent to the recovery phase via cementation. In fact, through variations in pH and temperature, with the addition of ammonium chloride (NH_4Cl), it is possible to precipitate vanadium and molybdenum as NH_4VO_3 and $(\text{NH}_4)_2\text{MoO}_4$.

2.3.1.1 TEST I

100 g of catalyst was first roasted for three hours at 850°C to perform the GULF process. Then, after its cooling, 24 g of sodium bicarbonate (sodium carbonate was not available in the laboratory) was mixed with 60.38 g of roasted catalyst sample. The mixture was subjected to a calcination treatment for two hours and 30 min at 800°C . After cooling, three grinding tests were carried out with the Fritsch Pulverisette 7 planetary ball mill (with stainless steel container and grinding balls) at different rotation speeds (300, 450, and 600 rpm) for 30 minutes.

These tests aimed to obtain different-size fractions and perform solubilization tests to verify their effect on leaching. At the end of each grinding test, a sieve with an opening of 0.85 mm was used to separate the solid from the grinding spheres. It should be noted that a certain amount of material does not pass through the sieve openings under these conditions. The retained material from each sieve was collected, and the quantity was measured by weight. Furthermore, the same procedure with the same amount of sample and NaHCO_3 was repeated, with the only difference being that the grinding was performed manually in a mortar with a pestle.

Leaching aims to solubilize vanadium and molybdenum complexes such as sodium vanadate and molybdate in water. The leaching process was performed in 4 stages connected by countercurrent. Each leaching stage was carried out at approximately 85°C ($\pm 3^\circ\text{C}$), under magnetic stirring (approximately 200 rpm) for 2-3 hours and at a solid concentration of 15 % wt./vol. For this reason, 200 mL of distilled water was first heated on the heater to approximately 80°C , then 30 g of roasted and calcined catalyst sample was added. Temperature control was performed with a hand thermometer. At the end of each test, the solution was separated by vacuum filtration or centrifugation and reused for the subsequent leaching phase.

150 ml of solution from leaching with four countercurrent stages was subjected to a first basification phase at pH 9 with a concentrated sodium hydroxide solution (20% wt./vol.). Then, 40 g/L of MgO was added into an ammonia chloride solution (15% wt./vol.). 2 ml was mixed with the solution already adjusted to pH and left to react for 2 hours. Subsequently, the precipitate was removed from the solution by filtration and then dried in an oven. Then, 100 ml of solution was subsequently acidified to pH 6.7 with concentrated HCl (37% wt./vol.), heated to approximately 40°C and mixed with 25 ml of ammonia chloride solution (25% wt./vol.). After a 2-hour process, the mixture was subjected to vacuum filtration. The recovered solid was dried in an oven at 105°C and then roasted in a muffle oven for 1 hour at 500°C . All solutions and washing waters obtained were analyzed for their vanadium, molybdenum, nickel, aluminum, and arsenic content by ICP-OES.

2.3.1.2 TEST II

100 g were taken from the LCF sample and subjected to a double heat treatment. The first roasting was performed at 850°C for two hours. Subsequently, after a cooling phase, the sample was mixed with 22.31 g of NaHCO_3 (i.e., with an excess of 50% compared to the stoichiometric quantity required for the reaction with vanadium and molybdenum) and subjected to the second roasting for two hours at 800°C . After cooling, grinding was performed for 10 minutes. The abovementioned procedure was repeated on two other initial 100 g samples to have sufficient material for the leaching phase.

The procedure described above was subsequently repeated by changing the quantity of NaHCO_3 (bicarbonate was used due to the immediate unavailability of Na_2CO_3). In this case, a first roasting was carried out at a temperature of 800°C for two hours, and, subsequently, 17.55 g of NaHCO_3 was mixed (i.e., with an excess of 20% compared to the stoichiometric quantity required for the reaction with V and Mo). The second roasting took place at 850°C for two hours.

Two distinct processes were performed to treat the material with 50% excess NaHCO_3 (process 1) and 20% excess NaHCO_3 (process 2).

Process 1 was performed in 3 stages connected in countercurrent. Each leaching stage was carried out at a temperature of 85°C ($\pm 3^\circ\text{C}$), under magnetic stirring (approximately 200 rpm) for 2 hours, and at a solid concentration of 15% wt./vol. For this reason, 200 ml of distilled water was heated on a magnetic plate to approximately 80°C for the first test. Subsequently, 30 g of roasted and calcined

catalyst sample was added. Temperature control was carried out using a manual thermometer. At the end of each test, the solution was separated by centrifugation and used for the subsequent leaching phase. **Figure 20** shows the scheme followed for the various tests of process 1 to obtain the three countercurrent stages. At the end of each cycle, the residual solid from the centrifuge was dried in an oven at 60 °C for 24 h and subsequently weighed to determine the weight loss compared to the initial sample.

Process 2 is very similar to Process 1. However, in this case, 100 ml of solution was used for each trial. Since the solid concentration was set at 15% wt./vol., for the first test of this process, 15 g of roasted and calcined catalyst samples were added to 100 ml of distilled water at a temperature of 85°C (± 3 °C). **Figure 21** shows the scheme followed for the various tests of process 2 to obtain the three countercurrent stages. As already mentioned for process 1, at the end of each cycle, the residual solid coming out of the centrifuge was dried in the oven and subsequently weighed.

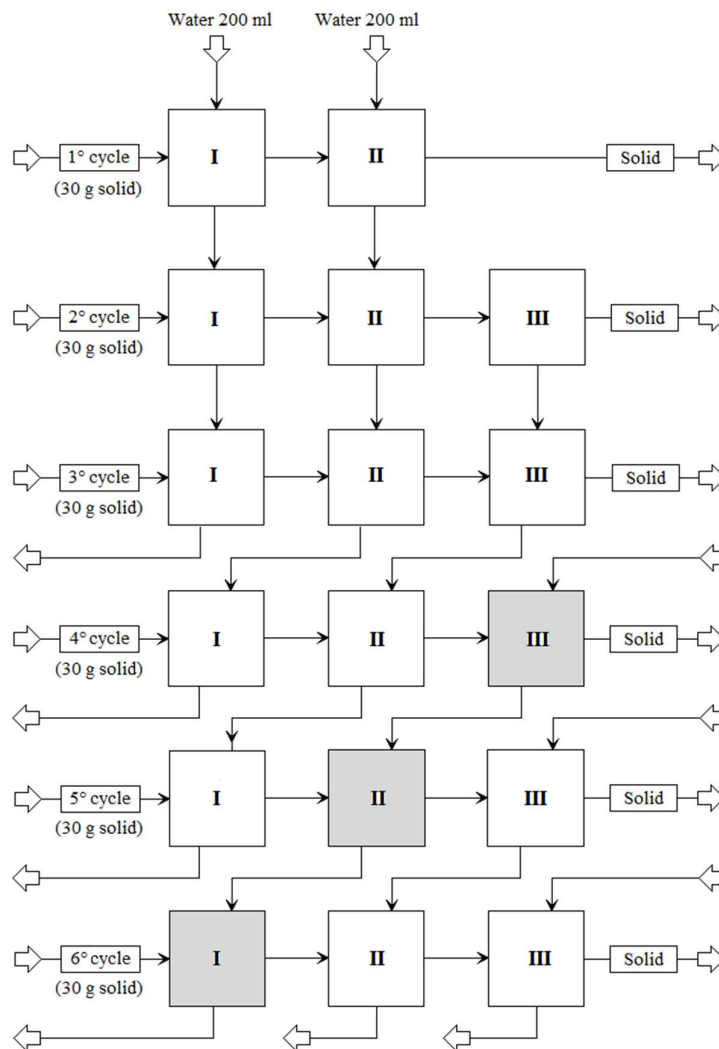


Figure 20. Simplified block diagram of the tests performed for process 1 with the three countercurrent stages highlighted.

The solutions from the various steps were analyzed regarding vanadium concentration via ICP-OES. In the case of process 2, analyses of the solutions were also carried out in terms of Al concentration.

The solutions emerging from the first step of the fifth and sixth cycle of process 1 were mixed. Four V precipitation tests were performed by varying different parameters. All four tests were conducted on 80 ml of the "mix 5-6" solution at 40 °C. **Table 11** summarizes the conditions of the four tests.

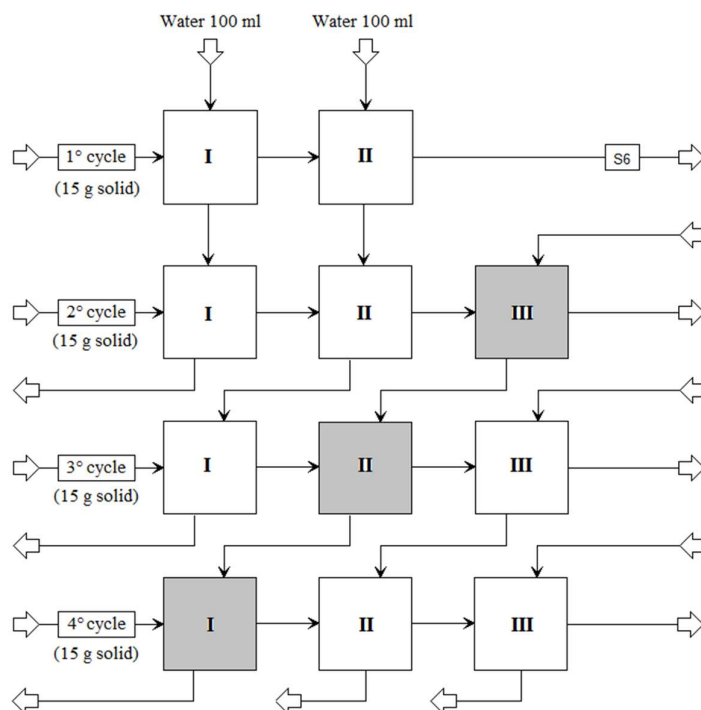


Figure 21. Simplified block diagram of the tests performed for process 2 with the three countercurrent stages highlighted.

Table 11. Precipitation tests condition.

Test	Solution [mL]	t [min]	pH	NH ₄ Cl [g]	T [°C]
1	80	30	8	2,31	40
2	80	60	8	4,51	40
3	80	30	6,7	2,31	40
4	80	60	6,7	4,51	40

First, HCl (37% wt./vol.) was added gradually to the 80 ml of the starting solution until it reached the pre-established value expected for the test. Then, the temperature was raised by heating with a magnetic plate to 40°C, and NH₄Cl in solid form was added. Once the test was completed, the solution obtained was separated from the solid by vacuum filtration. A wash was performed with a solution obtained by mixing 30 ml of distilled water and 0.6 g of NH₄Cl. ICP-OES analyzed both the solution obtained from filtration and the washing water.

The solid was subjected to 2 drying steps: the first for 24 h at 60°C and the second for two hours at 600°C. The residue was weighed to determine the weight loss and evaluate the moisture content in the cake.

2.3.1.3 TEST III

Two LCF samples of 100 g each (called A and B) were taken and subjected to a double heat treatment. The first roasting was performed at 850°C for two hours. Subsequently, after a cooling phase, sample A was mixed with 17.83 g of Na₂CO₃ (i.e., with an excess of 50% compared to the stoichiometric quantity required for the reaction with vanadium and molybdenum), while sample B was mixed with 25 g of Na₂CO₃ (i.e., with 110% excess). Then, both samples were subjected to the second roast for two hours at 800°C. After cooling, grinding was performed for 10 minutes.

Two distinct processes were carried out to treat samples A and B, and subsequently, four single-step leaching tests were carried out (2 for each sample).

The two processes were carried out with three leaching stages connected in countercurrent. Each leaching stage was carried out at a temperature of 85°C (±3°C), inside a thermostatic bath with a stirring speed of 150 rpm for 2 hours and at a solid concentration of 25% wt./vol. For this reason, for the first test, 60 mL of distilled water was heated to a temperature of approximately 80°C, and 25 g of the sample was added. At the end of each test, the solution was separated by centrifugation and used for the subsequent leaching phase. **Figure 22** shows the scheme followed for the various process tests to obtain the three countercurrent stages. At the end of each cycle, the residual solid emerging from the centrifuge was dried in an oven at 60°C for 24 h and subsequently weighed to determine the weight loss compared to the initial sample.

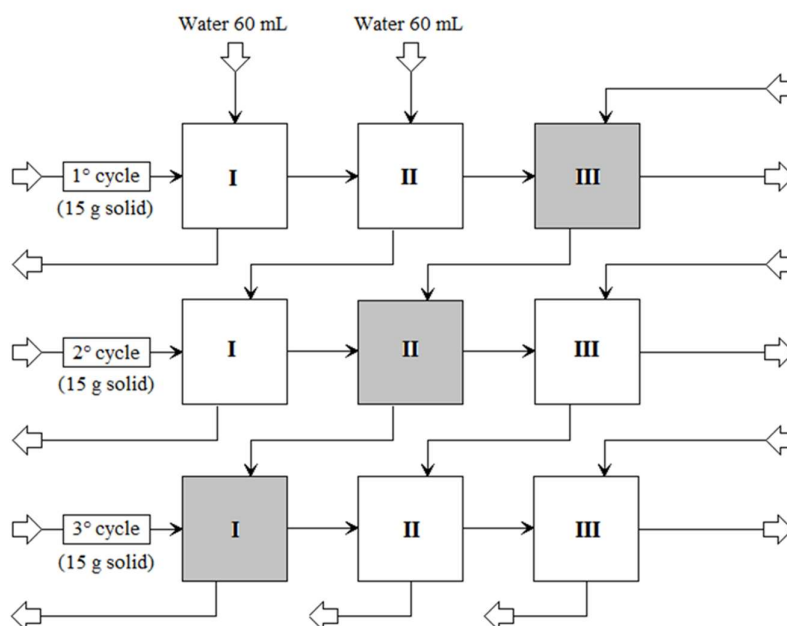


Figure 22. Simplified block diagram of the tests performed for process.

The four single-step tests were performed on a magnetic stirring plate and through the use of a manual thermometer in order to evaluate the effect of the different stirring mechanisms between the thermostatic bath and the magnetic plate. The parameters of the four tests are reported in **Table 12**.

Table 12. Tests conditions.

Sample	Test	T [°C]	t [h]	S/L (% wt./vol.)
A	I	85	2	25%
	II	85	2	15%
B	I	85	2	25%
	II	85	2	15%

2.3.1.4 Sedimentation test

Three leaching tests were carried out in a single step at different stirring speeds (0, 100, and 300 rpm) to determine this parameter's influence on the V recovery yield. Each test was conducted at 85°C ($\pm 3^\circ\text{C}$) for 2 hours and at a solid concentration of 15% wt./vol. For this reason, 100 ml of distilled water was heated on a magnetic plate up to approximately 80°C. Subsequently, 15 g of roasted catalyst sample (with 50% excess NaHCO_3) was added.

Subsequently, a sedimentation test was carried out for each of the three tests. The solution was poured into a graduated cylinder, and the progression of the solid-liquid interface was observed until complete sedimentation. For this purpose, at the end of the leaching, 1 ml of H_2O_2 was added to make the solution more transparent and to observe the sedimentation of the suspended particles. The precipitate was recovered, weighed, and dried in an oven at 60°C for 24 hours to evaluate its weight loss. Subsequently, chemical attacks were carried out on the residual solids with aqua regia, and ICP-OES analyzed the solution to determine the residual V content.

The sediment clarified was characterized in terms of vanadium content by ICP-OES.

To study the effect of the presence of a polyelectrolyte on the sedimentation speed, three samples of LC Finer of 50 g each were taken. Each of these samples was subjected to a different thermal treatment to evaluate, together with the sedimentation speed, the best roasting and calcination conditions for vanadium recovery. The heat treatments for each sample are summarized in **Table 13**.

Table 13. Conditions of heat treatments.

Run	Pre-Treatment	Roasting Conditions	Calcination	Calcination agent
1	-	850°C - 2 h	800°C - 2 h	NaHCO_3
2	-	850°C - 2 h	800°C - 2 h	Na_2CO_3
3	Washing with Acetone + Air drying for 2 h	-	800°C - 2 h	Na_2CO_3

A 50% excess of the calcination agent was set for all three samples, compared to the stoichiometric quantity necessary to oxidize vanadium and molybdenum.

The same leaching test was performed for each sample at the end of all heat treatments. For each test, 250 mL of distilled water was heated to 85°C ($\pm 3^\circ\text{C}$) using a magnetic stirring plate and a manual thermometer. The leaching was carried out for two hours with an agitation of 300 rpm and a solid concentration of 15% wt./vol.

At the end of the leaching, four cylinders of 50 mL were prepared, into which the solution and the polyamine were poured in different quantities (0, 0.25, 0.5, and 1 mL). Then, the advancement of the solid front as time passed was observed, and the data was recorded. It was decided to carry out the sedimentation tests on samples 1 and 2 at two different temperatures and evaluate the effect of temperature on the sedimentation speed. The clarified solution was subsequently analyzed in terms of vanadium and molybdenum concentrations.

Two vanadium precipitation tests were carried out for each clarified solution, varying the test time (1 and 2 h). Below are the parameters used for the four tests. The quantity of NH_4Cl used was calculated by multiplying the moles necessary for the stoichiometric reaction with vanadium by a factor $\alpha = 3$.

Table 14. Conditions of vanadium precipitation conditions.

Run	Pre-Treatment	Solution [mL]	NH_4Cl [g]	T [$^\circ\text{C}$]	t [min]
1a	Na_2CO_3	100	4.015	40	60
1b	Na_2CO_3	100	4.015	40	120
2a	NaHCO_3	100	4.071	40	60
2b	NaHCO_3	100	4.071	40	120

At the end of the precipitation, the solution was filtered under vacuum. The clarified was analyzed in terms of vanadium and molybdenum concentrations by ICP-OES. The solid was dried in an oven at 105°C for 24 h and then placed in a muffle at 600°C for one hour. At the end of the various drying steps, chemical attacks with aqua regia were carried out on the residual solids to evaluate their content.

2.3.2 Citric acid Process

A test was carried out to evaluate the efficiency of citric acid as a leaching agent. Before leaching, manual grinding in a mortar with a pestle was performed on the sample previously washed with acetone and water and then roasted for two hours at 850 °C. For this purpose, 1,649 g of ground sample were immersed in 50 mL of 1 M citric acid solution. The process lasted four hours, and a continuous stirring speed of 300 rpm was applied. The leaching test was performed at room temperature and atmospheric pressure.

2.3.3 ORIM-CAT2 Process

2.3.3.1 Preliminary considerations

The thermal oxidation reactions of the spent catalyst are highly exothermic and the presence of hydrocarbons on the surface of the catalyst often leads to an excessive increase in temperature. This increase in temperature must be kept under control to avoid exceeding 850°C, i.e. the sintering temperature of alumina. In the GULF process, the first roasting step is fundamental for the removal of the organic fraction that most influences the temperature increase. It is clear that the removal of the organic component is fundamental for the success of any process.

Thus was born the idea of using a solvent in order to solubilize the hydrocarbons present on the catalyst without having to resort to a thermal treatment. Different ways have been analyzed to try to remove the organic component from LFC catalysts. In **Figure 23**, the results of the tests conducted are presented in terms of concentrations of C, H and S and the removal efficiency compared to the treatment applied.

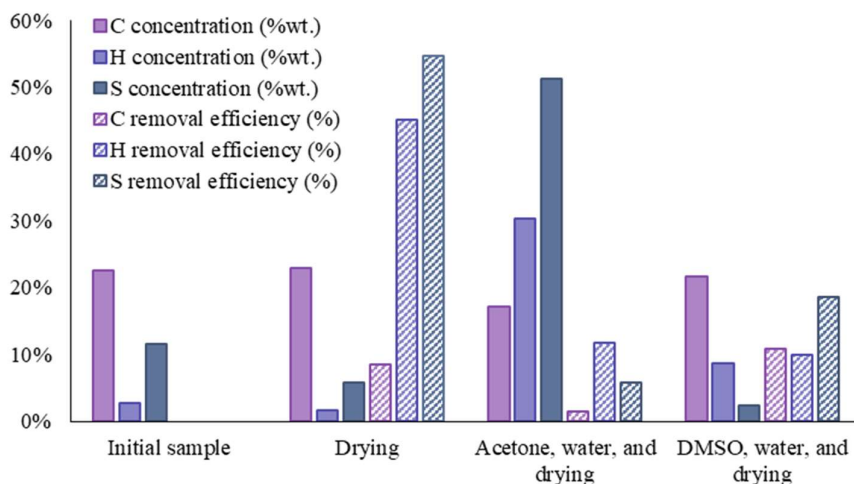


Figure 23. CHNS results and removal efficiency for different treatments.

The data in this figure demonstrates that washing with acetone is the most efficient process for removing C (removing more than 30% of this element). Furthermore, more than 51% of the H contained in the initial sample was removed with this treatment. A lower removal efficiency of both C and H was achieved by drying the sample. A much lower efficiency was obtained in the case of sample treatment with dimethyl sulfoxide (DMSO). Acetone has better efficiency because, being a polar solvent (**Figure 24**), it is miscible with most organic components. It is possible to interpret the data in the following way:

- Drying removes the more volatile components of the fuels imbibed in the sample, and therefore, a higher % removal of H compared to carbon is observed;
- The samples washed with acetone instead show a significant reduction in carbon and an increase in H removal compared to the simple drying process, a sign that heavier hydrocarbon components have been removed. Furthermore, sulfur reduction in both the drying and washing processes with acetone indicates the presence of hydrocarbons linked to this element.

Table 15. CHNS results of the initial sample and the sample after washing with acetone and water.

Sample	C (%)	C removal efficiency (%)	H (%)	H removal efficiency (%)	S (%)	S removal efficiency (%)	N (%)
Before treatment	22.67	-	2.65	-	11.45	-	-2.76
After treatment	17.24	30.34	1.41	51.26	11.77	5.84	-6.11

The acetone wash was performed for 30 minutes with a solid/liquid ratio of 20%. Then, the solid was removed from the organic solvent and further washed with water (the same volume of water as the organic solvent was used). The treated solid was dried in an oven for 6 hours at 105°C (until its weight stabilized). The obtained samples were analyzed with the CHNS analytical method. **Table 15** presents the results obtained and already anticipated in **Figure 23**.

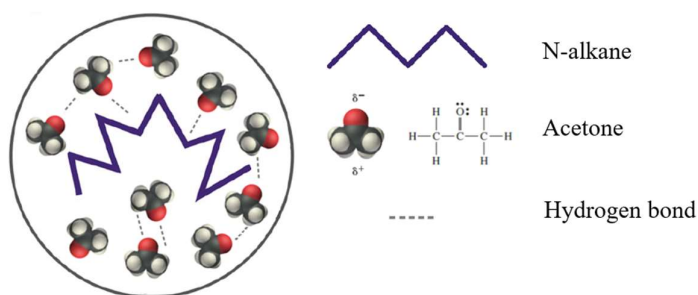


Figure 24. Removal mechanism of the organic component by Acetone.

Acetone is widely used in various chemical industry sectors as an organic solvent; it is a colorless, flammable liquid with a characteristic odor. We chose to use acetone as a solvent for the removal of the organic component present on the exhausted LC-Finer and H-OIL catalysts for several reasons:

- It is possible to obtain a high recovery of the organic component;
- Its low boiling point, compared to that of the solubilized organic component, allows for high recovery of the solvent used (distillation);
- The cost of the solvent is undoubtedly lower than that of other solvents with similar characteristics (e.g., ethanol).

However, some critical aspects related to the use of acetone must be taken into consideration:

- Being a highly flammable compound, its use within the system would lead to various issues in terms of safety.
- Being a highly volatile compound, some operations during the washing process may be slightly more complicated.

IV. The solution obtained from steps III-A or III-B is mixed with the washing water, and everything is sent to an arsenic and phosphorus purification section. Subsequently, neutralization with an inorganic acid (sulfuric acid or hydrochloric acid) is envisaged for the selective precipitation of vanadium with ammonium chloride or ammonium sulfate. Subsequently, the solid precipitate is separated from the solution through filtration; the residual solid is washed through a solution of ammonium chloride or ammonium sulfate.

V. The solution and the washing water of step IV are mixed and sent to the neutralization step with hydrochloric or sulfuric acid for the selective precipitation of molybdenum with the addition of a cationic polyelectrolyte solution or via ammonium chloride or ammonium sulfate.

VI. The residual solid from the steps III-A or III-B leaching process is leached with an acidic solution of sulfuric acid and hydrogen peroxide; at the end of the reaction, the residual solid is separated from the solution by filtration and then washed with water.

VII. Step VI leach solution is sent to the nickel and/or cobalt recovery stage; nickel recovery can be done by electrolysis or precipitation, and cobalt recovery can be done by precipitation. Precipitation for both elements is carried out by neutralizing the solution with sodium hydroxide and subsequent addition of sodium carbonate or oxalic acid; in the case of joint treatment of Ni-Mo and Co-Mo catalysts, solvent extraction can be used, for example, using di-(2-ethylhexyl)phosphoric acid or CIANEX in an organic diluent such as n-heptane.

VIII. The step V solution is treated with an organic solvent to remove residual molybdenum and vanadium ions.

2.3.3.3 Experimental procedures

Numerous tests were conducted to study and optimize the new process. In this sense, the catalyst was washed with acetone to remove the fuel present. The washing was performed for 20 minutes with a solid/liquid ratio of 20%. At the end of the washing, filtration was carried out using a pressure filter, which reduced the loss of acetone compared to vacuum filtration. The loss of acetone was approximately 6% (compared to approximately 20% loss in vacuum filtration). Then, the solid was further washed with distilled water (the same volume of water as the organic solvent was used). The treated solid was dried in the air for 24 hours.

Subsequently, it was decided to carry out a factorial experiment to evaluate the influence of different parameters on the extraction yields of vanadium and molybdenum. The catalyst sample was ground using a Fritsch Pulverisette 7 planetary ball mill (with stainless steel container and grinding balls). The dried solid was divided into two parts of equal weight and ground at the same speed twice to obtain a different particle size. The first part was ground at 600 rpm for 10 minutes, while the second was at 600 rpm for 20 minutes. The particle size distribution of the two ground fractions was analyzed using a series of 6 sieves of different diameters (850 μm , 425 μm , 212 μm , 125 μm , 53 μm , and 40 μm). It was seen that the correct separation of the particles through the different sieves was hindered by the humidity of the sample (due to the organic substances still present). Then, the two fractions were mixed, and prolonged sieving was carried out using three sieves of different diameters (425 μm , 250 μm , and 212 μm). Based on the quantity of material obtained, it was decided to use the fraction with a diameter less than 212 μm for the low level of the parameter D (particle diameter) and the fraction with a diameter between 212 μm and 250 μm for the high level.

In order to determine the influence of specific parameters on the leaching yield of molybdenum and vanadium with NaOH and H₂O₂, a factorial experiment with four parameters and two levels was performed. A total of 2⁴ tests were performed with four replications at the central level to estimate the experimental error. Table 3 and 4 summarizes the scheme of the implemented factorial plan.

Table 16. Parameters and levels of the factorial plan.

Factors		Levels		
		-	o	+
A	NaOH concentration	1 M	1.5 M	2 M
B	H ₂ O ₂ concentration	1 M	1.5 M	2 M
C	Temperature	25 °C	42.5 °C	60 °C
D	Particle size	< 212 mm	< 250 mm	250 > 212 mm

Table 17. Diagram of the tests performed with the 2 levels of the 4 parameters A, B, C, D: high level (+) and low level (-). The 4 replications at the central level (o) are also shown below.

Run	Factors			
	A	B	C	D
1	-	-	-	-
a	+	-	-	-
b	-	+	-	-
ab	+	+	-	-
c	-	-	+	-
ac	+	-	+	-
bc	-	+	+	-
abc	+	+	+	-
d	-	-	-	+
ad	+	-	-	+
bd	-	+	-	+
abd	+	+	-	+
cd	-	-	+	+
acd	+	-	+	+
bcd	-	+	+	+
abcd	+	+	+	+
R1	o	o	o	o
R2	o	o	o	o
R3	o	o	o	o
R4	o	o	o	o

All tests were conducted for three hours without stirring and with a solid concentration of 10% wt./vol. In this regard, 4 g of solid and 40 mL of solution were always used. Hydrogen peroxide was added in 3 steps during the three hours of the test: 1/3 at the beginning, 1/3 after one hour, and 1/3 after two hours. This procedure reduces the degradation of hydrogen peroxide over time (especially when working with temperatures at middle or high levels). It ensures an excess of oxygen, which is necessary for leaching. At the end of each test, vacuum filtration was performed to separate the residual solid from the leaching solution, and the solid was washed with 12 ml of distilled water (30% vol. of the leaching solution). ICP-OES analyzed the solution and the washing water to determine vanadium and molybdenum content. The residual solid was dried in an oven at 60°C for 24 h and subsequently weighed to determine the humidity and weight loss compared to the initial sample.

2.4 RESULTS AND DISCUSSIONS

2.4.1 GULF Process

2.4.1.1 TEST I

The experiments were performed on the roasted and calcined LCF sample. The procedure involved solubilizing the soluble sodium complex with vanadium and molybdenum in water. The process occurred at approximately 85°C ($\pm 3^\circ\text{C}$), under magnetic stirring (approximately 200 rpm) for 2 hours and at a solid concentration of 15%. For this reason, 200 ml of distilled water was first heated on the heater to approximately 80 °C, then 30 g of toasted catalyst sample was added. Temperature control was performed with a hand thermometer.

At the end of the process, the solution was separated by vacuum filtration. The filtration process lasted approximately three hours. Then, washing with 60 ml of distilled water and vacuum filtration were attempted. However, filtration was not possible for this step due to the time being too long. Therefore, in order to achieve solid separation, the centrifugation process (5 minutes - 4000 rpm) was performed.

The recovered solid was placed in an oven for drying. The weight loss of the solid after the leaching process was 43.48%. The volume of the recovered solution was 160 ml, and that of the wash water was 54.5 ml. Then, to store the analysis solution, 20 ml was collected.

In the remaining 140 ml of solution, 60 ml of distilled water was added, and the temperature was then increased to approximately 80°C. Then, 28 g of solid sample was added and reacted with water for another 2 hours at 85°C ($\pm 3^\circ\text{C}$). Then, two tests were performed on the leaching test mixture with a cationic polyelectrolyte (polyamine) to improve the filtration process. 100 ml of the mixture was removed from the container and cooled to room temperature. 0.5 ml of polyamine solution (10% wt./vol.) was added to the rest of the mixture. After 2-3 manual agitations, the mixture was allowed to stabilize for 1 minute, and then filtration was attempted with the same vacuum filtration system. Complete filtration of the solution was achieved within 20 minutes by adding polyamine. At the end of this test, 82 and 30 ml of solution and wash water, respectively, were recovered.

0.5 ml of polyamine solution was added to the cooled mixture, which was further stirred manually 2-3 times and allowed to stabilize for 1 minute. The vacuum filtration test of this mixture lasted 28 minutes. It took 30 minutes to filter the 30 ml of wash water. The recovered volumes were 95 ml for the solution and 30 ml for the wash water.

The solid residues from both tests were dried in an oven. 8.981 g of dried solids were recovered from hot solution filtration, and 7.095 g of dried solids were recovered from the test performed at room temperature. The weight loss of accumulated solids was 42.58%. The same approach was used for the third and fourth phases of the process. The results obtained are presented in.

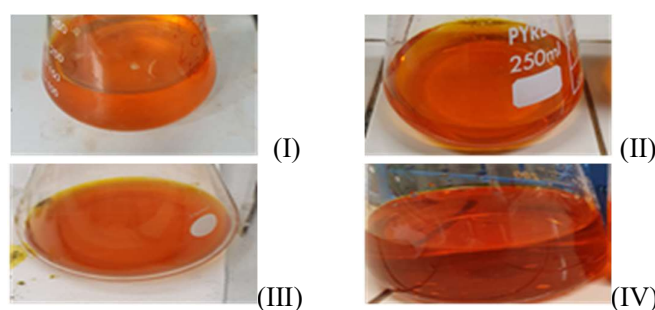


Figure 26. Photographic aspect of leaching solution for the four tests.

Table 18. Results of leaching step for the four tests.

Process	Solution type	Volume (mL)	Polyamine (% wt./vol.)	Filtration time (min)	Weight loss (%)	pH
I leaching	LL	162		180		6.68
	WW	60	-	Centrifugation (5 min - 4000 rpm)	43.48	-

II leaching	LL (85 °C)	82	0.5	20	42.58	6.72
	WW	30		20		-
	LL (25 °C)	95	0.5	28		6.56
	WW	30		30		-
III leaching	LL	154	-	180	37.47	6.68
	WW	61		Centrifugation (5 min- 4000 rpm)		-
IV leaching	LL	180	-	Centrifugation (5 min- 4000 rpm)	33.15	6.68
	WW	60		Centrifugation (5 min- 4000 rpm)		-

Table 19. Concentration and recovery for tests I and II.

Element	Parameter	I leaching		II leaching			
		LL	WW	LL (85 °C)	WW	LL (25 °C)	WW
V	Concentration [g/L]	12.20	2.99	19.42	6.78	17.28	5.37
	Recovery (%)	66.54	6.05	40.13		40.39	
	Total recovery (%)	72.59		80.52			
Mo	Concentration [g/L]	3.08	0.81	5.42	2.52	4.92	1.50
	Recovery (%)	33.28	3.24	24.81		24.30	
	Total recovery (%)	36.52		49.11			
Al	Concentration [g/L]	114	39	164	73	166	55
	Recovery (%)	0.42	0.05	0.22		0.27	
	Total recovery (%)	0.47		0.49			
Ni	Concentration [g/L]	21.35	6.46	18.59	8.30	19.58	8.29
	Recovery (%)	0.32	0.04	0.06		0.09	
	Total recovery (%)	0.36		0.15			
P	Concentration [g/L]	1.91	0	0.92	0.588	0	0.68

A good solubilization efficiency was obtained for vanadium. However, a further increase in leaching time can positively affect the recovery of this element. Furthermore, low efficiency was obtained for molybdenum. This result may also be due to the length of the process. A low degree of solubilization was obtained for aluminum, nickel, and phosphorous. Arsenic was not detected in any of the solutions tested. Furthermore, it was noted that the filtration time was significantly reduced by adding the cationic polyelectrolyte and filtering a smaller volume of solution.

Table 20. Concentration and recovery for tests III and IV.

Element	Parameter	III leaching		IV leaching	
		LL	WW	LL	WW
V	Conc. [mg/L]	26.96	1.92	27.82	0.94
	Recovery (%)	57.26	3.88	48.01	1.9
	Total recovery (%)	61.13		49.91	
Mo	Conc. [mg/L]	-	-	-	-
	Recovery (%)	-	-	-	-
	Total recovery (%)	-		-	

Al	Conc. [mg/L]	-	-	220	-
	Recovery (%)	-	-	-	-
	Total recovery (%)	-		-	
Ni	Conc. [mg/L]	47.85	11.65	44.57	2.84
	Recovery (%)	0.2	0.06	0.12	0.02
	Total recovery (%)	0.27		0.14	
P	Conc. [mg/L]	-	-	-	-

As shown in **Table 18**, the filtration process took longer when the same concentration of cationic polyelectrolyte per volume of solution was used. This result may be due to the formation of a large amount of solid particles on the surface of the filter, which does not allow the solution to be filtered. Determination of molybdenum concentration was not possible for these tests because there were several measurement interferences. Furthermore, the solution also creates measurement problems for other elements (aluminum and arsenic) in low concentrations. Therefore, only the efficiency for vanadium and nickel was calculated for these two tests.

It was noted that vanadium recovery decreased during these tests. This aspect is mainly because the roasted sample has a larger particle size than it was manually ground.

The results of the first precipitation step to remove aluminum, nickel, arsenic, and phosphorous impurities are shown in **Table 21**.

Table 21. Results of first precipitation.

Elements in residual solution	V	Ni
Concentration (mg/L)	24,681	0.16
Total recovery (%)	11.28	99.6

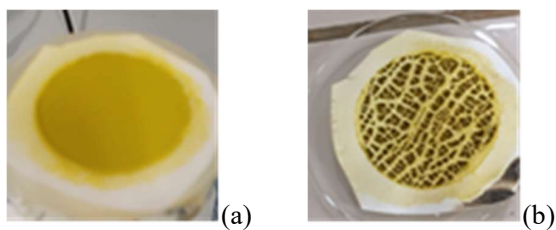


Figure 27. Photographic aspect of precipitate.

The evaluation of the precipitation of other elements was not possible for this test. The results of the second precipitation process for V recovery are shown in **Table 22**.

Table 22. Results of second precipitation.

Elements in residual solution	V	Ni
Concentration (mg/L)	940	0.44
Total recovery (%)	95.23	0

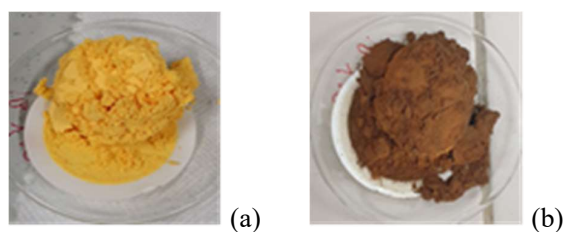


Figure 28. Photographic aspect of second precipitate before (a) and after (b) calcination.

The obtained roasted product weighed 4.25 g, and according to the composition of the precipitate, the degree of recovery of V from the solution was 90.48%. The approach used made obtaining a high-quality product possible, but the process can be further optimized.

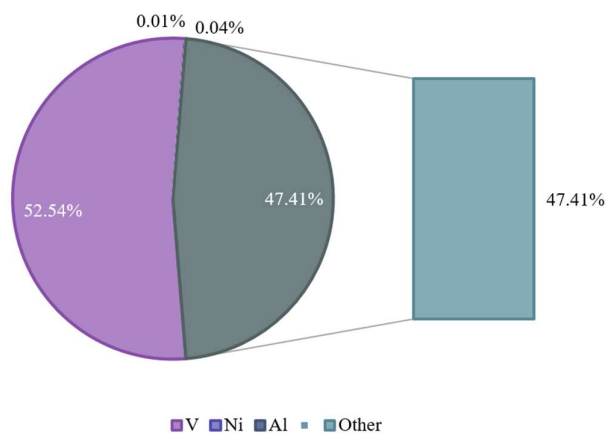


Figure 29. Elemental composition of second precipitate.

2.4.1.2 TEST II

Table 23 shows the results relating to the two phases of roasting and calcination.

Table 23. Results of roasting and calcination steps.

Process	ε NaHCO ₃	Wt. Loss (%) - I Roasting	Wt. Loss (%) - II Roasting	Wt. final [g]
1	50%	33.70	14.89	83.66
2	20%	29.32	19.25	79.06



Figure 30. Photographic aspect of the two pre-treated processes.

For process 1 there is a vanadium concentration in the initial solid of 10.26%, while for process 2 there is a vanadium concentration in the solid of 10.70%. The results of the different leaching steps for the 2 processes carried out are shown in **Table 24** **Table 26**.

Table 24. Concentrations of different elements for all leaching steps and cycles.

Cycle	Step	Process 1		Process 2			
		V [mg/L]	V [mg]	V [mg/L]	V [mg]	Al [mg/L]	Al [mg]
1°	I	7111	1080	11107	944	90	7.7
	II	1105	202	1459	128	26	2.3
2°	I	13021	1207	20613	1710	150	12.5
	II	2748	284	3257	293	42	3.9
	III	609	114	707	63	98	8.8
3°	I	20391	1503	13728	1180	125	10.8
	II	4227	314	2182	194	32	2.9
	III	1582	299	591	47	117	9.5
4°	I	16252	2164	13727	1125	118	9.7
	II	3395	336	1850	170	32	3.0
	III	822	150	215	19	33	3.1
5°	I	18511	2683				
	II	2834	366				
	III	581	104				
6°	I	18190	2666				
	II	2564	370				
	III	473	82				

Table 25. Vanadium recovery and weight loss for all leaching steps and cycles of process 1.

Cycle	Step	V Recovery (%)	V Cycle Recovery (%)	Wt. Solid after drying [g]	Wt. Loss (%)
1°	I	35.1	41.7	18.51	38.31
	II	6.6			
2°	I	39.2	52.1	18.55	38.17
	II	9.2			
	III	3.7			
3°	I	48.8	68.8	17.48	41.72
	II	10.2			
	III	9.7			
4°	I	70.3	86.1	16.57	44.78
	II	10.9			
	III	4.9			
5°	I	83.6	98.3	15.90	47.00
	II	11.4			
	III	3.3			
6°	I	83.1	97.2	15.60	48.01
	II	11.5			
	III	2.56			

The yields of the first and second cycles are lower because, before calcination with bicarbonate, the latter and the roasted material were not homogenized. This aspect led to an incomplete reaction with vanadium and molybdenum to form sodium molybdate and sodium vanadate (water-soluble compounds).

Table 26. Vanadium recovery and weight loss for all leaching steps and cycles of process 2.

Cycle	Step	V Recovery (%)	V Cycle Recovery (%)	Wt. Solid after drying [g]	Wt. Loss (%)
1°	I	58.8	66.83	9.34	37.75
	II	8.0			
2°	I	51.2	66.01	9.42	37.17
	II	10.8			
	III	4.0			
3°	I	56.7	68.15	9.28	38.13
	II	8.4			
	III	3.0			
4°	I	58.7	67.74	9.35	38.90
	II	7.8			
	III	1.2			

The total recovery yield of the three countercurrent steps was calculated as the sum of the individual yields. For process 1, a recovery of 99.4% was achieved, while for process 2, a recovery of 71.1%.

Table 27 **Table 28** show the results of the vanadium precipitation tests in terms of vanadium concentrations for the solution obtained through filtration and washing water.

Table 27. Results of vanadium precipitation tests.

Run	HCl [mL]	pH pre-filtration	Solution [mL]	V [mg/L]	Washing Water [mL]	V [mg/L]
1	0.55	7.42	81	3188.1	30	186.62
2	0.55	7.23	79	170.54	31	203.57
3	2.19	6.50	84	11076.16	30	1282.54
4	2.20	6.13	83	9257.68	31	1764.03

Table 28. Results of precipitates drying.

Run	60° drying			600° drying		
	Wt. solid pre-drying [g]	Wt. solid post-drying [g]	Wt. Loss (%)	Wt. solid pre-drying [g]	Wt. solid post-drying [g]	Wt. Loss (%)
1	1.339	0.921	31.22	0.917	0.707	22.90
2	3.454	3.323	3.79	3.323	2.553	23.17
3	1.084	0.828	23.62	0.837	0.687	17.92
4	1.932	1.552	19.67	1.518	1.183	22.07

Subsequently, a chemical attack was carried out on the residual solids in order to determine their purity. The results of this analysis are reported in Table 23.

Table 29. Composition of precipitates in terms of elements and as V_2O_5 .

Run	Product [g]	V (%)	Ni (%)	Al (%)	V_2O_5 (%)
I	0.707	56.036	0.072	0.254	100.04
II	2.553	55.970	0.000	0.100	99.92
III	0.687	51.133	0.117	0.117	91.28
IV	1.183	48.740	0.055	0.166	87.01

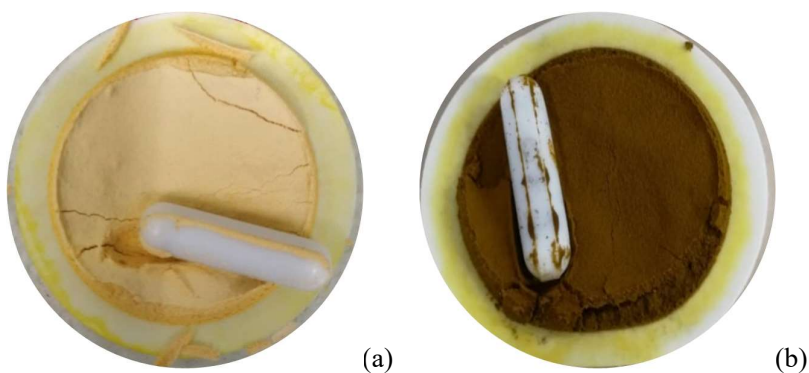


Figure 31. Photographic aspect of precipitate I before (a) and after (b) drying.

The appearance of values above 100% can be attributed to analytical errors.

Table 30. Results of vanadium precipitation tests for the two different calculation methods.

Run	V recovery (%)	
	Calculation 1	Calculation 2
I	28.40	60.03
II	102.44	98.63
III	25.18	26.61
IV	41.34	41.20

Table 30 shows the recovery of vanadium for the various precipitation tests. The calculation was carried out in two ways. First, based on the vanadium in the final product and the starting solution (Calculation 1); second, based on the vanadium in the final product and the residual vanadium of the final solutions (Calculation 2).

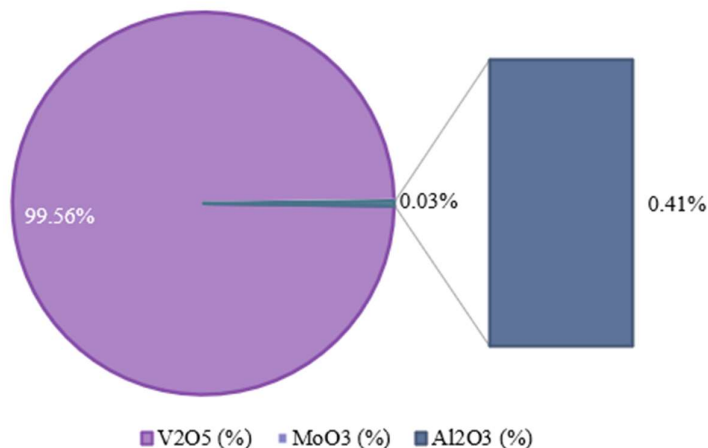


Figure 32. Composition of precipitate II.

2.4.1.3 TEST III

The table below presents the results relating to the heat treatment of the two samples.

Table 31. Results of roasting and calcination for the samples.

Sample	Roasting	Wt. loss (%)	Calcination	ϵ Na ₂ CO ₃	Na ₂ CO ₃ [g]	Wt. loss (%)
A	850 °C - 2 h	32.13	800 °C - 2 h	50%	17.829	3.35
B	850 °C - 2 h	32.28	800 °C - 2 h	110%	25.000	4.98

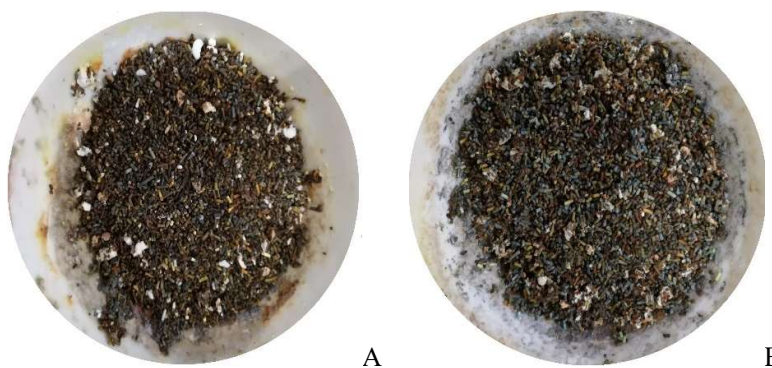


Figure 33. Photographic aspect of the two samples after the thermal pre-treatments.

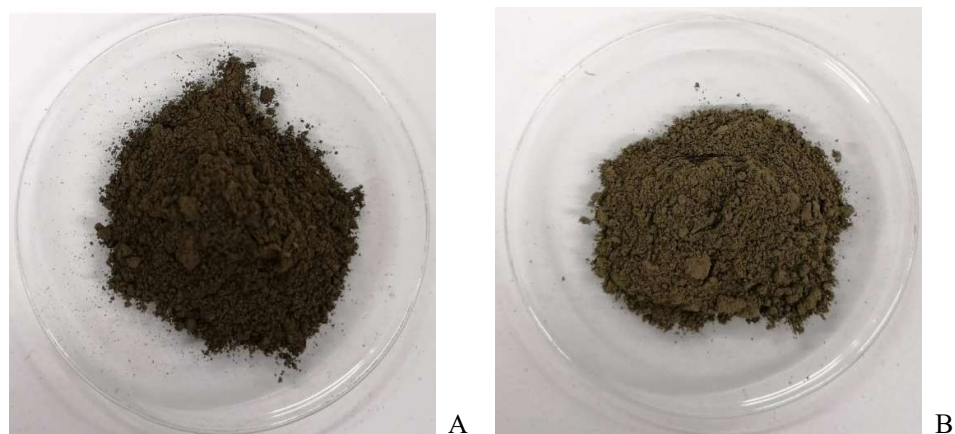


Figure 34. Photographic aspect of the two samples after milling.

Table 32 shows the results for the 2 countercurrent 3-stage processes used to leach the 2 samples. Vanadium recovery is calculated for all steps and for all cycles.

Table 32. Results of leaching steps for the two samples.

Cycle	Step	Sample A			Sample B		
		V [mg/L]	V Recovery (%)	Cycle Recovery (%)	V [mg/L]	V Recovery (%)	Cycle Recovery (%)
1°	I	9346.20	31.33		17719.50	62.11	
	II	1484.50	5.45	40.17%	4503.80	17.28	82.04%
	III	908.76	3.39		681.29	2.66	
2°	I	10352.01	30.66		19491.14	51.34	
	II	2094.57	4.54	38.06%	2972.27	8.83	64.53%
	III	777.32	2.85		1116.34	4.36	
3°	I	11197.56	30.56		21608.44	62.91	
	II	2253.08	5.46	39.34%	4648.58	13.62	80.86%
	III	888.36	3.32		1129.54	4.33	

The total recovery yield of the three countercurrent steps was calculated as the sum of the individual yields. For sample A, a recovery of 38.5% was achieved, while for sample B, a recovery of 74.4%.

Table 33. Weight and moisture losses of solid residues after drying in an oven at 60 °C for 24 h.

Cycle	Process A		Process B	
	Humidity (%)	Wt. Loss (%)	Humidity (%)	Wt. Loss (%)
1	35.17	36.33	44.30	47.71
2	34.98	36.19	42.76	47.05
3	35.17	35.55	43.35	46.83

Single-step tests with magnetic agitation and manual temperature control were performed To evaluate the effect of the different agitation speeds. Four leaching tests were carried out (2 for each sample) where the ratio between the solid and the leaching liquid (distilled water at 85°C) was also varied.

Some important parameters of the tests and the results obtained are reported in **Table 34** and **Table 35**.

Table 34. Results of the four leaching tests.

Sample	Run	Solid [g]	Liquid [mL]	S/L	V Recovery (%)	Humidity (%)	Wt. Loss (%)
A	I	15	60	25%	32.25%	33.89%	29.19%
	II	15	100	15%	35.17%	33.90%	31.04%
B	I	15	60	25%	62.88%	39.40%	39.79%
	II	15	100	15%	66.93%	41.17%	42.05%

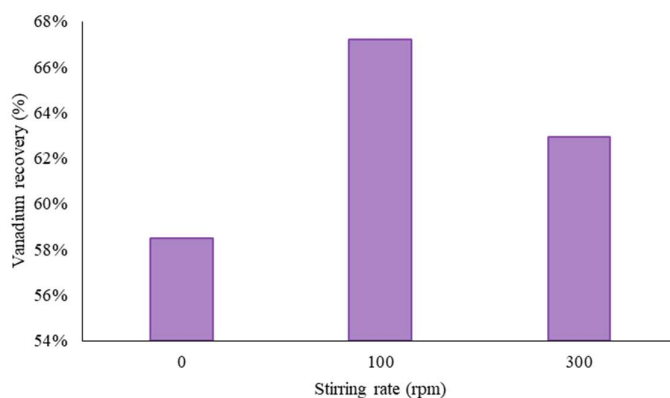
Table 35. Summary of different leaching tests.

Sample	Run	V Recovery (%)
A	50% Na ₂ CO ₃	3 step Counter Current
		1 step 25% wt./vol
		1 step 15% wt./vol
B	110% Na ₂ CO ₃	3 step Counter Current
		1 step 25% wt./vol
		1 step 15% wt./vol

The recovery yields so low compared to the expected values are certainly due to oxygenation problems of the material during the heat treatment. Samples A and B were placed simultaneously inside the oven during the calcination phase. This aspect may have resulted in a low oxygen concentration in the combustion chamber (the muffle has a relatively small combustion chamber) and, consequently, a relatively low conversion.

2.4.1.4 Sedimentation tests

Table 35 summarizes the results obtained in terms of vanadium recovery for each of the three tests performed (I for the test without stirring, II for the test at 100 rpm and III for the test at 300 rpm).

**Figure 35.** V recovery for the 3 tests performed in a single step (15% S/L, 2 h, 85°C).

The results of the sedimentation tests are reported below.

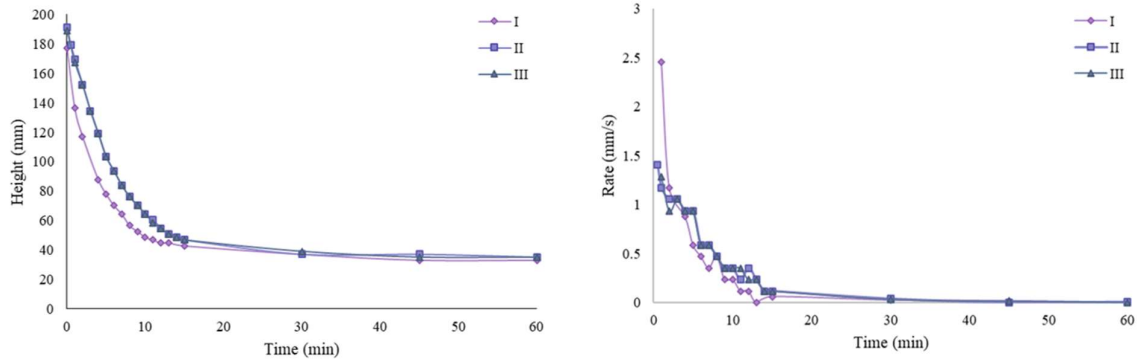
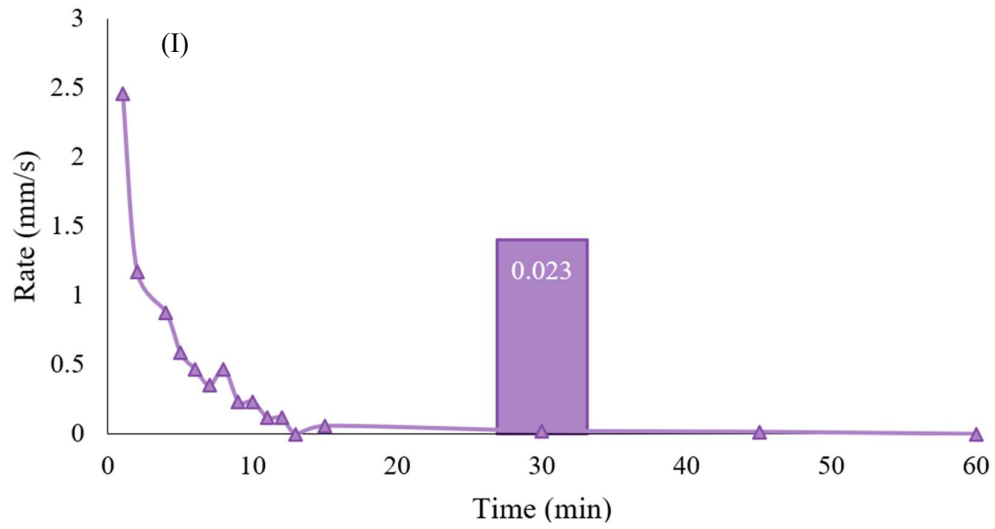


Figure 36. Variation of the height of the solid front and the sedimentation velocity for the three tests.



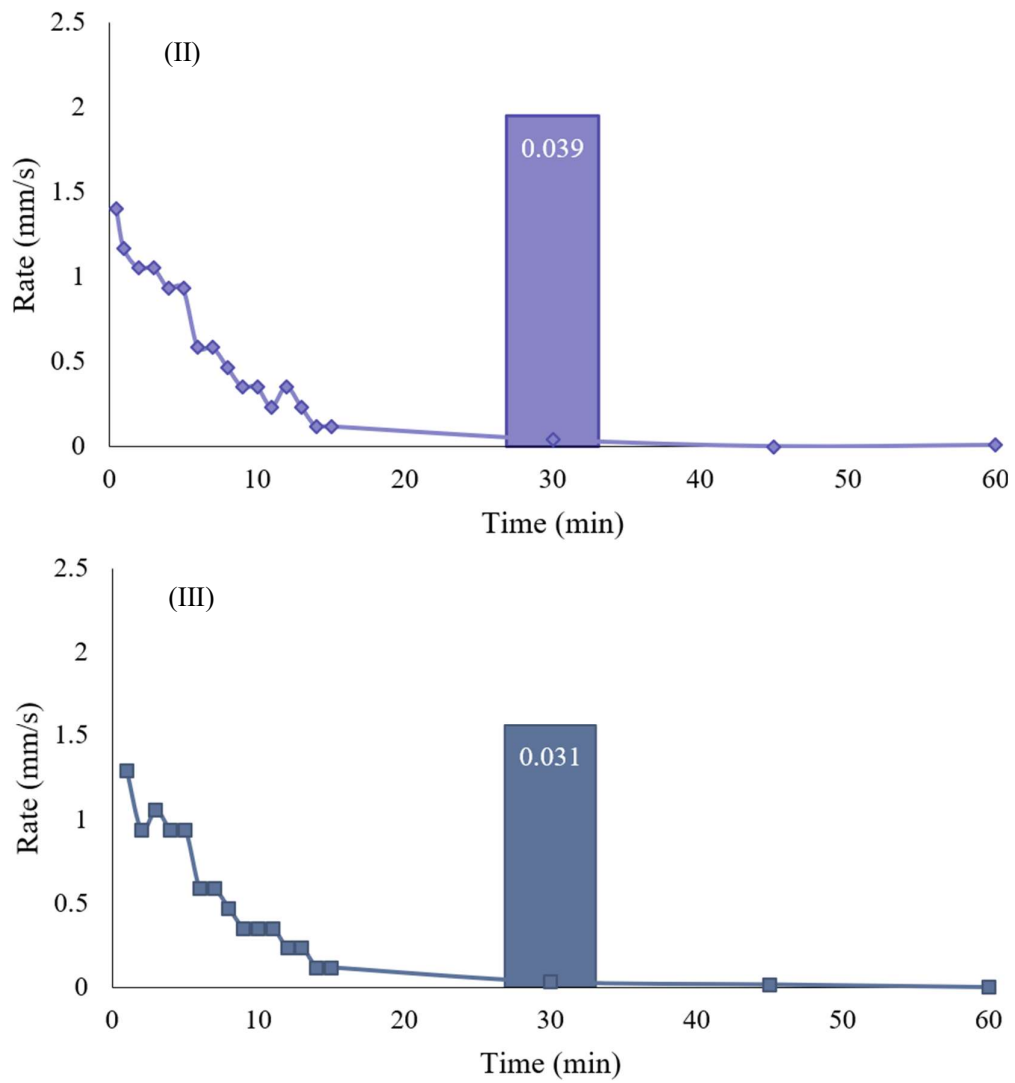


Figure 37. Sedimentation rate for the three tests vs time and sedimentation rate at 30 min.

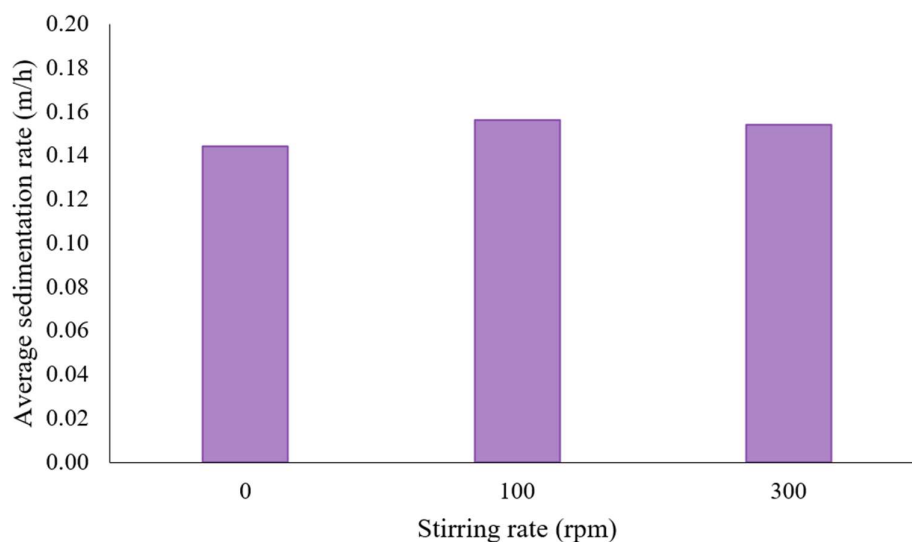


Figure 38. Average sedimentation speed for the three tests.

The results of the tests aimed at determining the effect of the polyelectrolyte are reported below.

Table 36 shows the results relating to the various heat treatments, while **Table 37** and **Table 38** illustrate the results relating to leaching.

Table 36. Results of thermal pre-treatments.

Sample	Pre-treatment	Wt. loss (%)	Roasting	Wt. loss (%)	Calcination	Wt. loss (%)
1	-	-	850°C - 2 h	32.82%	800°C - 2 h	15.53%
2	-	-	850°C - 2 h	32.86%	800°C - 2 h	3.74%
3	Washing with Acetone + air drying for 2 h	3.84%	-	-	800°C - 2 h	26.98%

Table 37. Results of leaching phase.

Sample	Solution [mL]	T [°C]	Solid [g]	t [h]	LL [mL]	V [mg/L]	Mo [mg/L]
1	250	85	37.5	2	229	12924.73	3428.26
2	250	85	37.5	2	224	12746.28	3835.94
3	250	85	37.5	2	225	5424.98	1721.81

Table 38. Recovery yields for vanadium and molybdenum.

Sample	V recovery (%)	Mo recovery (%)
1	73.35%	38.53%
2	71.47%	42.59%
3	31.49%	19.79%

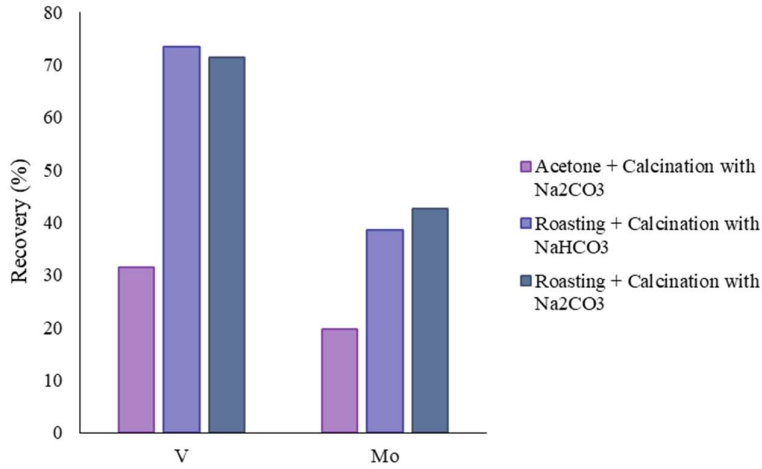


Figure 39. Summary of leaching results.

The results of the sedimentation tests with polyamine are reported below.

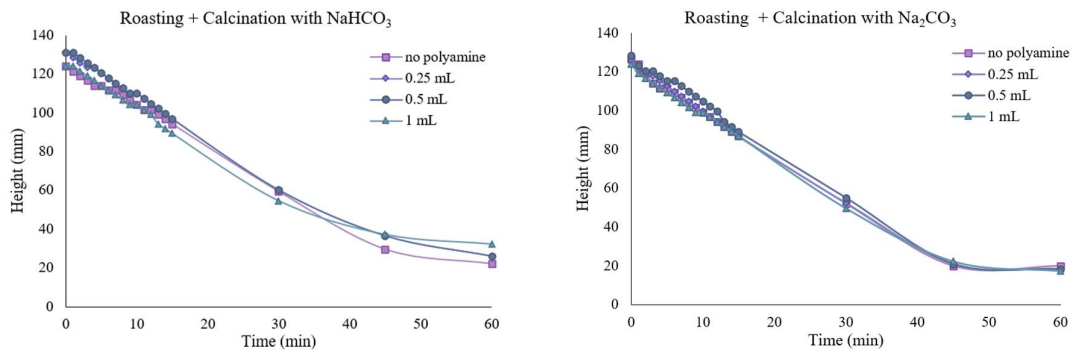


Figure 40. Time trend of the solid front for the sample.

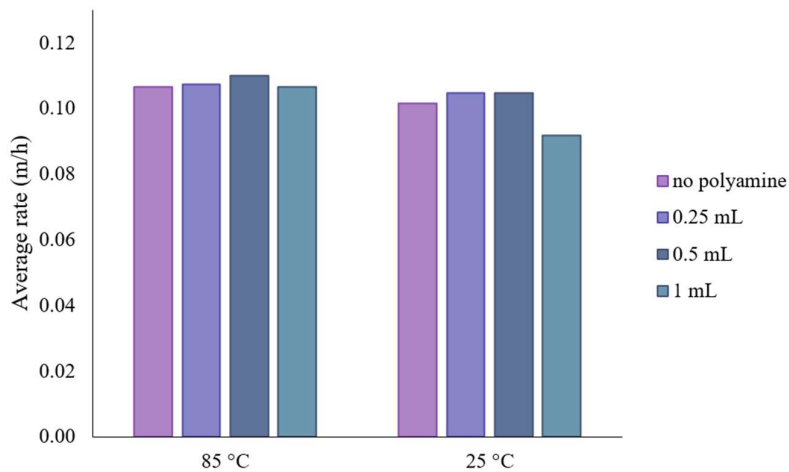


Figure 41. Average speed for the various sedimentation tests.

Figure 42 and Figure 43 summarize the results obtained from all the single-step leaching and sedimentation tests.

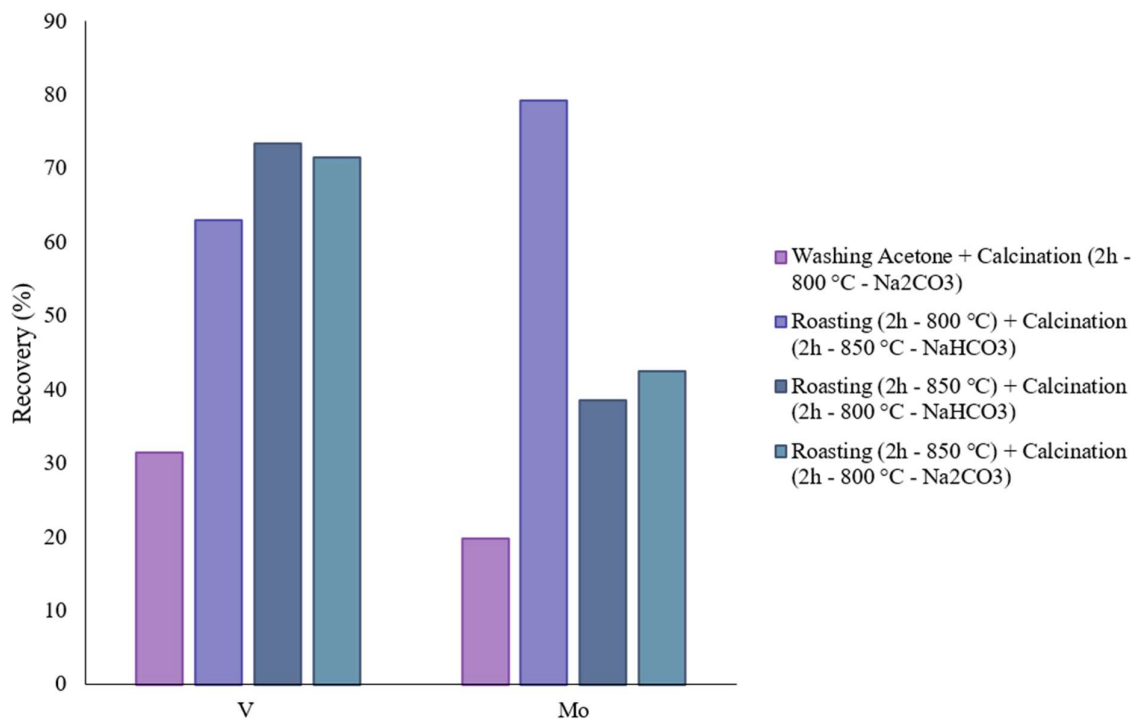


Figure 42. Summary of the recovery of vanadium and molybdenum for all tests carried out.

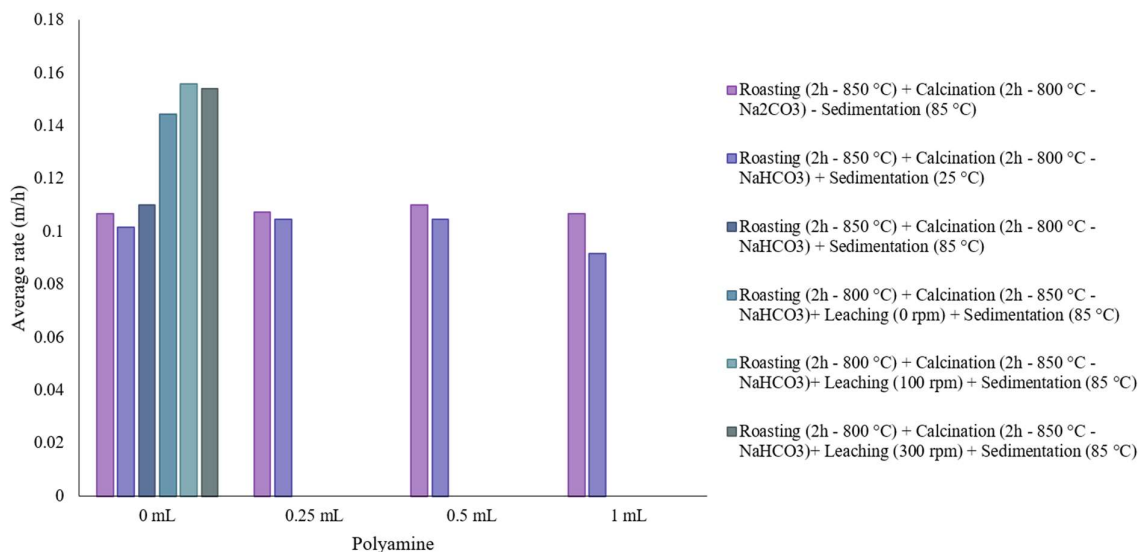


Figure 43. Average sedimentation rate for all sedimentation tests carried out.

Four precipitation tests were carried out with the clarified solution coming from the leaching of Sample 1 (treated with NaHCO₃) and Sample 2 (treated with Na₂CO₃). For each test, 100 mL of clarified solution was used. Using a magnetic stirring plate and a manual thermometer, the temperature was brought to 40°C and NH₄Cl was added.

Table 39. Conditions and results of leaching tests.

Run	Treatment	Solution [mL]	NH ₄ Cl [g]	T [°C]	t [min]	pH	Wt. loss (%) 105°C - 24 h	Wt. loss (%) 600°C - 1 h
1a	Na ₂ CO ₃	100	4.015	40	60	7.02	27.70%	9.10%
1b	Na ₂ CO ₃	100	4.015	40	120	7.04	27.92%	8.93%
2a	NaHCO ₃	100	4.071	40	60	7.46	38.84%	15.69%
2b	NaHCO ₃	100	4.071	40	120	7.47	36.32%	16.96%

**Figure 44.** Weight losses of the drying process (105°C, 24 h) and calcination (600°C, 1 h).**Table 40.** Recovery yields of vanadium and molybdenum for the various tests.

Run	V recovery (%)	Mo recovery (%)
1a	56.82%	18.50%
1b	65.52%	23.87%
2a	82.81%	10.31%
2b	86.47%	8.79%

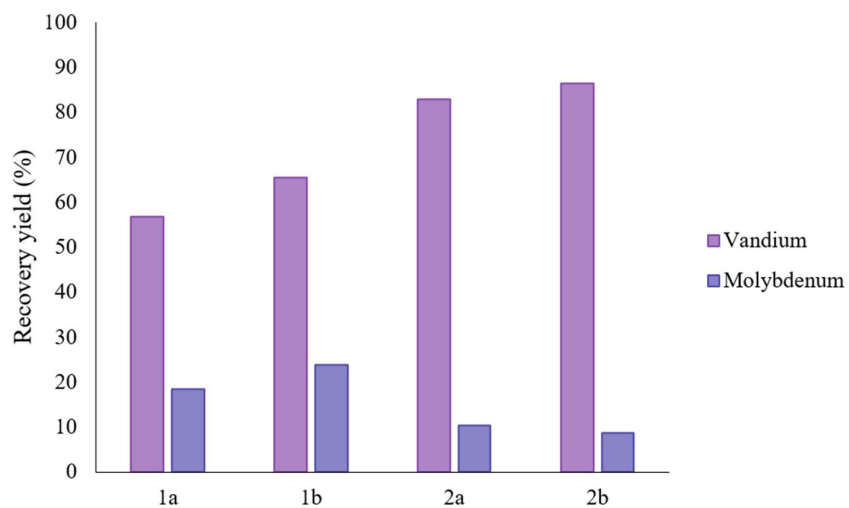


Figure 45. Recovery yields of vanadium and molybdenum.



Figure 46. Photographic aspect of precipitates after filtration.

Table 41. Composition of precipitates determined by analysis of chemical attack solutions.

Run	V (%)	Mo (%)	Ni (%)	Al (%)	V ₂ O ₅ (%)	MoO ₃ (%)	NiO (%)	Al ₂ O ₃ (%)
1a	52,04	2,47	0,01	0,14	92,90	3,70	0,01	0,26
1b	51,59	2,80	0,01	0,15	92,11	4,20	0,01	0,28
2a	54,57	1,34	0,02	0,10	97,42	2,01	0,02	0,19
2b	54,85	1,09	0,01	0,11	97,91	1,63	0,02	0,21

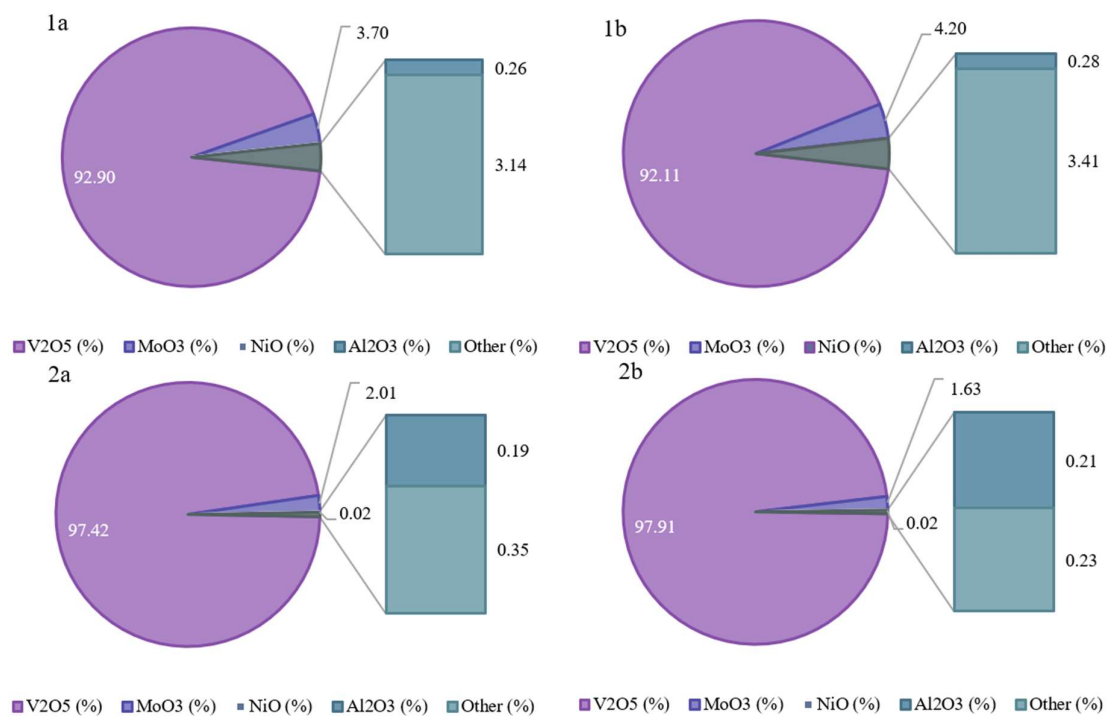


Figure 47. Composition of solid precipitates in terms of oxides.

The solid precipitates were subjected to XRD analysis. The results obtained are presented in the figures below for sample 1a.

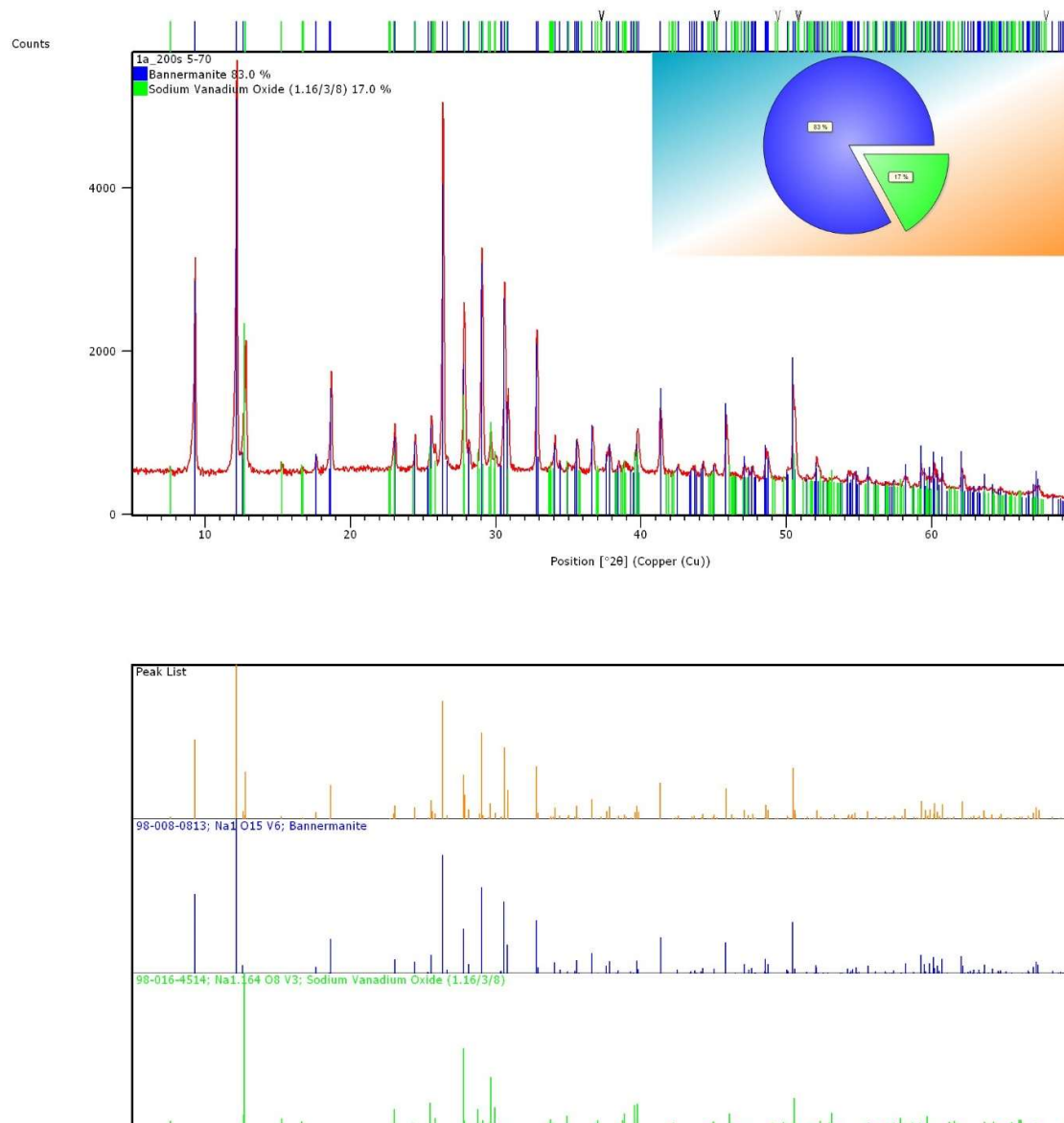


Figure 48. Results of the XRD analysis on precipitate 1a relating to vanadium.

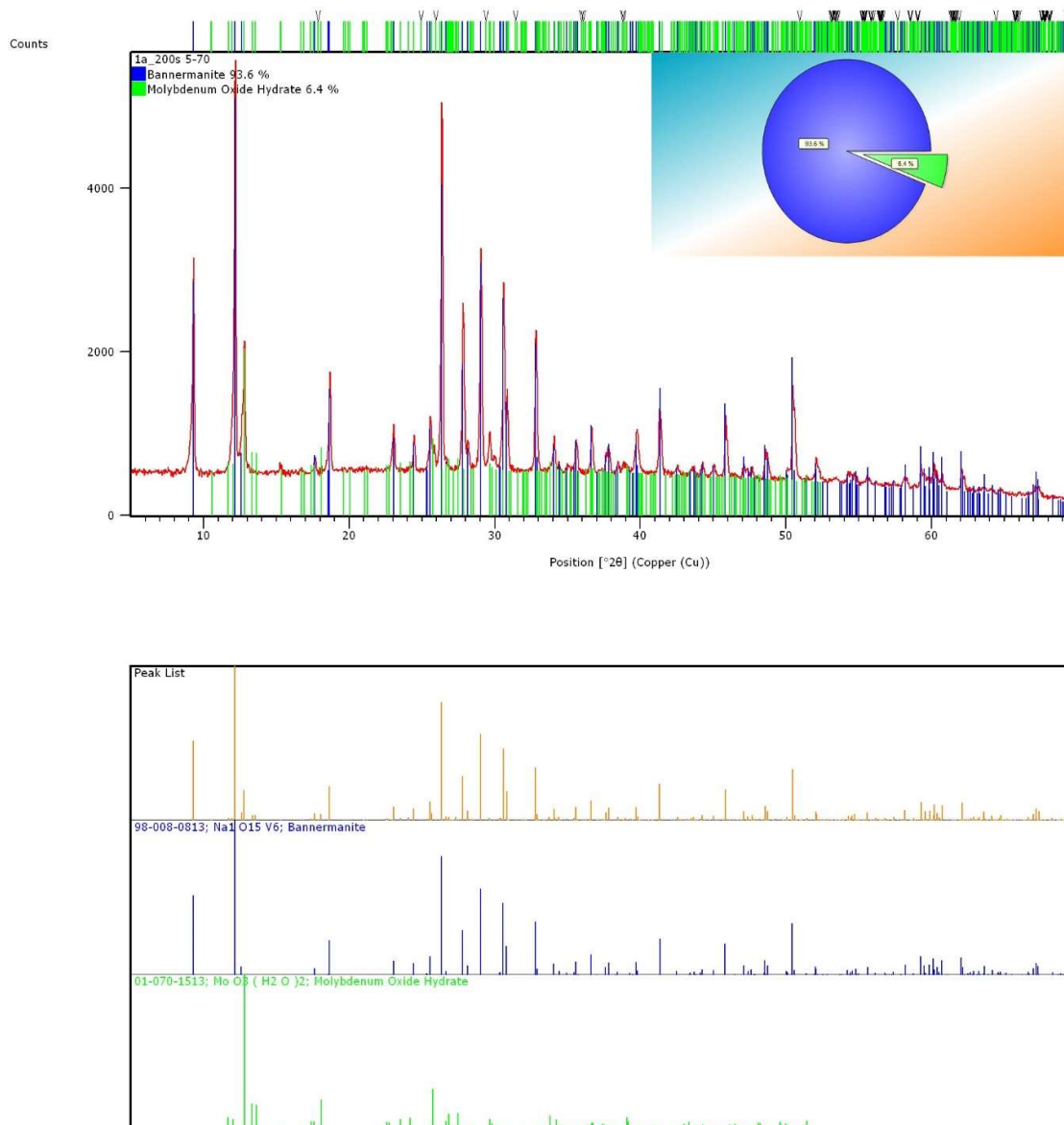
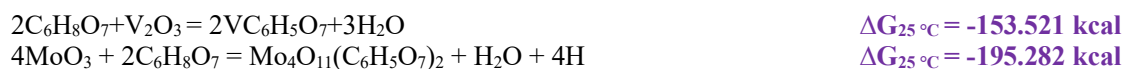


Figure 49. Results of the XRD analysis on precipitate 1a relating to molybdenum.

The results obtained show that all samples have a crystalline structure with Bannermanite as the main V-oxide complex.

2.4.2 Citric acid process

Vanadium and molybdenum oxides react with citric acid according to the following reactions.



After leaching with this organic acid, the resulting solution was analyzed for its vanadium, molybdenum, nickel, aluminum, arsenic, and phosphorous content. The results in terms of element concentration and degree of recovery are presented in **Table 42**.

Table 42. Results of citric acid leaching test.

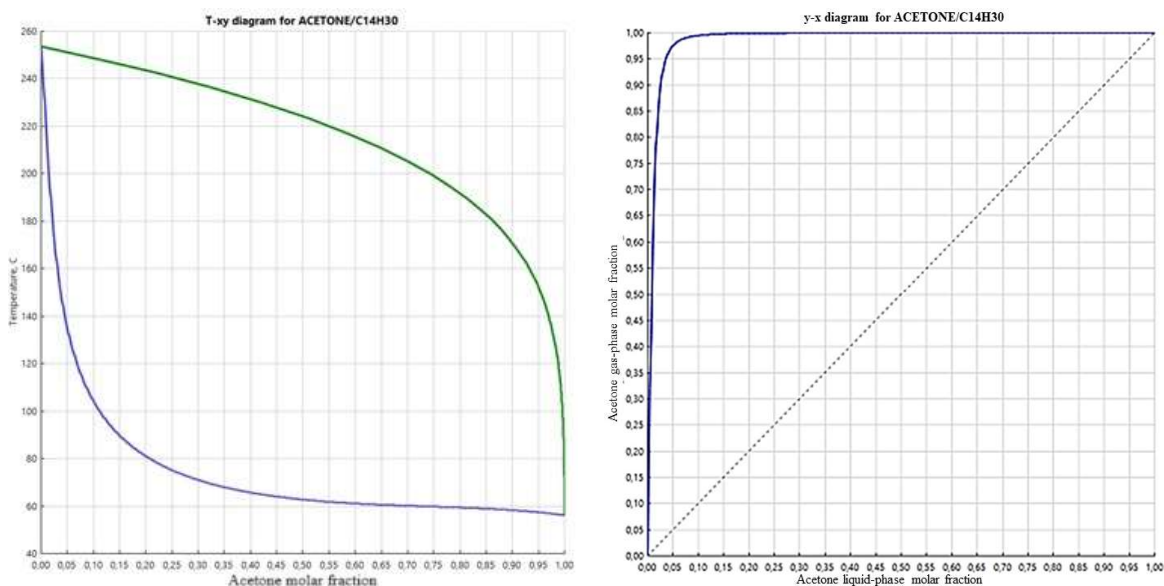
Element in solution	V	Mo	Ni	Al
Concentration (g/L)	2.80	0.28	0.04	0.08
Recovery (%)	67.24%	13.12%	2.74%	1.21%

The results show that the leaching with citric acid of this sample allowed a good degree of recovery for vanadium. From this sample, a good selectivity of vanadium leaching is obtained. This result may be because aluminum and nickel are probably not present as oxides within the treated sample.

2.4.3 ORIM-CAT2 Process

First, simulations were performed on the AspenPlusV10 process simulator to evaluate the feasibility of the acetone recovery and reuse process once the washing had been performed. N-tetradecane ($C_{14}H_{30}$) was chosen as the reference component for the organic component.

Thanks to the experimental data present in the Aspen (NIST) database, some thermodynamic models for the treated system have been validated. Finally, we chose to work with the IDEAL thermodynamic model, the simplest from a computational point of view but simultaneously precise and accurate. Below are some graphs relating to the liquid-vapor equilibrium of the acetone- $C_{14}H_{30}$ system.

**Figure 50.** T-xy (left) and partition (right) diagrams of the Acetone - $C_{14}H_{30}$ system.

As shown in the graphs, separating the acetone- $C_{14}H_{30}$ mixture through distillation is undoubtedly one of the most advantageous ways. In this regard, simulations were performed to evaluate the theoretical number of equilibrium stages of the distillation column. It has been seen that it is possible to recover practically all the acetone with a high degree of purity using even a single equilibrium stage.

Sensitivity analyses were conducted on this Flash stage to determine the optimal temperature value for acetone recovery and purity. **Figure 51** shows the summary graph of this analysis.

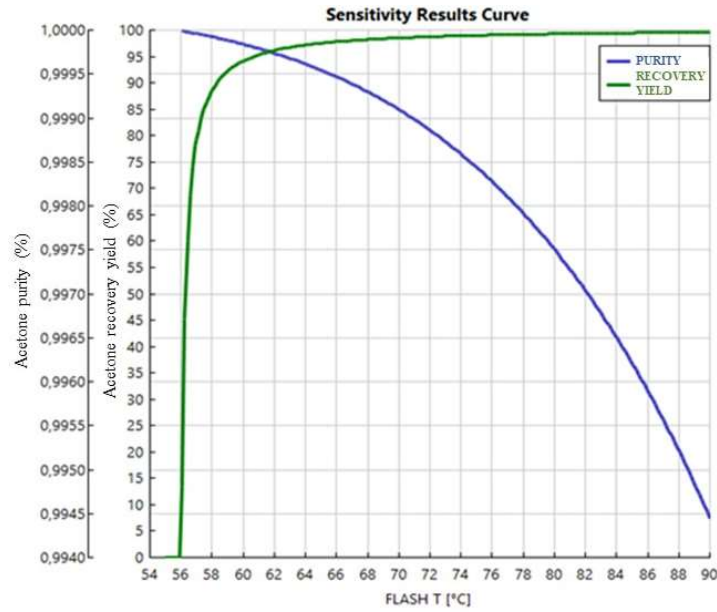


Figure 51. Results of sensitivity analysis.

An operating temperature of 57 °C was chosen for the Flash equipment as it allows for:

- Acetone recovery yield: >80.0%
- Purity of recovered acetone: >99.9%

Further studies were carried out to minimize the energy impact of the recovery section (the most energy-intensive section of the entire pretreatment). Figure 52 shows a system solution that allows reducing energy consumption thanks to the heating of the input stream with the liquid stream exiting the flash stage (liquid C₁₄H₃₀).

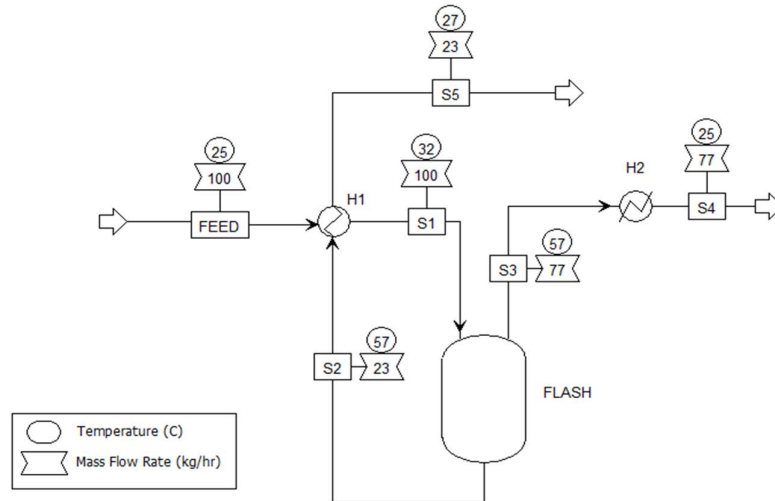


Figure 52. Flowsheet of acetone recovery process.

Table 43. Material and energy balance results of acetone recovery process.

	Units	FEED	S1	S2	S3	S4	S5
Phase		Liquid Phase	Liquid Phase	Liquid Phase	Vapor Phase	Liquid Phase	Liquid Phase
Temperature	C	25	32,22	57	57	25	27
Pressure	bar	1	1	1	1	1	1
Mass Vapor Fraction		0	0	0	1	0	0
Mass Liquid Fraction		1	1	1	0	1	1
Mass Solid Fraction		0	0	0	0	0	0
Mass Enthalpy	cal/gm	-999,33	-995,68	-929,97	-876,85	-1015,18	-945,70
Mass Entropy	cal/gm-K	-1,29	-1,28	-1,29	-0,86	-1,28	-1,33
Mass Density	gm/cc	0,79	0,78	0,74	0,00	0,79	0,78
Enthalpy Flow	cal/sec	-27759,05	-27657,89	-5981,55	-18717,14	-21669,86	-6082,72
Average MW		59,34	59,34	63,93	58,08	58,08	63,93
Mass Flows	kg/hr	100	100	23,155	76,845	76,845	23,155
<i>Mass Fractions</i>							
ACETONE		0,97	0,97	0,87057	0,99996	0,99996	0,87057
C14H30		0,03	0,03	0,12943	0,00004	0,00004	0,12943
Volume Flow	l/min	2,1205	2,1434	0,5195	605,2890	1,6245	0,4967

Through the simulation carried out, it was possible to estimate energy consumption for the recovery of the solvent equal to approximately 140 kcal/kg acetone recovered.

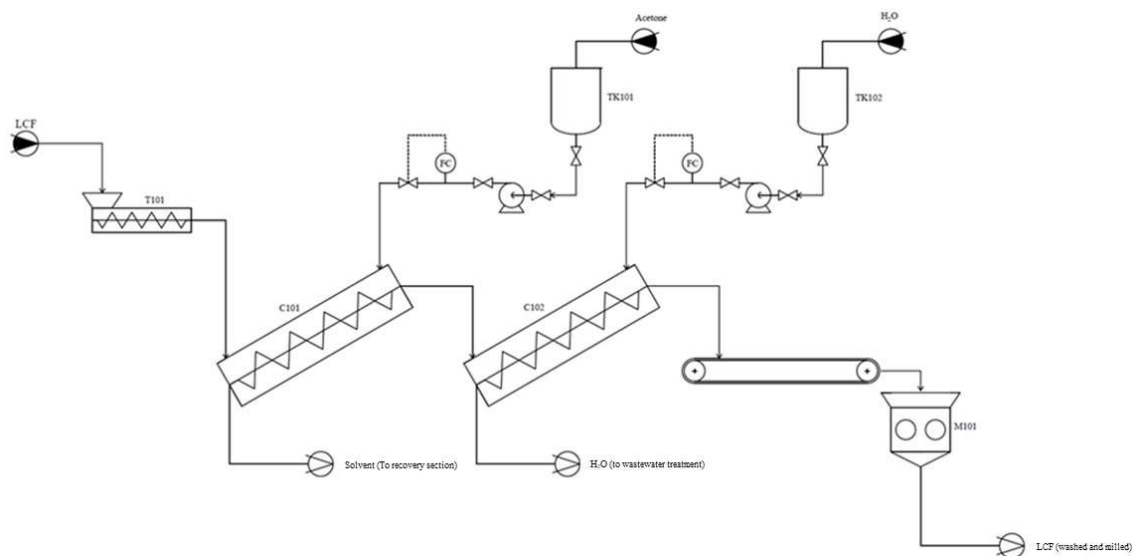
**Figure 53.** Catalyst washing diagram with Acetone.

Figure 53 shows the simplified process diagram of the catalyst washing section with acetone. The catalyst is fed through the T101 into C101 for the first wash performed with acetone. Acetone is fed into C101 from the TK101 tank through the use of a pump. Two different currents start from C101: a solid one made up of the washed catalyst and a liquid one composed mainly of acetone and the organic component initially present in the catalyst. The washed catalyst is sent to C102 for washing with water while the solvent is sent to the acetone recovery section.

The washing water is fed into C102 from the TK102 tank. 2 streams also come out of C102: a solid stream (washed catalyst) sent via a conveyor belt to the M101 ball mill, and a liquid stream (contaminated water) sent to the water treatment.

The M101 ball mill grinds the washed catalyst and makes it available for the subsequent leaching phase.

The calculation basis for a first material balance is approximately 5 ton/d of LCF catalyst. As already mentioned previously, an LCF/Acetone ratio of 20% is used.

Table 44. Material balance results of the washing section.

Feed	LCF	5	ton/d
		208	kg/h
	$C_{14}H_{30}$	23%	wt.
		48	kg/h
C101	Catalyst/Acetone ratio	20%	wt./vol.
	Initial acetone	1042	L/h
	Acetone lost in the wash	823	kg/h
	Final acetone	20%	-
C102	Final acetone	658	kg/h
	Catalyst/Water ratio	20%	wt./vol.
	Initial water	1042	L/h
	Water lost in the wash	1042	kg/h
		5%	-
	Final water	990	kg/h
To recovery section	Fraction of $C_{14}H_{30}$ removed	30%	-
	Acetone + $C_{14}H_{30}$	673	kg/h
	Acetone	98%	wt.
	$C_{14}H_{30}$	2%	wt.

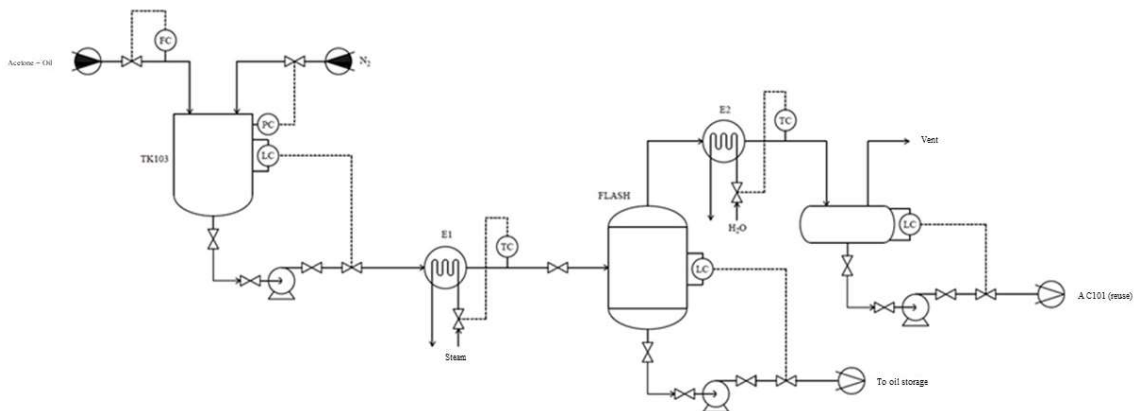


Figure 54. Simplified process diagram of the acetone recovery section.

Figure 54 shows the simplified process diagram of the acetone recovery section. The current coming out of C101 in the washing section is sent to the TK103 tank. This tank is inertized with nitrogen due to the high flammability of the mixture contained. From the TK103 tank, the acetone – $C_{14}H_{30}$ mixture is pumped to the E1 exchanger, which uses steam to bring the mixture's temperature to approximately 57°C. As seen in **Figure 53**, it is possible to preheat the incoming stream with the liquid stream coming out of the Flash stage and subsequently use the exchanger E1 for rectification; proceeding in this way can reduce the energy consumption of the recovery section but still need to insert a recuperator into the process.

Once heated, the current coming out of E1 enters the FLASH stage, where the acetone is separated from the organic component. The more volatile acetone leaves the head of the FLASH stage and is condensed via the E2 exchanger. Once the non-condensable present in the system has been eliminated, the acetone can be reused in C101.

The liquid stream from the FLASH stage is sent to a storage system and used as fuel.

Table 45. Material balance results of acetone recovery section.

Feed	Acetone + C ₁₄ H ₃₀	673	kg/h
	Acetone	98%	wt.
	C ₁₄ H ₃₀	2%	wt.
FLASH	Acetone recovered	83%	-
	Acetone purity	546	kg/h
	C ₁₄ H ₃₀	99,9%	wt.
		126	kg/h

The possibility of operating through gasification of the organic component on the surface of the exhausted LC-Finer catalyst instead of washing with acetone was also evaluated. For this reason, a process simulation was created using AspenPlusV10. The primary purpose of the simulation is to understand the thermodynamic behavior of the system under consideration to estimate the flow rate and composition of the Syngas produced.

In order to proceed with the calculation, it is necessary to know the composition of the organic component on the catalyst. The organic fraction is the residue of petroleum hydro-desulfurization processes and is therefore characterized by many hydrocarbons. From a literature analysis, it was decided to use n-Tetradecane (C₁₄H₃₀) to represent the various hydrocarbons.

The IDEAL thermodynamic model was used on the AspenPlusV10 process simulator since the operating conditions do not require the presence of high pressures (>10 bar) and require high temperatures.

The simulation was performed using the RGibbs equipment as it allows the equilibrium composition to be determined (specifying T and P) by minimizing the Gibbs free energy of the thermodynamic system (ΔG). In **Figure 55**, it is possible to see the flowsheet of the simulation carried out.

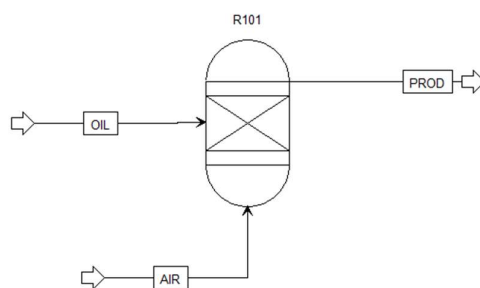


Figure 55. Flowsheet of simulation.

Through sensitivity analysis, the system was analyzed at equilibrium for different values of temperatures and air supplied to the reactor. From these analyses, the various graphs shown below were obtained where it is possible to see both the mass of C₁₄H₃₀ consumed (**Figure 56**) and the mass-produced of the different gases. **Table 46** summarizes the gases whose presence at equilibrium is hypothesized.

Table 46. Syngas components (excluding N₂ and O₂).

H ₂	Hydrogen
CH ₄	Methane
C ₂	Ethane, Ethylene
C ₃	Propane, Propylene
C ₄	N-butane, I-butane
CO ₂	Carbon dioxide
CO	Carbon monoxide

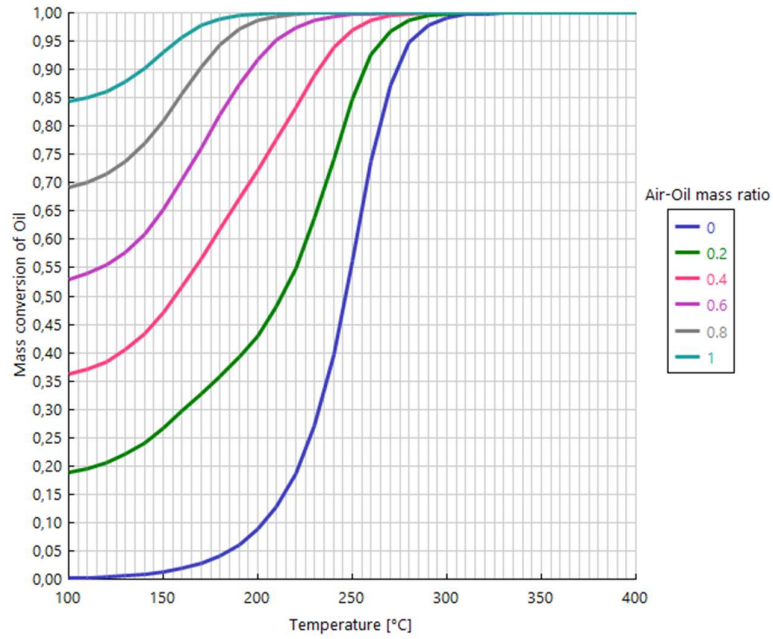


Figure 56. Mass conversion of Oil as function of Temperature and Air-Oil mass ratio.

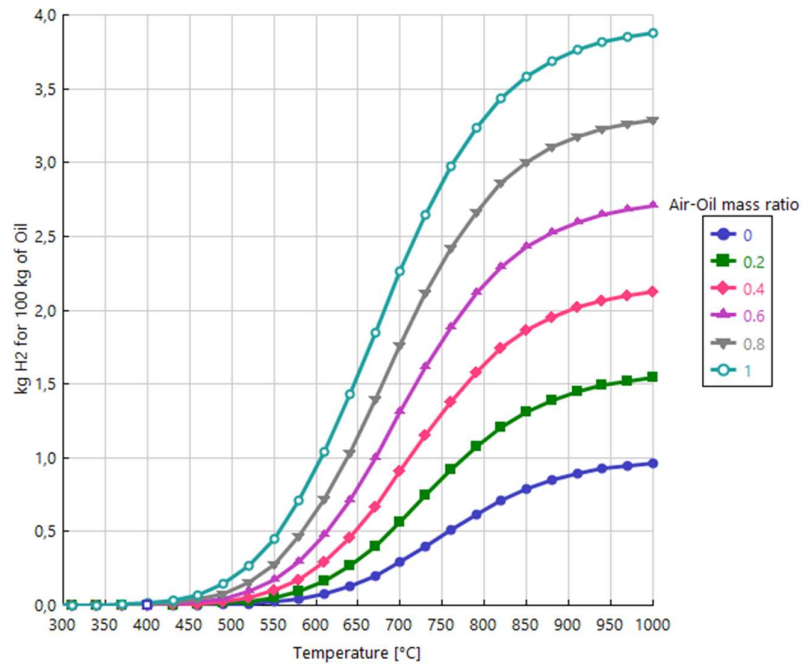


Figure 57. Hydrogen produced by 100 kg of Oil as function of Temperature and Air-Oil mass ratio.

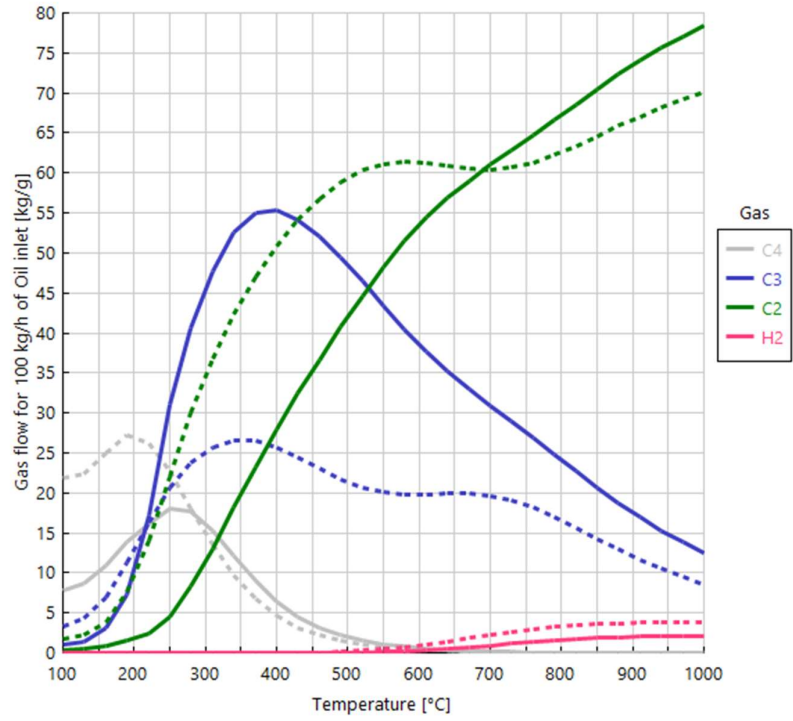


Figure 58. Syngas produced for 0.4 (—) and 1 (---) Air-Oil mass ratio.

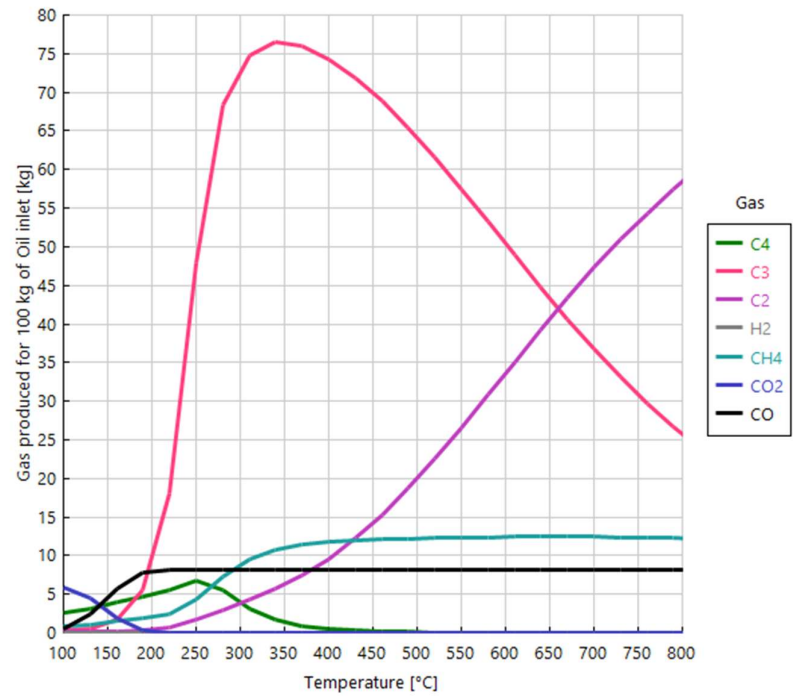


Figure 59. Syngas produced with 0.2 Air-Oil mass ratio.

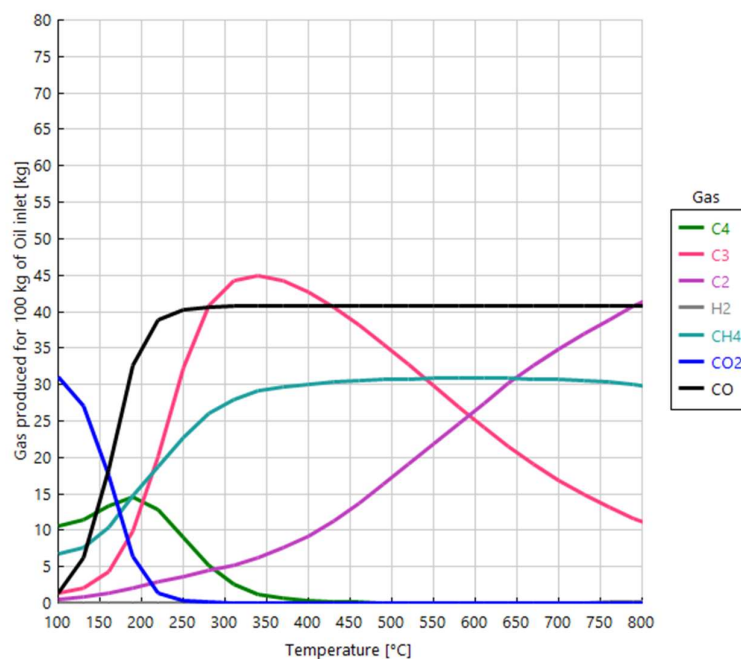
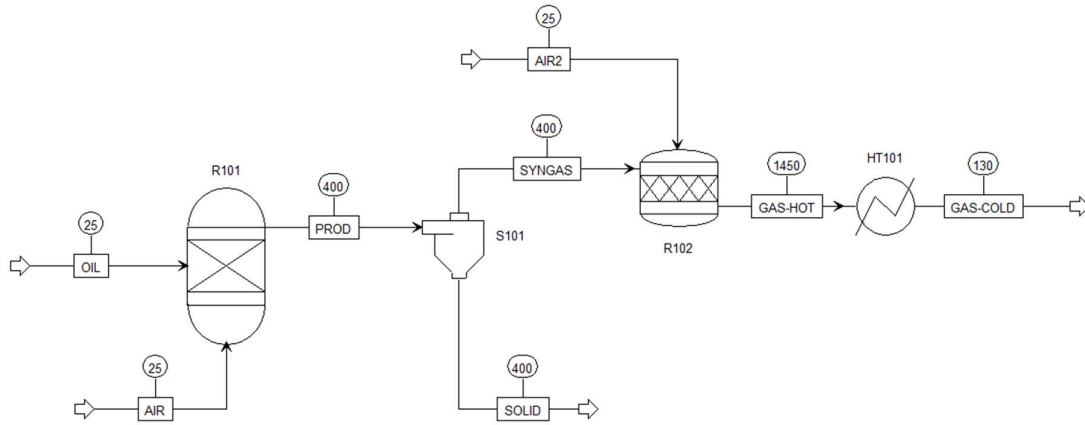


Figure 60. Syngas produced with 1 Air-Oil mass ratio.

Table 47. Composition of Syngas for 0.1 Air-LCF mass ratio and 400°C.

Composition	% wt.	Elements
METHANE	12,4%	
HYDROCARBONS C2	6,6%	Ethane, Ethylene
HYDROCARBONS C3	41,5%	Propane, propylene
HYDROCARBONS C4	0,3%	N-butane, I-butane
HYDROGEN	0,0%	
CARBON MONOXIDE	13,6%	
CARBON DIOXIDE	0,0%	
OXYGEN	0,0%	
NITROGEN	25,6%	



	Units	LCF	AIR	PROD	SOLID	SYNGAS	AIR2	GAS-HOT	GAS-COLD	
Temperature	°C		25	25	400	400	400	25	1450	130
Pressure	bar		1	1	1	1	1	1	1	1
Mass Enthalpy	kJ/kg		-13554.7	0.0	-11700.6	-16025.0	-168.8	0.0	-9.6	-1626.8
Average MW			112.9	28.9	61.0	102.0	29.4	28.9	28.8	28.8
Mass Flows	kg/h		1	0.1	1.1	0.8	0.3	5	5.3	5.3
Mass Fractions										
Oil			20.0%	0.0%	0.0%	0.0%	0.0%	0.0%	0.0%	0.0%
Carbon dioxide			0.0%	0.0%	0.0%	0.0%	0.0%	11.7%	11.7%	
Hydrogen			0.0%	0.0%	0.0%	0.0%	0.0%	0.0%	0.0%	
Carbon monoxide			0.0%	0.0%	3.7%	0.0%	13.6%	0.0%	0.0%	
Oxygen			0.0%	23.3%	0.0%	0.0%	23.3%	9.3%	9.3%	
Nitrogen			0.0%	76.7%	7.0%	0.0%	76.7%	73.8%	73.8%	
Ethane			0.0%	0.0%	0.3%	0.0%	1.0%	0.0%	0.0%	
Ethylene			0.0%	0.0%	1.5%	0.0%	5.6%	0.0%	0.0%	
Propane			0.0%	0.0%	0.1%	0.0%	0.4%	0.0%	0.0%	
Propylene			0.0%	0.0%	11.2%	0.0%	41.1%	0.0%	0.0%	
n-Butane			0.0%	0.0%	0.0%	0.0%	0.2%	0.0%	0.0%	
i-Butane			0.0%	0.0%	0.0%	0.0%	0.1%	0.0%	0.0%	
Methane			0.0%	0.0%	3.4%	0.0%	12.4%	0.0%	0.0%	
Alumina			80.0%	0.0%	72.7%	100.0%	0.0%	0.0%	0.0%	
Water			0.0%	0.0%	0.0%	0.0%	0.0%	5.1%	5.1%	
Volume Flow	L/h		0.46	85.92	570.35	20	570.15	4296.16	26408.77	6178.8%

Figure 61. Flowsheet of complete gasification process with M&E balance.

Table 48. Energy balance of gasification process.

Operation	Equipment	Heat energy [kWh/t LCF]	Electric energy [kWh/t LCF]
Gasification	R101	190	-
Syngas	R102	2400	750
Combustion			

Gasification requires approximately 25% of the electricity produced, making over 550 kWh_e/t LCF available.

Table 49. Comparison between process with acetone and pyrolysis.

Energy Consumption		Pyrolysis kWh/t LCF	Acetone kWh/t LCF
A1	Acetone-oil Flash		17
A2	Acetone-water Distillation		74
A3	Induction Pyrolysis	84	
A4	Electric furnace	226	0
A5	Electricity Production	514	259
A6	Thermal energy of pyrolysis gas	343	
A7	Thermal energy of calcination gas	52	1016
Chemical consumption and balance		kg/t di LCF	kg/t di LCF
B1	Acetone		16
B2	Washing water		104
B3	Recovered oil		79
B4	NaOH for H ₂ S washing	80	
B5	Na ₂ S solution	905	
Energy requirements (ORIM-CAT)		kWh/t LCF	kWh/t LCF
C1	Heating 1.5 m ³ /h of water	134	134
C2	Evaporation 2.5 m ³ /h of wastewater	2021	2021
C3	Evaporation Consumption with 3 Effects (fat. 2.6)	809	809
C4	Electric calcination oven	226	0
Estimates of % energy recovery and use		%	%
D1	% of Thermal Energy recovered (A6, A7)/ Request (C1, C3)	42%	108%
D2	% Electricity Required (A6, A7)/ Produced (A5)	60%	0%
Unit operations required			
E1	Pyrolysis with induction	x	
E2	H ₂ S cooling and washing (scrubber)	x	
E3	ICE (Internal Combustion Engine)	x	
E4	Acetone washing system		x
E5	Water washing system		x
E6	Acetone-oil Flash		x
E7	Acetone-water distillation		x
E8	Vacuum group		x
E9	VOC reduction		x
E10	Gas treatment (PC, bag filter, scrubber)	x	x
E11	Multiple effect evaporation for wastewater	x	x

Given all these considerations, we chose to work with washing using acetone. In this regard, numerous experimental tests were carried out to study and optimize the process with acetone.

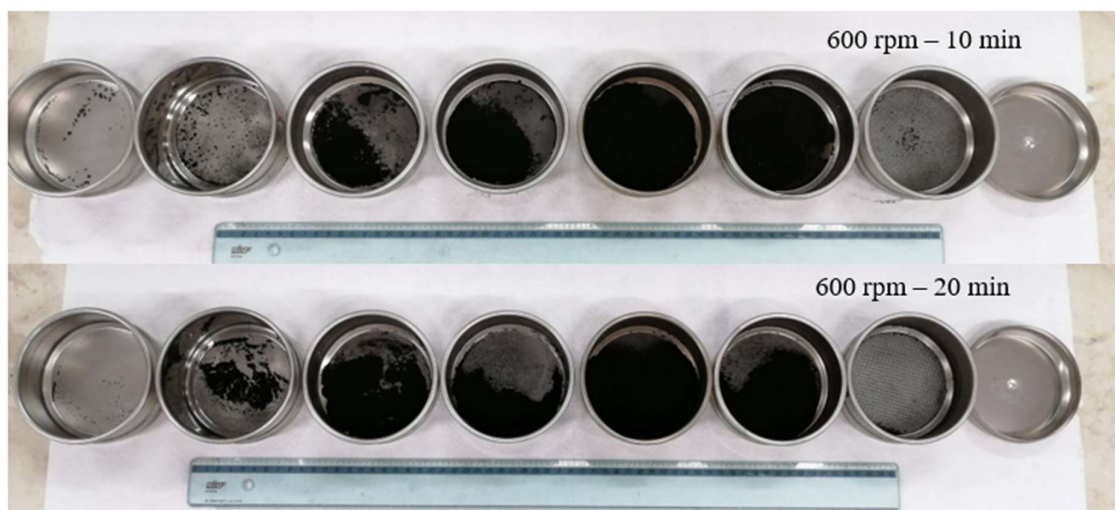
Table 50 summarizes some results of washing with acetone and water.

Table 50. Results of washing with acetone and water.

	LCF	150.00	g
In	Acetone	750	mL
	Water	750	mL
	Solid	159.29	g
Out	Acetone	705	mL
	Water	740	mL
	Acetone lost (%)	6.0%	-
	Water lost (%)	1.3%	-
	Post-drying solid weight	147.76	g
	Weight lost (%)	7.2%	-

**Figure 62.** Photographic aspect of the catalyst washed and dried in air for 24 h.

The particle size distribution was obtained following the two grindings using six sieves of different diameters. **Figure 63** shows the photographic appearance of the various fractions of the material in the sieves after the 2-particle size separations. **Figure 64** shows the results obtained.

**Figure 63.** Photographic aspect of the sample after two different grindings, following particle size separation.

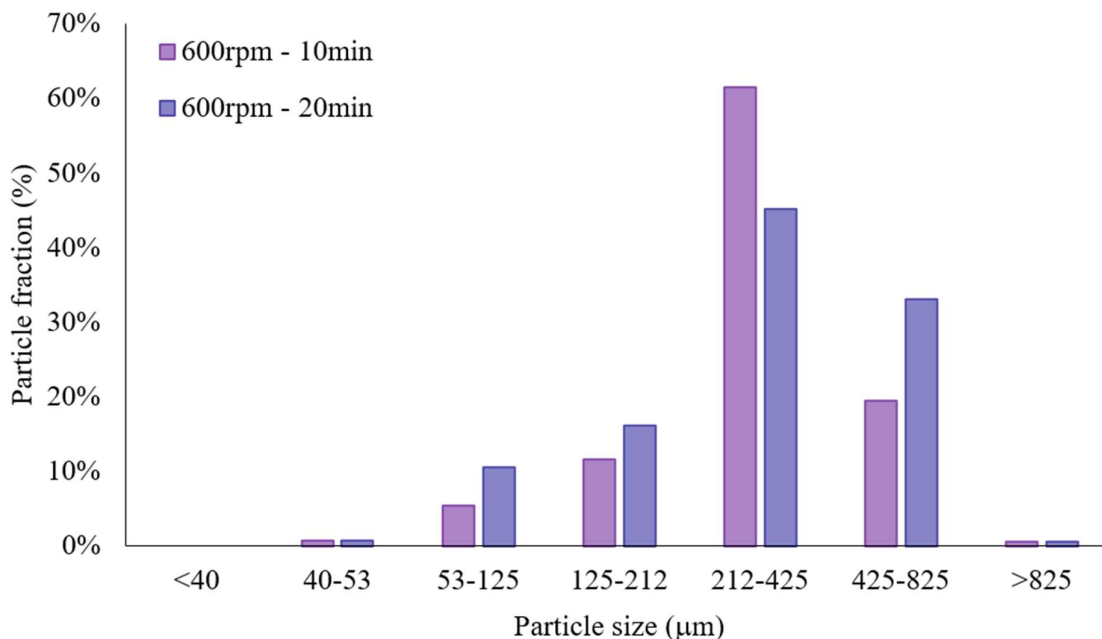


Figure 64. Particle size distribution of the sample for the two different grindings.

It was seen that the increase in grinding time did not cause a change in the particle size distribution. Furthermore, the humidity in the solid hindered separation via sieves. It was, therefore, decided to combine the two fractions and carry out new prolonged sieving through 3 sieves of different diameters, which allowed a more precise determination of the granulometry of the solid. The results obtained are presented in Figure 4.

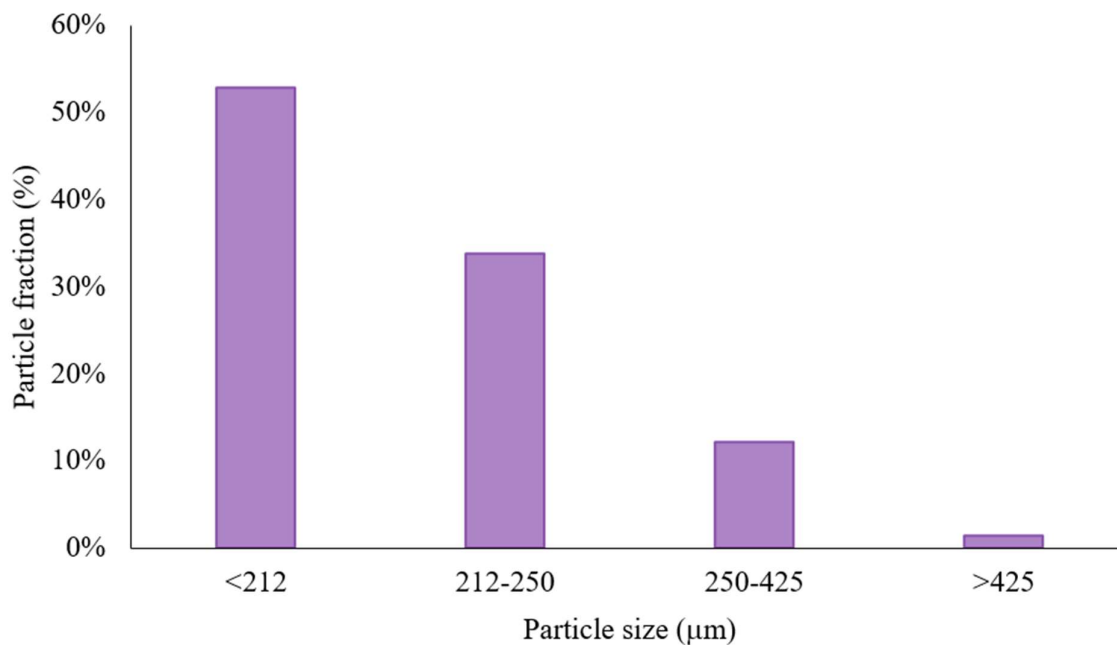


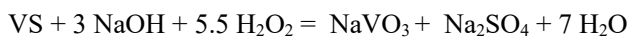
Figure 65. Particle size distribution of the two fractions ground and mixed together.

Based on the quantity of material obtained, the size of the particles was chosen to be considered as one of the factors of the factorial plan. In this sense, two fractions were used (with a diameter less than 212 μm and a diameter between 212 μm and 250 μm). For each of the two fractions, two chemical attacks were performed with aqua regia, and ICP-OES analyzed the resulting solutions to determine the vanadium and molybdenum content. The results obtained are reported below.

Table 51. Results in terms of V and Mo concentration.

Particle size		Element	V (%wt.)	Mo (%wt.)
(-)	< 212 mm	I	9.12%	2.13%
		II	9.10%	2.22%
		Media	9.11%	2.17%
		St. DEV	0.016%	0.061%
(+))	250 > 212 mm	I	9.23%	2.00%
		II	9.23%	2.15%
		Media	9.23%	2.08%
		St. DEV	0.000%	0.107%

The leaching process for vanadium and molybdenum sulfides with NaOH and H₂O₂ occurs according to the following chemical reactions.



The results obtained from the leaching tests are reported below.

Table 52. results of the factorial plan for leaching.

Run	Factors				V Recovery Yield (%)	Mo Recovery Yield (%)	Weight loss (%)	Humidity (%)
	A [NaOH]	B [H ₂ O ₂]	C T	D Diametro				
1	1 M	1 M	25 °C	< 212 mm	56.46	65.56	25.4	32.9
a	2 M	1 M	25 °C	< 212 mm	61.46	71.88	27.9	32.0
b	1 M	2 M	25 °C	< 212 mm	62.10	79.73	28.0	31.6
ab	2 M	2 M	25 °C	< 212 mm	71.16	76.95	29.9	33.5
c	1 M	1 M	60 °C	< 212 mm	73.78	72.51	27.1	30.6
ac	2 M	1 M	60 °C	< 212 mm	67.83	72.01	27.6	31.2
bc	1 M	2 M	60 °C	< 212 mm	67.64	77.96	27.6	32.3
abc	2 M	2 M	60 °C	< 212 mm	68.94	77.28	27.6	31.9
d	1 M	1 M	25 °C	212 < 250 mm	65.69	70.65	24.3	32.0
ad	2 M	1 M	25 °C	212 < 250 mm	55.95	77.61	27.5	31.4
bd	1 M	2 M	25 °C	212 < 250 mm	64.16	82.67	26.7	30.4
abd	2 M	2 M	25 °C	212 < 250 mm	72.13	86.18	29.9	31.5
cd	1 M	1 M	60 °C	212 < 250 mm	61.15	74.66	25.5	29.9
acd	2 M	1 M	60 °C	212 < 250 mm	63.46	76.62	27.1	30.8
bcd	1 M	2 M	60 °C	212 < 250 mm	65.25	74.74	25.6	31.5
abcd	2 M	2 M	60 °C	212 < 250 mm	71.25	77.97	27.8	30.8
R1	1.5 M	1.5 M	42.5 °C	< 250 mm	78.10	81.49	26.6	30.2

R2	1.5 M	1.5 M	42.5 °C	< 250 mm	69.97	75.83	26.0	30.8
R3	1.5 M	1.5 M	42.5 °C	< 250 mm	73.93	78.58	26.9	31.8
R4	1.5 M	1.5 M	42.5 °C	< 250 mm	73.48	78.73	26.3	32.3

From the values calculated thanks to the factorial experimentation, it is clear that the most significant recovery was obtained in the test called abd ([NaOH] 2M, [H₂O₂] 2M, T = 25°C and diameter between 250 and 212 μm). For this test, the following leaching yields were achieved: 72.1% for vanadium and 86.2% for molybdenum.

The data obtained from the tests were analyzed with ANOVA considering the Yates algorithm. **Figure 66** and **Figure 67** present plots of the significance and main effects of the factors on vanadium and molybdenum leaching.

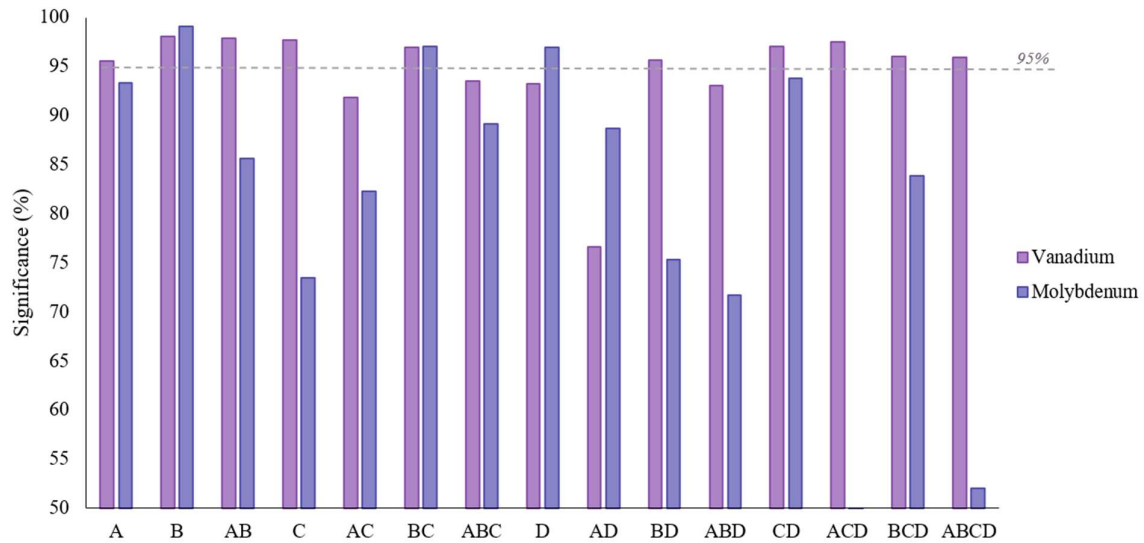


Figure 66. Significance of factors and their interactions on vanadium and molybdenum leaching.

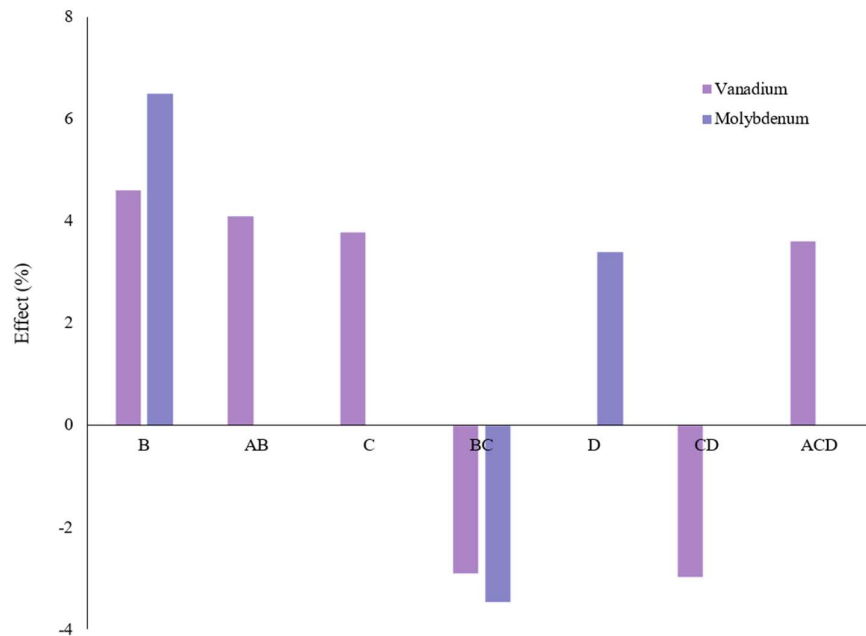


Figure 67. Effect of major factors on vanadium and molybdenum leaching.

The most important factor is the concentration of hydrogen peroxide, both for vanadium and molybdenum leaching. An increase in the H_2O_2 concentration from 1M to 2M has a positive effect of over 4% on the vanadium recovery yield and over 6% on the molybdenum recovery yield. Increasing the concentration of NaOH does not lead to a significant increase in the leaching yield of vanadium and molybdenum. However, the interaction of this factor with hydrogen peroxide, in particular, leads to higher leaching yields.

Regarding the temperature, there is an increase in the recovery yield from 25 °C to 60 °C; however, the interaction between temperature and H_2O_2 is responsible for an approximately 4% decrease in the leaching yield of both elements. This phenomenon can be explained by considering that a high temperature favors the degradation of hydrogen peroxide, which is fundamental for the process.

Furthermore, it can be seen that a larger particle diameter leads to a higher Mo leaching yield (for vanadium, there are no significant differences).

The chemical attacks on the ground fractions resulted in a molybdenum concentration of approximately 2.1 %wt., much lower than that measured when tests began with the LCF sample supplied by ORIM (4.55 %wt.). Some studies will be carried out to investigate this difference.

The response surface methodology (RSM) was used to optimize the studied process regarding chemicals concentration. In statistics, RSM explores the relationships between several explanatory variables (x_1, x_2, \dots) and one or more response variables (y_1, y_2, \dots). The main idea of RSM is to use a sequence of experiments designed to obtain an optimal response. Many applications of RSM involve regressing and testing the adequacy of a second-order model to the obtained experimental responses.

In our case, the explanatory variables used were the concentrations of H_2O_2 and NaOH, while the response variables were Vanadium and Molybdenum extraction yields. When varying the concentrations of the two chemicals, the scheme shown below was followed to guarantee some important properties of the model (for example, orthogonality).⁴²

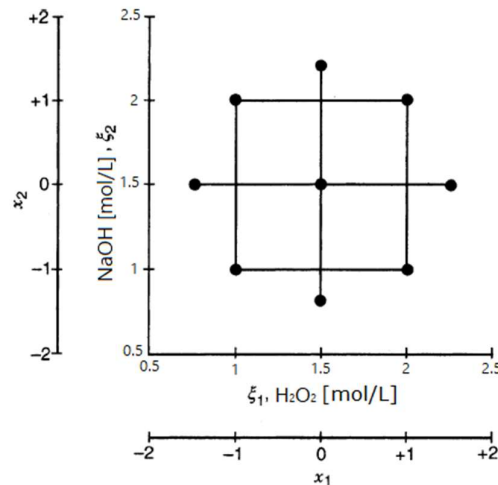


Figure 68. Central Composite Design (CCD) scheme.

The chosen design is a Central Composite Design widely used to create a second-order response surface. Note that the design consists of four tests at the corners of a square (trials already performed for the factorial plane and named 1, a, b, ab) plus four tests at the center of the square (trials already performed for the factorial plane and named R1, R2, R3, R4), plus four tests at the intersection of the circle that circumscribes the square with the axes (star points). In terms of explanatory variables the angles of the square are $(x_1, x_2) = (-1, -1), (1, -1), (-1, 1), (1, 1)$; the central points are $(x_1, x_2) = (0, 0)$; and the star points $(x_1, x_2) = (-1.414, 0), (1.414, 0), (0, -1.414), (0, 1.414)$.

The objective is to determine the parameters of the second-order model:

$$y = \beta_0 + \beta_1 x_1 + \beta_2 x_2 + \beta_{11} x_1^2 + \beta_{22} x_2^2 + \beta_{12} x_1 x_2 + \varepsilon$$

The relationships between the natural variables and the codified variables are as follows:

$$x_1 = \frac{[H_2O_2] - ([H_2O_2]_{low} + [H_2O_2]_{high})/2}{([H_2O_2]_{high} - [H_2O_2]_{low})/2}$$

$$x_2 = \frac{[NaOH] - ([NaOH]_{low} + [NaOH]_{high})/2}{([NaOH]_{high} - [NaOH]_{low})/2}$$

Table 53. Central Composite Design for the investigated process.

Observation	Run	H ₂ O ₂ [mol/L]	NaOH [mol/L]	x ₁	x ₂	V (%)	Mo (%)
		ξ ₁	ξ ₂			y ₁	y ₂
1	1	1	1	-1	-1	56,5	65,6
2	b	2	1	1	-1	62,1	79,7
3	a	1	2	-1	1	61,5	71,9
4	ab	2	2	1	1	71,2	76,9
5	S1	0,8	1,5	-1,414	0	45,5	64,6
6	S2	2,2	1,5	1,414	0	66,9	83,3
7	S3	1,5	0,8	0	-1,414	51,2	71,9
8	S4	1,5	2,2	0	1,414	61,0	74,0
9	R1	1,5	1,5	0	0	78,1	81,5
10	R2	1,5	1,5	0	0	70,0	75,8
11	R3	1,5	1,5	0	0	73,9	78,6
12	R4	1,5	1,5	0	0	73,5	78,7

The matrix method was used to estimate the model parameters. For this reason the model of the second was written as follows:

$$y = X\beta$$

Where, for vanadium:

$$y = \begin{bmatrix} 56,5 \\ 62,1 \\ 61,5 \\ 71,2 \\ 45,5 \\ 66,9 \\ 51,2 \\ 61,0 \\ 78,1 \\ 70,0 \\ 73,9 \\ 73,5 \end{bmatrix} \quad X = \begin{bmatrix} 1 & -1 & -1 & 1 & 1 & 1 \\ 1 & 1 & -1 & 1 & 1 & -1 \\ 1 & -1 & 1 & 1 & 1 & -1 \\ 1 & 1 & 1 & 1 & 1 & 1 \\ 1 & -1,414 & 0 & 2 & 0 & 0 \\ 1 & 1,414 & 0 & 2 & 0 & 0 \\ 1 & 0 & -1,414 & 0 & 2 & 0 \\ 1 & 0 & 1,414 & 0 & 2 & 0 \\ 1 & 0 & 0 & 0 & 0 & 0 \\ 1 & 0 & 0 & 0 & 0 & 0 \\ 1 & 0 & 0 & 0 & 0 & 0 \\ 1 & 0 & 0 & 0 & 0 & 0 \end{bmatrix} \quad \beta = \begin{bmatrix} \beta_0 \\ \beta_1 \\ \beta_2 \\ \beta_{11} \\ \beta_{22} \\ \beta_{12} \end{bmatrix}$$

And for molybdenum:

$$y = \begin{bmatrix} 65.6 \\ 79.7 \\ 71.9 \\ 76.9 \\ 64.6 \\ 83.3 \\ 71.9 \\ 74.0 \\ 81.5 \\ 75.8 \\ 78.6 \\ 78.7 \end{bmatrix} \quad X = \begin{bmatrix} 1 & -1 & -1 & 1 & 1 & 1 \\ 1 & 1 & -1 & 1 & 1 & -1 \\ 1 & -1 & 1 & 1 & 1 & -1 \\ 1 & 1 & 1 & 1 & 1 & 1 \\ 1 & -1.414 & 0 & 2 & 0 & 0 \\ 1 & 1.414 & 0 & 2 & 0 & 0 \\ 1 & 0 & -1.414 & 0 & 2 & 0 \\ 1 & 0 & 1.414 & 0 & 2 & 0 \\ 1 & 0 & 0 & 0 & 0 & 0 \\ 1 & 0 & 0 & 0 & 0 & 0 \\ 1 & 0 & 0 & 0 & 0 & 0 \\ 1 & 0 & 0 & 0 & 0 & 0 \end{bmatrix} \quad \beta = \begin{bmatrix} \beta_0 \\ \beta_1 \\ \beta_2 \\ \beta_{11} \\ \beta_{22} \\ \beta_{12} \end{bmatrix}$$

Through mathematical steps it can be demonstrated that:

$$\beta = (X^T X)^{-1} X^T y$$

Obtaining the following results:

$$\beta_{\text{vanadium}} = \begin{bmatrix} 73.870 \\ 5.705 \\ 3.488 \\ -7.181 \\ -7.233 \\ 1.014 \end{bmatrix} \quad \beta_{\text{molybdenum}} = \begin{bmatrix} 78.657 \\ 5.706 \\ 0.812 \\ -2.333 \\ -2.840 \\ -2.277 \end{bmatrix}$$

Finally, the desired model is obtained by converting the coded variables back into natural variables. In this way, it is possible to analytically determine the value of the extraction yield of both elements simply by knowing the concentrations of H_2O_2 and NaOH (obviously, the model is reliable if the chosen concentrations fall within the investigated space while it may not be reliable outside). The two determined equations are shown below.

$$V_{\text{rec}}(\%) = -74.304 + 91.491 \cdot [\text{H}_2\text{O}_2] + 87.688 \cdot [\text{NaOH}] - 28.723 \cdot [\text{H}_2\text{O}_2]^2 - 28.933 \cdot [\text{NaOH}]^2 + 4.058 \cdot [\text{H}_2\text{O}_2] \cdot [\text{NaOH}]$$

$$\text{Mo}_{\text{rec}}(\%) = -7.955 + 53.077 \cdot [\text{H}_2\text{O}_2] + 49.371 \cdot [\text{NaOH}] - 9.334 \cdot [\text{H}_2\text{O}_2]^2 - 11.361 \cdot [\text{NaOH}]^2 - 9.109 \cdot [\text{H}_2\text{O}_2] \cdot [\text{NaOH}]$$

Below are the graphs of the two surfaces described by the equations above.

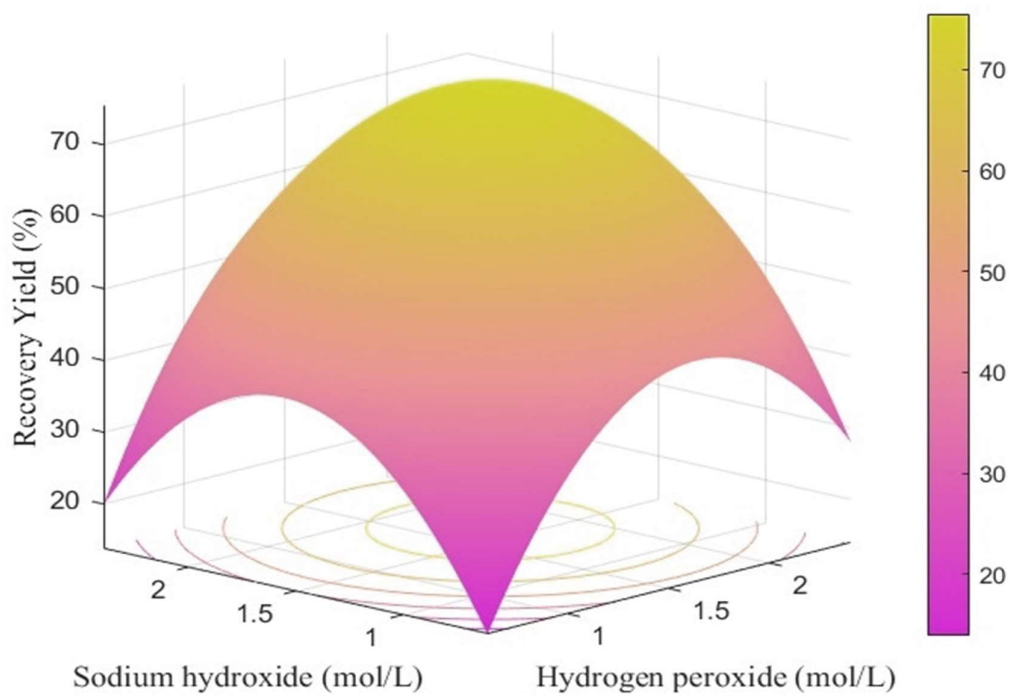


Figure 69. Vanadium recovery yield II-order polynomial model.

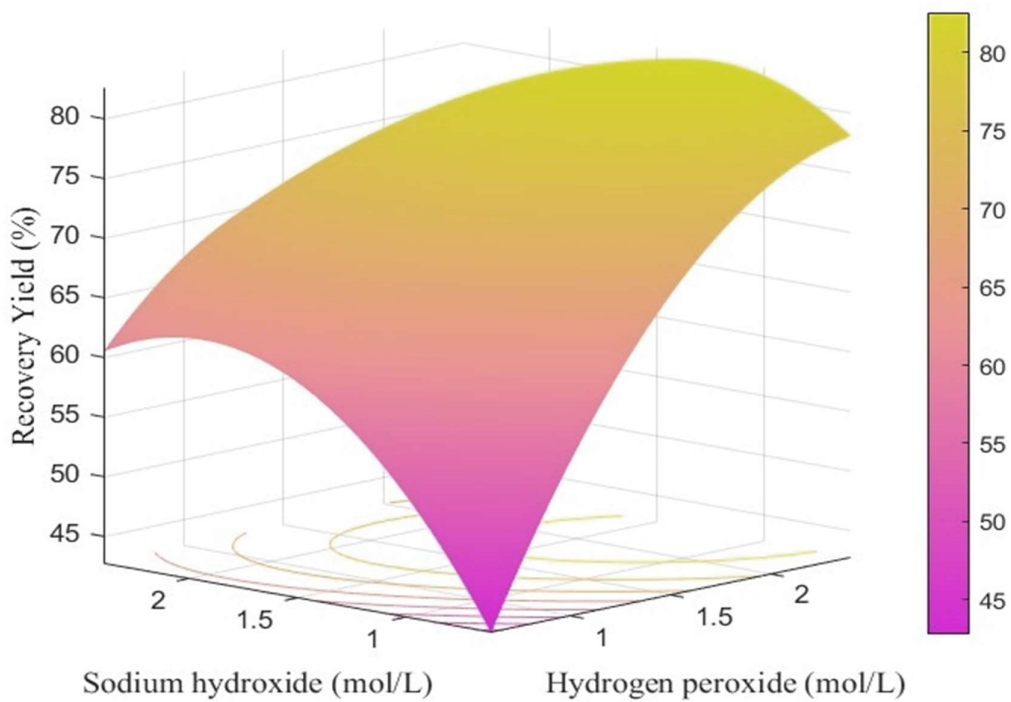


Figure 70. Molybdenum recovery yield II-order polynomial model.

By optimizing the extraction yields (and considering the economic value of the total recovery), the concentrations of the reagents were determined in optimal conditions. It has been seen that these concentrations are 1.708 M for H_2O_2 and 1.635 M for NaOH.

Several double-stage leaching tests were carried out with crossed currents and different solid/liquid ratios: 10% wt./vol., 15% wt./vol., 20% wt./vol. For this purpose, 40 mL of leaching solution was used for each stage. The values of H_2O_2 and NaOH concentrations were chosen to optimize the response of both elements. Below are the values of the different test parameters and the related results.

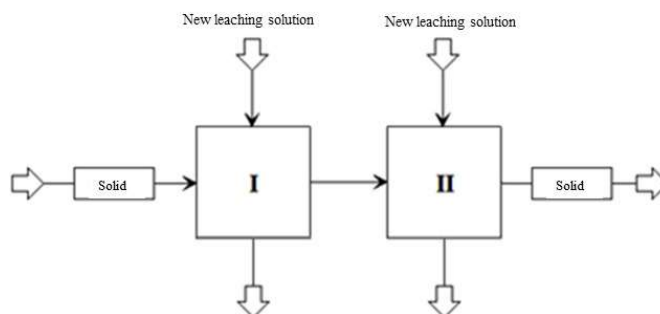


Figure 71. Simplified diagram of the 2-stage cross-current process.

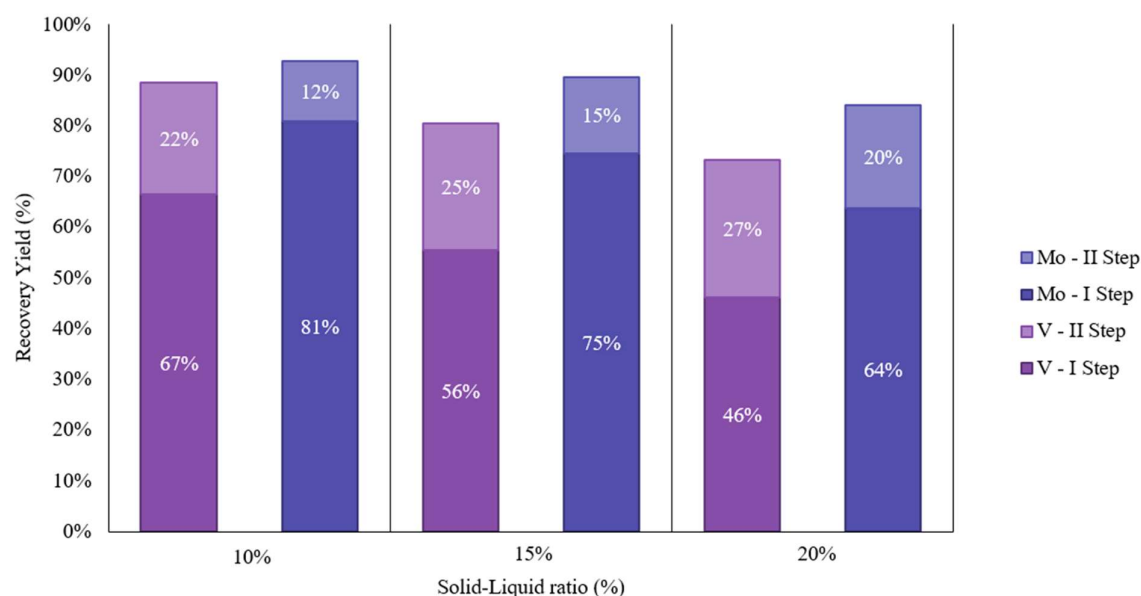


Figure 72. Extraction yields of vanadium and molybdenum as the solid/liquid ratio varies in the cross-current process Configuration Cross-currents with $[\text{H}_2\text{O}_2]=1.9$ mol/L and $[\text{NaOH}]=1.5$ mol/L.

Two processes were carried out with two leaching stages connected in countercurrent with different solid/liquid ratios: the first at 15% wt./vol., while the second at 20% wt./vol. Each leaching stage was carried out at 25°C ($\pm 1^\circ\text{C}$) inside a thermostatic bath without stirring for 3 hours. For this reason, 40 mL of solution with a concentration of H_2O_2 of 1.9 mol/L and NaOH of 1.4 mol/L were used for the first test. At the end of each test, the solution was separated by vacuum filtration and used for the subsequent leaching phase.

Figure 73 shows the scheme followed for the various tests of the process to obtain the two stages in countercurrent. At the end of each cycle, the residual solid was dried in an oven at 60°C for 24 h and subsequently weighed to determine the weight loss compared to the initial sample.

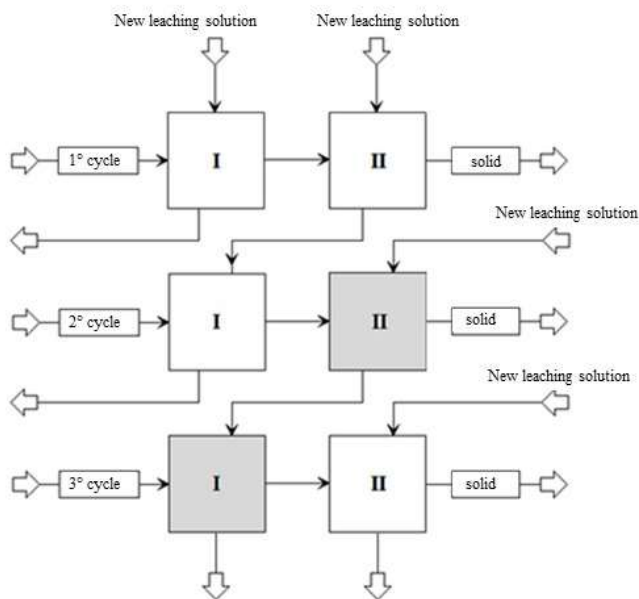


Figure 73. Scheme of tests performed for the countercurrent process.

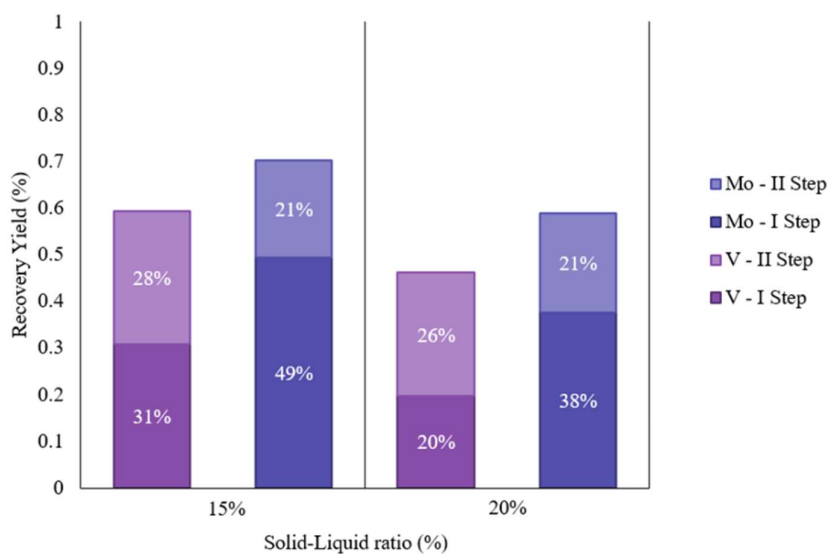


Figure 74. Vanadium and molybdenum extraction yields as the solid/liquid ratio varies for the countercurrent process Countercurrent configuration with $[H_2O_2]=1.9$ mol/L and $[NaOH]=1.5$ mol/L.

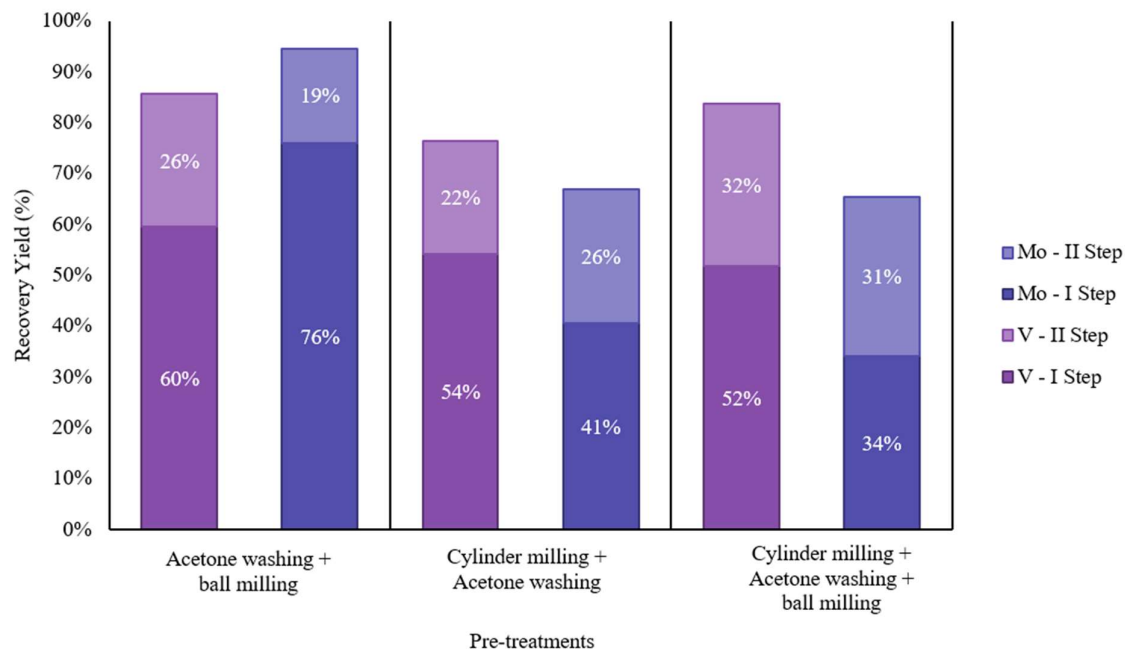


Figure 75. Vanadium end molybdenum extraction yields in the cross-current process with $[H_2O_2]=1.708$ mol/L and $[NaOH]=1.635$ mol/L, varying the applied pretreatment.

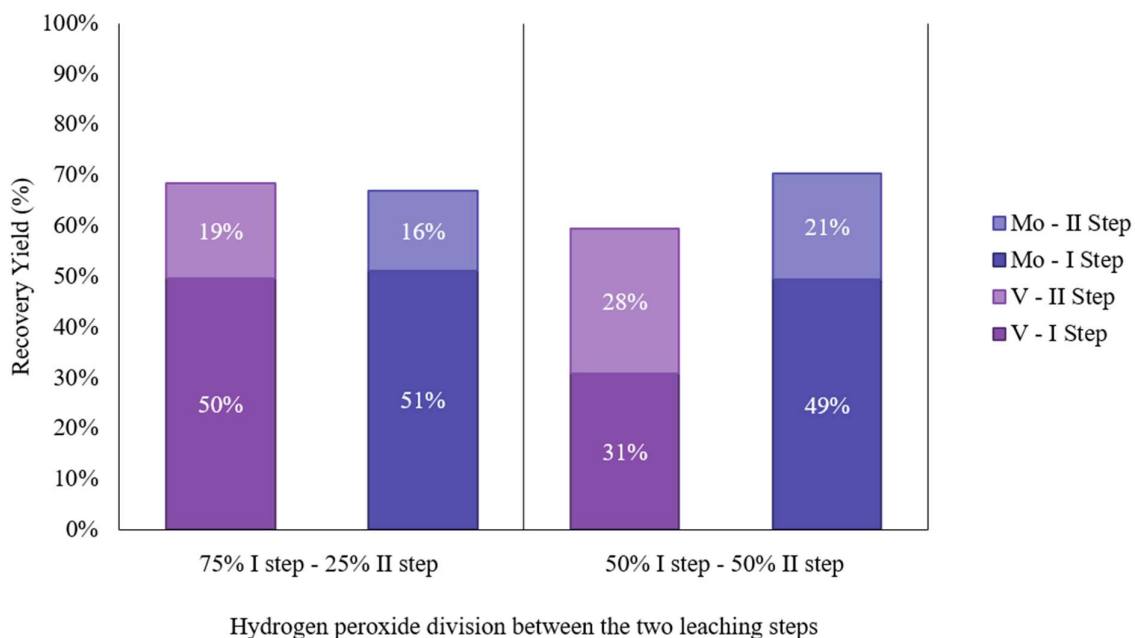


Figure 76. Vanadium and molybdenum extraction yields in the countercurrent process with 15% Solid/Liquid, $[H_2O_2]=1.708$ mol/L and $[NaOH]=1.635$ mol/L when varying the H_2O_2 addition method.

Table 54. Summary of recovery yields, chemicals consumption and costs for different processes.

Process	Pre-treatments	S/L ratio (%)	Leaching chemicals concentration [mol/L]		Rese (%)		Chemicals [kg/t LCF]			Products [kg/t LCF]		Costs [€/t LCF]	
			H ₂ O ₂	NaOH	V	Mo	H ₂ O ₂ ¹	NaOH	H ₂ O	V	Mo		
1	2-stage cross-current	- Washing with Acetone and Water - Ball milling	10%	1.9	1.5	88.5%	92.7%	3929	1085	14547	74,12	18,41	1.553,89 €
2	2-stage cross-current	- Washing with Acetone and Water - Ball milling	15%	1.9	1.5	80.4%	89.6%	2619	723	9698	67,31	17,79	1.035,93 €
3	2-stage cross-current	- Washing with Acetone and Water - Ball milling	15%	1.7	1.6	85.6%	94.1%	2347	773	9961	71,66	18,78	961,98 €
4	2-stage cross-current	- Cylinder milling - Washing with Acetone and Water	15%	1.7	1.6	76.4%	67.0%	1954	643	8293	52,95	14,13	800,85 €
5	2-stage cross-current	- Cylinder milling - Washing with Acetone and Water - Ball milling	15%	1.7	1.6	83.8%	65.4%	1954	643	8293	53,55	13,81	800,85 €
6	Counter-current ² 2-stage	- Washing with Acetone and Water - Ball milling	15%	1.9	1.5	59.4%	70.3%	1310	362	4849	49,57	13,96	517,96 €
7	Counter-current ³ 2-stage	- Washing with Acetone and Water - Ball milling	15%	1.7	1.6	68.3%	67.0%	1174	386	4981	57,18	13,30	480,99 €
8	2-stage cross-current	- Washing with Acetone and Water - Ball milling	20%	1.9	1.5	73.2%	84.0%	1964	543	7273	61,29	16,67	776,95 €
9	Counter-current 2-stage	- Washing with Acetone and Water - Ball milling	20%	1.9	1.5	46.2%	58.9%	982	271	3637	38,64	11,69	388,47 €

¹ H₂O₂ al 30% p/vol.² 50% di H₂O₂ I step; 50% di H₂O₂ II step³ 75% di H₂O₂ I step; 25% di H₂O₂ II step

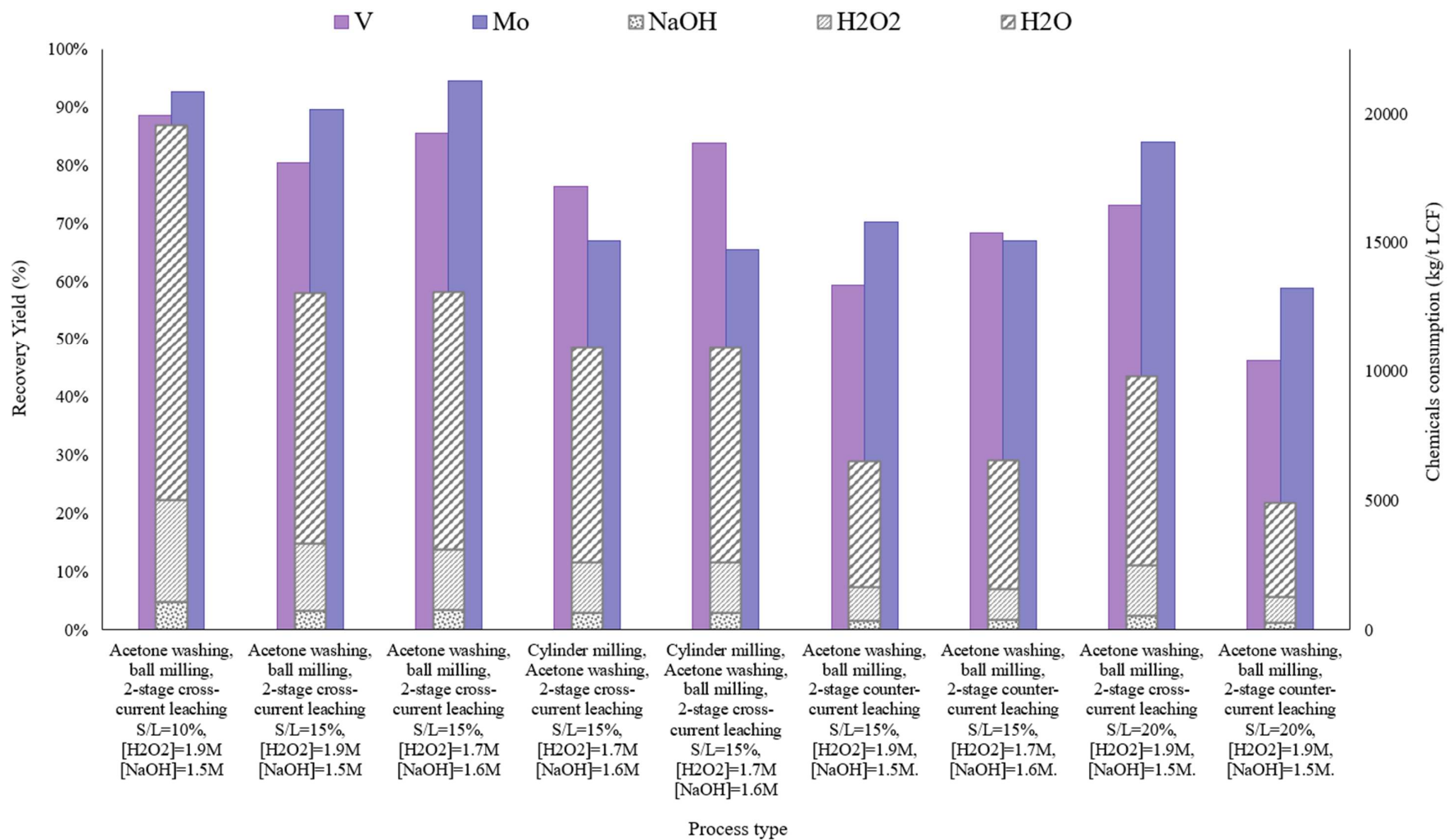


Figure 77. Summary of recovery yields and chemicals consumption for different processes.

2.4.4 Rotary Kiln Optimization

Rotary Kilns are fundamental elements within the chemical, metallurgical, and pharmaceutical industries. This particular type of kiln is the most advanced, high-productivity industrial kiln. The Rotary Kiln (RK) is the site of numerous chemical reactions and allows reaching temperatures of up to approximately 1500 °C. The most extensive application of RK is undoubtedly for the production of cement. However, its use has also been considered for roasting spent refinery catalysts within a plant to recover precious and base metals. The research presented in this chapter aims to determine the thermal profile of the various phases present in an RK used for roasting LC-Finer catalysts along the kiln's entire axis to determine and manage any temperature peaks. Knowing the thermal behavior of this system would allow us to avoid both damage to the construction materials of the RK and the unwanted behavior of the substances present in the kiln.

Unfortunately, inside an RK, we find ourselves in heterogeneous conditions with complex relationships between chemical reactions, mass transfer, heat transfer, and fluid dynamics. Numerous studies in the literature try to identify the best model for describing all the phenomena present in this technology. Despite the many difficulties, some research has focused on creating one-dimensional models capable of quantitatively describing the kiln operation while remaining computationally tractable for subsequent optimization studies.⁴³

Li et al.⁴⁴ were among the first to develop a complete and, at the same time, simple model for the description of heat transfer in an RK. In contrast, Mujumdar and Ranade⁴⁵ developed a one-dimensional model in which simple kinetics are present to approximate the reactions present inside the kiln. Given the limited availability of kinetic data, using complex kinetic models is undoubtedly the most complicated aspect.

Romero Valle⁴⁶ was the first to develop a one-dimensional thermal model combining the abovementioned studies.

Most of these studies aim at RKs operating in the cement industry. In contrast, the present study led to the creating of a completely general model, which was subsequently applied to an RK used for roasting LC-Finer catalysts.

2.4.4.1 Design

At the basis of the model presented, there are several simplifying hypotheses, without which there would be a very complex calculation code that would be difficult to handle for any sensitivity and optimization analyses. **Figure 78** shows the schematization of the RK. It was decided to consider the furnace in question as a two-phase PFR (gas-solid) in countercurrent with each other.

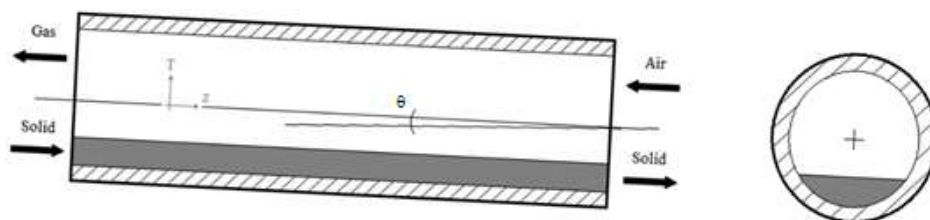


Figure 78. Rotary kiln scheme.

The first hypothesis is linked to the contact surface between the two phases; this surface has a variable shape depending on the rotation of the drum and the friction between the solid phase and the kiln wall but can be approximated to a flat (rectangular) surface.

Once the flow rate of the solid, the geometry of the kiln, and the number of revolutions are known, the percentage of the section occupied by the material can be calculated using the Heiligenstaedt equation:

$$\phi = \frac{W}{148nD^3 \operatorname{tg} \theta}$$

Where W is the spatial velocity of the solid, obtained by dividing the solid flow rate by the kiln volume. θ is the inclination of the kiln to the horizontal, n is the number of revolutions, and D is the internal diameter of the RK.

Once the section occupied by the solid has been determined, the passage sections of the solid and gas are calculated using the following equations.

$$S_s = \pi \frac{D^2}{4} \phi$$

$$S_g = \pi \frac{D^2}{4} (1 - \phi)$$

At this point, it is possible to calculate the angle of the solid's repose and the chord's length. The angle of repose and the chord can be calculated using the following equations, both of which can be easily obtained geometrically.

$$S_s = R^2 \left(\frac{\alpha}{2} - \sin \frac{\alpha}{2} \cos \frac{\alpha}{2} \right)$$

$$C = 2R \sin \frac{\alpha}{2}$$

Where S_s it is the section occupied by the solid, α the rest angle, C is the chord, and R the internal radius of the RK. Once C is known, it is possible to calculate the contact area between the two phases, which is a fundamental parameter in material and energy balances.

$$A_c = LC$$

Where A_c is the contact area, and L is the length of the kiln. Once the RK has been characterized geometrically it is possible to determine the average residence times of the two phases.

2.4.4.1 Reaction kinetics

The second step of the calculation concerns the chemical reactions inside the kiln. This aspect is undoubtedly the most delicate part of the model: there are many reactions in the system, and it is impossible to consider all of them in the calculation code; furthermore, in the literature, there is not much kinetic data relating to this type of reaction.

Chemical reactions are the basis of both the material and thermal balance. Therefore, paying attention to the various simplifications that would quickly lead to incorrect results is necessary.

In the specific case of the RK used for roasting catalysts in the Oil&Gas sector, a solid feed composed of an inert alumina matrix (Al_2O_3) on the surface of which variable percentages of metal sulfides and Oil were considered. The Oil was simulated as n-Tetradecane ($\text{C}_{14}\text{H}_{30}$), while the metal sulfides present are mainly Nickel, Molybdenum, and Vanadium sulfides. Only nickel and molybdenum sulfides were considered in the model, given the lack of kinetic data on vanadium sulfides. For all components, Arrhenius-type kinetics is considered.

$$\frac{dm_i}{dt} = -A_i e^{\left(-\frac{E_{a_i}}{RT} \right)} m_{O_2}$$

The main reactions within the RK are summarized in **Table 55**, together with the related kinetic data necessary for the balances. The kinetic parameters of the Oil were approximated to those typical for cyclo-alkanes.

Table 55. Main RK reactions and related kinetic data.

Reaction	A [1/s]	Ea [kJ/mol]	
$\text{NiS(s)} + 1.5\text{O}_2(\text{g}) \rightarrow \text{NiO(s)} + \text{SO}_2(\text{g})$	27.89	82.00	47
$\text{MoS}_2(\text{s}) + 3.5\text{O}_2(\text{g}) \rightarrow \text{MoO}_3(\text{g}) + 2\text{SO}_2(\text{g})$	10^8	143.16	48
$\text{C}_{14}\text{H}_{30} + 21.5\text{O}_2(\text{g}) \rightarrow 14\text{CO}_2(\text{g}) + 15\text{H}_2\text{O}(\text{g})$	10^{14}	125.50	49

Generally, a catalyst of the LC-Finer type (of the Ni-Mo family) includes an inert alumina matrix and an active part of Ni and Mo, present both as metals and oxides. At the end of its life, the catalyst will be composed of variable quantities of Ni and Mo sulfides and, as a consequence of the refining processes, also of Vanadium adsorbed on the surface of the catalyst both as an oxide and as a sulfide; obviously, Oil will also be present in variable percentages.

The presence of Oil significantly affects the calorific value of the catalyst. The study analyzed in detail how the variation of this percentage influences the temperatures present in the RK.

2.4.4.2 Energy and material balance

During the calculation, it is necessary to consider a series of complex heat exchange phenomena that occur inside the kiln and the heat released by the various highly exothermic reactions.

In a steady state, the heat developed by the oxidation reactions is such that it allows the process to be self-sustaining. The incoming solid, following grinding, enters the RK with a temperature equal to room temperature. It is assumed that the grinding is such that the gaseous stream has no solid entrainment.

Near the furnace entrance, the solid is heated by the gaseous current, which, being in countercurrent, has a much higher temperature than the incoming solid phase; here, drying and evaporation phenomena of some components (such as water, if present) occur. The temperature of the solid begins to increase until it reaches a value that triggers oxidation reactions. The highly exothermic reactions significantly increase the solid's temperature, which often greatly exceeds the temperature of the gaseous phase. Finally, once the limiting reactants are exhausted, the reactions end, and the solid begins to cool, releasing heat to the gaseous phase.

For simplicity of calculation, heat transfers that occur through radiation are neglected. The following equations report the heat balances of the two phases.

$$\begin{aligned}\Delta H_s &= Q_R + Q_c - Q_T - Q_{l,s} \\ \Delta H_g &= -Q_c - Q_{l,g} + Q_T\end{aligned}$$

Where Q_R it is the heat released by various reactions, Q_c is the heat exchanged by convection between the two phases, Q_T it is the sensible heat that comes out of the solid phase through the formation of gaseous products, and $Q_{l,s}$, $Q_{l,g}$ are the heat flows that pass through the walls of the RK from the solid and gaseous phases, respectively. Given the cylindrical geometry of the kiln, it is possible to derive the equations below.

$$\begin{aligned}Q_{l,s} &= \frac{T_s - T_e}{\frac{\ln \frac{r_2}{r_1}}{2\pi\Delta zk_1} + \frac{\ln \frac{r_3}{r_2}}{2\pi\Delta zk_2} + \frac{\ln \frac{r_4}{r_3}}{2\pi\Delta zk_3} + \frac{1}{2\pi r_4 \Delta zh_e}} C_s \% \\ Q_{l,g} &= \frac{T_g - T_e}{\frac{\ln \frac{r_2}{r_1}}{2\pi\Delta zk_1} + \frac{\ln \frac{r_3}{r_2}}{2\pi\Delta zk_2} + \frac{\ln \frac{r_4}{r_3}}{2\pi\Delta zk_3} + \frac{1}{2\pi r_4 \Delta zh_e}} C_g \%\end{aligned}$$

The two formulas reported above refer to a classic RK built with different materials and schematized in **Figure 79**. The heat exchanged between the solid and gaseous phases can be calculated with the following equation.

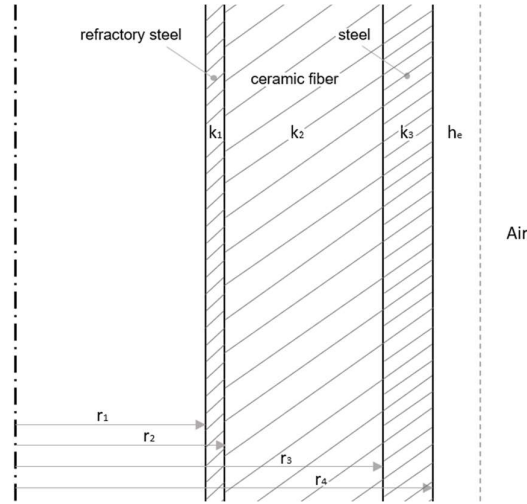


Figure 79. Rotary kiln section diagram.

$$Q_C = A_c h (T_g - T_s)$$

Where A_c is the contact area between the phases and h is the heat transfer coefficient. To determine h , the relationship proposed by Mujumdar et Ranade⁴⁵ was used:

$$h = 0.46 \frac{k_g}{D_e} Re_D^{0.535} Re_\omega^{0.104} \eta^{-0.341}$$

Where k_g is the thermal conductivity of the gas and D_e is the hydraulic diameter of the RK, with Re_D and Re_ω the axial and angular Reynolds number, respectively. Re_D and Re_ω are calculated with the following equations:

$$Re_D = \frac{\rho_g u_g D_e}{\mu_g}$$

$$Re_\omega = \frac{\rho_g \omega D_e^2}{\mu_g}$$

$$D_e = \frac{0.5D(2\pi - \alpha + \text{sen}\alpha)}{\pi - (\alpha/2) + \text{sen}(\alpha/2)}$$

$$\eta = \frac{\alpha - \text{sen}\alpha}{2\pi}$$

The following relationship is used for the heat released by the oxidation reactions:

$$Q_R = PCI \gamma \sum_{i=1}^R \Delta m_i^L$$

Where Δm_i^L is the mass of the limiting reagent consumed in the generic volume by the i -th reaction. γ is a corrective factor that can be determined from experimental measurements (in the proposed model $\gamma=1$ is considered). PCI is the calorific value of the solid, taken in its entirety and can be calculated experimentally or estimated empirically through various relationships. Below is the Dulong formula used in the calculation code.⁵⁰

$$PCI \left[\frac{MJ}{kg} \right] = PCS \left[\frac{MJ}{kg} \right] - 22.5\omega^H - 2.5\omega^{H_2O}$$

$$PCS \left[\frac{MJ}{kg} \right] = 32.79\omega^C + 150.4 \left(\omega^H - \omega^O/8 \right) + 9.26\omega^S + 4.97\omega^O + 2.42\omega^N$$

The heat that comes out of the solid phase through the formation of gaseous products is expressed with the following relationship:

$$Q_R = \sum_{i=1}^n \Delta m_{g,i} C_{pg,i} (T_s - T_{rif})$$

Where $\Delta m_{g,i}$ is the mass of the i -th gaseous product of the generic reaction and $C_{pg,i}$ the relative specific heat at the temperature of the solid phase. To calculate the specific heats, the data present on the Perry's⁵¹ and reported in **Table 56**.

Table 56. Relations for the specific heats at constant pressure of the substances present in the system.

Component	C _p (T=K)	
Al ₂ O ₃	22.08 + 0.008971T – 522.5/T ²	[cal/mol K]
NiS	9.25 + 0.00640T	[cal/mol K]
NiO	11.3 + 0.00215T	[cal/mol K]
MoS ₂	11.7 + 0.00315T	[cal/mol K]
MoO ₃	15.1 + 0.0121T	[cal/mol K]
SO ₂	7.70 + 0.00530T – 0.00000083T ²	[cal/mol K]
C ₁₄ H ₃₀	353.140 + 29.13T + 0.86116T ²	[J/kmol K]
CO ₂	10.34 + 0.00274T – 195.00/T ²	[cal/mol K]
H ₂ O	8.22 + 0.00015T + 0.00000134T ²	[cal/mol K]
O ₂	8.27 + 0.000258T – 187.00/T ²	[cal/mol K]
N ₂	6.50 + 0.00100T	[cal/mol K]

2.4.4.3 Results and discussions

For the application of the model presented previously, a catalyst containing C₁₄H₃₀ (4%wt.), MoS₂ (4%wt.), and NiS (4%wt.) was considered. The data related to the geometry of the kiln are summarized in **Table 57**. An average catalyst flow rate of 5000 ton/year and an air flow rate of 7000 kg/h were considered.

Table 57. Kiln parameters used in the calculation code.

Parameter	Symbol		
Useful length of kiln	L	12.00	m
Internal Diameter	D	1.30	m
Refractory steel thickness	s ₁	0.006	m
Ceramic fiber thickness	s ₂	0.146	m
External shell thickness	s ₃	0.010	m
Thermal conductivity refractory steel	k ₁	25	kW/m°C
Ceramic fiber thermal conductivity	k ₂	0.085	kW/m°C
Thermal conductivity of the outer shell	k ₃	26	kW/m°C
Kiln inclination	θ	3°	-
Rotation speed	n	0.7	rpm

The inlet temperature of the solid is 300 K, and an outlet temperature of the fumes of approximately 830 K has been hypothesized. If experimental data are available, it is possible to insert the precise values instead of the hypothesized ones and easily update the calculation code.

It has been seen that by dividing the total volume of the kiln into 20 smaller volumes with perfect mixing, satisfactory results are obtained; by increasing the number of these elements, the accuracy of the model increases but at the expense of computational complexity.

Figure 80 illustrates the thermal profile of the two phases along the entire axis of the kiln.

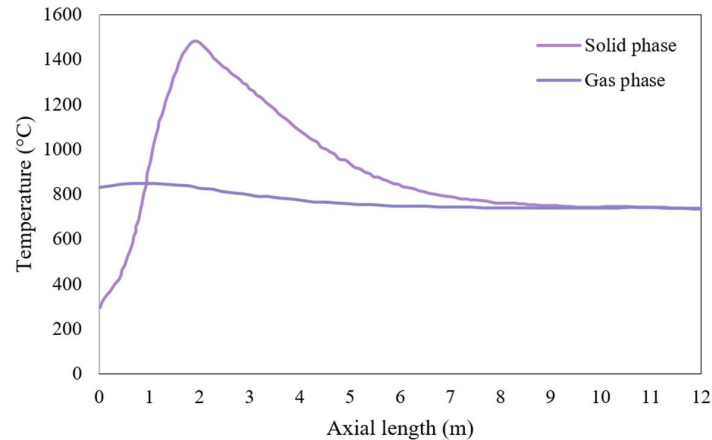


Figure 80. Axial thermal profile of the gas and solid phases in the kiln.

In the first meter of the RK, the temperature of the catalyst increases due to the heat exchange between the gaseous phase and the solid phase in countercurrent. Once the oxidation reactions (exothermic) have started, the temperature of the solid phase tends to increase until it exceeds that of the gaseous phase. In the first half of the kiln, the maximum temperature is reached, and the reactions end; the temperature of the solid phase tends to decrease due to the heat exchange with the gaseous phase at a lower temperature. In the descending section of the thermal profile, the tangent to the curve is undoubtedly lower than the ascending section; this is due to the low value of the convective heat exchange coefficient between the phases (h) and the high value of the heat released by the combustion reactions.

Sensitivity analyses were performed to see both the model's flexibility to the variation of specific inputs and the influence of the variation of the Oil concentration on the thermal profile of the two phases. In particular, it influences the maximum temperature reached inside the kiln. The results of these analyses are shown in **Figure 81**.

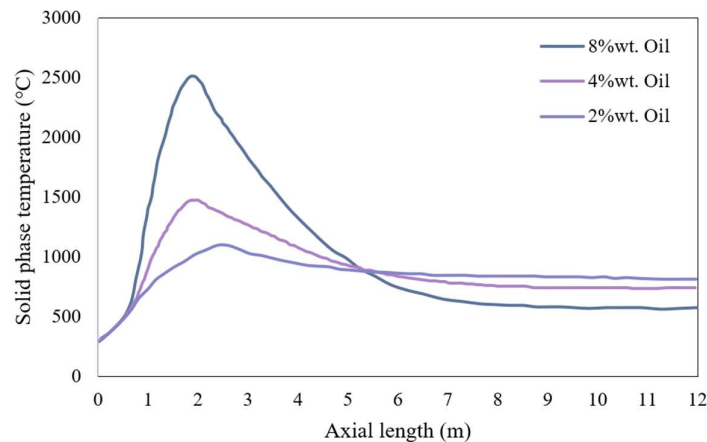


Figure 81. Thermal profile of the solid phase in the kiln for different inlet Oil concentrations.

As expected, a more significant percentage of oil in the catalyst leads to a significant increase in the temperature of the solid phase. The maximum temperature is certainly a value to keep under control in this process both for thermal degradation problems and for the onset of unwanted phenomena such as the sintering of alumina (at temperatures above 800 °C).

Figure 81 shows that it is necessary to bring the oil concentration to around 2% wt to avoid alumina sintering. It was decided to remove part of the oil by washing the catalyst with acetone to avoid alumina sintering. Using a solvent/Oil mass ratio of approximately 30% makes it possible to bring the concentration of Oil present in the solid phase below 2% wt. Since the solvent/oil ratio is relatively high, recovery and subsequent reuse of the acetone were considered.

2.5 CONCLUSIONS

Below are the main results obtained during the study and optimization of sustainable recovery processes for valorizing spent Oil&Gas Catalysts.

- The application of the Gulf process resulted in a relatively good recovery efficiency of vanadium and excellent purity of the final product. The configuration with three countercurrent steps achieved overall recovery yields even higher than 95%.
- The effect on the recovery yields of the excess NaHCO_3 compared to the vanadium and molybdenum content in the initial sample was evaluated. It was noted that by carrying out the process in countercurrent, the optimal recovery yield was obtained at an excess of approximately 50%. This aspect is due to the consumption of the reagent (NaHCO_3) in its reaction with the other elements present in the material.
- It was noted that with the various tests carried out on volumes of 80 mL for the precipitation of V using ammonium chloride with the optimal conditions (reaction time = 60 min, pH = 8, NH_4Cl = 4.51 g, and T = 40 °C) a vanadium precipitation yield of 98.6% was obtained and purity of the final product of 99.9% in terms of V_2O_5 . Furthermore, it was noted that the vanadium concentration in both the washing water and the residual solution is less than 200 ppm.
- It was observed that during the sedimentation tests, the agitation speed during leaching does not influence the sedimentation time but only the vanadium recovery. The leaching process depends on the transport of matter, and further ad hoc studies are necessary to understand better the reaction kinetics' limiting steps.
- It has been seen that acid leaching is a viable alternative to alkaline leaching. The possibility of using citric acid as a leaching agent was evaluated. This process would allow for a reduced environmental impact compared to inorganic acids. Through preliminary tests, it was seen that it is possible to obtain good vanadium recovery yields, even higher than 65% without optimization.
- A more in-depth study was carried out to evaluate the possibility of eliminating the classic thermal pretreatment phase with all the related problems of temperature management and the environmental impact of the overall process. It has been seen that two very promising avenues could be a washing pretreatment of the catalyst with a solvent or a pyrolysis pretreatment.
- Among the solvents analyzed, it was seen that acetone is the best performing both in terms of extraction yields of the organic phase (a phase that hinders leaching or which, in any case, was responsible for the high temperatures in the calcination kiln) and in terms of

recyclability. Since acetone is very volatile, it can be recovered through distillation processes and recirculated for a new washing cycle. Through experimental tests, it has been seen that the removal yields of organic elements by washing with acetone are 30% C removal efficiency, 51% H removal efficiency, and approximately 6% S removal efficiency.

- A predictive process simulation with the Aspen Plus V10 process simulator allowed the feasibility of acetone recovery following catalyst washing to be estimated. It has been seen that it is possible to recover the solvent with yields above about 80% with a simple Flash stage. The purity of the recovered acetone is found to be greater than 99%.
- Using the Aspen Plus V10 process simulator, the possibility of using pyrolysis to remove the organic phase from the exhausted catalyst was evaluated. The route seems very promising, but from the calculations, the route with washing with acetone and subsequent thermal oxidation of the washed catalyst appears to be more convenient both from a technical and economic point of view. The acetone process was patented under the name ORIM-CAT2 process.
- From experimental tests on a laboratory scale, the leaching process downstream of washing with acetone was optimized (ORIM-CAT2 process). Leaching is performed without a thermal oxidation step, and it is therefore necessary to introduce an oxidant (hydrogen peroxide or ozone) into the reaction environment. A 2k factorial plan was created to evaluate the effect of four factors on the leaching yield of V and Mo from LCF catalysts. The factors studied were NaOH concentration, H₂O₂ concentration, temperature, and diameter of the solid particles. It is necessary to work at room temperature and higher concentrations for both the complexing agent and the oxidant to yield more for both elements. The increase in temperature does not lead to a significant increase in the extraction yield. This aspect may be due to residual hydrocarbons in the material. The optimal concentrations of the two reagents were determined through optimization with RSM. It has been seen that these concentrations are 1.71 M for H₂O₂ and 1.64 M for NaOH.
- Different process solutions have been evaluated for the ORIM-CAT2 process. In particular, it is possible to operate both with multiple steps in co-current and counter-current, obtaining good yields in both cases. The possibility of grinding with different types of mills, cylinder or ball mills, was evaluated. In this case, the yields are better for grinding with a ball mill.
- A one-dimensional model capable of simulating the behavior inside a rotary kiln has been developed. This model is highly flexible and can accurately describe the phenomena that occur in the combustion chamber for different compositions of the inlet flow rate compared to the previous ones published in the literature. Its flexibility allows for determining the thermal profile of the various phases in the kiln, even for applications other than the typical ones (mainly in the cement industry). The case of a rotary kiln used as a roasting kiln for spent catalysts in the Oil&Gas sector was analyzed; this operation is of considerable interest in recovering precious and base metals such as Ni, Co, Mo, and V.
- Simulating the behavior of the kiln with an LC-Finer-type catalyst inside shows how great attention must be paid to the incoming concentration of Oil. The Oil deposited on the catalyst during the various refining processes has a high calorific value and is mainly responsible for the increase in temperature.
- From the results obtained from the model, it is also noted that the part near the entrance of the solid flow is undoubtedly the most stressed from a thermal point of view. This result suggests greater attention in this specific area in the choice of construction materials and their thicknesses, as well as in monitoring and control.

- At the basis of the model, some simplifying hypotheses are necessary to obtain a simple calculation code from a computational point of view and, therefore, immediately available for subsequent sensitivity and optimization studies. The physical phenomena that underlie this process are numerous, and some are complicated to describe. To have an even more accurate simulation, for example, the thermal transmission mechanisms that occur transversally and longitudinally should be investigated in depth; the kinetics of the reactions that occur in the kiln and the diffusion mechanisms of oxygen in the pores of the kiln should be investigated in detail. Furthermore, fluid dynamic studies should analyze the degree of mixing between the phases. Various adjustable parameters were introduced to take all these phenomena into account.

3

Printed Circuit Boards

3.1 INTRODUCTION

The global market for printed circuit boards (PCBs) has seen rapid expansion in recent years, mainly due to the continuous development of consumer electronic devices and the growing demand for PCBs in all electrical and electronic equipment. Televisions, smartphones, smartwatches, smart speakers, kitchen appliances, and other consumer electronics use printed circuit boards to function correctly.

Directive 2012/19/EU defines "electrical and electronic equipment," or "EEE", as equipment that depends on electric current or electromagnetic fields to function correctly.

The integral component of any electronic equipment is the printed circuit board (PCB), as it electrically connects and mechanically supports the other electronic components.

A printed circuit board is a rigid electronic structure of embedded metal wires, called traces, and large metal areas, called planes.⁵² The printed circuit can be mechanically defined as "rigid", "flexible," or "rigid-flexible", if it is made up of rigid parts connected by flexible sections. The production process becomes progressively more complex and expensive depending on the number of conductive layers present in the printed circuit. Based on the technological complexity, proportional to the number of layers, we talk about:

- "single face" or "mono copper" (single conductive layer);
- "double-sided" or "two layers" (two conductive layers);
- "multilayer" (in most applications, between 4 and 8 layers, but it is also possible to create 20 or more layers).

Depending on the type and application of PCBs, their composition varies. Printed circuit boards generally comprise approximately 28% metals and 23% plastics; the remaining percentage includes ceramic and glassy materials, of which approximately 90% comprises Tetrabromobisphenol A (TBBPA).⁵³ The plastic materials in PCBs mainly comprise C-H-O polymers such as polyethylene, polypropylene, polyesters, polycarbonates, phenol, formaldehyde, and others. In contrast, the rest of the plastics comprise halogenated and nitrogen-containing polymers. The PCB, regardless of the type, is made up of three fundamental parts: a non-conductive substrate or laminate, a conductive circuits printed on or within the substrate, and components mounted on the substrate.⁵⁴

These components, as well as the electronic board, contain several rare elements with high economic value. Some of these elements, due to their high supply risk and high economic importance, have been placed on the list of critical raw materials (CRMs) by the European Union (such as PGMs, Cobalt, Aluminum, Titanium, Copper, and Nickel).⁵⁵ Depending on the type and application of PCBs, their

composition varies. PCBs comprise about 28%wt metals, 22%wt plastics, and 50%wt ceramic and flame retardant (FR) materials.^{56,57}

The FR materials interfere with the chain of chemical reactions that occur during combustion, reduce the kinetics of the reaction, and decrease the amount of heat produced. FRs often protect electronic components from any in-fires that short circuits or overloads might cause. The flame retardancy on an electronic board depends on the type of material used and local or international fire safety regulations. Based on the type of FRs, four different types of electronic boards are classified: FR-1, FR-2, FR-3, and FR-4 PCBs. **Table 58** shows the main characteristics of the above types.^{58,59}

Table 58. Materials and main characteristics of various FRs.⁵⁹

	FR-1	FR-2	FR-3	FR-4
Materials	Paper and phenol-formaldehyde resin	Paper with a plasticized phenol formaldehyde resin	Cotton linter/alpha cellulose paper with epoxy resin formulation	Woven/Unwoven fiber-glass cloth with epoxy resin
Glass Transition Temperature	130 °C	130 °C	130 °C	140-170 °C
Chemical resistance	Low	Low	Medium	High

Printed circuit boards (PCBs) extracted from electronic waste (WEEE) stand out as prized elements within the waste stream despite constituting only a modest 3% of it.⁶⁰ The concentration of precious metals, notably Au, Ag, Pd, and Pt, far exceeds that found in their primary sources, rendering waste PCBs an economically appealing "urban mineral" for recycling. A rough estimate suggests that the primary metals within electronic boards include Cu (~16%), Sn (~4%), Fe (~3%), Ni (~2%), and Zn (~1%).⁶¹ Additionally, precious metals such as Au (~0.039%), Ag (~0.156%), and Pd (~0.009%), integral as contact materials or plating layers for electrical conductivity and chemical stability, are tenfold more abundant in WPCBs than in natural minerals.⁶¹

The imperative for PCB recycling revolves around two key objectives: mitigating pollution from improper disposal and reclaiming valuable metals. Given the mounting electronic waste, these boards have emerged as valuable material sources. Metal recovery is paramount to preventing environmental contamination, driving the exploration of eco-friendly processes amalgamating mechanical pre-treatment with hydrometallurgical techniques.⁶² Hydrometallurgical procedures necessitate solvents like nitric acid, hydrochloric acid, cyanide, halide, thiourea, and thiosulfate for metal dissolution or leaching.^{63,64} However, the recovery and separation processes generate waste streams, necessitating further management.⁶⁵

The recovery of base metals significantly influences process economics due to their substantial presence in PCBs. This recovery concurrently enriches precious metals in the solid residue, facilitating their subsequent extraction through leaching.⁶⁶ The solutions undergo separation and purification processes, such as impurity precipitation, solvent extraction, adsorption, and ion exchange, isolating and concentrating the metals of interest. Electrorefining, chemical reduction, or crystallization processes follow to recover the metals.⁶⁷ Modern hydrometallurgical processes for WPCBs yield high recovery rates for precious and base metals.^{64,65}

However, a challenge lies in the chemical coating covering the metals in electronic boards, primarily comprising organic compounds. This coating complicates metal recovery by inhibiting contact with the leaching agent.⁶⁸ Successful metal release before hydrometallurgical treatment relies on cumulative processes like shredding, crushing into powder, and effective metal–nonmetal separation techniques. Incorporating these pre-processing methods enhances the overall recycling process economics.⁶⁹

Physical separation processes encounter a notable issue: the substantial loss of precious metals. Factors include insufficient metal release due to close association with plastics, generation of fines

during size reduction, and inefficiency in separating metals from fine fractions. Hence, an alternative process to remove chemical coatings from PCBs without metal loss becomes imperative.⁶⁸

Thermal processes such as incineration, pyrolysis, and gasification emerge as promising methods to transform complex e-waste into valuable products. Thermal treatment aims to eliminate organic components (e.g., plastics) while preserving nonvolatile mineral and metallic phases for subsequent recovery. This removal of the plastic coating enhances metal exposure, leading to increased extraction yields during hydrometallurgical processes. Notably, the gaseous, liquid, or solid by-products post-cleaning can be harnessed for energy recovery.⁷⁰

This chapter summarizes the research activity carried out on this type of material in order to optimize some hydrometallurgical processes for the recovery of precious and base metals from WPCBs.

Experimental tests were carried out on a laboratory scale both for the characterization of different samples of WPCBs and leaching tests using the processes developed by the University of L'Aquila for the optimization and commercialization of the various technologies.

Furthermore, an Aspen Plus simulation was developed to explore the pyrolysis of printed circuit boards in this research.⁵⁶ The primary goal of this research activity is to construct a model elucidating the thermodynamic behavior of this operation on such complex materials, estimating the composition and flow rate of syngas and pyrolysis oil. Furthermore, the study analyzes how specific process characteristics or variations, such as steam and pyrolysis temperature, influence the final products.

3.2 MATERIALS

3.2.1 Arduino Board

The characterization of Arduino boards aims to assess the intrinsic economic value (IEV) associated with the metal content. Arduino, a widely employed electronic board, is primarily utilized for swiftly prototyping electronic projects. While the complete chemical composition of Arduino boards remains to be fully established, such characterization endeavors hold the potential to unravel the intricate chemical composition of conventional electronic components found in PCBs. Given its extensive use as an electronic board, Arduino can be viewed as a standardized reference sample, offering valuable insights for subsequent studies in this domain.

The electronic board used is Arduino Mega 2560⁷¹, shown in **Figure 82**.

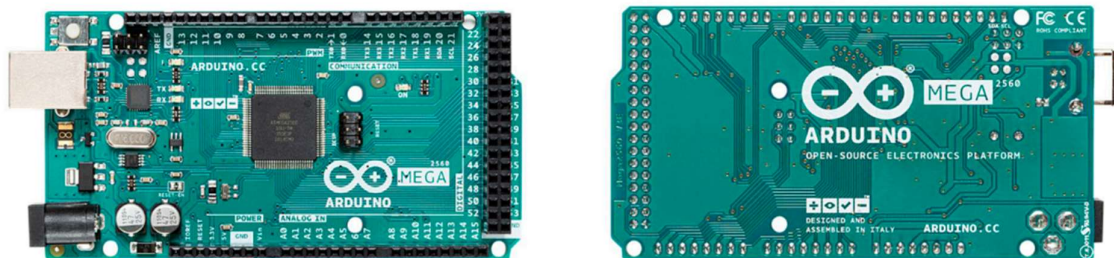


Figure 82. Photographic aspect of the Arduino board, front (**left**) and back (**right**).

3.2.2 EuroLCDs Board

As part of the European project TREASURE (see **Projects & Companies** section), the Gold-REC1 and Gold-REC2 processes for recovering precious and base metals from this type of board were studied with experimental tests on a laboratory scale.

The EuroLCDs company, a partner of the University of L'Aquila, provided the sample used in the TREASURE project. The photographic appearance of AF81 board used is shown in **Figure 83**.

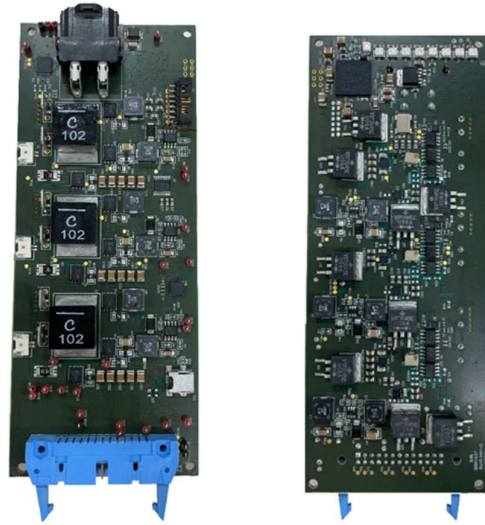


Figure 83. Photographic aspect of AF81 board, front (**left**) and back (**right**).

The characterization of the board was carried out through component disassembly, chemical attack with acid solutions, and analysis with ICP-OES. The results of these analyses are reported in **Figure 84**.

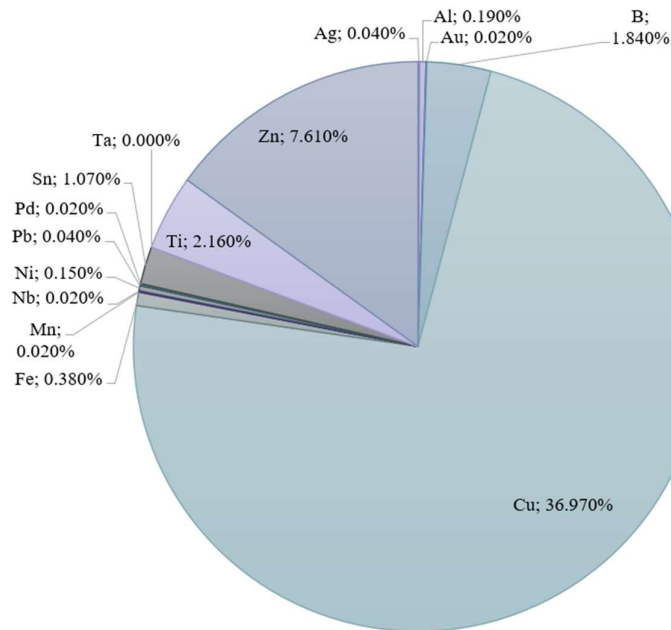


Figure 84. Total composition of AF81 board.

3.3 METHODS

3.3.1 Arduino disassembly

In order to proceed with the characterization of all the components on the electronic board, a disassembly step was provided using a hot air gun. The components obtained were weighed and subjected to a chemical attack with various aggressive solutions to solubilize all the metals in the solution. This way, it was possible to trace each component's composition and, consequently, the total

board. The equation used to calculate the mass fraction of the generic metal in the specific component of the board is reported below.

$$\omega_{i,j} = \frac{c_{i,j} \cdot L_j}{m_j}$$

Where i is the index for the analyzed element and j the index for the component. In this sense, $\omega_{i,j}$ is the mass fraction of element i for component j ; $c_{i,j}$ is the concentration of metal i in the chemical attack solution of component j ; L_j is the volume of the chemical attack solution of component j ; and m_j is the mass of component j subjected to chemical attack.

3.3.2 EuroLCDs Board Treatments

Several leaching tests were performed to evaluate the recovery efficiency of Au, Ag, Pd, Cu and Sn through Gold-REC1 and Gold-REC2 processes on the AF81 components. The Gold-REC1 process was performed for electronic board powders while Gold-REC2 was used for the different devices (for example back panel and connection devices).

3.3.2.1 Gold-REC1 Process for PCBs

The Gold-REC1 process was born as a process for the recovery of precious and base metals from WEEE.⁶⁴ The current hydrometallurgical procedure consists in the following operations:

- The waste printed circuit boards are firstly subjected to a physical mechanical procedure where the Al and Fe-based components are removed manually from PCBs surface. Then, the depopulated PCBs are shredded and milled to suitable particles sizes.
- The milled PCBs are then leached with water, sulfuric acid and hydrogen peroxide for the extraction of base metals.
- The separation of the solids from the leach liquid is carried out by filtration process followed by washing with water. The resulted solution (filtrate) is subjected to a precipitation process for Sn precipitation. Then, also this solid precipitate is separated from solution by filtration and further washed with water. The solution achieved after Sn recovery/removal(?) is sent to an electrowinning cell for Cu recovery.
- The resulted solution is recycled in the first leaching process for the leaching of another PCB material.
- The solid residue of base metals leaching process is involved into another leaching process with thiourea as reagent, ferric sulfate as oxidant in diluted sulfuric acid for Au and Ag dissolution.
- After removal of solid suspension from solution by filtration, the electrowinning process is also applied to this solution for Au and Ag recovery. Once the process is finished, the remaining solution discharged from Au and Ag can be also recycled for the leaching of precious metals for the treatment of other PCBs.

The conditions of the Gold-Rec1 test carried out on the powders are: a solid concentration of 15% wt./vol., a stirring rate of 200 rpm, the concentration of hydrogen peroxide is 20% vol., the concentration of H₂SO₄ is 10% vol., the concentration of Thiourea is 20 g/L, and the concentration of ferric sulfate is about 22.5 g/L. Before testing procedures, the electronic board without components was ground in a knife mill and subsequently analyzed to determine the content of the metals of interest (Au, Ag, Pd, Cu, and Sn), reported in **Table 59**. Based on the extraction, yields were calculated from the concentrations obtained.

Table 59. Characterization of PCBs powders.

Element	Concentration
Au (ppm)	73.37
Ag (ppm)	548.43
Pd (ppm)	38.66
Cu (%)	10.01%
Sn (%)	2.50%

3.3.2.2 Gold-REC2 Process for PCBs

The Gold-REC2 process is a patent of University of L'Aquila. It was born as a process for the recovery of precious and base metals from WEEE.⁶⁵ This hydrometallurgical process could be synthetically described as indicated below:

- The chemical process can be applied on the e-waste without grinding (with whole waste PCBs as an example) avoiding important loss of precious metals also described in the literature.
- The process uses a unique step of metals dissolution with a chemical leaching using HCl, H₂O₂, acetic acid in water solution at room temperature with a solid/liquid ratio of 10-20%. The chloroacetic acid is produced by in-situ chemical process within two steps: firstly, hydrochloric acid reacts with hydrogen peroxide and acetic acid to produce peracetic acid, water and chlorine; in the second step chloroacetic acid and hydrochloric acid are produced by the chlorination of the unreacted acetic acid.
- Precious (Au and Ag) and base metals (Cu, Sn, Zn, Ni, Pb) are dissolved leaving the waste PCBs with mainly epoxy resins and fiberglass structure intact (with some residues of metals);
- The liquid solution is easily separated from the S/L system and selective reduction-precipitations steps are considered in the process to recover the dissolved metals. These steps are synthetically described in the follow: reduction and precipitation of Au chloride to its metallic form by ascorbic acid; cooling the solution to less than 15 °C for precipitation of AgCl; selective reduction and precipitation of Cu by metallic Sn or co-reduction of both copper and tin ions with iron metal; reduction and precipitation of SnCl₂ by metallic Zn; exploitation of the residual solution for its recycling within the process or by adding iron in order to produce a FeCl₂-FeCl₃ solution useful for coagulation processes in the treatment of wastewaters;
- The main products are: Au (after melting process in an inductive electrical oven adding some slug forming compound), AgCl, Cu and Sn in powder forms (mainly in the range of 10-90 μm) and a residual chloride solution that can be regenerated by make-up with proper reagents concentration or treated with iron metal to achieve a high concentrated iron solution (extensively and usually utilized in the coagulation processes in wastewater treatments).

The conditions of the Gold-REC2 test carried out on back panels are the following: a solid concentration of 15% wt./vol., the stirring rate is 200 rpm, the concentration of hydrogen peroxide is 20% vol., the concentration of C₂H₄O₂ is 10% vol., and the concentration of HCl is 3.5 M. Before testing procedures, the back panels was analyzed to determine the content of the metals of interest (Au, Ag, Pd, Cu, and Sn), reported in **Table 60**. Based on the extraction, yields were calculated from the concentrations obtained.

Table 60. Characterization of back panels

Element	Concentration
Au (ppm)	174.55
Ag (ppm)	204.62
Pd (ppm)	742.00
Cu (%)	28.99%
Sn (%)	1.45%

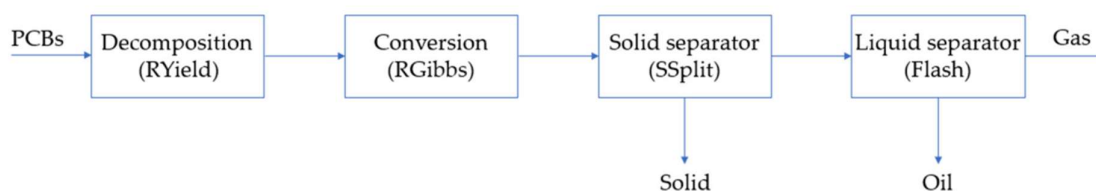
3.3.3 ASPEN PLUS Simulation

An innovative model for PCB pyrolysis was designed using the ASPEN PLUS v10 simulator. The heat treatment is essential for the elimination of the organic component of the boards with a consequent increase in the recovery yields of the metals of interest. Pyrolysis is a heat treatment that can remove the organic component and valorize it through conversion into products such as syngas and pyrolysis oil.

ASPEN PLUS is a software widely used in chemical engineering. It represents a solid pre-packaged basis for professional purposes, including most of the traditional equipment present in a chemical plant.

However, despite its standardized nature, ASPEN PLUS can be customized and enhanced by integrating FORTRAN or EXCEL code and importing user-defined custom models via Aspen Custom Modeler (ACM). This aspect fills gaps in the ASPEN PLUS template library, allowing for a complete simulation of the flowchart within a simulation tool.⁷²

In the specific context of pyrolysis, it was found that ASPEN PLUS does not have a predefined model, thus requiring the use of a combination of different blocks, as illustrated in **Figure 85**. To ensure an accurate implementation of the model, resorting to a FORTRAN code was necessary. This dynamic and flexible approach allows us to overcome the specific challenges of PCB pyrolysis and obtain detailed and reliable results.⁵⁶

**Figure 85.** Block diagram of the developed pyrolysis model.⁵⁶

In order to proceed with the calculation code, various assumptions were made: the conditions are stationary and isothermal, there is uniformity of temperature and pressure in the reactor, and the effect of particle size is neglected. The model was validated with experimental data published in the literature.⁷³

3.3.3.1 Component specification

In the software context, MIXCINC has been set as the global flow class for simulation. This configuration is employed when conventional and unconventional solids are present, and the material's particle size distribution (PSD) is unavailable. Indeed, it is generally assumed that the particle size distribution (PSD) does not significantly influence the pyrolysis process [15].

Unconventional components not present in the ASPEN PLUS database are modeled through proximate and ultimate analyses. Only enthalpy and density are the calculated properties for these components, derived from empirical correlations. Specific property methods for enthalpy and density, such as the HCOALGEN and DCOALIGT methods, are chosen for this purpose, both based on proximate and ultimate analyses.

Polychlorinated biphenyls (PCBs) are considered unconventional solids as they are not in the ASPEN database.

In addition to PCBs, the simulator also includes ash as an unconventional solid material. A proximate and ultimate ash content of 100% is assumed in this case.

Regarding decomposition products, bisphenol A ($C_{15}H_{16}O_2$) is considered the principal component of the organic fraction of PCBs. The choice of bisphenol A is due to the lack of thermodynamic data in ASPEN PLUS for the more appropriate TBBPA (one of the significant components in the brominated epoxy resin of PCB FR-4). Bisphenol A, described in Aspen with sufficient thermodynamic data, interacts in the RGIBBS reactor. It is important to note that using bisphenol A is undoubtedly a simplifying assumption that needs to account for the presence of bromine (the formation of HBr in the syngas needs to be addressed).

Since PCBs are entered into the software as unconventional solids, the analyses reported in **Table 61** and **Table 62** are necessary.^{56,73}

Table 61. PCBs proximate analysis.

Characteristic	wt%
Fixed Carbon	11.43%
Volatile Matter	20.15%
Ash (at 823 K)	68.41%
Moisture (at 378 K)	0.20%

Table 62. PCBs ultimate analysis.

Characteristic		wt%
Carbon	(C)	18.90%
Hydrogen	(H)	1.90%
Nitrogen	(N)	0.57%
Chlorine	(Cl)	0.09%
Sulphur	(S)	0.06%
Oxygen	(O)	5.96%

In addition to PCBs, the simulator incorporates ash as an unconventional solid. In this context, proximate and ultimate ash content are assumed to be 100%.

Concerning decomposition products, bisphenol A ($C_{15}H_{16}O_2$) is identified as the primary component in the organic fraction of PCBs. The selection of bisphenol A is driven by the absence of thermodynamic data in ASPEN PLUS for the most suitable TBBPA (a significant component in the brominated epoxy resin of PCB FR4). Bisphenol A, described in Aspen with ample thermodynamic data, actively participates in the RGIBBS reactor. Bisphenol A is undeniably a simplifying assumption that disregards the presence of bromine (the formation of HBr in the syngas has been overlooked).

Conventional components added to the simulation as potential pyrolysis products encompass aromatic compounds, alkanes up to pentane (C1-C5), alkenes, and other organic constituents.

The thermodynamic method selected for the simulation is based on the Peng–Robinson equation of state with Boston–Mathias modifications (PR-BM).⁵⁶

3.3.3.2 Simulation

The simulation of the pyrolysis process is based on the combined use of R-YIELD and RGIBBS reactors. R-YIELD transforms unconventional materials into several conventional products, while RGIBBS estimates pyrolysis products through thermodynamic equilibrium. In the R-YIELD block, bisphenol A is considered the only conventional component of the organic fraction. However, other reaction products are introduced to overcome limitations, which may disappear based on the thermodynamic equilibrium in RGIBBS.

The simulation was conducted on a flow rate of 100 kg/h of PCBs, converting PCBs into ash, water, and bisphenol A. In the RGIBBS block, the compounds exiting R-YIELD are transformed into different pyrolysis products. The temperature and atmospheric pressure were set at 873 K. Three devices

separated the produced phases, and a steam flow was introduced into the RGIBBS reactor to compare pyrolysis efficiency with that of steam gasification. The simulation assumes a reasonable knowledge of the possible pyrolysis products since adding a single component can affect the thermodynamic equilibrium. **Figure 86** shows the flowsheet of the simulation.⁵⁶

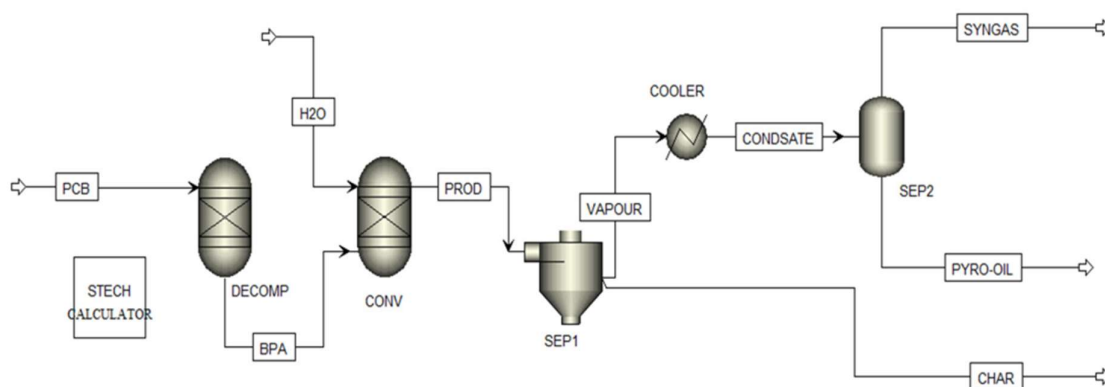


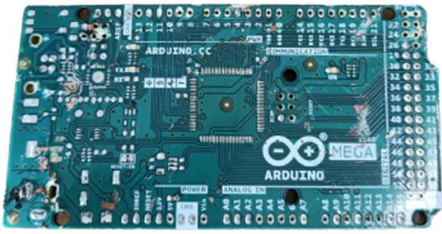



Figure 86. Flowsheet of the simulation.


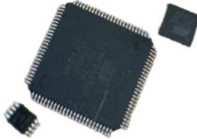










3.4 RESULTS AND DISCUSSIONS

3.4.1 Arduino Characterization

From the disassembly process, 16 components of the Arduino board were identified. **Table 63** shows these components with the methodology used to dissolve the metals present.

Table 63. Components removed from the Arduino board and chemical attack methods.

N.	Name	Image	Method
1	Board		Size reduction + AR
2	External pin		AR
3	USB-B port		AR
4	DC power jack		AR

5	Internal pin		AR
6	ICC ¹		Size reduction + AR
7	Capacitors		Size reduction + AR
8	Crystal Oscillator		AR
9	Reset		AR
10	Voltage regulator		Size reduction + AR
11	M7 Diode		AR
12	PolyFuse		AR
13	Power Led		AR
14	CMC		Size reduction, Calcination at 350 °C with KOH + DL
15	Transistors		AR
16	Plastic cover		-
17	Other ²	-	AR

¹ ICC: integrated circuit chips, ² Other: all unidentified residues of the disassembly process

The solutions resulting from the chemical attack were analyzed by ICP-OES so that the concentration of metals present could be determined. First, a qualitative analysis was carried out to understand the metals present. Second, a quantitative analysis was carried out for the solution of each component in order to identify the concentration of selected metals. The selected metals are those that are also most

present in other sheets analyzed in literature and metals that, although present in smaller quantities, have high economic value. **Table 64** and **Table 65** show the results of these analyses.

Table 64. Results of qualitative analysis.

	Ag	Al	Au	B	Ba	Ca	Co	Cu	Fe	Ga	Mg	Mn	Na	Ni	P	Pd	Pt	Si	Sn	Ti	Zn
Board	x		x	x	x	x		x	x		x	x	x	x		x		x	x	x	x
External pin	x		x					x						x		x			x		x
USB-B port	x		x					x						x		x			x		x
DC power jack	x		x					x	x			x		x	x	x	x		x		x
Internal pin	x		x	x				x						x	x	x			x		x
ICC	x		x				x	x	x					x	x	x			x		x
Capacitors	x	x	x	x				x	x							x	x		x		x
Crystal Oscillator	x		x				x	x	x			x		x		x			x		x
Reset	x	x	x	x				x	x			x		x		x			x		x
V. Regulator	x		x	x			x	x	x							x	x		x		x
M7 Diode	x		x					x								x			x		x
PolyFuse	x	x	x	x				x								x			x		x
Power Led	x	x	x	x				x	x	x				x	x	x			x		x
CMC	x				x	x		x	x			x		x		x		x	x	x	x
Transistors	x					x		x	x			x		x					x		x
Plastic cover																					
Other	x				x	x		x	x			x		x		x			x	x	x

Table 65. Results of quantitative analysis.

	Weight (g)	Plastic (g)	Base metals (wt%)							Precious metals (ppm)			
			Cu	Sn	Ni	Al	Zn	Fe	Ti	Ag	Au	Pd	
Board	20.251	n.a.	15.09	3.36	-	-	0.36	-	-	-	350	2	15
External pin	7.929	5.505	56.95	9.56	1.00	-	25.84	-	-	-	642	107	45
USB-B port	3.406	1.531	63.11	4.82	0.07	-	25.81	-	-	-	403	5	50
DC power jack	1.329	0.685	48.57	7.03	0.24	-	25.53	19.07	-	-	811	-	45
Internal pin	0.800	0.190	58.40	12.41	1.02	-	28.99	-	-	-	975	63	59
ICC	0.629	-	28.75	3.19	-	-	0.17	1.67	-	-	639	191	34
Capacitors	0.541	-	0.41	0.27	-	37.76	0.01	59.50	-	-	59	-	-
Crystal Oscillator	0.503	-	9.26	0.05	0.01	-	5.36	14.21	-	-	905	-	2
Reset	0.197	-	13.85	0.87	-	0.05	7.12	0.60	-	-	403	-	18
V. Regulator	0.129	-	42.80	2.96	-	-	0.29	0.02	-	-	3,754	-	58
M7 Diode	0.065	-	33.95	4.26	-	-	0.21	-	-	-	1,374	-	47
PolyFuse	0.028	-	38.41	9.38	0.67	0.49	0.24	-	-	-	2,801	727	53
Power Led	0.003	-	24.47	8.08	4.97	2.11	0.34	0.19	-	-	2,097	1,774	161
CMC	0.164	-	9.63	6.07	-	-	0.40	-	15.72	-	13,335	104	162
Transistors	0.093	-	3.46	5.46	-	-	0.04	-	-	-	2,032	581	-
Plastic cover	15.230	15.230	-	-	-	-	-	-	-	-	-	-	-
Other	0.115	-	3.42	8.31	-	-	0.05	-	0.48	-	1,813	52	300

Considering the weight of each component and its metal fraction composition, it is possible to determine the composition of the overall metal fraction of the Arduino device. Figure 2 shows the graph of the composition of Arduino's metal fraction

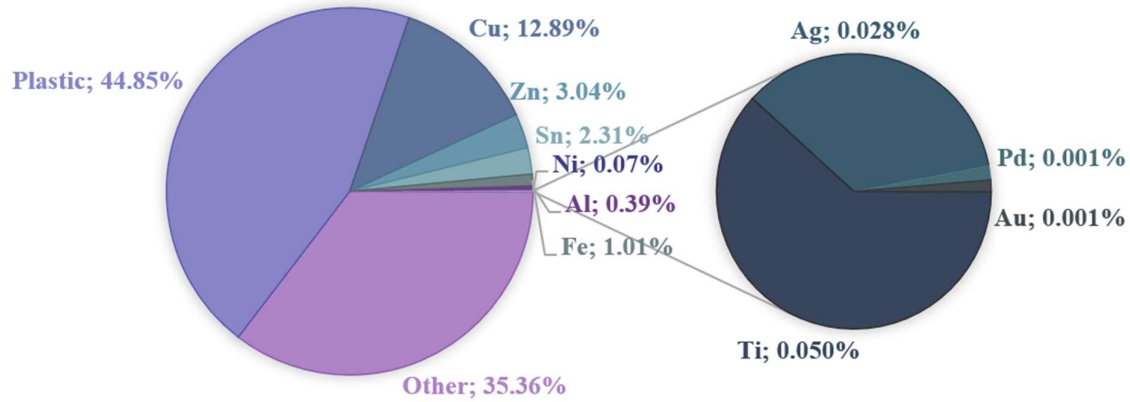


Figure 87. Total composition of Arduino Mega 2560.

By associating the mass fraction of each element with its market price, it is possible to trace the device's intrinsic economic value (IEV).

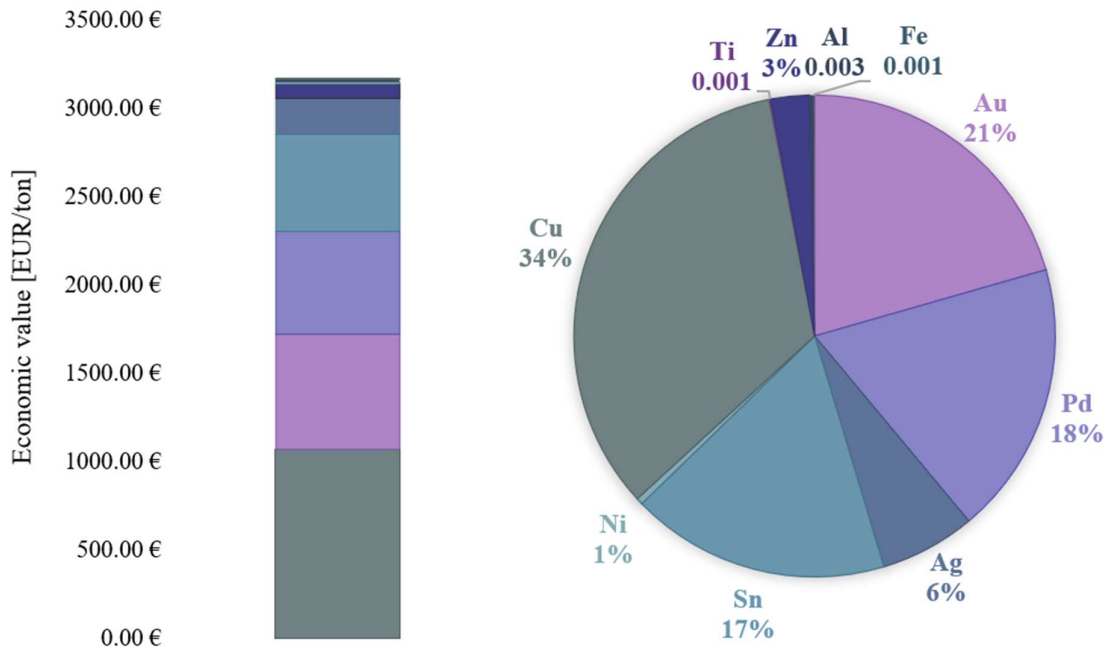


Figure 88. IEV of Arduino Mega 2560.

As can be seen from the figure above, the IEV of this material is about 3.165 €/ton. Also seen is how the weight of different metals on this important parameter. For example, gold accounts for about 21 percent of the IEV and therefore a hydrometallurgical process that recovers only this metal from this material will have a maximum operating economic margin of about 665 € per ton of material.

3.4.2 EuroLCDs Board Results

3.3.2.1 Gold-RECI Results

The test carried out was structured on four steps. The first three 90 min steps for the leaching of the base metals and the third 60 min step for the leaching of gold and silver by thiourea. Table 66 shows the results obtained in terms of recovery yields.

Table 66. Extraction yields for different AF81 powders

Metal	Extraction yields (%)				
	Step I	Step II	Step III	Step IV	Total
Au	0.64%	1.00%	0.45%	24.33%	24.33%
Ag	4.27%	3.34%	2.66%	52.27%	52.27%
Pd	57.33%	13.95%	5.51%	8.06%	57.33%
Cu	10.02%	53.48%	20.23%	0.81%	83.73%
Sn	27.92%	6.88%	8.07%	0.34%	42.87%

Such low extraction yields for precious metals are because only some of the necessary components have been removed. The yield to note is undoubtedly that of copper. The incomplete recovery of copper leads to a decrease in the extraction yield of precious metals in the leaching step with thiourea. Therefore, removing other components from the boards is necessary to lower the overall content of copper and other organic materials in the dust. For example, inductances (high copper content) should be removed.

3.3.2.2 Gold-REC2 Results

The test carried out was structured on two steps of 3 hours each. **Table 66** shows the results obtained in terms of recovery yields.

Table 67. Extraction yields for AF81 back panels.

Extraction yields	Step I	Step II	Total
Au	15.43%	67.94%	83.37%
Ag	60.83%	11.38%	72.21%
Pd	52.18%	45.11%	97.28%
Cu	85.54%	13.91%	99.45%
Sn	99.21%	0.35%	99.56%

As shown, the Gold-REC 2 process is very good at recovering precious and base metals from devices with high concentrations of precious metals.

3.4.3 ASPEN PLUS Simulation Results

3.4.3.1 Validation

The results derived from the model were compared with the experimental ones presented in the literature by Evangelopoulos et al.⁷³ In their study, Evangelopoulos et al. investigated the effect of atmospheric agents such as steam or nitrogen on the pyrolysis of PCBs. Since we adopted the values they reported in the next and final analyses, we expect our model's results to be consistent with those obtained in their work. We compared the results of pyrolysis (in an inert nitrogen environment) with those of steam gasification (in the presence of steam).⁷³

In the case of pyrolysis, we obtained approximately 85% by weight of solid residues, while the remaining fraction is divided between syngas and pyrolysis oil. In particular, 10 kg/h of syngas and 5 kg/h of oil were generated. The comparison is shown in **Figure 89**. Our model accurately describes the experimental results, with a slight discrepancy due to a higher prediction of solid residues from the simulation, resulting in a decrease in the fluid phase. The most significant difference concerns the composition of the fluid phase since the simulation predicts a more significant amount of syngas than the experimental data (with consequent reduction in the pyro-oil simulation). This discrepancy is attributable to the choice of organic components considered possible pyrolysis products. A precision improvement would require including several other complex compounds (subject to verification of adequate thermodynamic data in Aspen). However, since the primary interest is removing the organic

phase from PCBs and the subsequent energetic exploitation of the fluid phase, the model's accuracy is acceptable.⁵⁶

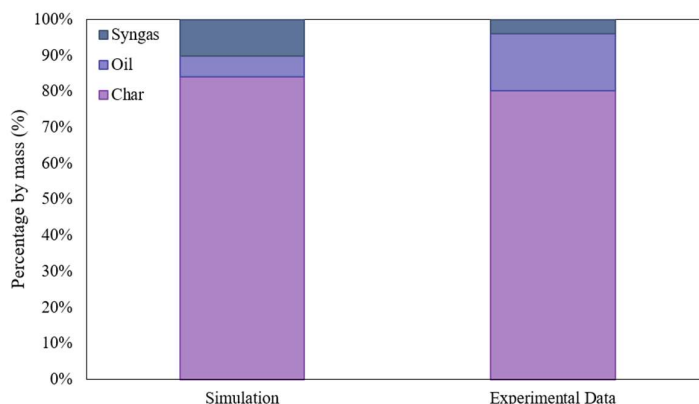


Figure 89. Comparison between experimental results and results predicted by the model in the case of an inert environment with nitrogen.

The syngas composition was also compared with the experimental results. **Figure 90** shows the comparison.

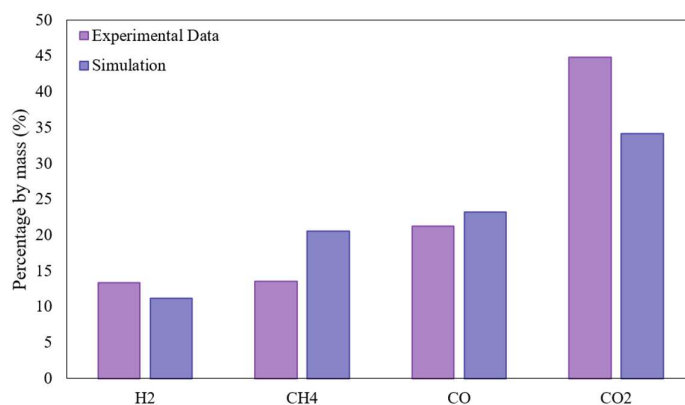


Figure 90. Syngas mass composition.

As highlighted in the graph, the composition data deriving from the simulation show considerable proximity to the experimental ones. The main discrepancy concerns the presence of methane and the composition of carbon dioxide. In the simulation, an increase in the amount of CH₄ and a decrease in CO₂ is observed compared to the experimental data. However, regarding H₂ and CO, the results obtained are comparable with the experimental ones.

To evaluate the model's versatility, the syngas composition was analyzed by adding steam at 393 K and atmospheric pressure inside the RGIBBS reactor. The results of this analysis are presented in **Figure 91**.

In this context, the discrepancy with experimental data manifests itself in hydrogen and carbon monoxide composition. The simulation returned a lower quantity of hydrogen and a more significant presence of carbon monoxide than observed by Evangelopoulos et al. The introduction of steam caused a notable increase in CO₂, attributable to the effect of the water gas shift reaction.

Regarding the liquid phase, the simplification resulting from using bisphenol A prevents adequate characterization. All simulations indicated the presence of a pyrolysis oil mainly composed of water, with traces of various gaseous organic compounds present and solubilized. This limitation, identified as the weak point of the model, starts to become negligible for temperatures above about 873 K, as a significant decrease in the amount of oil produced is experimentally observed.⁵⁶

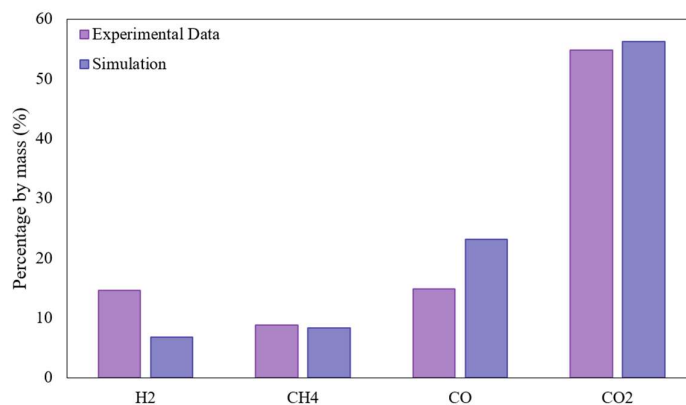


Figure 91. Syngas composition in case of steam added to the reactor.

3.4.3.2 Optimization

The sensitivity analysis examined the impact of the temperature and amount of steam introduced into the RGIBBS reactor on the conversion of the organic fraction initially present in the PCBs, also evaluating the effect on the flow rate and composition of the syngas. **Figure 92** illustrates the influence of temperature on various pyrolysis products in the absence of steam.

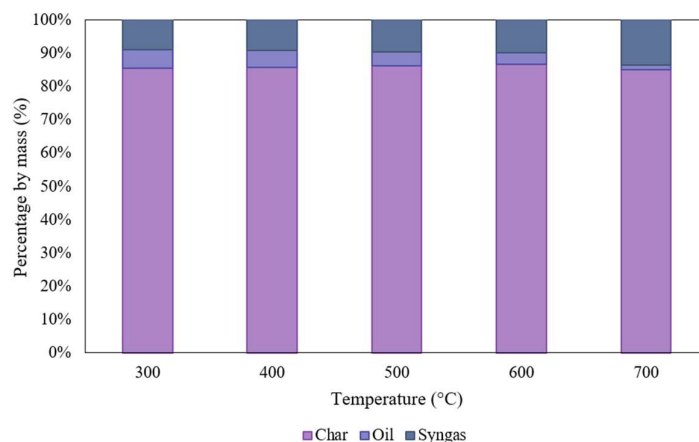


Figure 92. Pyrolysis products for different temperatures.

The solid phase shows a limited response to increasing temperature, while a significant effect on the composition of the fluid phase is observed. The increase in temperature translates into a decrease in the quantity of oil present and an increase in the quantity of syngas, taking into account that the model tends to slightly overestimate the quantity of syngas compared to the experimental data.

In **Figure 93**, we examine the effect of reaction temperature on the conversion of the organic fraction for different steam flow rates. It is noted that, in general, the increase in temperature leads to an increase in conversion, except in cases with low quantities of steam, where minimums around 823 K are highlighted. The observation suggests that the minimum is mainly influenced by the effect of temperature on conversion. As steam increases, the minimum tends to disappear, masked by the very positive effect of steam on conversion.

Increasing the steam flow rate leads to higher conversion. In particular, it is noted that the complete conversion of the organic fraction occurs at lower temperatures for higher steam flow rates (e.g., for 40 kg/h of steam, the complete conversion occurs at temperatures above 873 K). The solid residue produced by steam gasification not only contains a reduced amount of organic fraction, facilitating the subsequent leaching phase but also has an "open" structure, facilitating the hydrometallurgical process.⁵⁶

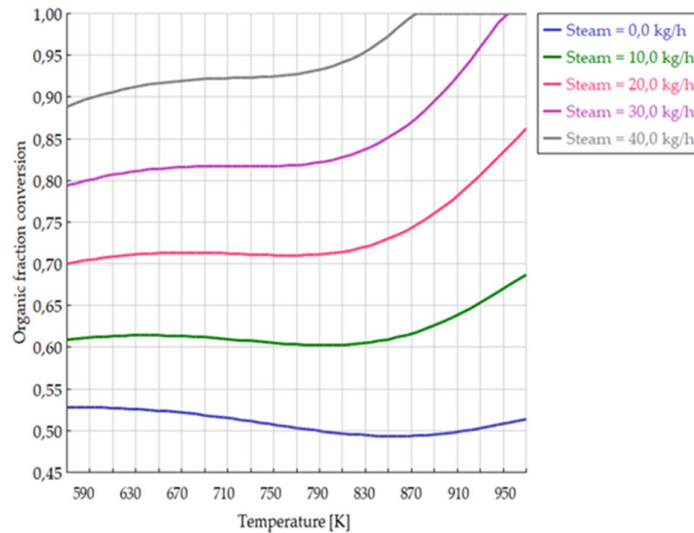


Figure 93. Effect of temperature over organic fraction conversion for different steam streams (feed: 100 kg/h).

3.5 CONCLUSIONS

The main results obtained during the study and optimization of sustainable recovery processes for valorizing end-of-life printed circuit boards are reported below.

- The study on the ARDUINO board highlighted the components with the highest precious and base metal content. In more detail, the chemical composition of the Arduino board's different components was determined. This information can be transferred globally to all other PCBs from various applications within a specific range of variability.
- It is seen that gold content is mainly related to pins and ICCs, while silver is detected in MLCCs. Palladium is present in small quantities in all devices. Among the base metals, copper, tin, and zinc are found in all components, while iron and aluminum are found in high concentrations in capacitors. The overall board was found to have the following mass fractions for the base metals: 12.9% copper, 3.0% zinc, 2.3% tin, 1.0% iron, 0.4% aluminum, 0.1% nickel, and approximately 0.1% titanium. The concentrations of precious metals were determined: 285 ppm of silver, 13 ppm of palladium, and 11 ppm of gold. The results obtained are comparable with those found in the literature for different electronic boards but with the analysis carried out on the overall grinding of the board.
- Based on these results, the intrinsic economic value of the Arduino board was calculated and found to be approximately €3165/ton. This value does not consider all the elements present, only those analyzed; however, precisely due to the criteria used in choosing the materials to analyze, this value represents an excellent approximation of the real value.
- The principal metals that contribute to the intrinsic economic value are copper, with an incidence of approximately 35%; gold, with an incidence of 21%; and silver, with an incidence of approximately 18%. These results are essential to define the metals to be recovered during the development of a recycling process. This research allows us to understand which metals must be recovered if an economically sustainable process is desired.

- From experimental leaching tests with the Gold-REC1 process on ground PCB powders, it was seen that the extraction yields were relatively low. This result made it possible to deduce that removing some components before grinding is essential to obtain high yields in recovering precious metals. In particular, it is necessary to remove all components with a high copper content, such as inductors.
- The experimental leaching tests with the Gold-REC2 process on the back panels of PCBs showed that the process has high recovery yields (around 90% for all precious metals). For this reason, the process is very suitable for treating devices with high concentrations of precious metals.
- The simulation with ASPEN PLUS to describe and study the thermodynamic behavior of the pyrolysis of electronic boards has proven to be very reliable as a predictive model. The results obtained through the simulation faithfully reflect those found in the literature. However, adding other organic compounds as possible pyrolysis products can further improve the model. The simplifying hypothesis of using bisphenol A as a reference component for the organic fraction of PCBs proved to be correct, given the results obtained.
- Thanks to the developed model, conducting a sensitivity analysis aimed at the optimal configuration and the best process conditions to remove the greatest possible quantity of organic fraction present in PCBs without numerous experimental tests was possible. Introducing steam into the Gibbs reactor or increasing the pyrolysis temperature improved the conversion. The sensitivity analysis showed that an excellent efficiency of the organic fraction coming from the boards is obtained by operating with a mass ratio between steam and feed of 0.4 at a reaction temperature of approximately 600 °C.
- Pyrolysis represents a technologically feasible solution as a pretreatment to improve printed papers with enormous optimization possibilities. This technology allows the removal of the organic fraction, which would hinder a possible leaching phase for the recovery of metals from the solid matrix and the valorization of the organic fraction by converting it into syngas. A model like the one presented in this work allows the optimization of numerous aspects without conducting complicated and expensive tests.

4

Photovoltaic panels

4.1 INTRODUCTION

Photovoltaic panels have become one of the most promising technologies in the field of renewable energy. Over the past few decades, their popularity has grown exponentially due to their ability to convert solar energy into clean, sustainable electricity. Photovoltaic panels, also known as solar modules, use the photovoltaic effect to generate electricity from sunlight. The photovoltaic effect is a phenomenon that occurs within certain materials, such as silicon, in which electrons are freed and set in motion when hit by photons from sunlight. These electrons can then be captured and directed to generate a usable electrical current.

Photovoltaic panels are commonly installed on buildings or stands, where they can capture sunlight to generate electricity. This electricity can be used immediately to power electronic devices or can be stored in batteries for future use. In some cases, when the photovoltaic system produces more energy than necessary, the excess energy can be fed into the electricity grid, allowing it to contribute to the overall energy supply.

The use of photovoltaic panels offers numerous advantages. First of all, solar energy is a renewable energy source, meaning it does not run out and does not contribute to the greenhouse gas emissions responsible for climate change. Furthermore, the installation of photovoltaic panels can reduce dependence on traditional energy sources and fossil fuels, contributing to greater energy independence. Solar panels are also relatively easy to install and require minimal maintenance over their useful life, which can be up to 25-30 years.

However, there are also some challenges associated with the use of photovoltaic panels. The initial cost of installing a solar system can be considerable, although prices have dropped significantly in recent years. Furthermore, the efficiency of photovoltaic panels can be affected by factors such as the orientation and inclination of the solar module relative to the sun, as well as local weather conditions. The production of photovoltaic panels also requires the use of materials and resources, which can have a negative environmental impact if not managed correctly.

Despite these challenges, the adoption of photovoltaic panels continues to grow globally. Governments, companies, and individuals increasingly invest in solar technologies to reduce carbon emissions, create jobs in the renewable energy sector, and contribute to the transition to a low-carbon economy. In many countries, financial incentives and support policies have been introduced to promote the installation of solar systems.

The increase in installations globally means that essential considerations are starting to arise regarding the current and future management of the quantity of waste coming back from the photovoltaic market. Considering that the first significant installations of photovoltaic modules were made about 50 years ago and that the average lifetime of this technology is 30 years, today, considerable quantities of

end-of-life photovoltaic panels are starting to be returned as waste. The trend over the years in the quantity of this waste is destined to rise exponentially. This type of waste falls into the WEEE category.

The recovery of precious metals from WEEE is of fundamental importance to support the adoption of a circular economy model. The aspiration for greater independence from foreign countries makes this practice even more important.

The rapid increase in the number of electronic devices raises important questions regarding the entire life cycle of such objects. The evolution of the "disposable" approach towards the recovery and recycling of precious materials contained in electronic waste is also dictated by the long-term trend of increasing their market value.

The regulatory framework governing WEEE is constantly evolving. Directive 2012/19/EU and its subsequent regulatory extensions regulate the WEEE sector, imposing collection objectives, such as reaching 45% of the products placed on the market in the three years 2016-2018, with projections reaching 85% of WEEE generated or 65% of the amount released for consumption starting from 2019.⁷⁴

On 15 August 2018, the "open scope" system (EU Directive 2018/849) came into force, which extends the definition of Electrical and Electronic Equipment (EEE) to include not only existing technological products but also other equipment not previously considered. This expansion has included many products not previously considered WEEE, such as credit cards with chips, electric or pedal-assisted bicycles, multiple electrical sockets, extension cords, automation equipment for gates, awnings, and electric closures. WEEE is classified into the following groups:

- R1 - Refrigerating equipment, e.g., refrigerators, freezers, air conditioning appliances;
- R2 - Great whites, e.g., washing machines and dishwashers;
- R3 - TVs and monitors, e.g., televisions, computer monitors;
- R4 - PED CE ITC, computers and IT equipment, telephones, lighting equipment, photovoltaic panels, vacuum cleaners, sewing machines, irons, and fryers.
- R5 - Light sources, e.g., neon, energy-saving lamps, mercury vapor, sodium, iodide.⁷⁴

The adequate management of electrical and electronic equipment represents a crucial challenge for many countries in terms of health and environmental impacts. However, it also offers significant opportunities for developing eco-businesses and jobs in the green sector. It is essential to implement appropriate treatment systems, adapted to local resources and available technologies, in order to prevent environmental damage and dangers to human health. In such a complex context, the organization of the electrical and electronic equipment management chain becomes fundamental. It is about designing an integrated system that thoroughly addresses the life cycle of this equipment.

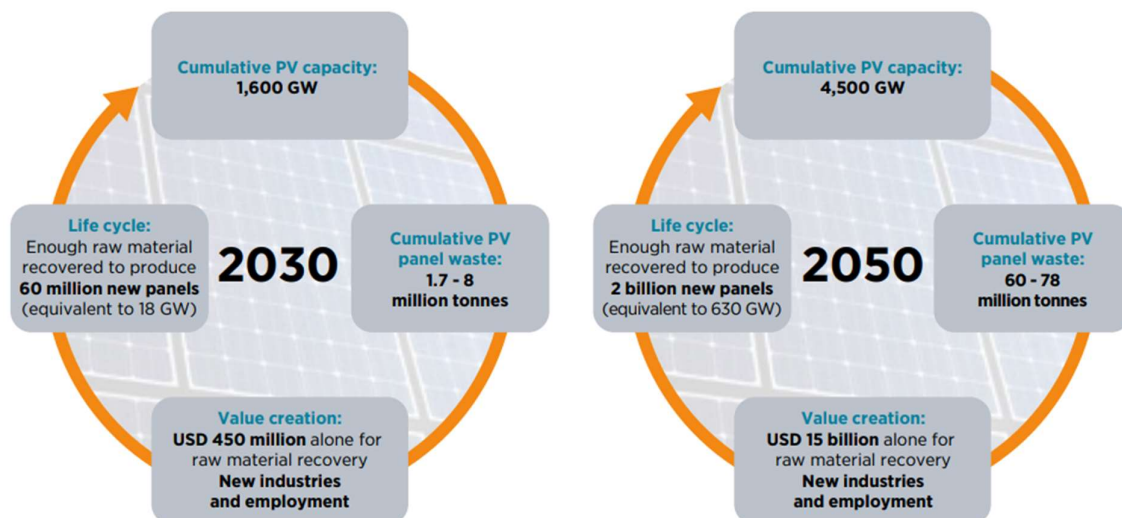


Figure 94. Potential value creation through PV end-of-life management.⁷⁵

In Italy, industrial activities relating to the end of life of electrical and electronic equipment are mainly concentrated on large household appliances classified in categories R1, R2, and R3, for which the treatment and recycling processes are well consolidated. The processing phases include operations such as securing, disassembly, crushing, selection of recoverable materials, and disposal of hazardous substances.

Recoverable materials are usually divided into broader categories that outline directions for subsequent treatments. Ferrous metals, non-ferrous metals, plastics, glass, and higher-value components are separated After a preliminary disassembly phase carried out in authorized centers. Non-recoverable materials are correctly disposed of, while recyclable materials are sold to other operators on the secondary raw materials market. Meanwhile, components or goods that can be remanufactured are sent to third-party manufacturers or operators for necessary remanufacturing operations.⁷⁴

Briefly, the end-of-life management for PV panels will spawn new industries, can support considerable economic value creation, and is consistent with a global shift to sustainable long-term development. **Figure 94** summarizes this concept.

4.1.1 PV Panel Market Share

The recycling of photovoltaic panels is one of the most important current challenges in waste management. This challenge's importance is due to the quantities involved (**Appendix A**) and to the economic and strategic value of the elements contained in the devices at the end of their life.

To understand how important the recovery of raw materials from end-of-life photovoltaic panels is, the composition of this type of waste must be taken into consideration. There are several photovoltaic panel technologies currently used on the market. Different types of technology typically differ in the materials used in their production and may contain different levels of hazardous substances that must be considered during handling and processing. **Table 68** summarizes these categories and their relative presence on the market.

Table 68. Market share of PV panels by technology groups (2014-2030).⁷⁵

Technology		2014	2020	2030
Silicon-base (c-Si)	Monocrystalline			
	Poly- or multicrystalline	92%	73.3%	44.8%
	Ribbon			
	a-Si (amorph/micromorph)			
Thin-film based	Copper indium gallium (di)selenide (CIGS)	2%	5.2%	6.4%
	Cadmium telluride (CdTe)	5%	5.2%	4.7%
Other	Concentrating solar PV (CPV)		1.2%	0.6%
	Organic PV/dye-sensitised cells (OPV)		5.8%	8.7%
	Crystalline silicon (advanced c-Si)	1%	8.7%	25.6%
	CIGS alternatives, heavy metals (e.g. perovskite), advanced III-V		0.6%	9.3%

As can be seen from the table, c-Si PV is the oldest and currently most widespread photovoltaic technology on the market. However, we can also see how this technology will lose importance in the market with the rise of new technologies that are still not widespread today. In particular, the most promising seems to be the advanced c-Si. The latter is estimated to reach approximately 26% of the total share of panels on the market in 2030.

4.1.2 PV Panel Components

The various components of the main photovoltaic panel technologies influence the materials used and the relative percentages, resulting in significantly different overall compositions of the panels depending on the technology. The technologies currently most present on the market are analyzed in detail below: Silicon-base and Thin-film based.

c-Si PV panel components

c-Si technology is based on thin sections of solar-grade silicon, commonly called wafers, which are transformed into cells and subsequently assembled into electrically connected panels.

The standard cell comprises a p-doped wafer with a highly doped pn-junction. The surface is typically textured and may exhibit pyramid structures (monocrystalline silicon), random structures (polycrystalline silicon), and an anti-reflective layer to minimize light reflection.

The front and back of the cell are connected using grid-patterned silver and aluminum pastes to generate an electric field. During a thermal process known as "firing," the aluminum diffuses into the silicon and forms the back surface field. Advanced cell concepts add layers to the wafer, employing laser structuring and contacting to optimize cell efficiencies.⁷⁵

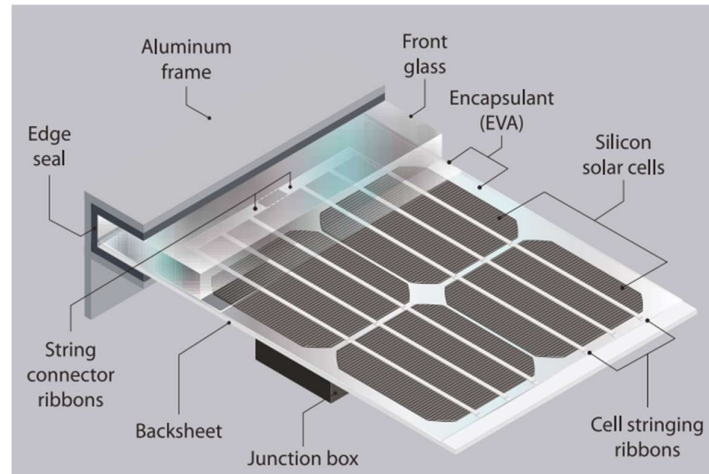


Figure 95. c-Si (monocrystalline) panel, National Renewable Energy Laboratory (NREL).⁷⁵

Thin-film PV panel components

Thin-film panels are comprised of slender layers of semiconducting material deposited onto expansive substrates, such as glass, polymer, or metal. The thin-film photovoltaic (PV) panel technologies can be categorized into two primary types: CIGS (Copper Indium Gallium Selenide) and CdTE (Cadmium Telluride).⁷⁵

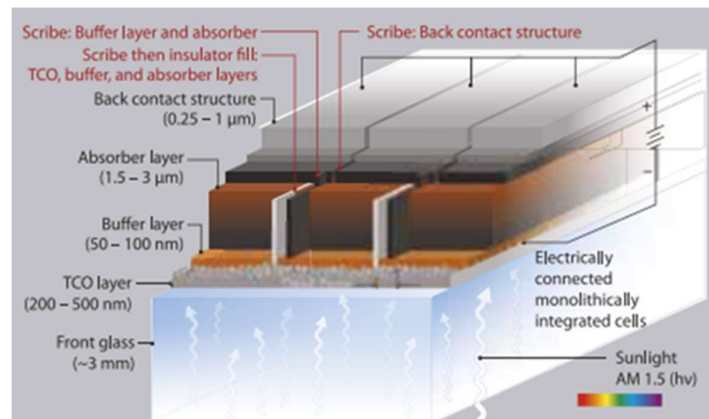


Figure 96. Thin-film (monolithic integration) panel, NREL.⁷⁵

4.1.3 PV Panel Composition

The composition of photovoltaic panels varies not only by panel type but has changed even over the years for the same category. This aspect is highlighted well in [Figure 97](#).

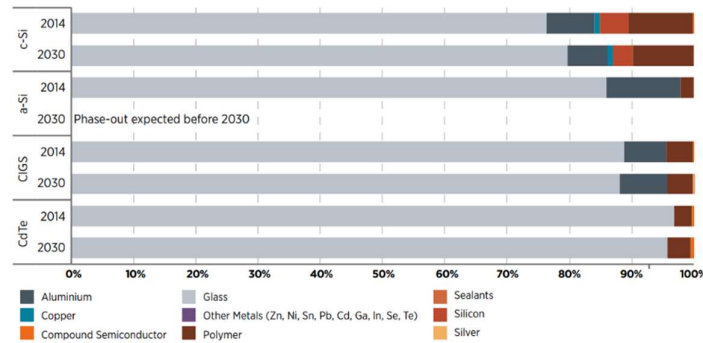


Figure 97. Evolution to 2030 of materials used for different PV panel technologies as a percentage of total panel mass.⁷⁵

c-Si PV panels

By weight, typical c-Si photovoltaic panels today contain approximately 76% glass (which makes up the outermost surface of the panel), 10% polymer (encapsulant and back sheet foil), 8% aluminum (primarily the frame), 5% silicon (solar cells), 1% copper (interconnectors) and less than 0.1% silver (contact lines).

By 2030, the glass content of c-Si panels is expected to increase by approximately 4% to reach 80% by weight of the panel. Significant material savings will include reduced silicon (5% to 3%) and aluminum (1% reduction).

Specific silver consumption will decrease through improved metallization processes and copper or nickel/copper layer replacements.

a-Si PV panels

a-Si photovoltaic panels have lost a significant market share over the last few years. This panel type does not contain significant concentrations of precious or dangerous materials. Therefore, they will likely not take a significant share of the future end-of-life waste recovery and recycling market.

CIGS panels

Today, CIGS panels comprise 89% glass, 7% aluminum, and approximately 4% polymers. The remaining percentage comprises copper, indium, gallium, and selenium. It is expected that by 2030, the percentage of glass will decrease by approximately 1%, in contrast to that of aluminum, which will see an increase of 1%. The polymers will remain stable over time, unlike the remaining metals, which will see a slight reduction of approximately 0.02%.

CdTe panels

Today, CdTe panels comprise approximately 97% glass and approximately 3% polymers. The remaining percentage is made up of semiconductors. It is expected that by 2030, the percentage of glass will decrease by approximately 1%, in contrast to that of the polymeric fraction, which will see an increase of 1% compared to today. The share of other metals (nickel, zinc, and tin) will grow from 0.26% to 0.41%.⁷⁵

The exponential growth of the photovoltaic sector leads to an equally significant growth in the amount of waste generated by these devices at the end of their life. The quantities of this waste generated by the photovoltaic panels sector are in the order of thousands and thousands of ton per year. For further details, see [Appendix A](#).

4.1.4 Recycling Processes

Generally, it is possible to identify three main categories of metallurgical processes for recovering raw materials from end-of-life photovoltaic panels: pyrometallurgical, hydrometallurgical, and bio-hydrometallurgical extraction processes. Pyrometallurgy allows very high recoveries of raw materials but with a notable environmental impact (high emissions of toxic substances). At the other extreme, we find bio-hydrometallurgy, which, although it is the greenest path, still requires consolidation at an industrial level due to a series of problems related to extraction yields and the more incredible difficulty of management compared to the other two technologies. At the center of these two extremes, we find hydrometallurgy. Hydrometallurgical processes have good recovery yields with reduced environmental impacts. **Figure 98** qualitatively summarizes what has just been described.⁵⁹

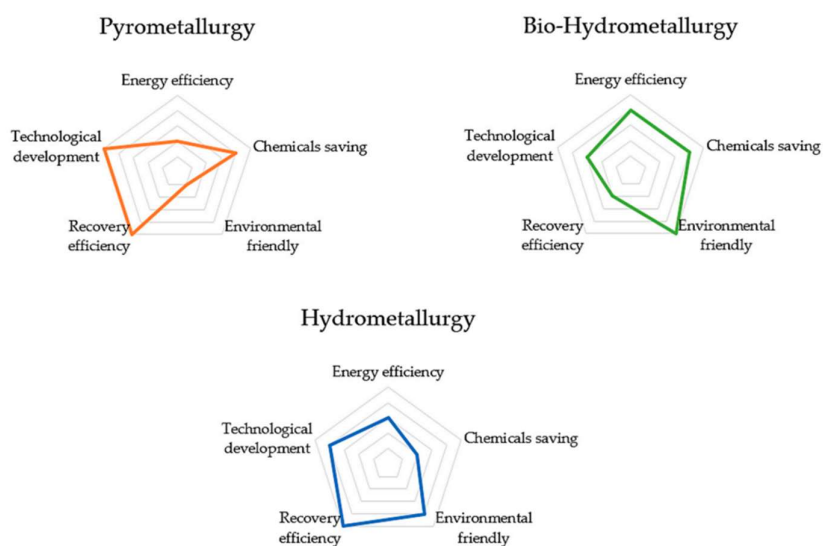


Figure 98. Qualitative comparison between the three major categories of metallurgical processes.⁵⁹

4.2 MATERIALS

Experimental tests were conducted on two samples of ground photovoltaic panel dust to develop, study, and optimize an efficient leaching process for the recovery of silver and silicon. The samples used during the experimental tests were supplied by two companies: Lorusso Estrazione S.r.l. (sample A) and Global Solution S.r.l. (sample B).

Sample A

Sample A consists of a powder obtained by grinding a silver-enriched fraction through initial pretreatments on the panels at the end of their life. Sample B was chemically attacked using aqua regia to favor the dissolution of the metals present. ICP-OES analyzed the solutions obtained, and the composition of the starting solid fraction was determined.

The analyzed ground material has a silver concentration of approximately 5100 ppm. Other substances, such as silicon and glass, are also present in the solid.



Figure 99. Photographic aspect of solid sample A.

Sample A was used to optimize the silver leaching phase of the Gold-REC1 process via the response surface method.

Sample B

Sample B was chemically attacked three times (to establish the average concentration and standard deviation) using aqua regia to favor the dissolution of the metals present. ICP-OES analyzed the solutions obtained, and the composition of the starting solid fraction was determined. The results obtained are reported in **Table 69**.

Table 69. Composition of solid sample.

	I	II	III	Avg.	Dev.St.
Ag	0.17%	0.18%	0.15%	0.17%	0.01%
Al	0.68%	0.68%	0.66%	0.67%	0.01%
Cu	0.28%	0.47%	0.38%	0.38%	0.09%
Fe	0.27%	0.29%	0.29%	0.28%	0.01%
Sn	0.38%	0.43%	0.53%	0.45%	0.08%

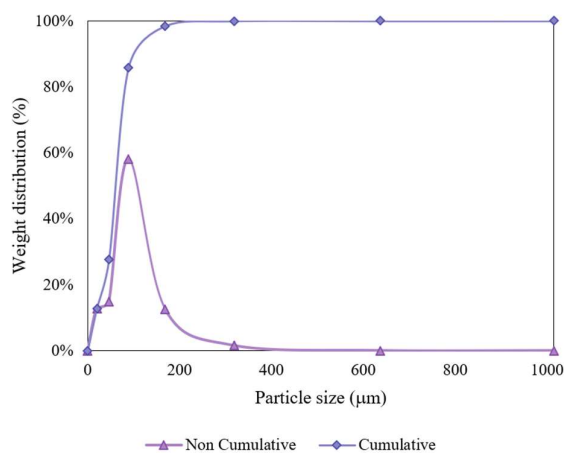


Figure 100. The particle size plot of sample B.

Sample B was used to study the kinetics and leaching mechanisms for the recovery of silver from photovoltaic panels with the Gold-REC1 process. For this reason it was necessary to analyze the granulometry of the sample.

4.3 METHODS

4.3.1 Process optimization

4.3.1.1 Gold-RECI Process for PV panels

The Gold-RECI process was born as a process for the recovery of precious and base metals from WEEE.⁶⁴ During this research activity, it was optimized and studied for the recovery of silver and silicon from spent photovoltaic panel waste. **Figure 101** shows the various steps of the process.

The ground cake is sent to the R101 reactor, where an aqueous solution containing thiourea ($\text{SC}(\text{NH}_2)_2$), sulfuric acid (H_2SO_4), and ferric sulfate ($\text{Fe}_2(\text{SO}_4)_3$) is added. The iron from the oxidation state +3 is reduced to +2, allowing the oxidation of silver with thiourea forming the compound $(\text{Ag}(\text{SC}(\text{NH}_2)_2)_3)^+$. Thiourea also partially reacts with the ferric ion, allowing the formation of formamide disulfide ($\text{C}_2\text{H}_6\text{N}_4\text{S}_2$), which decomposes into thiourea, cyanamide (CN_2H_2), and sulfide (S).

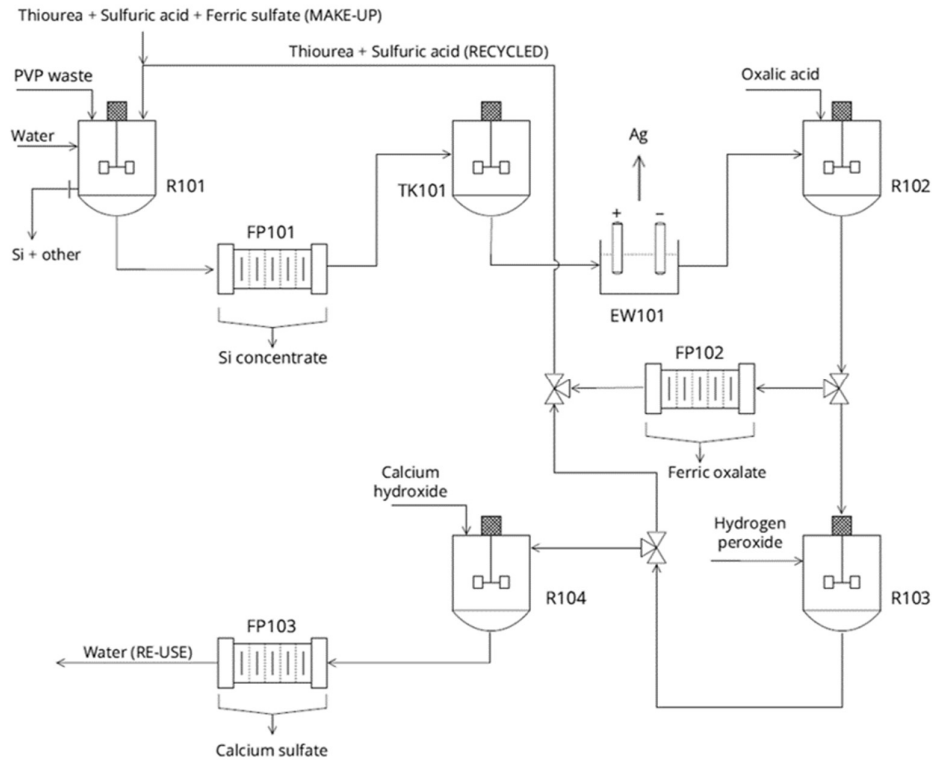
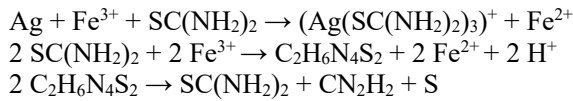
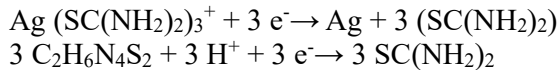


Figure 101. Gold-RECI process diagram for photovoltaic panels.

The leaching of silver follows the following chemical reactions:



The remaining solid Si residue and other components are separated from the leaching solution via the FP101 filter press. The liquid fraction is sent to the TK101 collection tank and to the EW101 electrolytic cells, where the silver present in the solution is recovered as metallic silver on the surface of the cathodes, and the thiourea is regenerated according to the reactions:



The liquid solution from EW101 is sent to the R102 reactor, where the iron in the solution reacts with the oxalic acid and forms iron oxalate. The stream leaving R102 is sent to a second FP102 filter press to remove the precipitated iron oxalate, and the filtered liquid is recirculated to the R101 leach reactor. A purge is provided for the sulfate and ferrous ion accumulated in the system, sent to the R103 reactor, in which the addition of hydrogen peroxide causes the oxidation of the iron ion from Fe^{2+} to Fe^{3+} (reusable in the reactor intended for R101 leaching). The solution from R103 can be recirculated to R101 with a new sulfate purge. This purge is sent to the R104 reactor with calcium hydroxide, in which calcium sulphate is formed which precipitates and, through the FP103 filter press, separates from the solution. The filtrate is mainly water, which can be reused in the R101 reactor.

The products of the process are concentrated silicon, metallic silver, and iron oxalate (for use in other applications). The waste, on the other hand, is the treated water to be reused in the process and the calcium sulfate (to be used in other applications).

4.3.1.1 Procedure

The experimental tests were carried out following a precise operational scheme, the overall duration of which was 3 hours and 45 minutes. Initially, the water with the thiourea is placed in a beaker and left for 10 minutes to allow good solubilization of the thiourea. Using a spatula, add the ferric sulfate and wait another 15 minutes; add the sulfuric acid through a pipette and wait another 20 minutes. Next, add the solid sample and wait 3 hours (reaction time between the leaching reagents and the silver). Finally, the solution is filtered with a vacuum filtration system, obtaining a permeate rich in Ag^+ ions. This liquid solution is then analyzed via ICP-OES to determine the concentration of the ions of interest. Each of the tests was carried out at room temperature and without stirring.

4.3.1.2 Design of Experiments

In many situations, the experimental outputs may be imprecise, and several input factors may be of interest. A Design Of Experiments (DOE) can provide more precise results. The cases of application of the DOE are those in which it is hypothesized that k factors influence the output of a given process, y . Typically, each factor is assigned a small number of levels (for example $\{-1, 0, 1\}$). The choice of DOE depends on how it is possible to optimize the expected amount of information among the various available alternatives. This criterion is often based on the precision or accuracy of the estimated input variables or on the predictions that can be made by the model fitted on the output variable.

A factorial plan with three factors at two levels was used, with three replications at the central point for estimating the experimental error to organize the tests. First, the factors (concentration of sulfuric acid, ferric sulfate, and thiourea) and levels were defined. **Table 70** shows the scheme of the factorial plan. Overall, 11 tests were carried out (2^3+3).

Table 70. Factors and levels of factorial plan.

Level	Factors		
	A – $\text{Fe}_2(\text{SO}_4)_3$	B – H_2SO_4	C – TU
low	0.2 M	0.2 M	10 g/L
central	0.3 M	0.3 M	20 g/L
high	0.4 M	0.4 M	30 g/L

4.3.1.3 RSM

In the RSM, first of all, it must consider the relationship between the output y and each of the factors x_1, x_2, \dots, x_k . If this relationship is not known, an appropriate system model is generated in which we attempt to describe the output or response. The response surface model is usually a first- or second-order polynomial function (linear or quadratic) based on continuous inputs such as temperature and reagent concentration. An appropriate DOE and an adequate analysis constitute the response surface method.

One of the most important features of RSM is the ability to designate experiments sequentially. Initially, when approaching a process, an initial screening can verify the role of each factor and eliminate

the less important ones. In this way, reducing the number of factors studied and the number of experimental runs required is possible.

Likewise, the determined model is used to understand whether the collected data is close to an ideal answer or how far away it is. This aspect allows us to investigate the problem's response space and identify the region of space in which the subsequent experimentation can take place. At this point, a comprehensive factorial plan allows us to develop an overview of the process response. The final factor plane will be centered around the global optimum point. It will be designed to generate the model that most accurately represents the process response in a small space with solid predictive capabilities.

Usually, a low-degree polynomial such as first order or second order is used as the initial model:

$$y=A_0+A_1x_1+A_2x_2 \quad \text{(I-Order Polynomial)}$$

$$y=A_0+A_{11}x_1^2+A_{22}x_2^2+A_{12}x_1x_2+A_1x_1+A_2x_2 \quad \text{(II-Order Polynomial)}$$

These polynomial functions are often good approximations but of small regions of space. In three-dimensional space, the first-order model is represented by a plane, while a surface represents the second-order model. Although the procedure is more straightforward to identify a first-order model, it is often not recommended to stop at it because it could be approximate. The second-order model considers local extrema, making it a more accurate tool for identifying the optimum/minimum point.

However, in the case of II-OP, the number of coefficients is increased, and the number of initial trials needs to be increased to estimate them. Needing more information, the so-called star points are added, identifiable by guaranteeing the Rotability property of the model (Figure 102), which allows you to "rotate" the factorial plane and carry out transformations without losing previous knowledge.^{42,76}

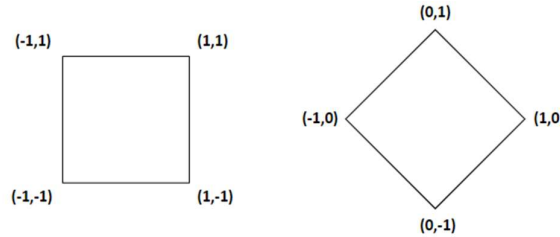


Figure 102. Rotability properties of a factorial plan.

The star points are all equidistant from the center of the model by one distance α (Figure 103). The distance α is calculated using the following relationship:

$$\alpha = \sqrt[k]{2^k}$$

where k is the number of factors to analyze and 2 are the levels with which we analyze each factor.

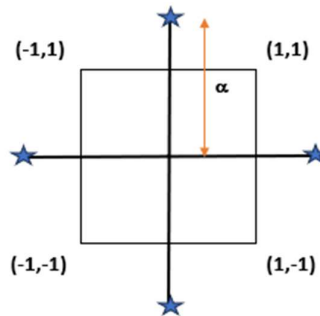


Figure 103. Overlaying star points with a factorial plane.

The geometric meaning of α depends on the number of factors studied. In a factorial analysis of 2 factors on two levels, $\alpha = \sqrt{2}$ represents the radius of a circumference circumscribed on the factorial plane passing through the vertices. The star points described so far refer to the CCC (circumscribed central composite) model, one of the most widespread models because it can keep the original shape of the factorial plane constant. In this case, the star points establish the new extremes for all factors' upper and lower configurations.⁴²

4.3.2 Kinetic Analysis

A kinetic model of a chemical reaction establishes the relationship between the time and the extraction yield of a generic component. It is usually possible to express the extraction yield or a function of the extraction yield with a proportionality relationship with time. In this sense, as time passes, the extraction yield increases. The constant of proportionality is called the kinetic constant and is often denoted by k . This constant is specific to a given chemical reaction and measures the rate at which the reaction occurs. In general, all things being equal, the higher the value of k , the faster the reaction. Since k is the constant of proportionality of a function of yield with time, its unit of measurement is the inverse of time.

Various models based on the conditions under which the reaction occurs describe this relationship. Generally, with heterogeneous reactions such as those of leaching of metals from solid matrices, reference is made to the Shrinking Core Model (SCM) theory.^{10,77}

According to the simplest case of the SCM, the single solid particle is assumed to be spherical. This sphere comprises a layer of non-reactive (or already reacted) material surrounding the nucleus, composed of material that has yet to react. The core reduces size as the reaction progresses, while the outer layer maintains the same diameter. **Figure 104** illustrates this concept for a heterogeneous gas-solid reaction.

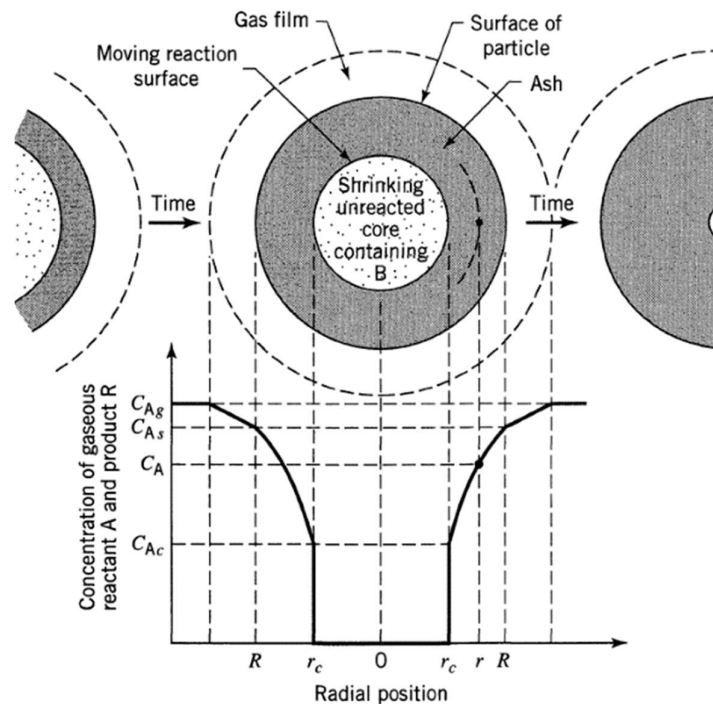


Figure 104. Representation of concentrations of reactants and products for the reaction $A(g) + bB(s) \rightarrow$ solid product for a particle of unchanging size.

Therefore, the kinetics of the process depend on how long it takes for the reactants present in the solution to reach the active site, which corresponds to the nucleus of the solid particles, and on the time it takes for the products to exit the particle. The speed with which this occurs depends mainly on three phenomena:

- the diffusion of the reactants through the fluid film surrounding the external surface of the particle;
- the diffusion through the external layer;
- the reaction kinetics between the liquid and solid reagents.

In particular, if one of these processes is much slower than the others, the reaction is said to be under the control of external diffusion, internal diffusion, or the control of the chemical reaction.

External diffusion control

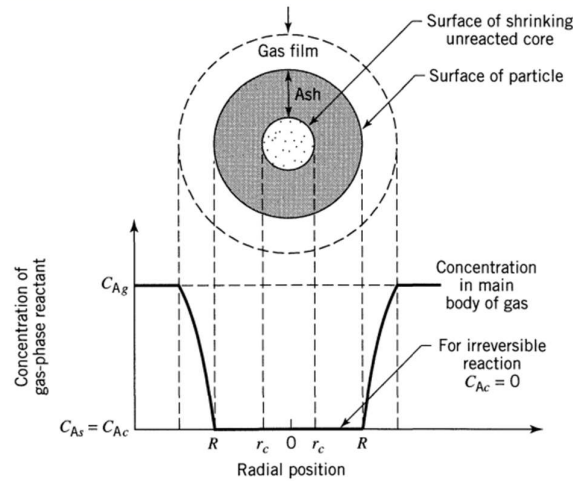


Figure 105. Representation of a reacting particle when external diffusion is the controlling resistance

Model: $X = kt$

Where k is the kinetic constant, t is the time, and X is the fraction of reactant that has been converted into product at time t .

Internal diffusion control

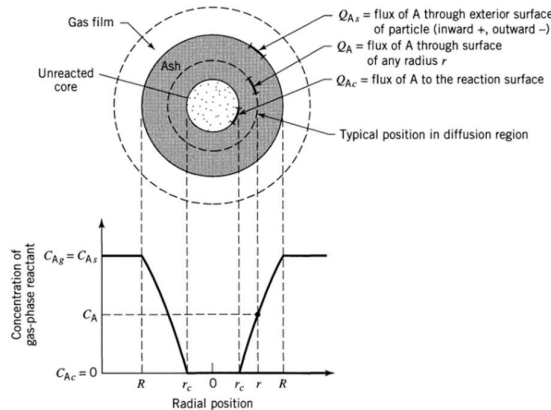


Figure 106. Representation of a reacting particle when internal diffusion is the controlling resistance.

$$\text{Model: } 1 - 3(1 - X)^{2/3} + 2(1 - X) = kt$$

Where k is the kinetic constant, t is the time, and X is the fraction of reactant that has been converted into product at time t .

Chemical reaction control

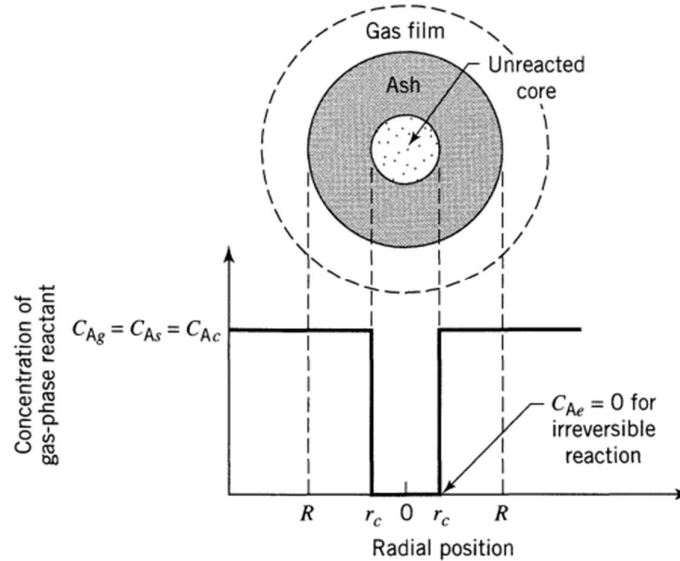


Figure 107. Representation of a reacting particle when chemical reaction is the controlling resistance.

$$\text{Model: } 1 - (1 - X)^{1/3} = kt$$

Where k is the kinetic constant, t is the time, and X is the fraction of reactant that has been converted into product at time t .

All three equations were obtained by assuming the reactant concentration in the solution was constant. This ideal condition approximates the cases where the solid-liquid ratio is very low.

The choice of one of these models is linked to the results obtained from the Analysis of Variance. A factorial plan can be set up with agitation, particle size, and temperature as factors; if agitation is significant compared to the other effects, the process that controls the kinetics is diffusion through the liquid layer. A similar discussion applies to the particle size linked to internal diffusion and the temperature associated with the reaction speed.

The mixing conditions mainly influence the thickness of the liquid film surrounding the particles and the presence of chemical species on the surface of the unreacted nucleus. In general, if agitation is intensified, the extraction rate increases until it reaches a maximum, after which it may decrease. The increase in extraction speed results from good mixing, which consists of the thinning of the liquid film and the increase in the available area of the particles, which facilitates both diffusion and reaction. Conversely, the inefficiency of too intense stirring can be attributed to flow problems (such as the formation of vortices, bubbles, etc.) that retard the diffusion of ions onto the surface of the unreacted nucleus.^{78,79}

The size of the particles is a parameter that affects the extraction speed. A greater surface area is available for smaller particles to interact with the liquid, and the boundary layer is thinner, leading to a faster extraction.⁷⁷

Temperature can influence extraction kinetics in several ways. It can accelerate the diffusion rate, promote the speed of chemical reactions, influence the solubility of compounds (reactants and products),

and change the direction of reversible reactions. In general, the effect of temperature on the extraction rate can be represented by the Arrhenius equation:

$$k = k_0 \exp\left(-\frac{E_a}{RT}\right)$$

Where k is the kinetic constant, E_a is the activation energy, T is the temperature, R is the universal gas constant, and k_0 is the pre-exponential factor.

Depending on the value of the activation energy, the temperature can strongly or weakly influence the extraction rate. The reaction rate is very slow at low temperatures and may be the controlling mechanism. Increasing the temperature increases the chemical reaction's speed more rapidly than diffusion since the activation energy of a chemical phenomenon is greater than that of a physical phenomenon.⁷⁷ As a result, diffusion is much slower than the chemical reaction at high temperatures, and increasing the temperature can lead to a shift from control of the chemical reaction to control of diffusion (both internal and external). The apparent activation energy when under control of the chemical reaction is generally greater than 40 kJ/mol. In comparison, it is less than 20 kJ/mol when the mechanism controlling the kinetics is diffusion. If intermediate values of E_a are obtained, both chemical reaction and diffusion significantly affect the leaching kinetics.⁷⁸

Each of the models described was considered and compared with the others during the interpretation of the experimental data. For the calculation of the E_a and the pre-exponential parameters, the one with the greatest fit compared to the experimental data and which best explains the results obtained on a theoretical level will be chosen each time.

Before starting the tests, a 2³ factorial plan (three factors, two levels) was established. **Table 71** shows the tests carried out with the relative levels.

Table 71. Factorial plan for PV panels kinetic analysis.

Level	Factors		
	A – Stirring rate	B – Particle size	C – Temperature
low	60 rpm	< 53µm	25°C
central	120 rpm	53-125µm	40°C
high	180 rpm	> 125µm	55°C

4.3.2.1 Procedure

The experimental tests were carried out according to a precise setting. A 100 mL solution was prepared for each test with the Gold-REC1 steps already described previously. Once the solution was prepared, 2g of ground and enriched photovoltaic panel powder was added. 1 mL samples were taken at pre-established times to evaluate the silver and silicon concentration over time. Starting from the concentrations determined via ICP-OES, the extraction yield was calculated about the content of the metal of interest in the initial solid.

4.4 RESULTS AND DISCUSSIONS

4.4.1 Process optimization

The ANOVA showed that the Thiourea concentration is the most significant factor in the silver extraction yield. The most significant interaction is between ferric sulfate and sulfuric acid (BC). The results of the ANOVA are shown in **Figure 108**. The effect due to the passage from low to high level of factor A (thiourea concentration) is approximately 56%. The BC interaction positively affects approximately 7% of the recovery yield. These results are because sulfuric acid and ferric sulfate were probably added with appropriate excesses compared to the stoichiometric quantities, unlike the complexing agent, which is far from the optimal concentration. A lack of the complexing agent has a very high effect on the recovery yield, not allowing the stability of the ions in the solution.

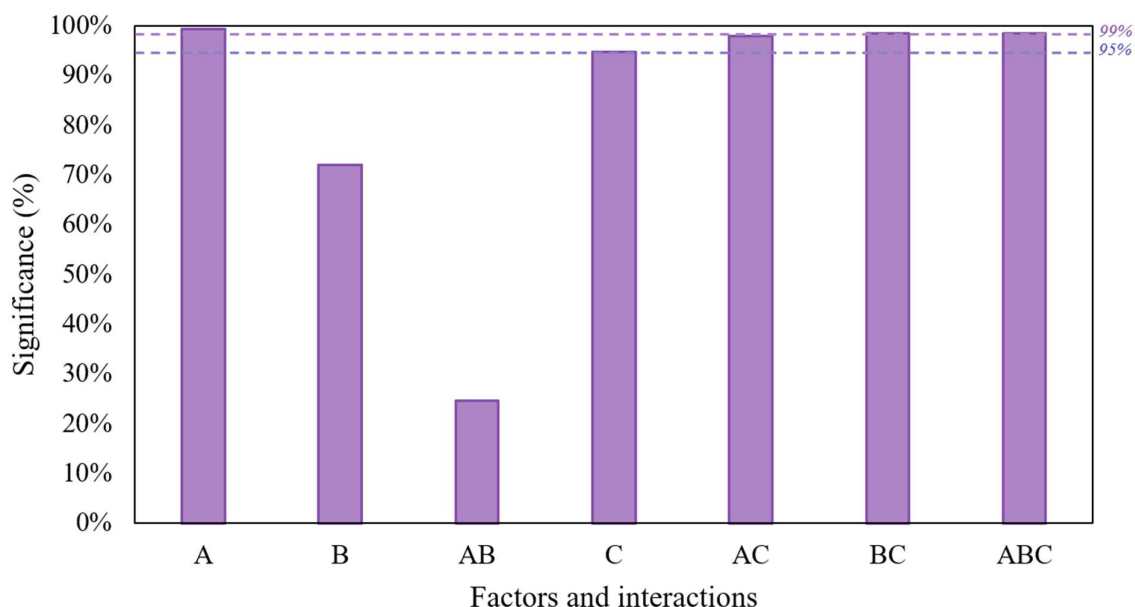


Figure 108. Significance of factors and interactions on silver extraction yields.

To understand the role of thiourea and the other two reagents, the experimental space of investigation was extended by carrying out a new factorial plan with zero concentration of the complexing agent and varying the concentrations of sulfuric acid and ferric sulfate. Furthermore, the influence of temperature was also evaluated. For this purpose, the factorial plan summarized in **Table 72** was created. The table also shows the values of the recovery yields obtained.

Table 72. New factorial plan with silver extraction yields (without Thiourea).

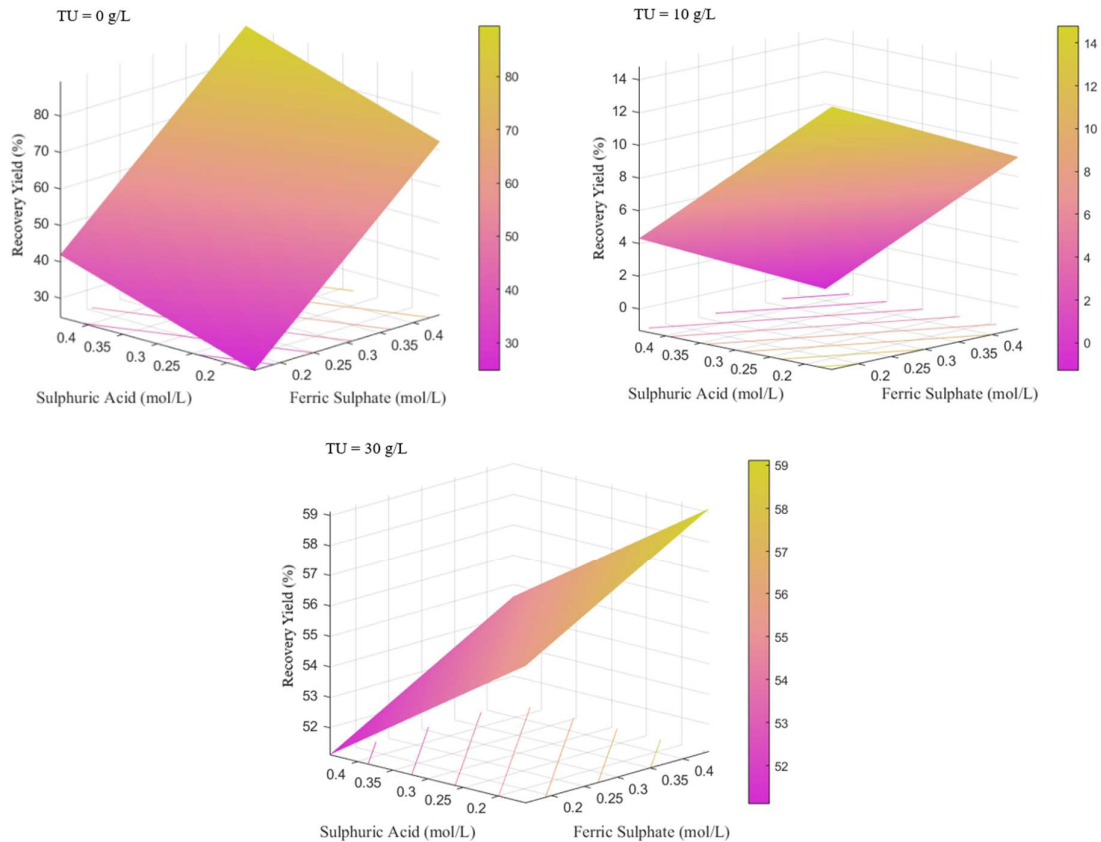
Run	A – Temperature (°C)	B – H ₂ SO ₄ (M)	C – Fe ³⁺ (M)	Ag rec (%)
(1)	25	0.1	0	0.06%
a	50	0.1	0	0.20%
b	25	0.3	0	0.07%
ab	50	0.3	0	0.05%
c	25	0.1	0.4	61.45%
ac	50	0.1	0.4	62.66%
bc	25	0.3	0.4	78.44%
abc	50	0.3	0.4	79.50%
R1	37.5	0.2	0.2	37.62%
R2	37.5	0.2	0.2	36.36%
R3	37.5	0.2	0.2	37.36%

From the recovery yields obtained, the total absence of the oxidant leads to zero silver yield. Temperature does not have a high effect on recovery yield. Finally, the transition from a sulfuric acid concentration of 0.1 M to 0.3 M leads to a significant increase in yield.

With the results obtained from the two factorial plans, polynomial models were created to understand the extraction yield trend better as the different factors vary. In this regard, we moved on to RSM. The results obtained for the I-Order polynomial are reported below. Thiourea was taken as a parameter to visualize the trend of extraction yields with 3D graphs. Variables 1 and 2 mean the concentration of ferric sulfate and sulfuric acid.

Table 73. Parameters of the I-OP surfaces with the related coefficients of determination.

TU	Coefficient	R^2
0 g/L	A_0	-12.2
	A_1	169.9
	A_2	61.2
10 g/L	A_0	24.0
	A_1	-20.0
	A_2	-37.5
30 g/L	A_0	56.2
	A_1	12.5
	A_2	-16.1

**Figure 109.** Response surfaces I-OP for silver recovery yield.

Since the value of the coefficient of determination is very low in the case $TU = 10 \text{ g/L}$ and $TU = 30 \text{ g/L}$, the star points of the CCC model were added to the factorial plan. By doing so, the factorial field is adequately expanded, and further experimental points necessary for the regression with II-Order polynomial are obtained.

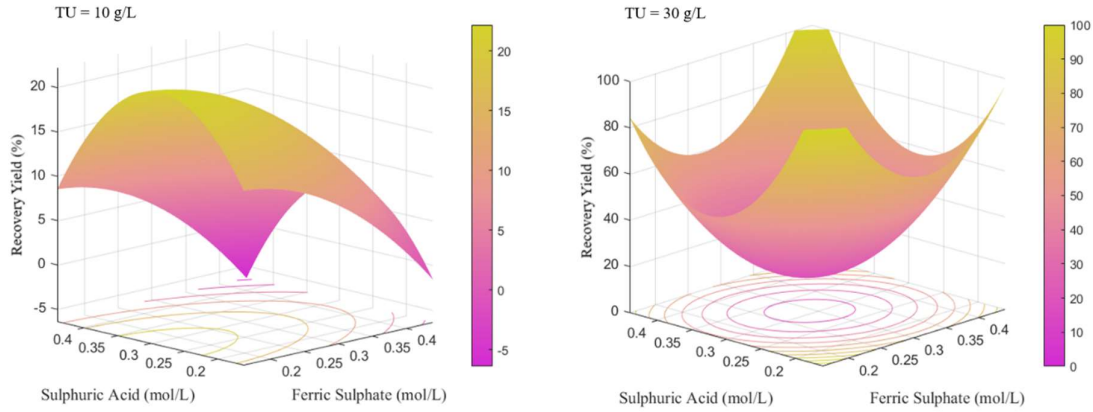


Figure 110. Response surfaces II-OP for silver recovery yield.

Table 74. Parameters of the II-OP surfaces with the related coefficients of determination.

Element	Coefficient	R ²	
10 g/L	A_0	-27.4	
	A_1	49.6	
	A_2	323.2	
	A_{11}	-171.5	0.35
	A_{22}	-567.3	
	A_{12}	0.1	
30 g/L	A_0	495.3	
	A_1	-1414.6	
	A_2	-1767.2	
	A_{11}	2020.1	0.87
	A_{22}	2532.1	
	A_{12}	725.4	

In the case of TU = 0 g/L, the optimal value in terms of silver recovery yield occurs for high concentration values of both reagents; in the case of TU = 10 g/L, it is possible to observe the presence of an absolute maximum in the investigation area. By optimizing the extraction yield, the following optimal operating conditions are determined.

Table 75. Optimal leaching conditions (10 g/L).

Parameter	Value
Ferric Sulphate (mol/L)	0.14
Sulphuric Acid (mol/L)	0.29

In the case of TU = 30 g/L, there is not a single optimal working point but multiple optimal points at the edges of the response surface. For this reason, the optimal working conditions are for low concentrations of reagents, as it is convenient to operate with reduced sulfuric acid and ferric sulfate consumption.

From an economic point of view, by combining the revenue due to the recovered silver and the costs associated with the consumption of reagents, it is seen that the best solution is related to the solution with 30 g/L of Thiourea.

4.4.2 Kinetic results

Before the kinetic analysis, preliminary tests were carried out according to a factorial plan 2³. In the factorial plan created, the following factors were studied:

- A: Stirring rate
- B: Particle size
- C: Temperature

In order to proceed with calculating the recovery yields, the three different particle size fractions used in the factorial plan were characterized. In this way, it was possible to evaluate any effects of grinding on the division of metals into different fractions. **Table 76** shows the results of the three characterizations.

Table 76. Chemical composition of different size fractions.

Size fraction (μm)	Value	Solid composition (%wt.)					
		Ag	Si	Al	Cu	Fe	Sn
<53	μ	0.187%	0.040%	7.000%	0.217%	0.680%	0.583%
	σ	0.060%	0.007%	0.130%	0.027%	0.048%	0.077%
53-125	μ	0.253%	0.025%	0.445%	0.138%	0.149%	0.332%
	σ	0.073%	0.013%	0.018%	0.019%	0.022%	0.106%
>125	μ	0.199%	0.036%	0.972%	1.703%	0.184%	0.594%
	σ	0.019%	0.008%	0.777%	0.644%	0.058%	0.071%

The results obtained were analyzed via ANOVA to establish the effect and significance of the effect of each factor and the related interactions on the recovery yields of the various elements. The ANOVA was performed three times to evaluate better the significance of the effects of factors and interactions throughout the reaction time. The results obtained from this analysis are reported below.

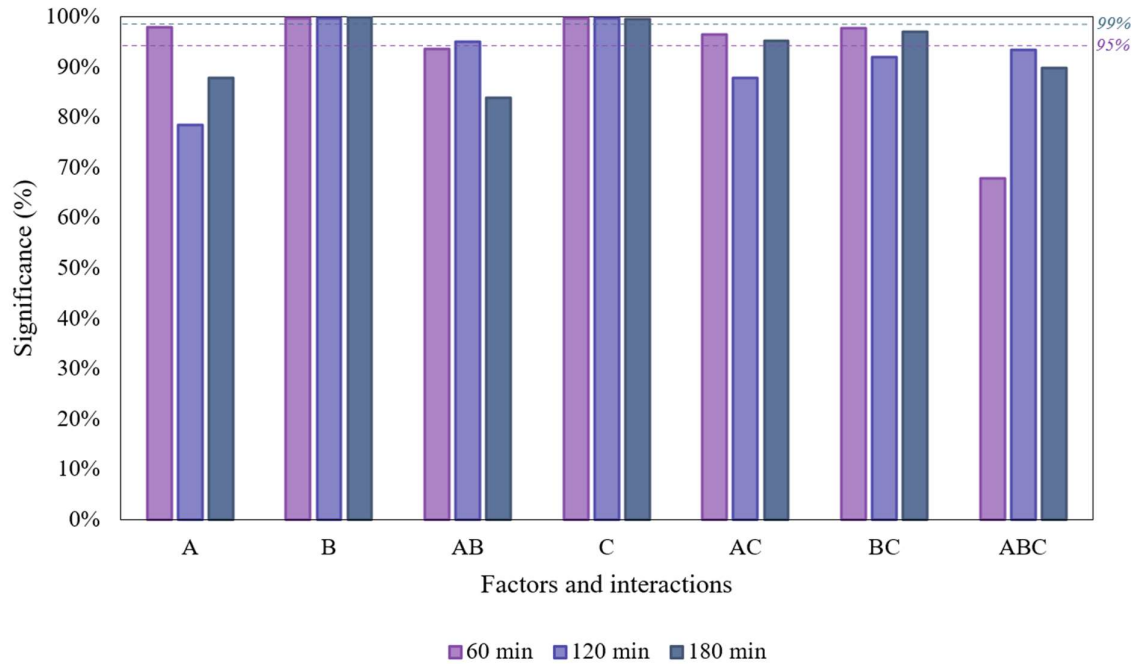


Figure 111. Significance of factors and interactions on silver extraction yields.

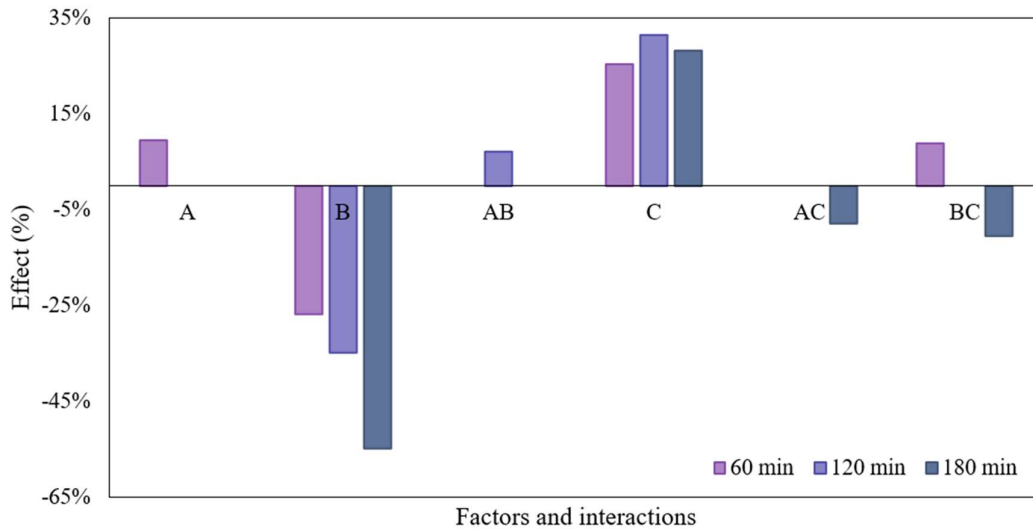


Figure 112. Main factors and their interaction effects on silver leaching.

First of all, it is possible to see how the significance of the effects is very similar for different times. From the ANOVA, the most significant effects are those linked to temperature and particle size. The strong dependence on temperature and particle size suggests that the process may be controlled by chemical reactions or internal diffusion. In particular, an increase in the temperature and a decrease in the particle size positively affects the extraction yield.

It was possible to analyze the trend of silver recovery yields over time through sampling made at pre-established times. Figure 113 shows this trend for the various tests conducted.

The results highlight what was obtained statistically through ANOVA.

The different SCM models were evaluated from the yields obtained to determine the rate-determining step (RDS). In this regard, the kinetic constants and coefficients of determination for the regressions carried out were estimated. Below are the results obtained for each element.

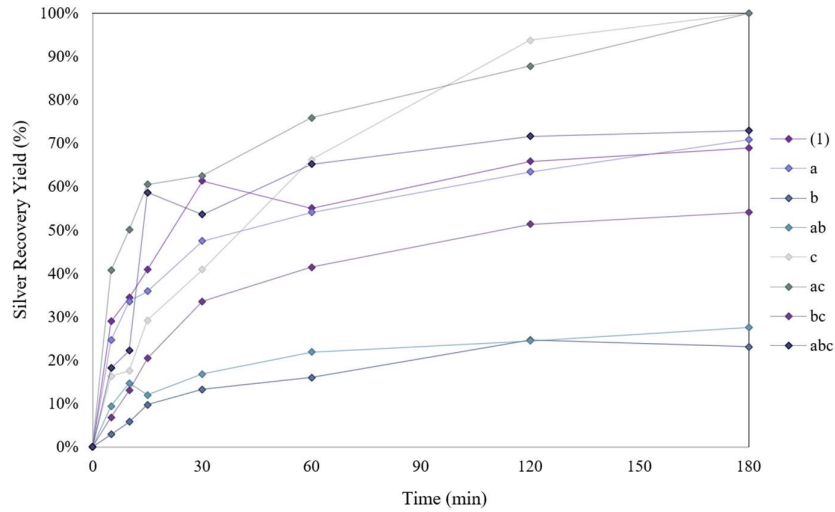


Figure 113. Silver recovery yields vs time for each run of the factorial plan.

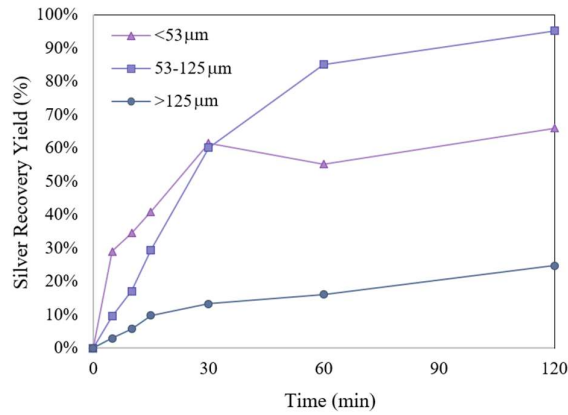


Figure 114. Silver recovery yield for different particle size fractions (Temperature: 25 °C, Stirring rate: 60 rpm).

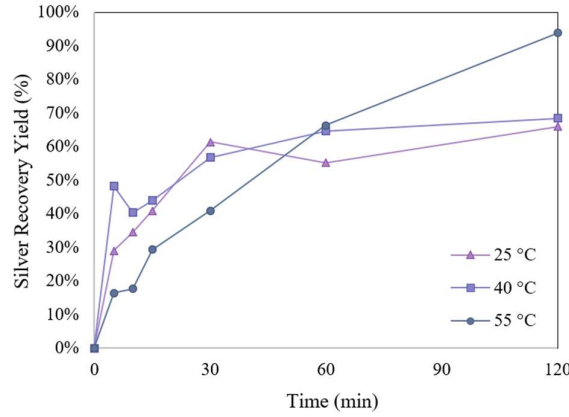


Figure 115. Silver recovery yield for different temperatures (Particle size: <53 μm, Stirring rate: 60 rpm).

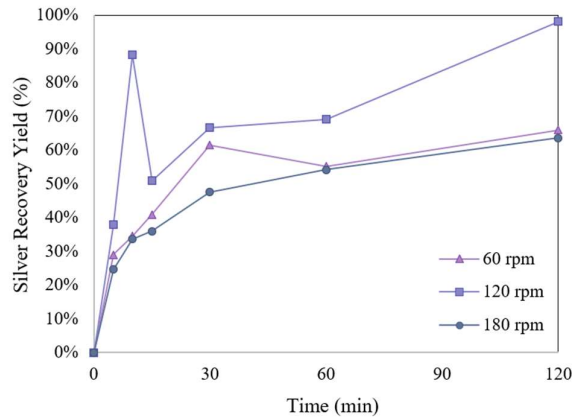


Figure 116. Silver recovery yield for different stirring rate (Particle size: <53 μm, Temperature: 25 °C).

Observing the effect of the particle size variation overtime on the silver recovery yield, it is once again confirmed that the particle size is one of the most influential parameters in the leaching process. In fact, in **Figure 114** the curves appear much further from each other than those reported in **Figure 115** and **Figure 116**.

Table 77. Silver kinetic constants (min⁻¹) and determination coefficients at different run.

Run	x		(1 - x) ^{1/3}		1 - 3(1 - x) ^{2/3} + 2(1 - x)	
	Slope	R ²	Slope	R ²	Slope	R ²
1	0.0051	0.697	0.0023	0.746	0.0017	0.848
2	0.0050	0.760	0.0023	0.825	0.0016	0.956
3	0.0024	0.908	0.0006	0.866	0.0001	0.932
4	0.0020	0.767	0.0007	0.784	0.0002	0.931
5	0.0068	0.910	0.0054	0.997	0.0053	0.984
6	0.0071	0.735	0.0054	0.930	0.0052	0.977
7	0.0039	0.845	0.0016	0.877	0.0009	0.963
8	0.0055	0.717	0.0026	0.764	0.0020	0.848

The results reported in **Table 77** clearly show that the model that best describes the phenomenon considered is internal diffusion to the solid particle. This model has the highest coefficient of determination compared to the other two.

Of the other two models, the temperature control model certainly comes much closer to reality than the external diffusion control model. For further confirmation that the leaching process is under the control of internal diffusion, the activation energy was estimated by linearization of the Arrhenius equation. The order of magnitude of this parameter is an index of the RDS. **Figure 117** shows the graph for estimating the Arrhenius parameters, constructed using the kinetic constants.

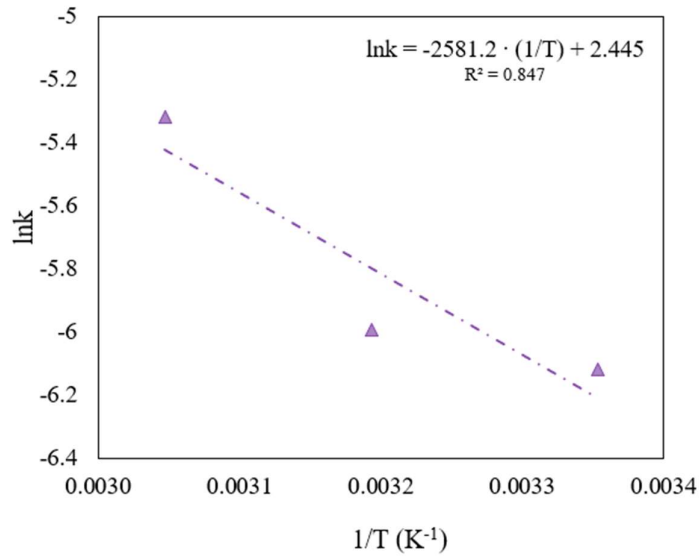


Figure 117. Graph for estimating Arrhenius parameters (Particle size: <53 μm ; Stirring rate: 60 rpm).

The activation energy is approximately 21 kJ/mol. This value, compared with other research, confirms that the internal diffusion phenomenon is the mechanism underlying the leaching kinetics. E_a values lower than 20 kJ/mol suggest that the "rate determining step" (RDS) is diffusion, while for values higher than 40 kJ/mol, the RDS is the chemical reaction. Different mechanisms alternate over time when E_a takes intermediate values to control the process.

Finally, the correlation between the silver extraction yields and those of silicon was evaluated. The latter represents another important raw material, the recovery of which would lead to significant advantages from an economic point of view. Knowing the correlation between silver and silicon would allow us to understand how to separate the two elements (if there was a high correlation) or recover the silicon from the solid residue (if there was a low correlation). **Figure 118** shows the correlation matrix between the two metals of interest.

	Ag	Si
Ag	1	
Si	0.5728	1

Figure 118. Correlation matrix between silver and silicon.

The correlation between the two elements is low. However, as shown in **Figure 119**, silicon extraction yields exceed 30%. This result means that it will be necessary to provide an integrated solution where

the silicon will be recovered from the leaching solution, where it is present with the silver and extracted from the residual solid through a new extraction system.

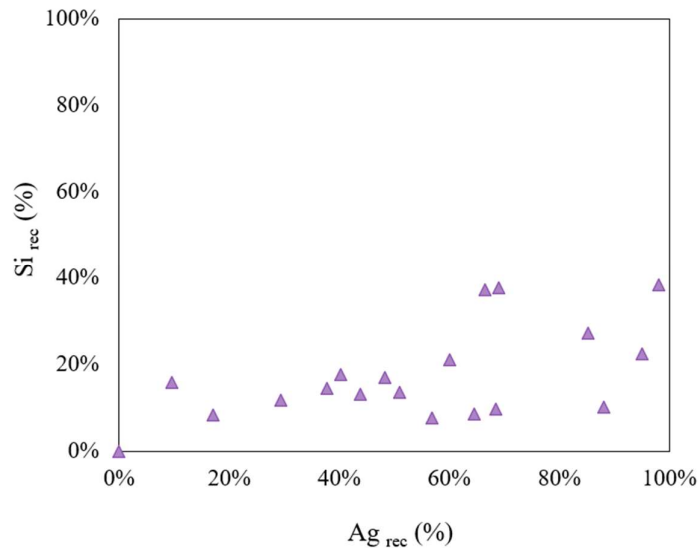


Figure 119. Correlation graph between the recovery yields of silver and those of silicon.

4.5 CONCLUSIONS

The main results obtained during the study and optimization of sustainable recovery processes for valorizing end-of-life photovoltaic panels are reported below.

- Through experimental activity on a laboratory scale, the influence on the leaching process of 3 factors analyzed on two levels was evaluated: thiourea (TU = 10 g/L and TU = 30 g/L), sulfuric acid ($[\text{H}_2\text{SO}_4] = 0.2 \text{ M}$ and $[\text{H}_2\text{SO}_4] = 0.4 \text{ M}$) and ferric sulfate ($[\text{Fe}_2(\text{SO}_4)_3] = 0.2 \text{ M}$ and $[\text{Fe}_2(\text{SO}_4)_3] = 0.4 \text{ M}$). By carrying out the ANOVA test, it was obtained that the main effect of thiourea and the interaction between ferric sulfate and sulfuric acid are the effects with greater significance.
- A leaching system in the absence of thiourea was evaluated to expand the experimental space investigated and better clarify the contribution of each reagent. This way, 3 cases were analyzed: TU = 0 g/L, TU = 10 g/L and TU = 30 g/L. The least squares method identified First-order surfaces that describe the silver recovery yield throughout the investigated plane. The R^2 values obtained were good only for the case without TU. A second-order model was created for the other two cases with very low R^2 values.
- To increase the precision of the model in the cases TU = 10 g/L and TU = 30 g/L, the star points were calculated, which allowed moving from a first-order model to a second-order model. By doing so, it was possible to identify areas of local maximums and minimums.
- From the observations of the three surfaces, it was understood that the maximum silver extraction yield is reached in the case of TU = 0 g/L at high concentrations of sulfuric acid and ferric sulfate. In the case of TU = 10 g/L at the operating point with $\text{Fe}_2(\text{SO}_4)_3 = 0.14 \text{ M}$ and $\text{H}_2\text{SO}_4 = 0.29 \text{ M}$. In the case of TU = 30 g/L at low concentrations of sulfuric acid and

ferric sulfate. By superimposing the graphs of the surfaces obtained, it is possible to continue investigating only the cases $TU = 0$ g/L and $TU = 30$ g/L.

- Through a further factorial plan and a new ANOVA, the mechanisms underlying the leaching of silver from photovoltaic panels were analyzed. It has been seen that the most influential parameters on the silver extraction yield are the temperature and the particle size of the solid material. In particular, it was seen that by increasing the temperature from 25°C to 55°C (all other parameters being equal), the silver recovery yield increased by approximately 30% after one hour of reaction. As regards the particle size, the transition from the low level (<53 μm) to the high level (>125 μm), involves a decrease in the silver extraction yield of approximately 40% after one hour of reaction.
- From the ANOVA results, it is clear that among the phenomena that most influence the kinetics of silver extraction, we find the solid particle's chemical reaction and internal diffusion. Temperature and particle size are the factors that influence the two models.
- Through a more in-depth kinetic study, it was demonstrated that the "Shrinking Core" mathematical model that best approximates the experimental data is the one relating to internal diffusion. Therefore, this diffusion phenomenon regulates the leaching process of the ground photovoltaic panels via the Gold-REC1 process.
- The activation energy of the leaching reaction confirms this result. This value, estimated via regression on the linearization of the Arrhenius equation, is approximately 21 kJ/mol. It is possible to state that the RDS is internal diffusion (below 40 kJ/mol).

5

Permanent magnets

5.1 INTRODUCTION

The definition of a magnet is that of a body that generates a magnetic field. A permanent magnet is a body that has been magnetized, creating its own autonomous magnetic field. All substances react in some way to the presence of a magnetic field, but some materials react more intensely: they are ferromagnetic (or ferrimagnetic) materials. Some examples are iron, nickel, cobalt, rare earth alloys, and some natural minerals such as magnetite. They are materials strongly attracted to a magnet and can be magnetized to create a permanent magnet.

A permanent magnet is, therefore, made of ferromagnetic material magnetized thanks to a very intense external magnetic field and maintains magnetization even when it is no longer subjected to the external magnetic field.

To understand what happens inside a permanent magnet, we need to go down to the level of the particles that make up the substances. Each particle has its magnetic field, established by the so-called spin. Usually, however, the spins "point" in different directions; therefore, at a macroscopic level, they cancel each other out. In permanent magnets, however, there is a "long-range" ordering of the spins because the particles interact. The greater the "order" created between the particles' spins, the greater the magnetic field generated by the permanent magnet.

Permanent magnets are one of the critical components of electric car motors.

They are used in many industrial sectors; in particular, sintered neodymium (NdFeB) magnets are the most widespread on the market.

The most common permanent magnets are samarium-cobalt magnets, aluminum-nickel-cobalt (AlNiCo) magnetic materials, and neodymium-iron-boron magnets.

As already anticipated in Chapter 1, many REEs can present a ferromagnetic behavior in certain thermal conditions, with Curie points⁴ usually lower than room temperature. However, alloying with iron and some transition metals such as cobalt and nickel leads to intermetallic compounds that have a curie temperature much higher than room temperature and retain the notable uniaxial crystalline anisotropy typical of rare elements. The latter is related to the exchange interaction at the level of the 4f shell and largely extends on an atomic, rather than lattice, scale. For this reason, in the literature, it is preferred to cite the expression "single-ion anisotropy" for ferromagnetic intermetallic compounds containing REEs.⁸⁰

⁴ In fisica e in scienza dei materiali, la temperatura di Curie o punto di Curie, è la temperatura al di sopra della quale alcuni materiali perdono le loro proprietà magnetiche permanenti, che possono (nella maggior parte dei casi) essere sostituite dal magnetismo indotto.

Technological progress and growing demand on a global scale have oriented research towards increasingly lighter, mechanically resistant, and corrosion-protected devices through appropriate coating techniques for metal layers, especially nickel and copper. According to the most recent and ordinary meaning, permanent magnets can be divided into three main categories based on their composition:

- to first-generation samarium (consisting of the compound SmCo_5) or to second-generation samarium (having the generalized formula $\text{Sm}_2\text{Co}_{17}$);
- aluminum-nickel-cobalt (AlNiCo);
- neodymium (formed from the $\text{Nd}_2\text{Fe}_{14}\text{B}$ alloy, more commonly abbreviated with NdFeB).

First-generation samarium magnets (SmCo_5)

The first samarium magnets marketed on a large scale comprise a compound with a hexagonal crystalline structure, with the formula SmCo_5 . The magnetic performance of the material remains almost unchanged up to temperatures of around 500 °C. A further advantage lies in the fact that this material does not contain high quantities of critical rare earths, such as dysprosium, from the supply point of view. However, samarium magnets are typically very fragile, which must be considered in the design as it severely limits their final volume and shape.

The production process consists of melting, casting, and solidifying the constituents, phases followed by grinding the material to obtain single-crystalline particles with an average diameter of approximately 10 μm . Subsequently, the powder obtained is subjected to a magnetic field capable of aligning the easy magnetization axes of each particle according to the flow, an operation usually performed simultaneously with compaction in a mold of a suitable shape.

The final sintering at temperatures above 1000 °C allows the finished magnet to be obtained. In order to further improve the magnetic performance, a specific quantity of powder containing excess samarium and low melting temperature at the sintering temperature is added before the heat treatment. The process, therefore, takes place in the presence of a liquid phase.

Unlike other types of permanent magnets widely available on the market, the SmCo_5 compound has the notable advantage of being magnetized with applied fields much less intense than its intrinsic coercivity, with consequent savings in production costs.⁸⁰

Second-generation samarium magnets ($\text{Sm}_2\text{Co}_{17}$)

Magnets formed from the $\text{Sm}_2(\text{Co}, \text{Fe}, \text{Cu}, \text{Zr})$ family of alloys fall under the generalized notation $\text{Sm}_2\text{Co}_{17}$. These materials have a very fine particle microstructure formed by bands of SmCo_5 crystals that separate regions of these particular alloys. Unlike first generation samarium magnets, a much larger field must be applied to magnetize it.

The manufacturing cycle is similar to SmCo_5 devices, except for the complex heat treatment required to obtain the desired microstructure. Following the advent of samarium magnets obtained by casting, innovative industrial processes were developed to produce powders made up of compounds containing REEs and transition metals starting from REO oxides. For example, samarium oxide is reduced with calcium in the presence of cobalt. Alternatively, the marked tendency of rare earths to absorb hydrogen gas at ambient pressure and temperature can be exploited, with consequent microstructural variations that induce the subsequent pulverization of the material following the substantial lowering of pressure, which in turn is necessary for the expulsion of H_2 from the solid. This technique is called hydrogen decrepitation (in permanent magnet recycling technologies).

Although they are still exploited today for low and high-temperature applications, Sm-Co magnets are not generally used in renewable energy technologies.

Despite their intrinsic mechanical fragility, Samarium-Cobalt magnets remain irreplaceable where constant performance at high temperatures is required and where high salinity and humidity are present in the air. They guarantee a consistency of performance not found in any NdFeB grade in the various operating conditions.⁸⁰

Aluminium-nickel-cobalt magnets (AlNiCo)

AlNiCo magnets are permanent magnets composed of an aluminum-nickel-cobalt alloy. Other metals such as iron, copper, or titanium are often added to this alloy, allowing it to take on even more attractive properties. Mixing these metals and the manufacturing process make these magnets truly super permanent. Among these, a distinction is also made between isotropic and anisotropic magnets, which can have different magnetic remanence or coercivity values.

AlNiCo magnets can withstand temperatures around 500°C without losing their magnetic properties. They present a high-temperature resistance (250-350°C), while neodymium magnets can only be used up to 200 °C.

Furthermore, AlNiCo magnets are corrosion-resistant for most acids, solvents, and oils, thanks to the alloy's high nickel content. Since AlNiCo magnets are rigid and brittle, they cannot be cut but can be ground. Due to their properties, AlNiCo magnets are used everywhere, thanks to the material's resistance to high temperatures. They are ideal magnets for sensors, magnetic switches, motors, measuring devices, etc.

AlNiCo magnets are permanent magnets made through a melting or sintering process. The raw elements obtained are subjected to precipitation hardening to obtain homogenization of the phases. CoFe magnetic needles are present inside the AlNi grid. If an electromagnetic field is applied during the formation phase, the CoFe needles align with it; in this case, the magnet is considered an anisotropic magnet that can only be magnetized in one direction. If the phase formation process occurs without an electromagnetic field, the CoFe needles align as desired.⁸¹

Magneti al neodimio (NdFeB)

A neodymium magnet is made of a highly magnetic, silvery-white alloy of boron, iron, and neodymium, fragile and easily damaged. Since the material is very delicate and the power is so high, it often happens that these splinter each other, especially if they collide uncontrollably.

There are neodymium magnets of different grades: the grade is a code that always starts with the letter N (abbreviation of neodymium) and is followed by two digits (e.g., N27, N30, N33, N35, N38, N40, N42, N45, N48, N50) and indicates the energy product. The higher the quality of the magnetization, the higher the energy product and, therefore, the adhesive strength. A suffix consisting of one or two letters of the alphabet, which sometimes follows the number (H, M, SH, EH, UH, etc.), indicates the so-called Curie temperature, upon reaching which the magnets demagnetize irreversibly.

There are magnets on the market with grades between N24 and N55; however, grades higher than N52 are not easily available; in the laboratories, it is possible to create N56 grade magnets, while N64 is the theoretical limit.

Thanks to the special NdFeB (Neodymium-Iron-Boron) alloy, it is possible to achieve a high attraction force starting from small dimensions. For this reason, neodymium magnets are defined as Supermagnets and are also known as high-performance magnets.

An essential characteristic of neodymium magnets is the use temperature of the material, which remains much lower; also for this reason, as well as for the raw material, neodymium is a rare earth metal, and these super magnets are much more expensive than conventional ferrite ones.

Small and light but extremely powerful, super-magnets are currently widely used in the industrial sector. They are used in constructing electric motors or as blocks in the modeling world. In short, among the advantages of using neodymium permanent magnets, it is possible to find:

- super powerful attraction force;
- suitable in case of limited space (miniaturization);
- smaller neodymium magnets are already as powerful as more giant conventional ferrite magnets.

In addition to the three main alloying elements, a low percentage of dysprosium (2-4%) is usually also present to increase the resistance to demagnetization in opposition to the increase in temperature. Although dysprosium has one of the highest magnetic moments of the REEs, it is still not an element capable of completely replacing neodymium in the alloy.

Similarly, the reasons for the success linked to the commercialization of NdFeB magnets are based, above all, on economic, practical, and technological aspects. Introducing iron and neodymium alloys to replace samarium (and partly cobalt) makes obtaining a much less expensive product possible.

Furthermore, these magnets have a higher mechanical resistance, extending their applicability because of the larger dimensions and more complex shapes obtainable with classic production techniques. In this regard, maintaining a production cycle similar to that envisaged for manufacturing other intermetallic materials and compounds has allowed a rapid introduction of NdFeB devices linked to ferromagnetics in the global panorama.⁸⁰

The applications of neodymium supermagnets, whether rectangular, ring-shaped, or cylindrical, are extremely diverse. It is undoubtedly suitable wherever strong magnetic fields are needed. Thanks to their characteristics, they can be used in a versatile way. Some of the standard applications of earth magnets are:

- Engines and Generators
- Wind generators
- Magnetic adhesion systems
- Semiconductor technology (Hall) (as a generator magnet)
- Filter systems
- Message boards
- Improvement in vehicle consumption
- Meters
- Automotive (clamps, sensors)
- Aerospace
- Separation (bars, grids)
- High-performance magnetic clamps and pot magnets
- They are used in computer hard drives
- Rare earth magnets also find their utility in high-end speakers

With the energy transition promoted by numerous states, the demand for permanent magnets is experiencing exponential growth. This growth leads to generating a large amount of end-of-life device waste. This waste represents the most important secondary source of REEs. **Appendix A** reports the study on the market analysis conducted for end-of-life permanent magnets

5.1.1 Recycling processes

Over the last few years, numerous solutions have been developed to recover rare earths from end-of-life permanent magnets. The recovery methods commonly used to recover REEs generally belong to three broad areas: pyrometallurgical, hydrometallurgical, and bio-hydrometallurgical processes. Pyrometallurgical methods are usually suitable for recovering rare earths from devices when they are present in high concentrations. These processes usually require a lot of energy and produce various by-products that harm humans and the environment.

Bio-hydrometallurgy uses organisms sensitive to operating conditions such as pH and temperature; consequently, this process is difficult to control. In comparison, hydrometallurgical processes offer the advantages of working at low temperatures and being easily manageable. As a result, hydrometallurgical processes have been extensively studied and widely used. To date, they indeed represent the most promising path. **Figure 120** shows a diagram of the most used technologies for recovering REEs from different types of waste.⁸²

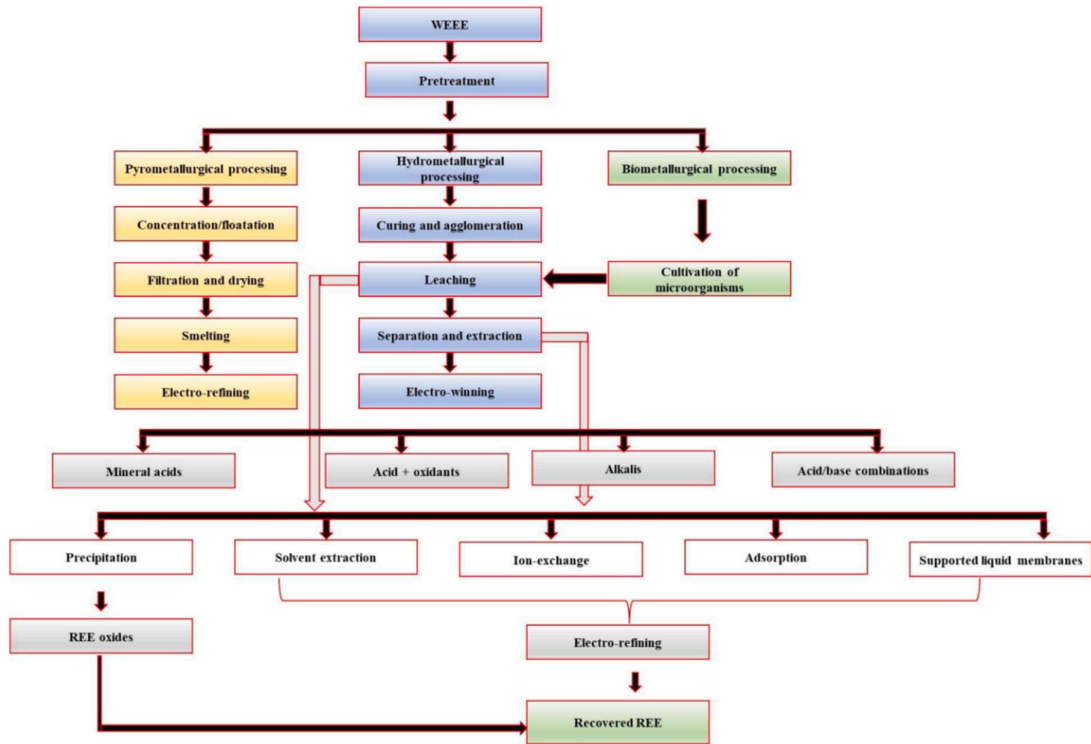


Figure 120. Hydrometallurgical, pyrometallurgical, and biometallurgical processes for the recovery of REEs.⁸²

5.2 MATERIALS

An Italian company provided the sample during the various laboratory-scale experimental tests. It represents a waste from treating end-of-life permanent magnets through hydrogen decrepitation and has the same chemical composition as the starting permanent magnet. **Figure 121** shows the photographic appearance of the sample.



Figure 121. Photographic aspect of permanent magnet sample.⁸³

Through a chemical attack with aqua regia (HCl + HNO₃, in a molar ratio of 3:1), it was possible to determine the chemical composition of the starting material. **Table 78** summarizes the weight percentage of the metals of interest.

Table 78. Mass composition of the PM sample.

	B	Fe	Pr	Tb	Dy	Nd	Other
μ (wt.%)	0.91%	56.80%	4.21%	0.33%	2.92%	21.17%	13.66%
σ (wt.%)	0.003%	0.426%	0.045%	0.036%	0.359%	2.454%	

As can be seen from the data resulting from the experiments, in the material analyzed, there are considerable concentrations especially of iron, at 56.8%, and neodymium, at 21.2%, followed by praseodymium with 4.2%, dysprosium with almost 3%, boron with almost 1% and terbium with 0.33%. A solid residue was noted during the chemical attack, which may be due to the presence of plastic material. This fraction falls within the "Other" category.

Granulometric analysis was carried out on this sample using the sieve method, the results of which are shown in **Figure 122**. Based on the quantity of solid available for each diameter range, it was possible to determine the levels of the factorial experimentation aimed at determining the influence of the particle size on the recovery yield.

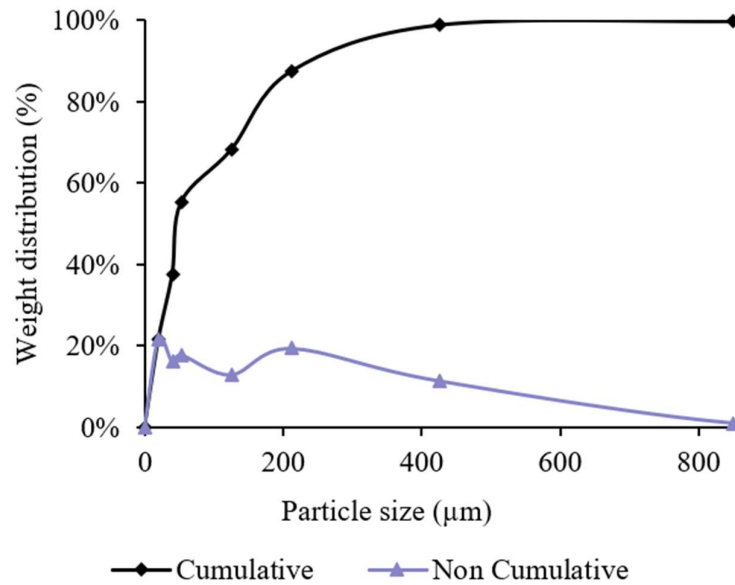


Figure 122. The particle size plot of PM sample.

Through the study conducted, it was seen that the analyzed sample has an average diameter of solid particles of approximately 190 μm .

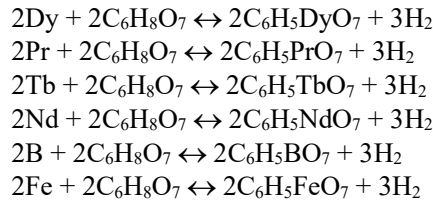
5.3 METHODS

5.3.1 Process optimization

5.3.1.1 Hydro-Nd Process

The process that will be studied and optimized is the Hydro-Nd process, patented by the University of L'Aquila.⁸⁴ This hydrometallurgical process allows the selective recovery of REEs, iron, and boron from end-of-life permanent magnets. **Figure 123** shows the simplified block diagram of the process.

The permanent magnets are sent to an oven for the thermal demagnetization phase at approximately 400°C. The oven is powered by the hydrogen produced in the extraction phase, described below. Once demagnetized, the magnets are removed from the rotors and subjected to a grinding process. The granulate is then introduced into the reactor, where the REEs, iron, and boron contained in the demagnetized powders are leached with a citric acid solution. The following oxidation-reduction reactions are involved in the process:



In the overall chemical reaction, in addition to the solubilization of REEs (Nd, Pr, Dy, Tb), boron, and iron, H₂ is developed, which is extracted from the reactor and sent to the demagnetization furnace to be used as a green fuel.

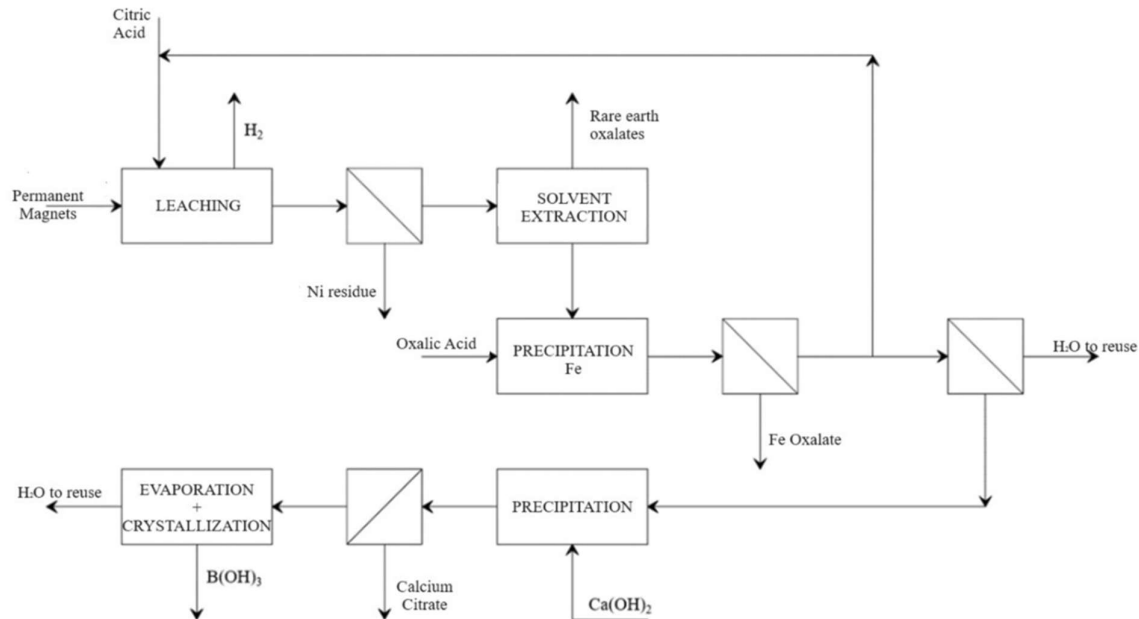


Figure 123. Simplified block diagram of the Hydro-Nd process.

The solution containing the solubilized chemical elements, such as citrates, is sent to a filter press, where the residual solid is separated from the solution containing the REEs. The residual solid consists of a concentrate of metallic nickel with a percentage greater than 70%. Third parties then valorize this fraction according to the typical circular economy criteria. The filtered solution is sent to the solvent extraction section. The rare earths from the aqueous solution pass into the organic phase (consisting of n-heptane), thus separating the rare earths from the iron citrate. Once separated by decantation, the organic extract (organic phase) extracts the REEs while the refined (aqueous phase) remains rich in iron citrate in solution and excess citric acid.

The process at this point is divided into two parallel lines:

- Iron recovery line and citric acid regeneration line
- REEs recovery line

Line A passes into a reactor where oxalic acid is added, which causes the iron to precipitate as iron-oxalate. Once filtered, the solution mainly contains citric acid, which is reused for the extraction described previously. More than 90% of the citric acid is recycled, while the water will be partly reused as process water and partly sent to a treatment plant. A purge is sent to the citrate precipitation section via $\text{Ca}(\text{OH})_2$. Other purges containing mainly phosphoric acid are also conveyed in this section. The neutralization reaction will then produce calcium citrate and phosphate concentrate, which will be used as fertilizers.

Line B involves sending the organic phase into a mixer-settler, thus coming into contact with an aqueous solution of H_3PO_4 . Rare earths are extracted into the aqueous phase and precipitate as insoluble phosphates. After separating the rare earth phosphates, the organic phase is reused in the solvent extraction process. In contrast, the aqueous phase containing residual H_3PO_4 is partly reused for a subsequent stripping phase and partly sent to the citrate precipitation section for the neutralization with lime, resulting in precipitation of Ca-phosphate, as previously described. The solid phase rich in rare earth phosphates is sent to a reactor, in which the phosphates are transformed into rare earth oxalates by adding oxalic acid. The rare earth concentrate, in the form of oxalates, is recovered by filtration.

5.3.1.1 Procedure

In order to optimize the extraction of the elements of interest from the starting sample, several experimental tests were carried out (the details of each test were established according to a factorial plan reported below). The experimental procedure was implemented in this way:

- The reagents and the sample were weighed.
- The quantity of water necessary was measured.
- The material of the single test was inserted into a flask left on the stirrer at 150 rpm at room temperature for the time established by the factorial plan.

At the end of the time established for the test, the solution obtained was filtered thanks to a vacuum filtration system to separate the solid phase from the liquid one. The solution is analyzed via ICP-OES to quantify the content of metals present in the solution.

5.3.1.2 Design of Experiments

A factorial plan with three factors at two levels was used, with three replications at the central point for estimating the experimental error to organize the tests. First, the factors (concentration of sulfuric acid, ferric sulfate, and thiourea) and levels were defined. **Table 79** shows the scheme of the factorial plan. Overall, 11 tests were carried out (2^3+3).

Table 79. Factors and levels of factorial plan.

Level	Factors		
	A – Citric Acid	B – Time	C – Solid/Liquid ratio
low	1 M	1 h	10%
central	2 M	2 h	15%
high	3 M	3 h	20%

5.3.1.3 RSM

The factorial plan reported above, implemented with star points as already described in chapter 4.3.1.3, was used to determine polynomial models. First, a first-order polynomial model was used to describe the extraction yield of the metals considered as a function of the three factors of the plan. Subsequently, a second-order polynomial was also used. For each of the surfaces created, the coefficient of determination was calculated to have an idea of the goodness of the regression.

5.3.2 Kinetic Analysis

Before starting the tests, a 2^3 factorial plan (three factors, two levels) was established. **Table 80** shows the tests carried out with the relative levels.

Table 80. Factorial plan for kinetic analysis.

Level	Factors		
	A – Stirring rate	B – Particle size	C – Temperature
low	60 rpm	< 53 μ m	25°C
central	120 rpm	53-212 μ m	50°C
high	180 rpm	> 212 μ m	75°C

5.3.2.1 Procedure

Each leaching test involves a series of samplings carried out at certain pre-established times from the beginning of the experiment. For each treatment, 100 mL of 1 M citric acid solution was used in which 1 g of solid was reacted (1% S/L ratio). Such a low percentage of the solid-liquid ratio was chosen to ensure that the concentration of the reagents was constant throughout the test. This aspect allows us to use all the SCM's integral relations without starting from the differential equation of the material balance around a generic solid particle.

Below is the procedure carried out for each treatment. 21.014 g of citric acid monohydrate in powder form is mixed with 100 mL of distilled water in a flask. The flask is inserted into the Dubnoff stirrer and brought to the process temperature. 1 g of solid is then inserted, and the treatment level establishes the particle size. Each sampling carried out at the established time is first filtered with a filter and then set aside to be analyzed later. In this discussion, for the calculations carried out, the reduction in volume due to the sampling was assumed to be negligible (1 mL of solution each). At the end of the test, the solution is filtered using a vacuum pump, then the acid solution and the retained solid are disposed of appropriately.

Once the tests have been carried out and analyzed at the ICP-EOS, we proceed with the analysis of variance to determine the effects and their significance. We then proceed to calculate the kinetic constants. With time, the extraction yield function is graphed using one of the SCM models. Straight lines whose slope is the kinetic constant k are obtained. Reference is made to the coefficient of determination of these regressions to estimate the reliability of these parameters. We then calculate the activation energy and the pre-exponential parameter, graphing the temperature with the kinetic constants obtained.

5.4 RESULTS AND DISCUSSIONS

5.4.1 Process optimization

Through the analysis of the samples performed with ICP-OES, it was possible to measure the concentration of rare earth metals in the leaching solution (LL) and the cake-washing water (WW). **Table 81** shows the results in terms of concentrations.

Table 81. Concentration of metals in solutions after leaching.

Run	Volume [mL]	Concentration (ppm)						
		Nd	Pr	Dy	Tb	Fe	B	
1	LL	55	3877	1737	442	69	12327	193
	WW	15	1059	461	126	21	4549	78
2	LL	70	2527	1034	292	35	6377	92
	WW	15	1150	468	137	20	4272	67

3	LL	54	8603	2868	1039	164	30070	436
	WW	16	1809	589	215	31	8856	115
4	LL	68	8731	2565	1116	160	29277	395
	WW	17	2910	760	398	54	16942	139
5	LL	55	6324	2551	710	90	19905	279
	WW	15	1914	738	233	29	7352	127
6	LL	68	7971	2635	913	107	24198	334
	WW	15	3655	1464	422	79	16467	236
7	LL	54	10983	3242	1273	152	17909	260
	WW	16	325	1029	41	51	6825	90
8	LL	68	15915	4093	2005	225	19829	323
	WW	16	5725	1690	843	103	10742	149
9	LL	58	9678	3356	1163	175	33964	481
	WW	16	4845	1216	616	71	13996	220
10	LL	58	10163	3301	1237	176	34823	492
	WW	16	2738	959	334	56	12967	189
11	LL	60	8386	3155	1016	162	32000	459
	WW	15	3095	894	393	52	11430	171
12	LL	59	11539	3343	1320	175	36222	511
	WW	15	4211	1097	539	64	13915	206

In the experimental procedure, the volume of washing water was calculated to be 30% of the volume of the aqueous solution used for leaching. to determine possible relationships between them. For this purpose, a correlation matrix was created, shown in **Figure 124**. The correlation matrix is a square matrix, which shows the correlation coefficients between pairs of variables. Ultimately, it is a table that allows us to evaluate the degree of interdependence of a series of quantities, in this case, the concentrations of individual elements in solution.

	Nd	Pr	Dy	Tb	Fe	B
Nd	1					
Pr	0.959	1				
Dy	0.995	0.942	1			
Tb	0.963	0.967	0.963	1		
Fe	0.780	0.837	0.758	0.856	1	
B	0.817	0.874	0.794	0.885	0.985	1

Figure 124. Correlation matrix between the concentrations of the elements in solutions.

As can be seen from the matrix, the concentrations have a reasonable degree of correlation with each other. This result is because some elements behave similarly in the leaching environment examined. In particular, it is possible to note the high correlation index between the analyzed lanthanides: neodymium, praseodymium, dysprosium, and terbium, which instead present a somewhat different behavior compared to the other elements, iron, and boron. The two different categories are linked to the position of the elements on the periodic table.

It is also possible to visualize this degree of relationship thanks to the graphs shown in **Figure 125**. From the graphs, we obtain confirmation of the results obtained from the correlation matrix: the elements best correlated with each other are dysprosium and neodymium, and while neodymium maintains a good correlation with terbium and less so with praseodymium, iron, and boron prove to be well correlated with each other.

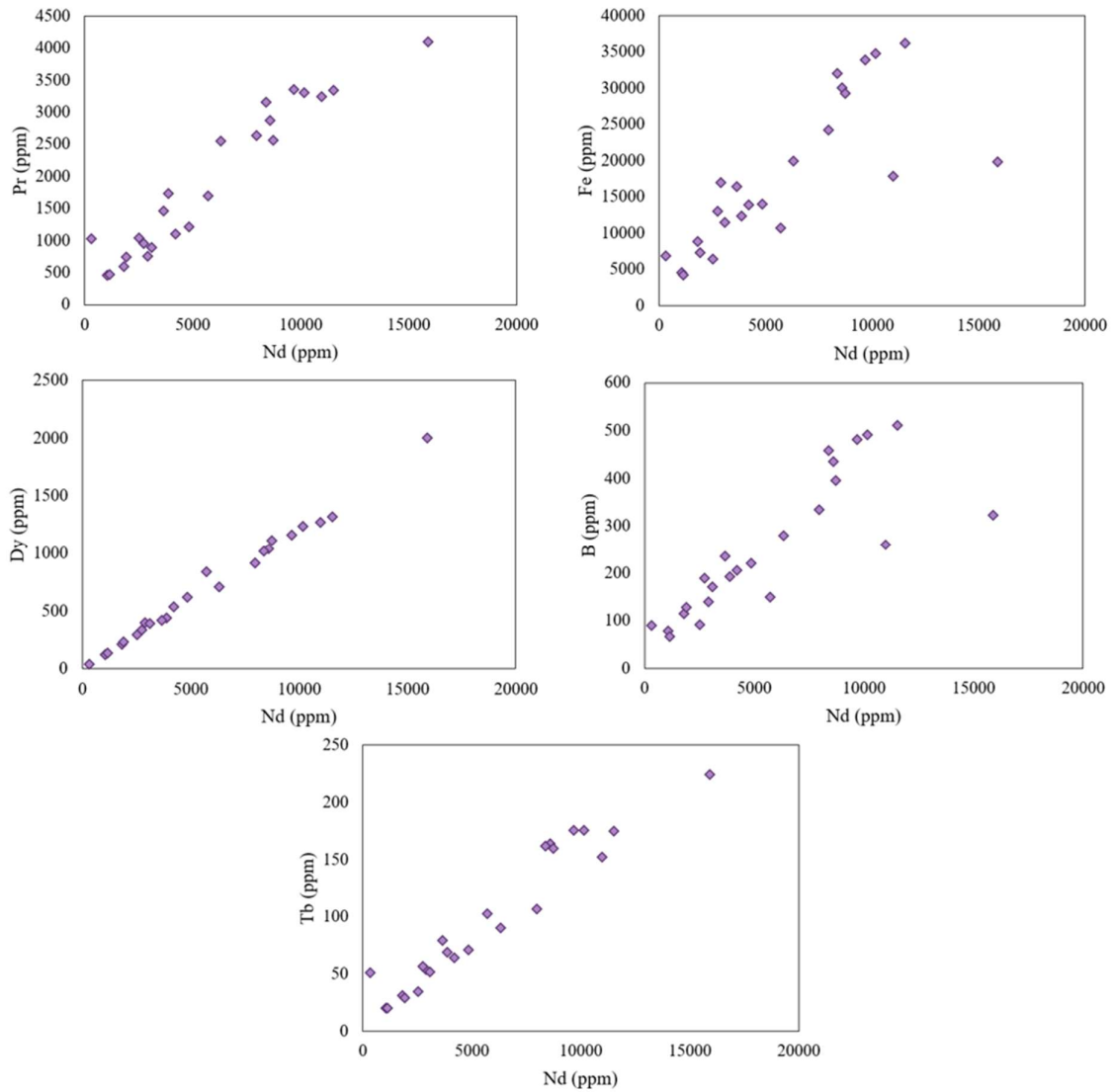


Figure 125. Correlation graphs between the concentrations of the different elements, in relation to the concentration of neodymium.

Based on the concentrations obtained, the extraction yields for each element were calculated using the equation below:

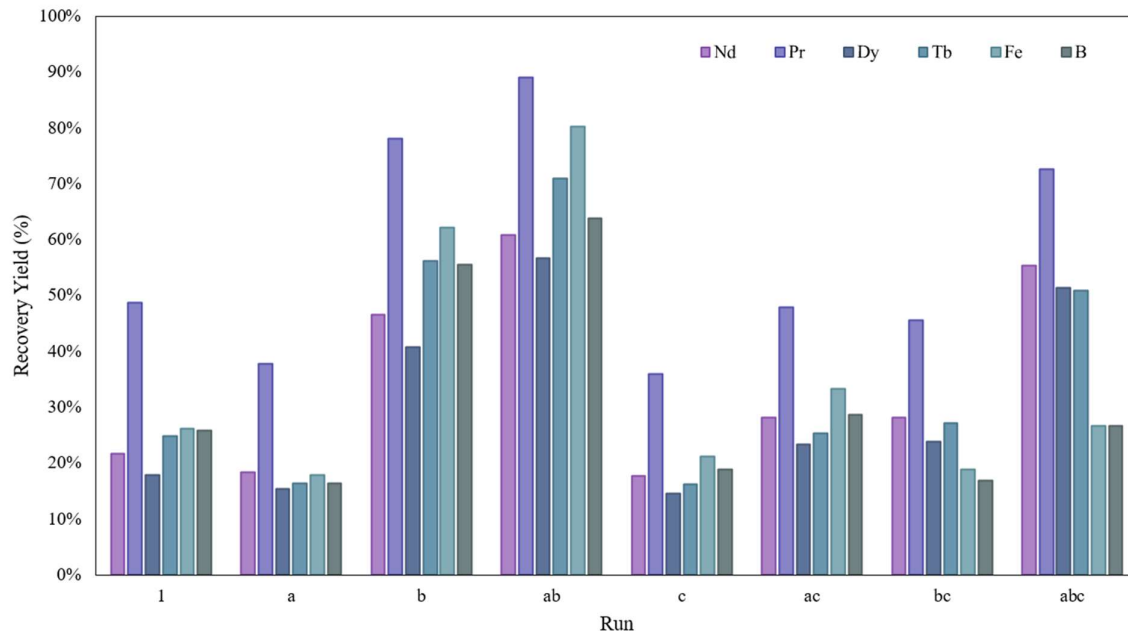
$$Me_{rec}(\%) = \frac{(C_{Me}^{LL} \cdot V^{LL} + C_{Me}^{WW} \cdot V^{WW})}{(C_{Me}^S \cdot m^S)}$$

Where C_{Me}^{LL} is the metal concentration in the leach liquor, V^{LL} is the leach liquor volume, C_{Me}^{WW} is the metal concentration in washing water, V^{WW} is the washing water volume, C_{Me}^S is the metal concentration in the initial solid sample, and m^S is the mass of the used solid sample. **Table 82** shows the obtained results.

Table 82. Metals recovery yields.

Run	Recovery Yield (%)					
	Nd	Pr	Dy	Tb	Fe	B
1	21.64%	48.73%	17.95%	24.81%	26.27%	25.80%
a	18.34%	37.77%	15.43%	16.48%	17.97%	16.34%
b	46.62%	78.14%	40.81%	56.21%	62.16%	55.48%
ab	60.76%	89.11%	56.67%	70.89%	80.24%	63.90%
c	17.79%	36.00%	14.58%	16.22%	21.21%	18.89%
ac	28.19%	47.83%	23.46%	25.41%	33.32%	28.70%
bc	28.26%	45.55%	23.79%	27.14%	18.95%	16.91%
abc	55.45%	72.63%	51.36%	50.92%	26.76%	26.66%
R1	40.23%	67.89%	35.34%	45.34%	51.50%	45.79%
R2	39.88%	65.57%	35.25%	44.45%	52.28%	45.99%
R3	34.61%	64.29%	30.56%	42.12%	49.09%	43.88%
R4	46.86%	67.77%	39.30%	45.21%	55.06%	48.48%

The graph in **Figure 126** was created to visualize better the yields obtained and the progress of the tests.

**Figure 126.** Graph of metal recovery yields.

Through the ANOVA method, it was possible to determine the actual influence of the parameters involved on the recovery yields and their significance. By significant, we mean any parameter whose significance calculated through the F-test is greater than or equal to 95%. The results of the analysis can be seen in **Figure 127**.

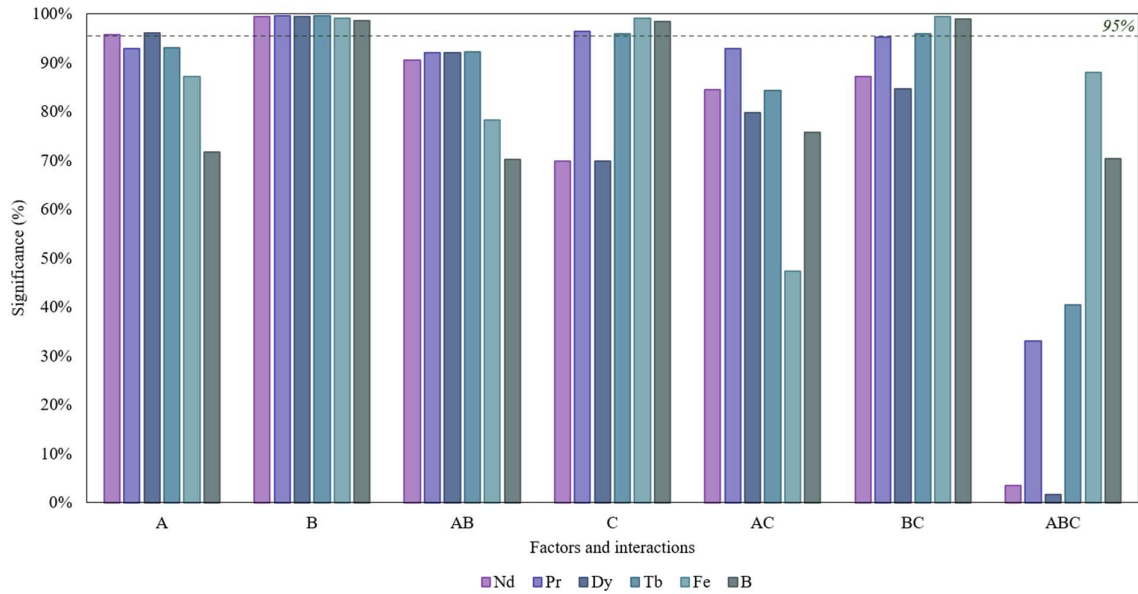


Figure 127. Significance of factors and interactions on extraction yields.

Based on the significance obtained for the different factors and interactions, the graph shown in the table was constructed where the effects of the significant factors and interactions are reported (with significance greater than 95%).

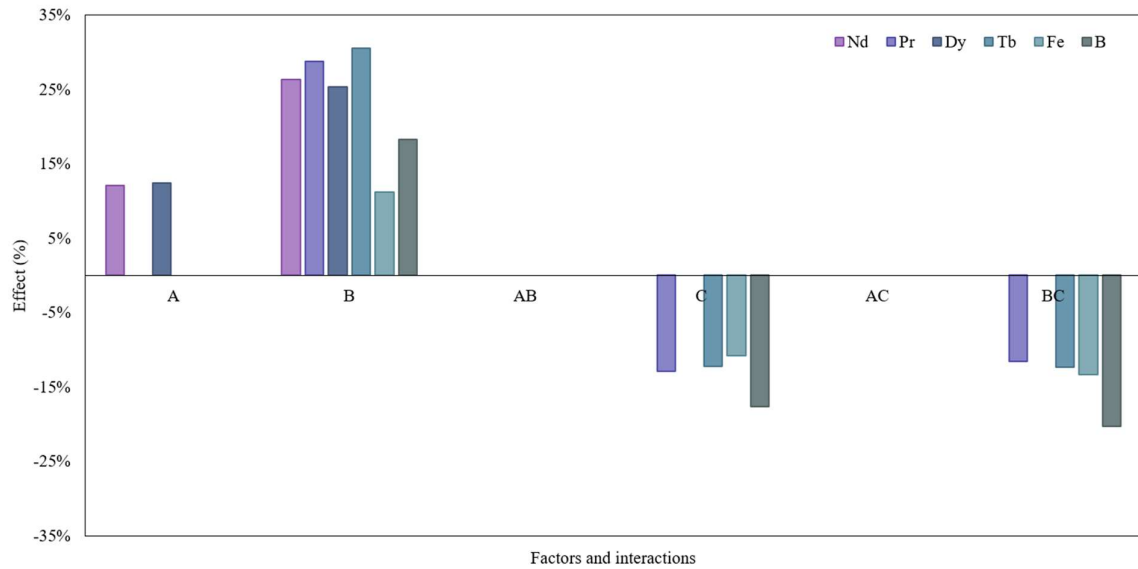


Figure 128. Main factors and their interaction effects on leaching.

Factor B (reaction time) is highly significant for all metals; this suggests that its kinetics greatly influence the process. By studying the effects of the parameters analyzed, it was possible to determine that parameter C is the only factor capable of negatively influencing the process, although not significant for each element. For this reason, the statistical analysis was carried out with the method of the response surface considering two parallel analyses that see the C factor as a fixed parameter at two different

levels: the low level, which corresponds to the solid-liquid ratio at 10%, and the high level which corresponds to the solid-liquid ratio at 20%. **Table 83** and

Table 84 show the results of the statistical analysis of the response surface, performed for the I-order-polynomial with fixed values of C, the equation of which is reported below.

$$Y = A_0 + A_1 \cdot X_1 + A_2 \cdot X_2$$

Considering X_1 and X_2 as factors A and B, respectively.

Table 83. RSM I-order polynomial (S/L=10%).

Element		Coefficient	Err standard	Stat t
<i>Nd</i>	A_0	-0.005	0.087	-0.058
	A_1	0.027	0.030	0.911
	A_2	0.169	0.030	5.668
<i>Pr</i>	A_0	0.245	0.079	3.107
	A_1	0.000	0.027	0.001
	A_2	0.202	0.027	7.451
<i>Dy</i>	A_0	-0.048	0.076	-0.636
	A_1	0.033	0.026	1.287
	A_2	0.160	0.026	6.186
<i>Tb</i>	A_0	-0.029	0.079	-0.364
	A_1	0.016	0.027	0.583
	A_2	0.215	0.027	7.874
<i>Fe</i>	A_0	-0.046	0.103	-0.451
	A_1	0.024	0.035	0.693
	A_2	0.245	0.035	6.958
<i>B</i>	A_0	0.051	0.081	0.630
	A_1	-0.003	0.028	-0.093
	A_2	0.193	0.028	6.944

Table 84. RSM I-order polynomial (S/L=20%).

Element		Coefficient	Err. Standard	Stat t
<i>Nd</i>	A_0	-0.013	0.108	-0.116
	A_1	0.094	0.037	2.543
	A_2	0.094	0.037	2.553
<i>Pr</i>	A_0	0.218	0.156	1.400
	A_1	0.097	0.053	1.820
	A_2	0.086	0.053	1.607
<i>Dy</i>	A_0	-0.051	0.096	-0.526

	A_1	0.091	0.033	2.756
	A_2	0.093	0.033	2.807
<i>Tb</i>	A_0	0.024	0.142	0.170
	A_1	0.082	0.049	1.696
	A_2	0.091	0.049	1.874
<i>Fe</i>	A_0	0.330	0.250	1.318
	A_1	0.050	0.086	0.580
	A_2	-0.022	0.086	-0.257
<i>B</i>	A_0	0.266	0.215	1.237
	A_1	0.049	0.074	0.662
	A_2	-0.010	0.074	-0.136

With the calculated coefficients, graphing the surfaces to analyze the process yield better was possible. **Figure 129** represents the neodymium response surfaces for the two levels of factor C. The two surfaces have slightly different orientations, and from the contour, it can be seen how the two factors considered, A and B, have different influences; that of A is not very significant.

Figure 130 shows the results obtained for praseodymium; the effect of factor A on the surface with the low level of factor C is zero, in agreement with the results of **Figure 127**.

In **Figure 131**, the RSM for the first order of dysprosium is shown. In this case, the concentration of citric acid, i.e., factor A, returns to have a specific importance for both examined levels of factor C.

Next, in **Figure 132**, terbium is shown, and, as in the other situations examined, the factor with the predominant influence is factor B, time.

Finally, with iron and boron, in **Figure 133** and **Figure 134**, respectively, we note, in contrast with what we have seen so far, an almost total inversion of slope between the two levels of C: while the surface with the solid-liquid ratio confirms and follows the trend observed in the previous metals, the surface with the highest level of the factor used as a parameter seems to be the mirror image of the previous ones.

In Table 9 and Table 10, in addition to the quadratic sums with the relative degrees of freedom, the R^2 values for the determined functions are reported.

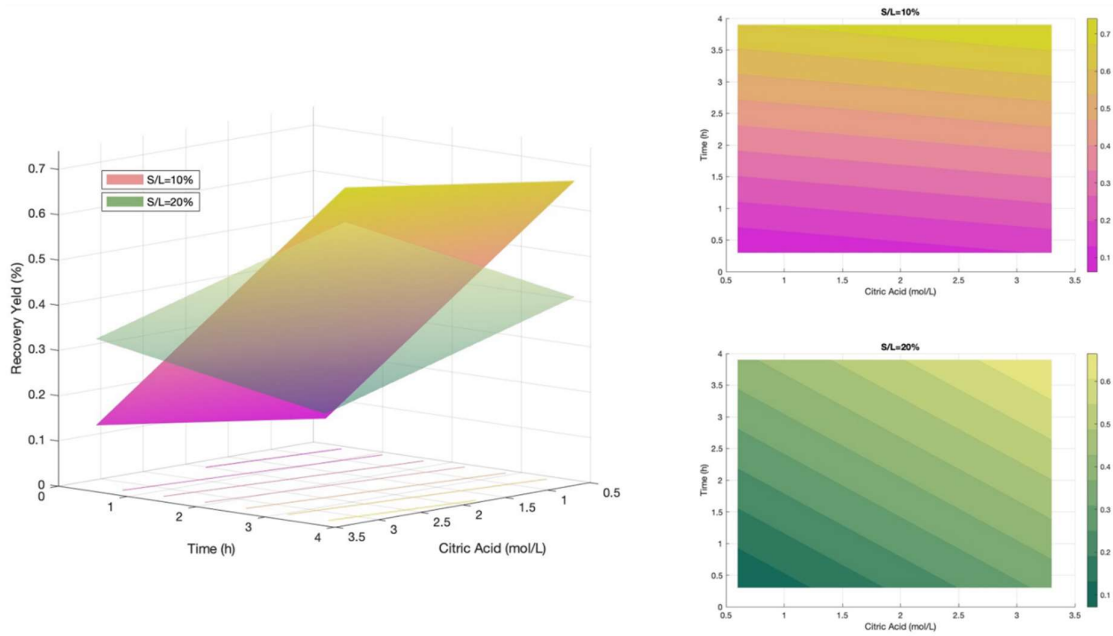


Figure 129. Nd RSM I-order polynomial.

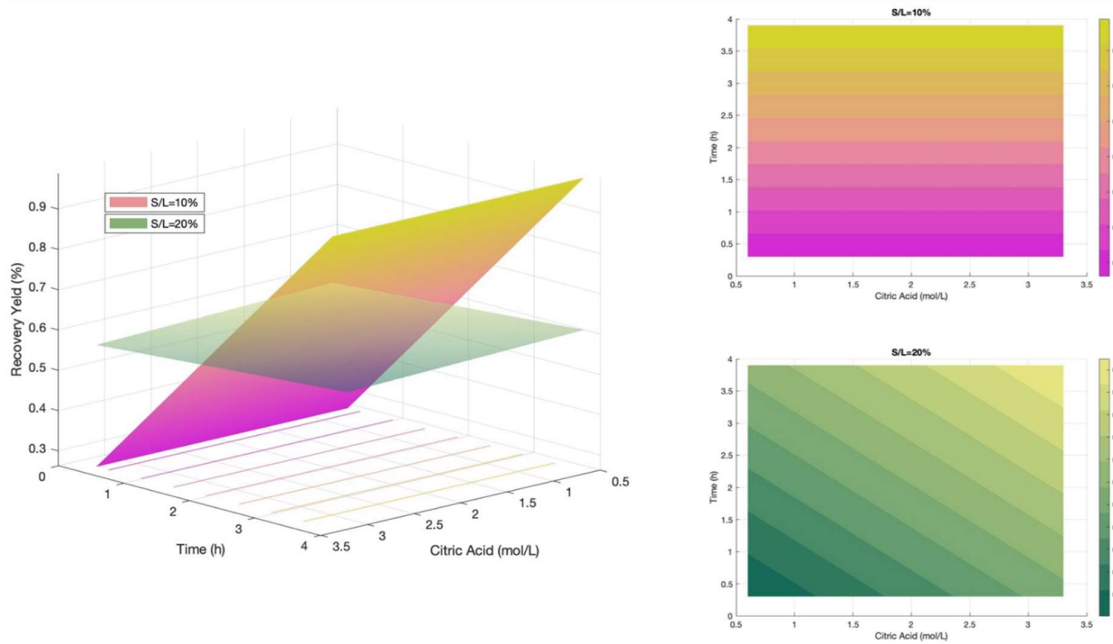


Figure 130. Pr RSM I-order polynomial.

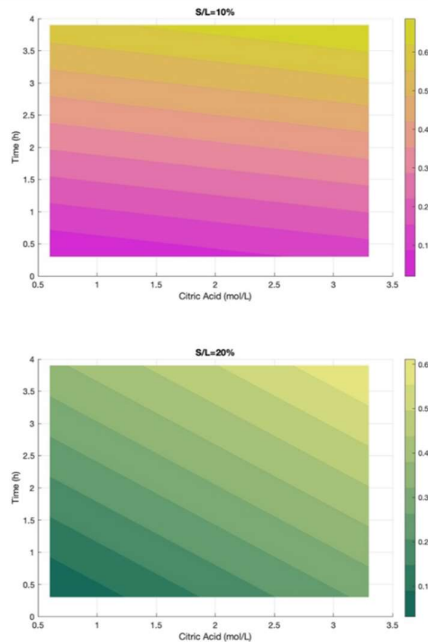
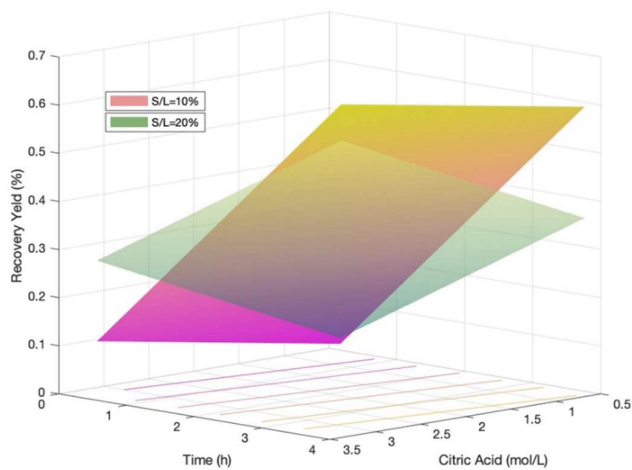


Figure 131. Dy RSM I-order polynomial.

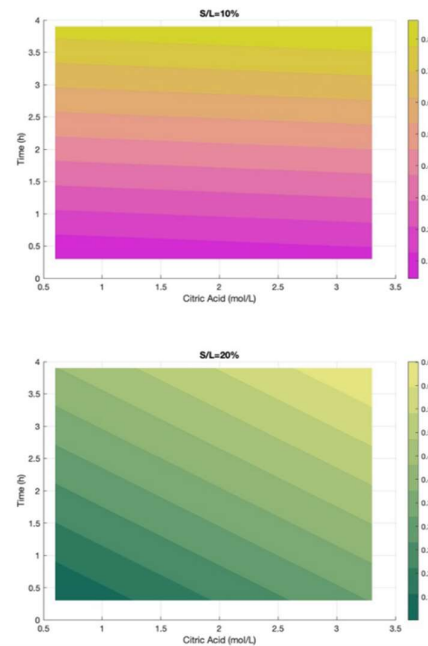
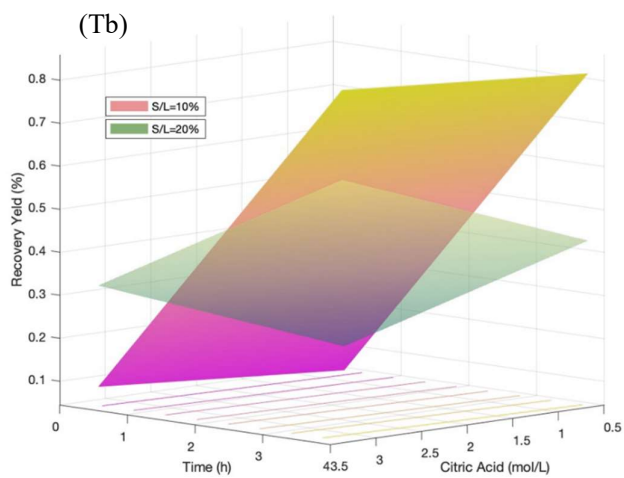


Figure 132. Tb RSM I-order polynomial.

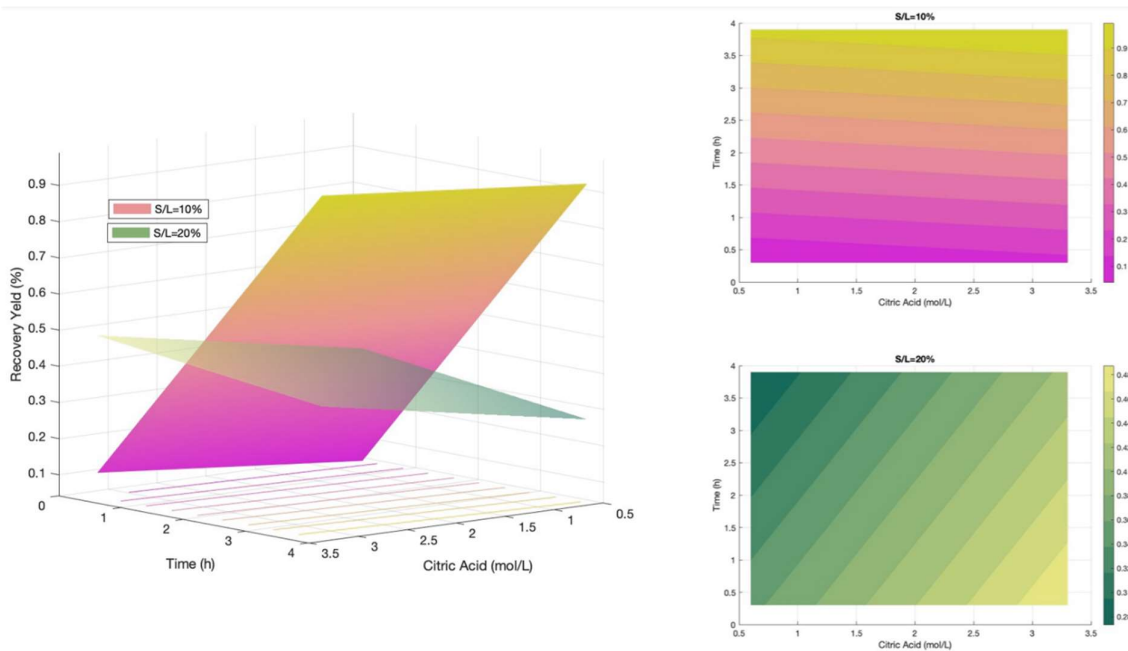


Figure 133. Fe RSM I-order polynomial.

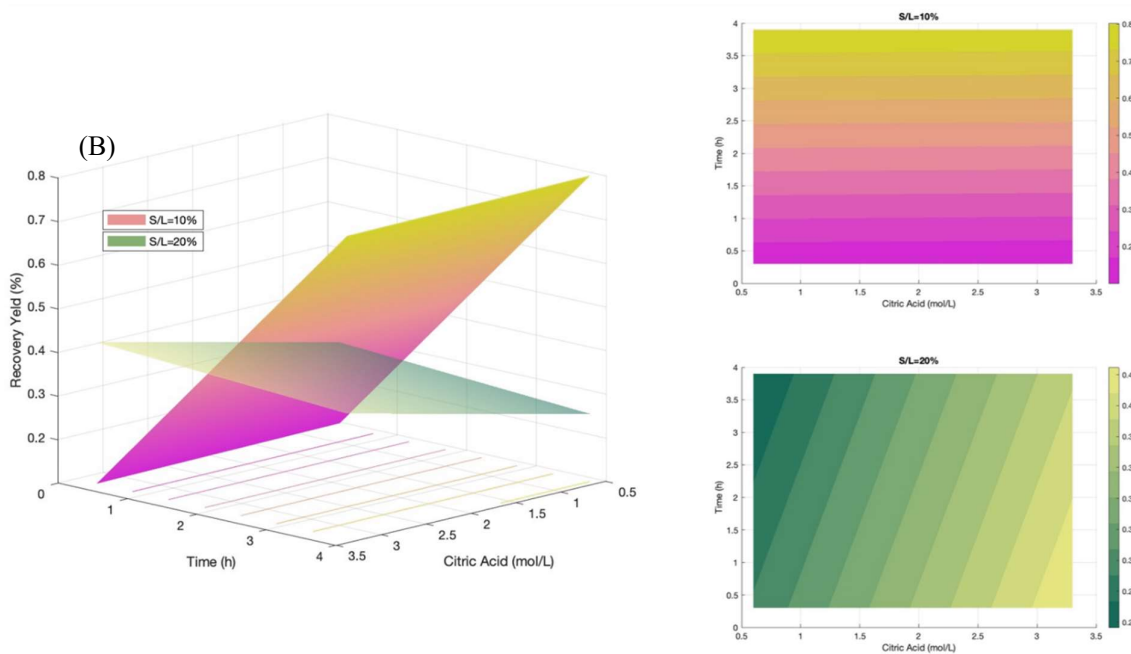


Figure 134. B RSM I-order polynomial.

Table 85. Regression analysis results for RSM I-Order polynomial in terms of R^2 and SS (S/L=10%).

	R^2	SSR	SSE	SST	n_R	n_E	n_T
<i>Nd</i>	0.868	0.1165	0.0177	0.1342	2	5	7
<i>Pr</i>	0.917	0.1630	0.0147	0.1776	2	5	7
<i>Dy</i>	0.889	0.1072	0.0134	0.1206	2	5	7
<i>Tb</i>	0.926	0.1851	0.0148	0.1999	2	5	7
<i>Fe</i>	0.907	0.2432	0.0249	0.2681	2	5	7
<i>B</i>	0.906	0.1492	0.0155	0.1646	2	5	7

Table 86. Regression analysis results for RSM I-Order polynomial in terms of R^2 and SS (S/L=20%).

	R^2	SSR	SSE	SST	n_R	n_E	n_T
<i>Nd</i>	0.722	0.0709	0.0273	0.0982	2	5	7
<i>Pr</i>	0.541	0.0673	0.0571	0.1245	2	5	7
<i>Dy</i>	0.756	0.0676	0.0219	0.0895	2	5	7
<i>Tb</i>	0.561	0.0603	0.0472	0.1076	2	5	7
<i>Fe</i>	0.075	0.0119	0.1472	0.1591	2	5	7
<i>B</i>	0.084	0.0100	0.1092	0.1191	2	5	7

The R^2 values are low for the S/L parameter fixed at 20%. The lowest calculated value is that of iron, which is equal to 0.075.

In this regard, it was chosen to include star points in the factorial experimentation, which allows second-order statistical analysis with the II-Order-Polynomial. In this way, it is possible to have a better approximation of the process and, therefore, higher R^2 values. The new factorial plan is illustrated in **Table 87**.

Table 87. Full factorial plan with star points.

	A [M]	B [h]	C
1	1	1h	10%
a	3	1h	10%
b	1	3h	10%
ab	3	3h	10%
c	1	1h	20%
ac	3	1h	20%
bc	1	3h	20%
abc	3	3h	20%
R1	2	2h	15%
R2	2	2h	15%
R3	2	2h	15%
R4	2	2h	15%
S1	2	2	23.4%
S2	2	2	6.6%

S3	3.682	2	15%
S4	0.318	2	15%
S5	2	3.7	15%
S6	2	0.3	15%

The results in concentrations of the elements of interest, measured in the LL and WW via ICP-OES, are reported in **Table 88**. Subsequently, the yields were calculated, and the results obtained are summarized in **Table 89**.

Table 88. Results in terms of concentrations for star points.

		Volume [mL]	Nd [ppm]	Pr [ppm]	Dy [ppm]	Tb [ppm]	Fe [ppm]	B [ppm]
S1	LL	55	19708	3786	2269	228	52022	764
	WW	16	7000	1204	846	82	19389	291
S2	LL	62	8213	1328	1035	102	22194	325
	WW	16	1893	306	250	26	5447	85
S3	LL	71	9179	1709	1090	98	23346	345
	WW	16	4914	831	606	58	13741	205
S4	LL	50	5441	1099	611	49	11354	173
	WW	16	1302	255	149	12	3132	74
S5	LL	62	18698	3157	2248	245	57928	762
	WW	16	5028	791	629	67	15001	236
S6	LL	59	3653	914	382	26	4220	80
	WW	16	1911	409	200	17	3972	65

Table 89. Results in terms of recovery yields for star points.

Run	Recovery Yield (%)					
	Nd	Pr	Dy	Tb	Fe	B
S1	48%	46%	41%	36%	48%	44%
S2	77%	63%	71%	61%	78%	71%
S3	46%	43%	40%	32%	44%	41%
S4	18%	19%	15%	11%	15%	14%
S5	78%	66%	68%	65%	90%	74%
S6	16%	19%	12%	7%	7%	8%

Thanks to the new experimental results obtained, it was possible to proceed with the statistical analysis of the second order, estimating for each element the 6 parameters: A_0 , A_1 , A_2 , A_{11} , A_{22} , A_{12} , of the II-Order-Polynomial:

$$Y = A_0 + A_1 \cdot X_1 + A_2 \cdot X_2 + A_{11} \cdot X_1^2 + A_{22} \cdot X_2^2 + A_{12} \cdot X_1 \cdot X_2$$

Considering X_1 as factor A and X_2 as factor B (the concentration of citric acid and the process time, respectively).

Table 90. RSM II-order polynomial (S/L=10%).

Element		Coefficient	Err. Standard	Stat t
<i>Nd</i>	A_0	-0.113	0.338	-0.335
	A_1	0.217	0.196	1.105
	A_2	0.131	0.196	0.665
	A_{11}	-0.061	0.036	-1.712
	A_{22}	-0.010	0.036	-0.272
	A_{12}	0.044	0.064	0.681
<i>Pr</i>	A_0	-0.097	0.360	-0.268
	A_1	0.292	0.210	1.391
	A_2	0.247	0.210	1.177
	A_{11}	-0.090	0.038	-2.354
	A_{22}	-0.048	0.038	-1.251
	A_{12}	0.055	0.068	0.803
<i>Dy</i>	A_0	-0.110	0.314	-0.349
	A_1	0.187	0.183	1.021
	A_2	0.117	0.183	0.637
	A_{11}	-0.055	0.033	-1.663
	A_{22}	-0.011	0.033	-0.327
	A_{12}	0.046	0.060	0.770
<i>Tb</i>	A_0	-0.031	0.335	-0.093
	A_1	0.160	0.195	0.822
	A_2	0.097	0.195	0.500
	A_{11}	-0.055	0.035	-1.555
	A_{22}	-0.004	0.035	-0.102
	A_{12}	0.058	0.063	0.906
<i>Fe</i>	A_0	-0.236	0.256	-0.920
	A_1	0.289	0.149	1.939
	A_2	0.199	0.149	1.337
	A_{11}	-0.090	0.027	-3.307
	A_{22}	-0.021	0.027	-0.790
	A_{12}	0.066	0.049	1.356
<i>B</i>	A_0	-0.269	0.240	-1.120
	A_1	0.296	0.140	2.124
	A_2	0.227	0.140	1.625
	A_{11}	-0.082	0.025	-3.213
	A_{22}	-0.032	0.025	-1.270
	A_{12}	0.044	0.045	0.959

Table 91. RSM II-order polynomial (S/L=10%).

Element		Coefficient	Err. Standard	Stat t
<i>Nd</i>	A_0	-0.160	0.373	-0.430
	A_1	0.269	0.217	1.238
	A_2	0.124	0.217	0.570
	A_{11}	-0.066	0.040	-1.679
	A_{22}	-0.015	0.040	-0.376
	A_{12}	0.042	0.071	0.593
<i>Pr</i>	A_0	-0.284	0.212	-1.340
	A_1	0.425	0.124	3.444
	A_2	0.292	0.124	2.365
	A_{11}	-0.105	0.022	-4.662
	A_{22}	-0.063	0.022	-2.790
	A_{12}	0.038	0.040	0.947
<i>Dy</i>	A_0	-0.145	0.345	-0.421
	A_1	0.230	0.200	1.145
	A_2	0.108	0.200	0.537
	A_{11}	-0.061	0.037	-1.658
	A_{22}	-0.016	0.037	-0.439
	A_{12}	0.047	0.065	0.715
<i>Tb</i>	A_0	-0.196	0.390	-0.504
	A_1	0.286	0.227	1.262
	A_2	0.145	0.227	0.638
	A_{11}	-0.069	0.041	-1.676
	A_{22}	-0.018	0.041	-0.430
	A_{12}	0.036	0.074	0.493
<i>Fe</i>	A_0	-0.570	0.532	-1.071
	A_1	0.553	0.310	1.787
	A_2	0.342	0.310	1.106
	A_{11}	-0.115	0.056	-2.038
	A_{22}	-0.047	0.056	-0.825
	A_{12}	-0.011	0.101	-0.106
<i>B</i>	A_0	-0.462	0.443	-1.042
	A_1	0.458	0.258	1.777
	A_2	0.306	0.258	1.185
	A_{11}	-0.098	0.047	-2.086
	A_{22}	-0.049	0.047	-1.035
	A_{12}	0.000	0.084	-0.002

With the new coefficients obtained, it was also possible to represent the II-order response surfaces. As in the previous case, the first metal analyzed in **Figure 135** is neodymium. The graphs with the II-order surfaces confirm what was also observable with the first analysis order: the highest yields are obtained for the lowest solid-liquid ratio value, set at 10% for the low level of the C factor.

In **Figure 136**, where praseodymium is analyzed, the trend of the surfaces is more curved and highlights a peak for factor B equal to approximately 3 hours and factor A equal to approximately 3 M.

With dysprosium, in **Figure 137**, as expected from the correlation analysis, which sees the two metals very well correlated, a trend almost superimposable to that of neodymium returns.

Moving forward with terbium, in **Figure 138**, we note that the surfaces for the two levels of factor C are more detached at the points of maximum yield than the previous elements, supporting the thesis that the highest yields are obtained for the lowest C value.

This trend is even more evident in the following graphs: **Figure 139** for iron and **Figure 140** for boron. Iron and boron, closely linked in the correlation analysis, like neodymium and dysprosium, present overlapping trends.

The following tables show the values of the quadratic sums with the relative degrees of freedom and the new values of R^2 .

Table 92. Regression analysis results for II-Order polynomial in terms of R^2 and SS (S/L=10%).

	R^2	SSR	SSE	SST	n_R	n_E	n_T
<i>Nd</i>	0.752	0.398	0.131	0.529	5	8	13
<i>Pr</i>	0.732	0.408	0.149	0.557	5	8	13
<i>Dy</i>	0.750	0.341	0.114	0.455	5	8	13
<i>Tb</i>	0.781	0.460	0.129	0.588	5	8	13
<i>Fe</i>	0.907	0.740	0.076	0.815	5	8	13
<i>B</i>	0.874	0.457	0.066	0.524	5	8	13

Table 93. Regression analysis results for II-Order polynomial in terms of R^2 and SS (S/L=20%).

	R^2	SSR	SSE	SST	n_R	n_E	n_T
<i>Nd</i>	0.685	0.348	0.160	0.508	5	8	13
<i>Pr</i>	0.876	0.368	0.052	0.420	5	8	13
<i>Dy</i>	0.687	0.300	0.137	0.437	5	8	13
<i>Tb</i>	0.660	0.340	0.175	0.515	5	8	13
<i>Fe</i>	0.553	0.403	0.326	0.729	5	8	13
<i>B</i>	0.566	0.295	0.226	0.521	5	8	13

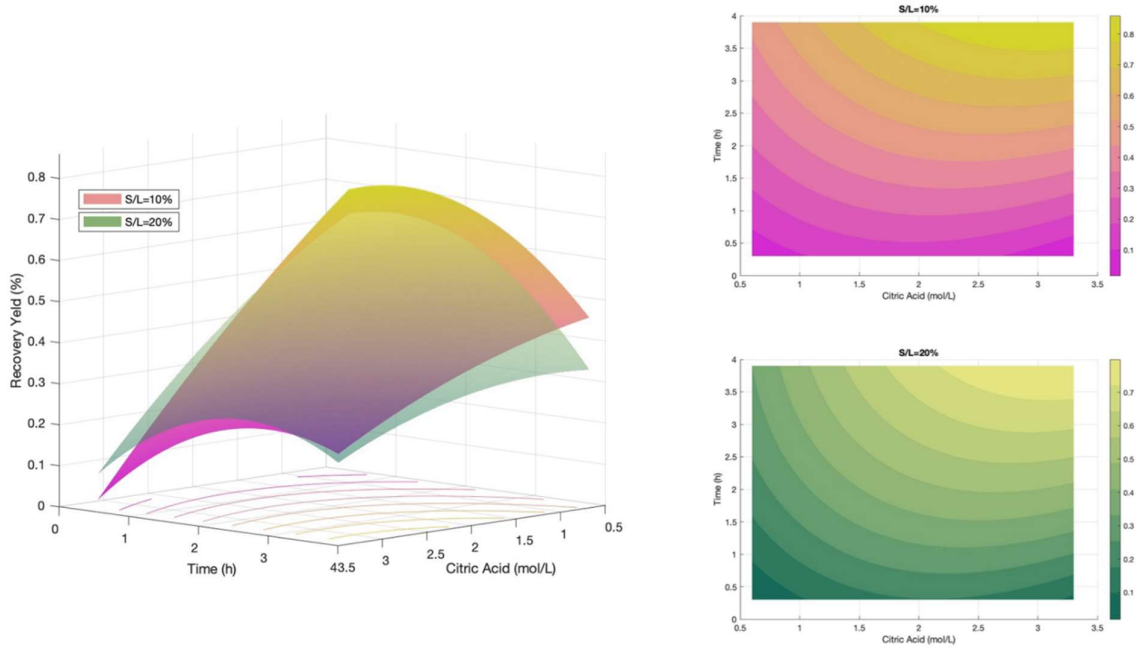


Figure 135. Nd RSM II-order polynomial.

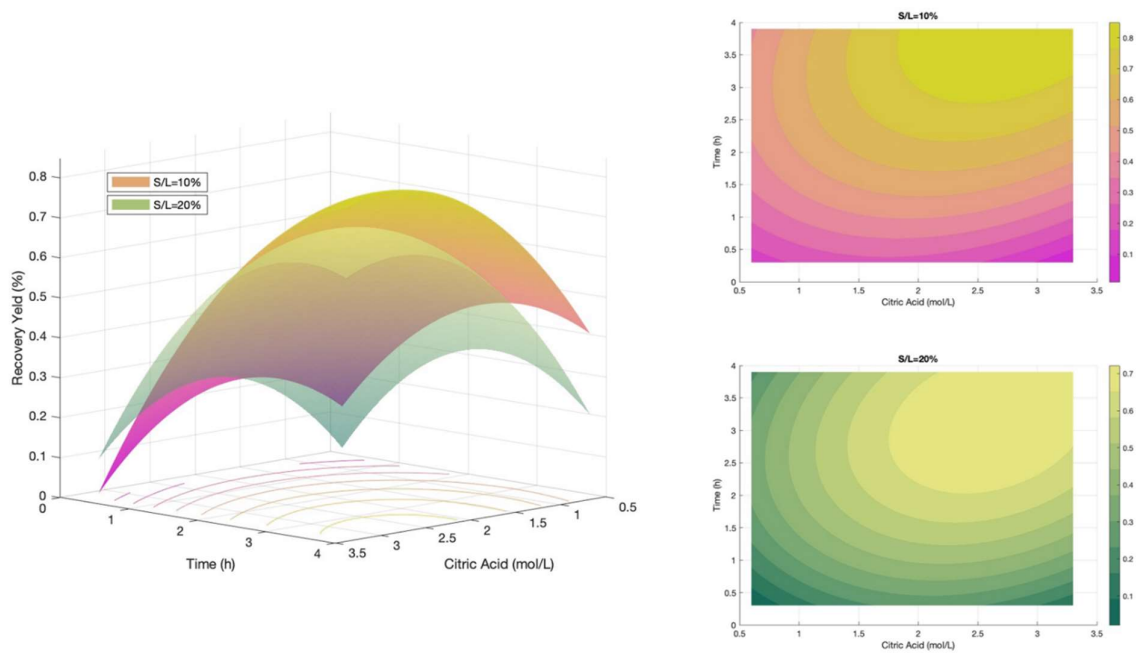


Figure 136. Pr RSM II-order polynomial.

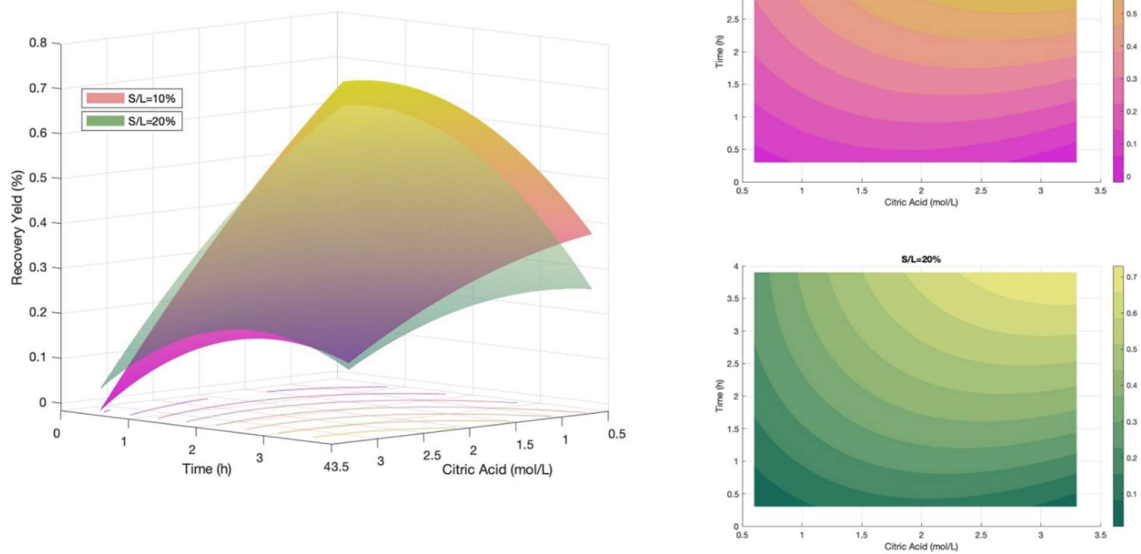


Figure 137. Dy RSM II-order polynomial.

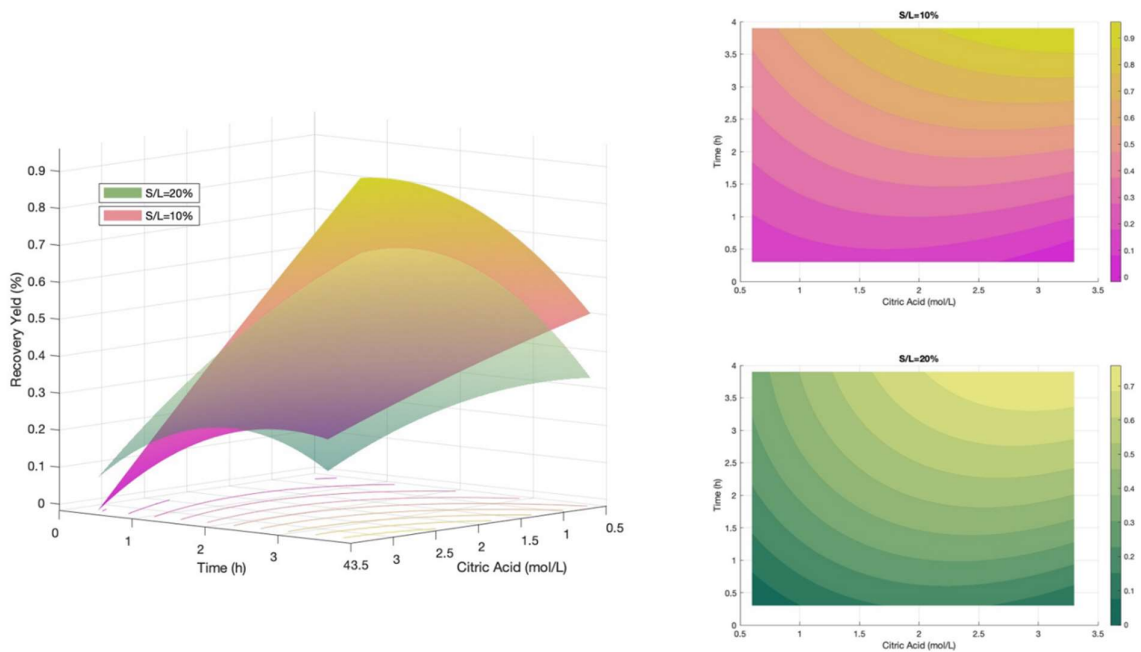


Figure 138. Tb RSM II-order polynomial.

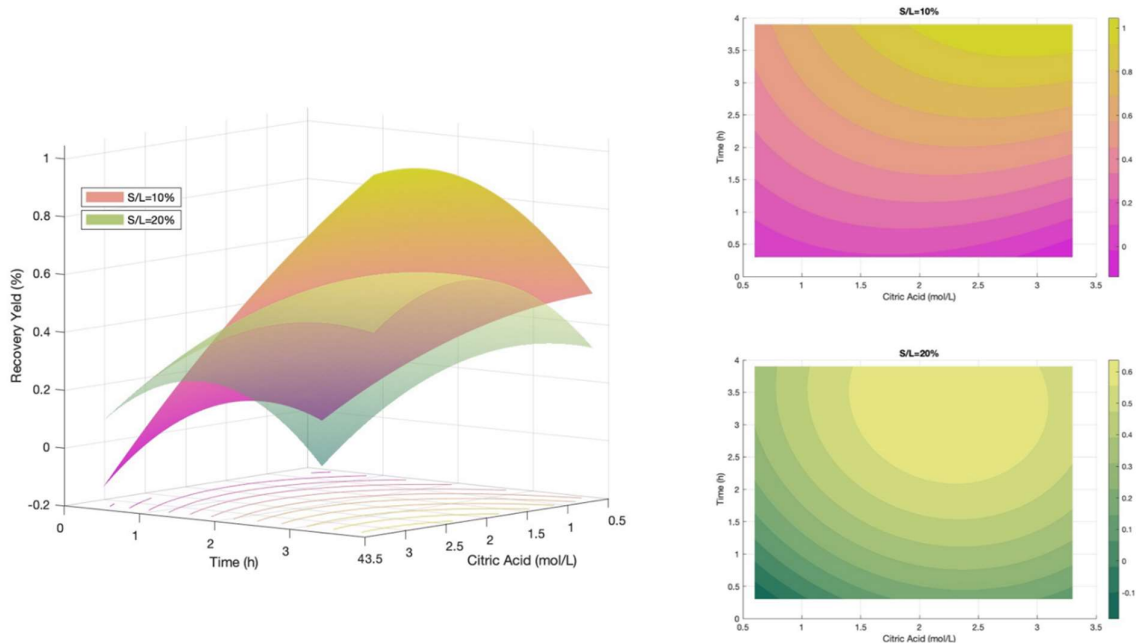


Figure 139. Fe RSM II-order polynomial.

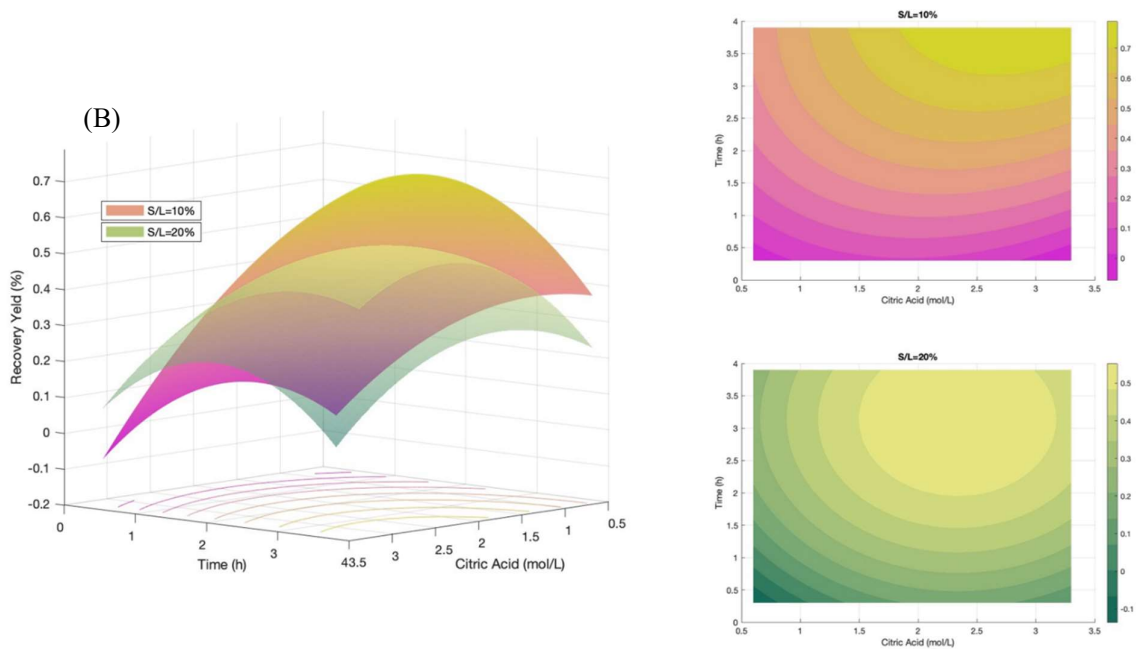


Figure 140. B RSM II-order polynomial.

The second-order statistical analysis gives a clearer vision of the progress of the process under examination. However, the analysis of the coefficient of determination did not lead to the expected results. In **Table 93** the values are significantly higher than those calculated in the previous analysis, but the same does not happen with the values in **Table 92**.

This table shows the R^2 values for the surfaces of most significant interest, those with the value of the solid-liquid ratio fixed at 10%, which, compared to those of the first order, are significantly lower.

Finally, to demonstrate the goodness of the regression carried out, we create scatter diagrams for all the elements for the data calculated with the I-Order-Polynomial illustrated in **Figure 141**.

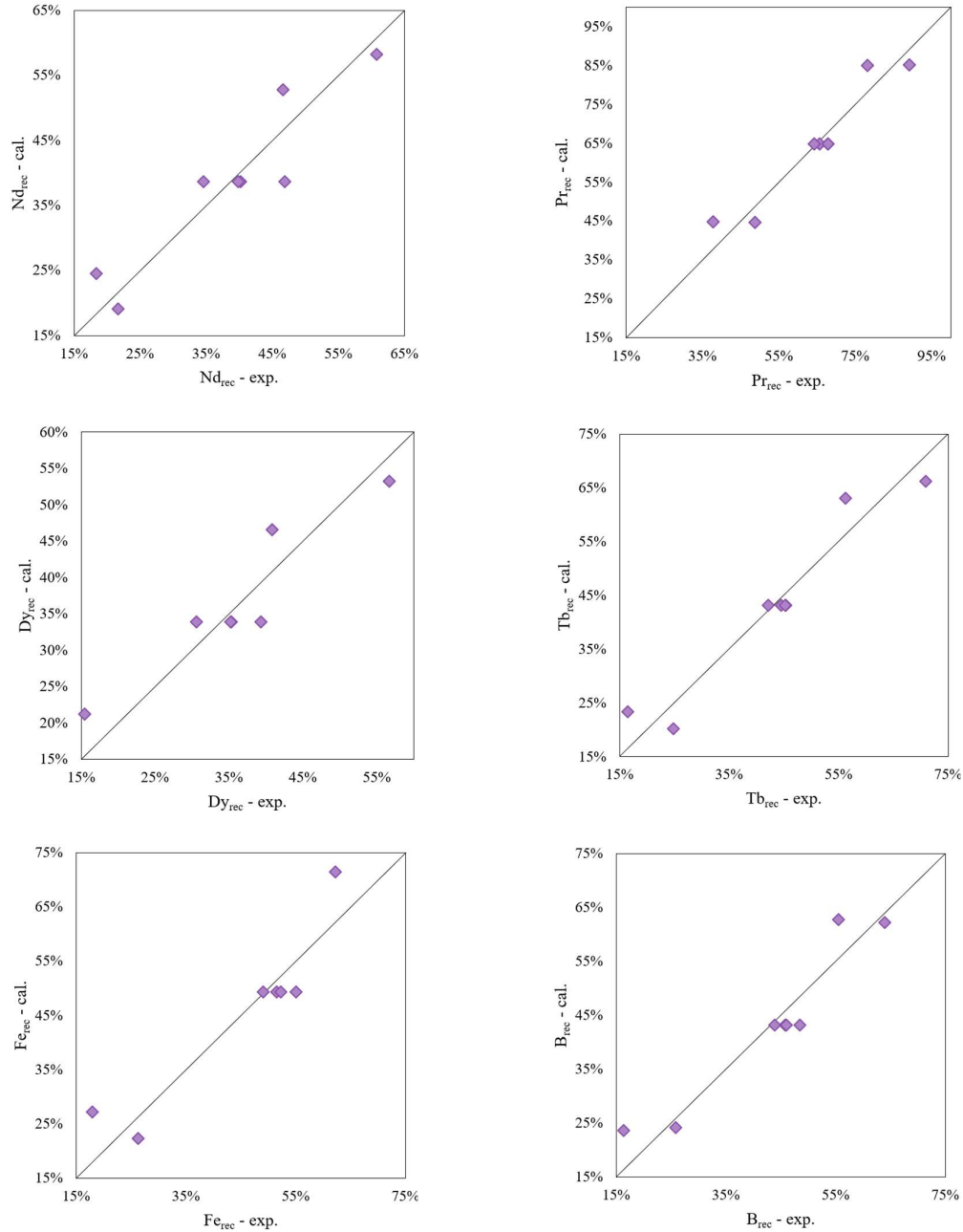


Figure 141. Scatter diagrams for the I-Order polynomial (S/L=10%).

Analyzing the results obtained with the RSM makes it possible to determine an optimal working point regarding recovery yields of the elements of most significant interest. **Table 94** shows the optimal

working conditions obtained. With these conditions, thanks to the coefficients of the first-order response surfaces, the optimal extraction yields are calculated for each element studied, as reported in **Table 95**.

Table 94. Optimal leaching conditions.

Parameter	Value
A – Citric Acid concentration [M]	3
B – Reaction Time [h]	3.5
C – Solid-Liquid ratio [%]	10

Table 95. Recovery yields in optimal leaching conditions.

Element	Recovery Yield (%)	
	I-OP	II-OP
Nd	67%	78%
Pr	95%	82%
Dy	61%	71%
Tb	77%	85%
Fe	89%	95%
B	72%	74%

5.4.2 Kinetic results

Before the kinetic analysis, preliminary tests were carried out according to a factorial plan 2³. In the factorial plan created, the following factors were studied:

- A: Stirring rate
- B: Particle size
- C: Temperature

In order to proceed with calculating the recovery yields, the three different grain size fractions used in the factorial plan were characterized. In this way, it was possible to evaluate any effects of grinding on the division of metals into different fractions. **Table 96** shows the results of the three characterizations.

Table 96. Chemical composition of different size fractions.

Size fraction (μm)	Value	Solid composition (%wt.)					
		Dy	Pr	Tb	Nd	B	Fe
<53	μ	7.30%	5.32%	0.52%	40.13%	1.06%	51.12%
	σ	0.06%	0.16%	0.01%	0.25%	0.02%	0.43%
53-212	μ	6.74%	4.80%	0.60%	42.32%	1.06%	51.12%
	σ	0.17%	0.11%	0.01%	0.80%	0.02%	0.43%
>212	μ	4.73%	3.91%	1.00%	43.82%	1.07%	51.12%
	σ	0.07%	0.06%	0.02%	0.79%	0.02%	0.43%

The results obtained were analyzed via ANOVA to establish the effect and significance of the effect of each factor and the related interactions on the recovery yields of the various elements. The results obtained from this analysis are reported below.

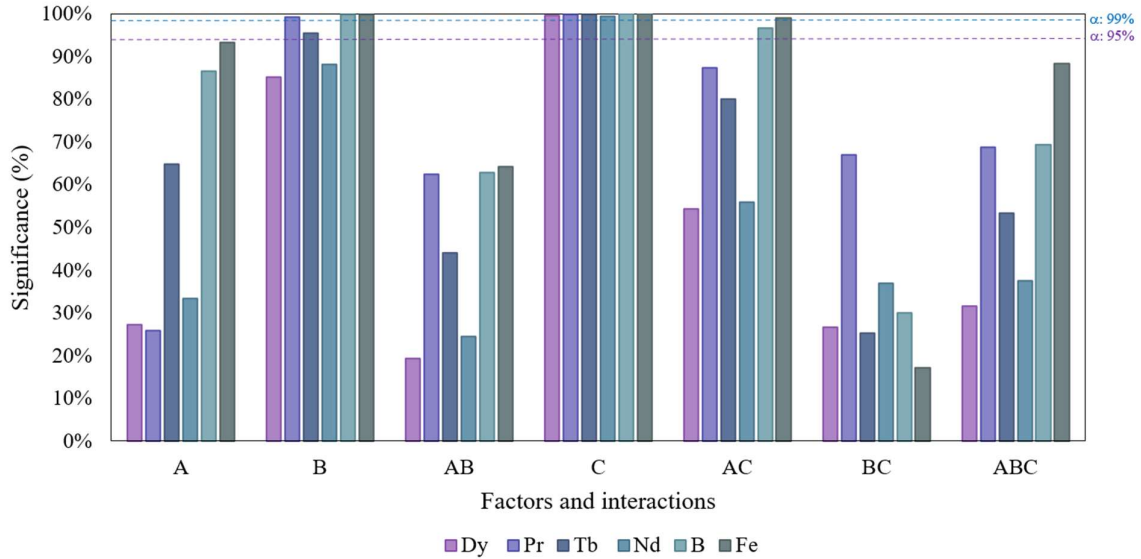


Figure 142. Significance of factors and interactions on REEs extraction yields.

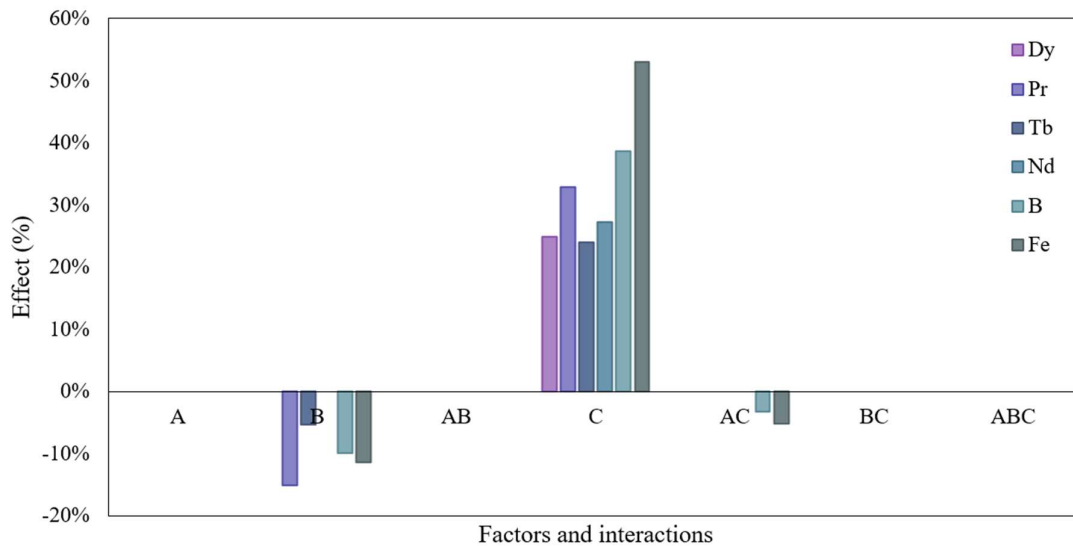


Figure 143. Main factors and their interaction effects on REEs leaching.

From ANOVA, the most significant effects are those linked to temperature. The strong temperature dependence suggests that the process may be under the control of the chemical reaction. However, the effect of B is also significant, suggesting a particular influence of internal diffusion on the extraction yield. In particular, an increase in the temperature positively affects the extraction yield.

The ANOVA results are similar for most of the items analyzed. The only differences are related to the level of significance of the effects.

It was possible to analyze the trend of recovery yields over time through sampling taken at pre-established times. **Figure 144** shows this trend for each of the metals considered.

From the graphs shown, it is seen that all the elements considered behave similarly for the different tests carried out. This result agrees with what was seen through the correlation matrix shown in **Figure 124**. Furthermore, the results highlight what was obtained statistically through ANOVA. It is possible to see a significant change in recovery yields when moving from lower temperature tests to higher temperature tests.

Although to a lesser extent, the negative effect of B can be noted by observing the slight difference between the yields for tests (1) and a (higher yields) from tests b and ab (lower yields).

The different SCM models were evaluated from the yields obtained to determine the rate-determining step (RDS). In this regard, the kinetic constants and coefficients of determination for the regressions carried out were estimated. Below are the results obtained for each element.

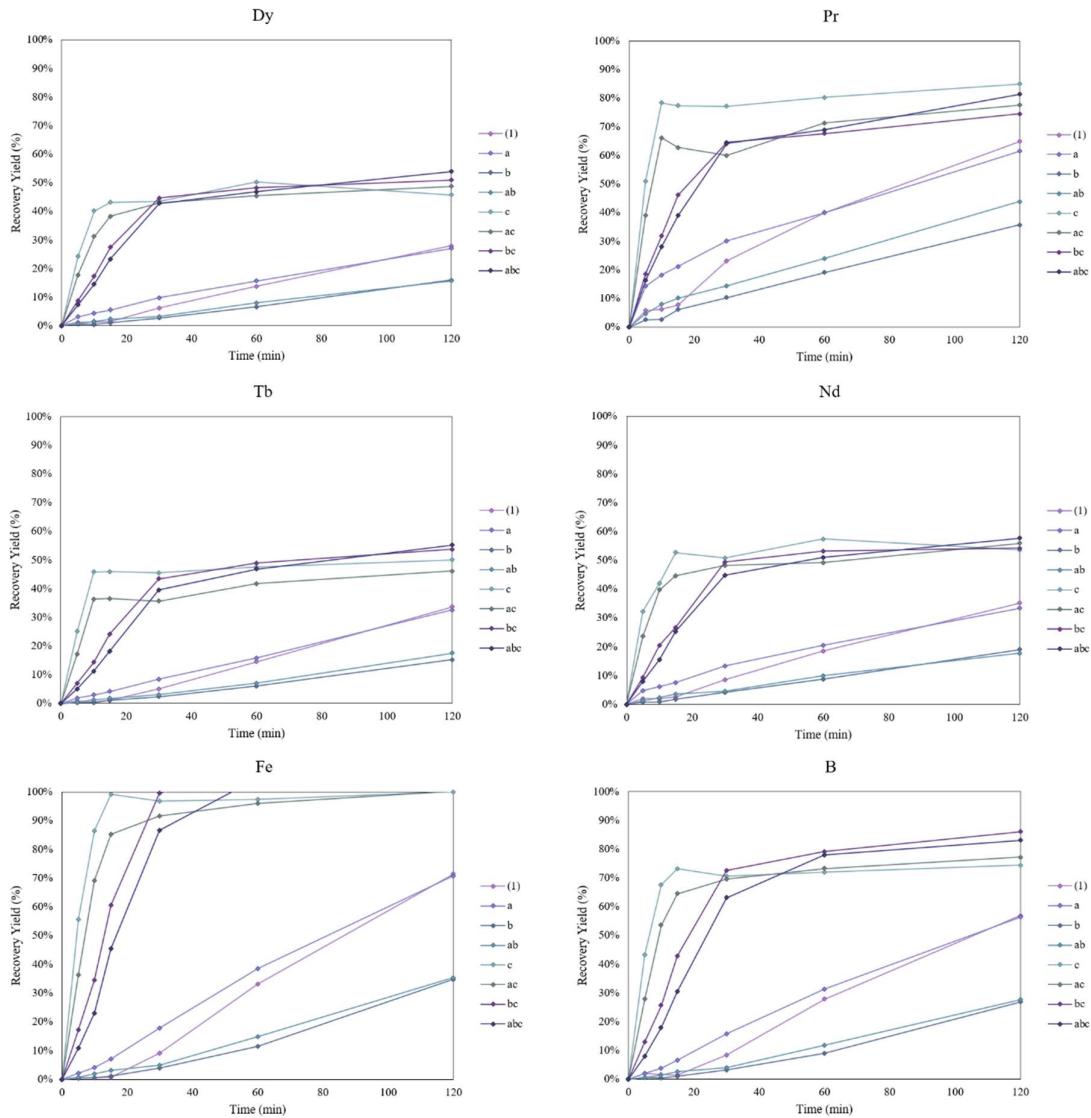


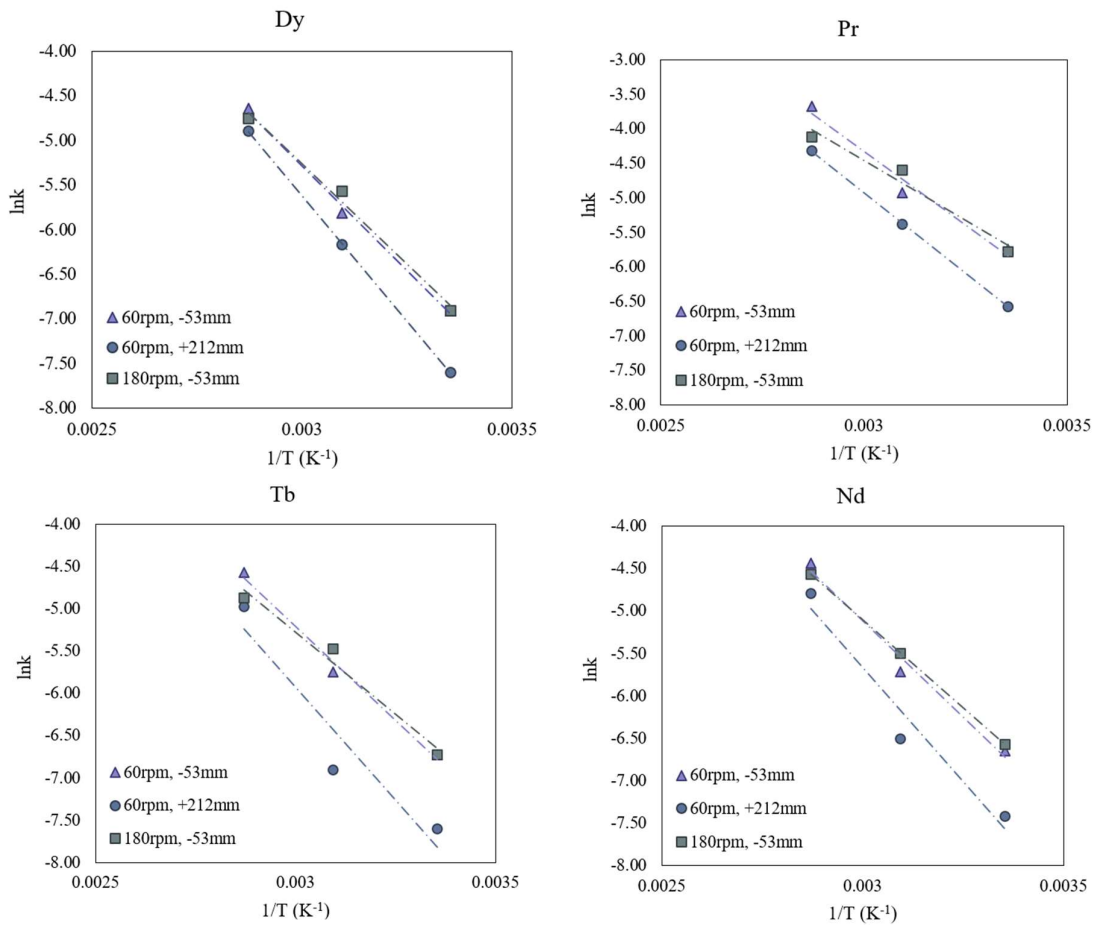
Figure 144. Extraction yields over time of the metals of interest for each test of the factorial plan.

Table 97. Kinetic constants (min^{-1}) and determination coefficients at different run.

Run	x		$(1-x)^{1/3}$		$1-3(1-x)^{2/3}+2(1-x)$		
	Slope	R^2	Slope	R^2	Slope	R^2	
Dy	1	0.0023	0.995	0.0008	0.992	0.0001	0.869
	2	0.0024	0.980	0.0009	0.987	0.0001	0.970
	3	0.0013	0.986	0.0004	0.983	0.0000	0.858
	4	0.0013	0.998	0.0005	0.998	0.0000	0.878
	5	0.0198	0.822	0.0078	0.832	0.0035	0.865
	6	0.0181	0.891	0.0071	0.906	0.0029	0.960
	7	0.0158	0.992	0.0061	0.998	0.0025	0.943
	8	0.0145	0.999	0.0056	0.999	0.0021	0.911
Pr	1	0.0058	0.986	0.0025	0.997	0.0009	0.920
	2	0.0058	0.905	0.0025	0.946	0.0011	0.999
	3	0.0030	0.996	0.0011	0.999	0.0002	0.932
	4	0.0038	0.981	0.0015	0.990	0.0003	0.975
	5	0.0361	0.788	0.0181	0.802	0.0154	0.814
	6	0.0288	0.770	0.0127	0.768	0.0084	0.748
	7	0.0243	0.966	0.0105	0.987	0.0064	0.977
	8	0.0230	0.986	0.0098	0.999	0.0059	0.944
Tb	1	0.0026	0.980	0.0010	0.973	0.0000	0.762
	2	0.0027	1.000	0.0010	0.999	0.0001	0.911
	3	0.0012	0.981	0.0004	0.978	0.0000	0.849
	4	0.0014	0.989	0.0005	0.986	0.0000	0.943
	5	0.0211	0.807	0.0085	0.812	0.0022	0.716
	6	0.0165	0.809	0.0063	0.811	0.0015	0.794
	7	0.0147	0.998	0.0057	0.998	0.0019	0.953
	8	0.0128	0.997	0.0049	0.991	0.0016	0.955
Nd	1	0.0029	0.997	0.0011	0.996	0.0004	0.911
	2	0.0030	0.967	0.0011	0.978	0.0003	0.970
	3	0.0015	0.997	0.0005	0.995	0.0001	0.889
	4	0.0015	0.992	0.0005	0.995	0.0001	0.937
	5	0.0232	0.822	0.0095	0.836	0.0050	0.872
	6	0.0210	0.858	0.0085	0.874	0.0040	0.928
	7	0.0170	0.995	0.0068	0.999	0.0030	0.922
	8	0.0154	0.998	0.0060	0.999	0.0024	0.918
B	1	0.0046	0.983	0.0019	0.973	0.0010	0.876
	2	0.0048	0.998	0.0020	0.998	0.0011	0.918
	3	0.0020	0.963	0.0007	0.954	0.0002	0.824
	4	0.0022	0.988	0.0008	0.982	0.0002	0.864
	5	0.0329	0.805	0.0155	0.820	0.0065	0.708

	6	0.0298	0.880	0.0136	0.908	0.0061	0.866
	7	0.0251	0.996	0.0114	0.996	0.0065	0.949
	8	0.0206	0.998	0.0088	0.985	0.0056	0.964
Fe	1	0.0067	0.970	0.0035	0.940	0.0031	0.840
	2	0.0071	0.999	0.0036	0.980	0.0031	0.890
	3	0.0030	0.960	0.0012	0.940	0.0004	0.820
	4	0.0032	0.990	0.0012	0.980	0.0005	0.860
	5	0.0530	0.820	0.0680	0.860	0.0750	0.950
	6	0.0470	0.880	0.0540	0.940	0.0560	0.930
	7	0.0400	0.990	0.0420	0.900	0.0130	0.850
	8	0.0330	0.999	0.0310	0.880	0.0062	0.820

The model that best approximates the experimental results is the Chemical reaction control model. Indeed, the high regression coefficients for this model suggest that the process may be under the control of the chemical reaction, in agreement with ANOVA. However, the other models may also be suitable for describing the kinetics of these metals during leaching with citric acid.



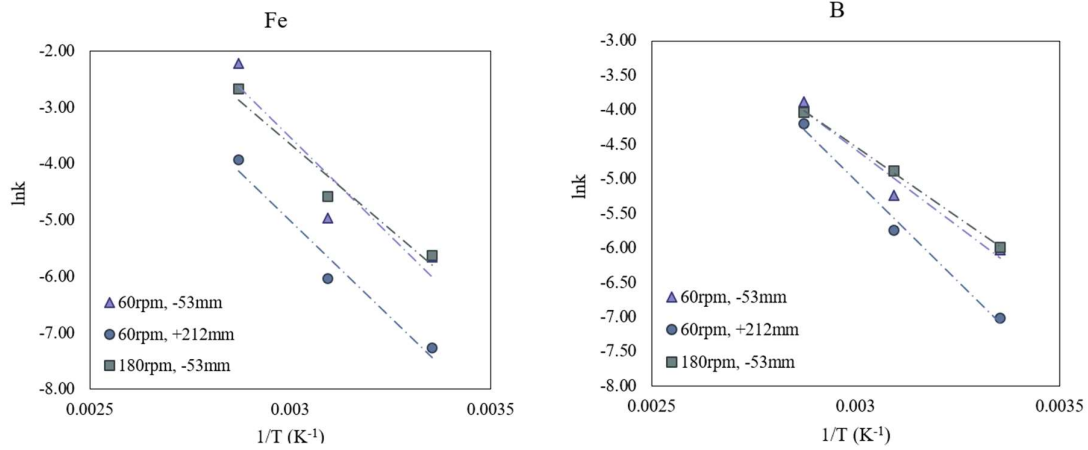


Figure 145. Graphs for estimating Arrhenius parameters.

For each element, we proceed with the calculation of the activation energy, first starting from both low levels of A (stirring) and B (grain size), then when A is low and B high, finally when A is high and B low (the tests used to calculate the E_a for each case are highlighted in Figure 146). The model that refers to the chemical reaction as a process control mechanism was used for each element studied, consistent with what was said previously.

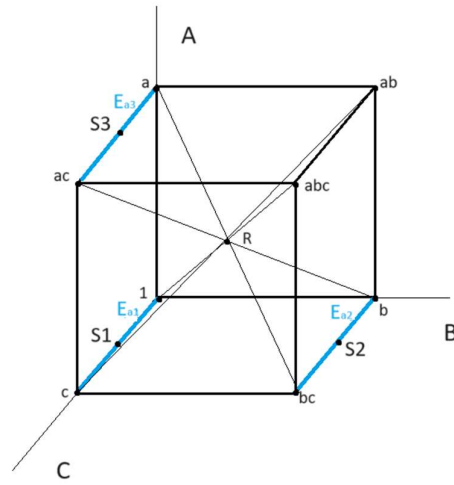


Figure 146. Design of experiments for Arrhenius parameters estimation.

The results of the regressions in Figure 145 regarding Arrhenius parameters are reported in Table 98. They provide interesting insights into how the apparent activation energy depends on particle size and agitation. In particular, it can be seen how, as the diameters of the particles increase, the activation energy increases. The physical interpretation of this phenomenon is linked to the mechano-chemical action of grinding. When the magnets are ground, their crystalline grains break and the solid tends to become amorphous; this means that when the acid attacks the metal, the energy barrier to overcome is lower than that of an intact crystal.

Table 98. Arrhenius parameters for different conditions.

Conditions		Dy	Pr	Tb	Nd	B	Fe
60 rpm; <53 μm	E_a (kJ/mol)	38.93	33.46	37.11	37.84	36.78	50.30
	k_0 (s^{-1})	106.4	36.3	60.1	85.5	99.4	479.5*
60 rpm; >212 μm	E_a (kJ/mol)	46.72	38.84	45.18	45.20	48.34	60.90
	k_0 (s^{-1})	1268	148	660	790	4097	12678*
120 rpm; <53 μm	E_a (kJ/mol)	37.30	28.90	32.31	34.61	33.83	46.49
	k_0 (s^{-1})	60.20	6.54	9.88	26.9	35.9	122.9*

* min^{-1}

Generally, the apparent activation energy is greater than 40 kJ/mol when the chemical reaction is under control. At the same time, it is less than 20 kJ/mol when the mechanism controlling the kinetics is diffusion. In this case, the values fluctuate around 35-40 kJ, except for iron, which has a higher activation energy. For this reason, the chemical reaction and particle size are among the most critical mechanisms influencing the leaching kinetics. However, the agitation is quite significant.

5.4 CONCLUSIONS

The main results obtained during the study and optimization of sustainable recovery processes for valorizing end-of-life permanent magnets are reported below.

- Through experimental activity on a laboratory scale, the behavior of the REEs present in the solid waste analyzed during leaching with citric acid was studied. The behavior was studied thanks to a factorial plan considering the reaction time, the citric acid concentration, and the solid-liquid ratio.
- Through ANOVA, it was seen that some factors influence the yield more. Of the three factors, the most significant was the reaction time, which was significant for each metal analyzed. The longer the time, the greater the yield. The other two factors were also significant but with lower percentages and not for all factors. The only factor that has a negative effect on yield is the increase in the solid-liquid ratio.
- Through the correlation matrix, it was possible to establish how similar the behaviors of the various rare earth metals are in citric acid. In this way, it is possible to create a single mathematical model to predict the behavior of all the reactions analyzed. From this analysis, it was possible to establish that all lanthanides have good correlations with each other, particularly neodymium and dysprosium, which have a correlation index very close to unity. They differ from the behavior of the other metals iron and boron, which, despite having little relationship with the other elements, nevertheless demonstrate an excellent correlation with each other.
- To describe the behavior of the extraction yields, various models were created: in particular, the Response Surface Method was used with the I-Order Polynomial and the II-Order Polynomial. It was decided to use one of the three factors (solid-liquid ratio) as a fixed parameter and to create two different models for each level of analysis. Each of these allowed the exploration of the analysis space in search of optimal conditions. The analysis of the goodness of the regression revealed that the model that best approximates the natural trend

of the data is the I-OP studied for the parametric level of the fixed solid-liquid ratio at a minimum.

- Once the best regression model was chosen, the optimal point of the process was established. The selection criteria respond to physical and economic needs. Having established that the optimal solid-liquid ratio is the low level, evaluating the concentrations of citric acid and the associated costs is also necessary. A similar discussion has been made over time. Although the yield increases with time, it is impossible to consider that the reaction lasts indefinitely. Given these considerations, the optimal working point was the one with a solid-liquid ratio of 10%, 3.5 h of reaction, and 3 M citric acid concentration. Under the chosen conditions, the extraction yields of each metal were calculated.
- The composition of the different grain size fractions was studied through chemical attacks. This study allows us to identify the quantity of each metal in the initial sample and understand the subdivision of each into particle-size fractions.
- Using ANOVA, it was possible to identify the main factors influencing the extraction yield and their interactions. We have seen how time is a significant factor in the 0-120 min range. This result allowed us to think about a kinetic study in the interval considered to optimize the leaching phase.
- The temperature is the most significant factor of the new factorial plan and the new ANOVA. This result suggests a Shrinking Core kinetic model with chemical reaction control. However, several kinetic models were analyzed to understand the mechanism underlying the leaching of the REEs present and of iron and boron. Among these, we find the model that describes the control by the chemical reaction, that for diffusion through the boundary layer and that for diffusion inside the solid particle. Each analyzed model was found to be very good for describing the process. In particular, the one relating to control by the chemical reaction seems better than the others. This result is in agreement with what was obtained from the ANOVA.
- The activation energy for the reactions considered was determined through linearization of the Arrhenius equation. Each activation energy falls in the range of 30-60 kJ/mol. This result suggests limited control by the chemical reaction. Based on all the results obtained, it would seem that there is no predominant effect on the others. However, an integrated model is probably necessary for a more accurate description of the phenomena.
- The results obtained can be of great help for various future developments. Knowing the value of the kinetic parameters will allow us to estimate the quantity of hydrogen produced over time, thus allowing us to take adequate measures to eliminate fire risks, especially on a pilot and industrial scale. So, starting from the kinetic parameters, it will be necessary to proceed backward, building models for each reaction (considering the stoichiometric ratios), then adding them and obtaining the total quantity of hydrogen produced over time. Furthermore, the study of the influence of grain size on the extraction yield clashes with safety issues related to the explosiveness of permanent magnet dust, which tends to oxidize in specific temperature and humidity conditions, increasing the risk of ignition.

6

Conclusions

The research activities carried out and partially reported in this work achieved important objectives and conclusions. In this chapter, the most important results achieved for each material are reported point by point.

- **Oil&Gas Catalysts**

By optimizing existing processes for recovering vanadium and molybdenum from LC-Finer-type catalysts, new process solutions have been developed that surpass the old methodologies in numerous aspects.

In particular, among the processes developed, the ORIM-CAT2 (patented during this research activity) was found to be the most promising from both an economic point of view and lower environmental impact.

The developed and patented process is economical, easily manageable, and innovative since the processes reported so far in the literature consist either of thermal processes or of a combination of thermal and aqueous processes, or even of hydrometallurgical processes, but with the use of acid leaching solutions. Furthermore, the process operates at atmospheric pressure and at a temperature not exceeding 60 °C, which is very advantageous in operation, particularly in terms of energy used. Finally, it is very flexible and can be easily adapted to different types of waste without significant changes to the process scheme and plant layout.

- **Printed Circuit Boards**

Through an advanced characterization study and the integration of process simulations with experimental tests, the Gold-REC1 and Gold-REC2 processes (patented by the University of L'Aquila) were evaluated for the recovery of precious and base metals from end-of-life printed circuit boards.

The study allowed us to identify some critical issues in the Gold-REC1 process. This process requires the careful removal of specific surface mount devices to achieve high recovery yields for precious metals.

In this regard, further optimization of the process is underway to make it more efficient in terms of recovery yields and in terms of energy and reagent consumption.

The study highlighted the excellent performance of the Gold-REC2 process for the recovery of precious metals from devices with high intrinsic economic value. With high recovery yields and low environmental impact, this process could represent a truly cutting-edge technology for the sector considered.

- **Photovoltaic Panels**

Although the Gold-REC1 process was found unsuitable for the study on Printed Circuit Boards, it proved to be an excellent starting point for the valorization of end-of-life photovoltaic panels. In this case, it is possible to have very high silver extraction yields, usually having materials with a reduced content of both organic fraction and copper (elements that hinder the leaching of precious metals).

From the study, some critical issues in the Gold-REC1 process were overcome, and new technologies were introduced to improve recovery efficiency and environmental impact. Among the technologies introduced, we find electrolysis, which allows for regenerating part of the reagents used during leaching.

All these aspects have led to the development of a new process which the University of L'Aquila is currently patenting. Also, for this sector, the proposed process could represent a point of reference for companies and institutions that would like to enter the business of treating and valorizing end-of-life photovoltaic panels.

- **Permanent Magnets**

As part of two European projects (NEW-RE and INSPIREE), the Hydro-Nd process for recovering REEs from end-of-life permanent magnets was studied and optimized in numerous aspects.

Thanks to the study, it was possible to resolve numerous critical issues related to the technical aspects and safety considerations of the plants using this process.

The experimental results allowed the creation of mathematical models for designing two plants (a pilot plant with the NEW-RE project and the first industrial plant in Europe to recover REEs from end-of-life permanent magnets with the INSPIREE project).

The final aim of the optimizations was to improve numerous aspects of the process to make it even more advantageous and economically and environmentally sustainable compared to other solutions currently on the market.

Bibliography

1. Commissione Europea. Resilienza delle materie prime critiche: tracciare un percorso verso una maggiore sicurezza e sostenibilità. <https://eur-lex.europa.eu/legal-content/IT/TXT/PDF/?uri=CELEX:52020DC0474>.
2. Ellen Macarthur Foundation. Universal circular economy policy goals. <https://www.ellenmacarthurfoundation.org/universal-policy-goals/overview>.
3. Ferro, P. & Bonollo, F. Materials selection in a critical raw materials perspective. *Mater Des* **177**, (2019).
4. European Commission. Methodology for establishing the EU list of Critical Raw Materials. *Publications Office of the European Union* (2017).
5. Domenico Colonna. Analisi sperimentale e di processo per il revamping dell'impianto di trattamento rifiuti dell'azienda ORIM S.p.a: recupero di Critical Raw Materials (CRM). (University of L'Aquila, 2021).
6. Commissione Europea. Comunicazione Della Commissione Al Parlamento Europeo, Al Consiglio, Al Comitato Economico E Sociale Europeo E Al Comitato Delle Regioni. <https://eur-lex.europa.eu/legal-content/IT/TXT/HTML/?uri=CELEX:52017DC0490>.
7. Study on the Critical Raw Materials for the EU 2023 Final Report. doi:10.2873/725585.
8. SCREEN. CRMS 2023. <https://screen.eu/crms-2023/>.
9. The Silver Institute. The Global Source. <https://www.silverinstitute.org/>.
10. Chiara Lanzone. Studio della Cinetica e dei Meccanismi di Lisciviazione per il Recupero di Argento da Pannelli Fotovoltaici con Processo Gold-Rec1. (University of L'Aquila, 2023).
11. Abraham, I. Rare earths: The cold war in the annals of travancore. in *Entangled Geographies: Empire and Technopolitics in the Global Cold War* (2011). doi:10.7551/mitpress/9780262515788.003.0005.
12. Tao, Y. *et al.* Distribution of rare earth elements (REEs) and their roles in plant growth: A review. *Environmental Pollution* vol. 298 Preprint at <https://doi.org/10.1016/j.envpol.2021.118540> (2022).
13. Gauß, R. *et al.* Rare Earth Magnets and Motors : A European Call for Action. *A report by the Rare ...* (2021).
14. P, D. CRC Handbook of Chemistry and Physics. *J Mol Struct* **268**, (1992).
15. Royal Society of Chemistry. Periodic Table. <https://www.rsc.org/periodic-table/>.
16. EUROSTAT 2021. Annual detailed enterprise statistics for industry (NACE Rev. 2, B-E). https://ec.europa.eu/eurostat/databrowser/view/SBS_NA_IND_R2__custom_1126320/default/table?lang.
17. Lee, J. C. *et al.* A review on the metallurgical recycling of vanadium from slags: Towards a sustainable vanadium production. *Journal of Materials Research and Technology* vol. 12 Preprint at <https://doi.org/10.1016/j.jmrt.2021.02.065> (2021).
18. IMO. Essential for life. <https://www.imoa.info/index.php>.
19. AFV. Mappa dei paesi con le maggiori riserve di petrolio.

BIBLIOGRAPHY

20. Toppr. Petroleum Refining and Formation Process. <https://www.toppr.com/guides/chemistry/coal-and-petroleum/petroleum-and-refining-of-petroleum/>.
21. Davide Ansovini. "Modellazione di un forno rotativo per il trattamento di catalizzatori esausti. (2009).
22. Wang, J. *et al.* Recovering valuable metals from spent hydrodesulfurization catalyst via blank roasting and alkaline leaching. *J Hazard Mater* **416**, (2021).
23. Llanos, Z. R. & Deering, W. G. GCMC's integrated process for recovery of metals from spent catalysts. *Proceedings of the Air & Waste Management Association's Annual Meeting & Exhibition* Preprint at (1997).
24. Dufresne, P. Hydroprocessing catalysts regeneration and recycling. *Appl Catal A Gen* **322**, (2007).
25. Wiewiorowski, E., Tinnin, R. & Cronojevich, R. Cyclic Process for Recovery of Metals from Spent Catalysts. (1987).
26. H. Mashima, K. Matsuda & S. Toda. JPS62176917A - Separation of molybdenum from vanadium. (1987).
27. S. Al-Fulaij *et al.* Spent Catalyst Treatment and Utilization. Preprint at (1985).
28. Moxba Metrex. The Catalyst in Waste Recycling. <https://moxba.com/>.
29. Wang, M. V. Recycling of metals and engineering materials. *The Minerals, Metals and Materials Society* Preprint at (2000).
30. AMG Vanadium. Company Profile. <https://amg-v.com/sustainability/>.
31. Sumitomo Metal Mining Co., L. A Subsidiary to Withdraw from Recovery Operations. [9] https://www.smm.co.jp/E/news/release/uploaded_files/e100122-2.pdf.
32. GfEMetalle und MaterialienGmbH. Vanadium Sourcing in Terms of Environmental Technologies and Services. <https://www.gfe.com/en/products-and-solutions/technologies>.
33. SCR - Spent Catalyst Recycling GmbH. Company Brochure. www.spentcat.net/services.htm (2007).
34. AURAMET - AURA Metallurgical GmbH. Company Profile. www.auramet.de/sp_process (2007).
35. Marafi, M. Process for recovering boehmite and γ -Al₂O₃ from spent hydroprocessing catalysts. (2012).
36. Marafi, M. Method or process for recovering Mo, V, Ni, Co and Al from spent catalysts using ultrasonic assisted leaching with EDTA. (2012).
37. Marcantonio P.J. Process for metals recovery from spent catalyst. (2007).
38. Chuling L. Method for recycling vanadium and molybdenum from waste petroleum catalyst. (2016).
39. Pak J.J. *et al.* Recovery method of valuable metals from spent catalyst. (2012).
40. HyVent Technology. Spent Catalysts. <http://www.hyvent.nl/spent%20catalyst.html>.
41. Birloaga, I., Romano, P., Vegliò, F. & Mancini, A. Hydrometallurgical process for the selective recovery of vanadium, molybdenum and other base metals from various types of industrial waste. (2023).
42. Montgomery, D. C. Montgomery: Design and Analysis of Experiments. *John Willy & Sons* Preprint at (2017).
43. Hanein, T., Glasser, F. P. & Bannerman, M. N. One-dimensional steady-state thermal model for rotary kilns used in the manufacture of cement. *Advances in Applied Ceramics* **116**, (2017).
44. Li, S. Q., Ma, L. B., Wan, W. & Yao, Q. A mathematical model of heat transfer in a rotary kiln thermo-reactor. *Chem Eng Technol* **28**, (2005).
45. Mujumdar, K. S. & Ranade, V. V. Simulation of rotary cement kilns using a one-dimensional model. *Chemical Engineering Research and Design* **84**, (2006).
46. M. A. Romero Valle. Numerical Modelling of Granular Beds in Rotary Kilns. *Thesis* (2012).
47. Štrbac, N., Živković, D., Mihajlović, I., Boyanov, B. & Živković, Ž. Mechanism and kinetics of the oxidation of synthetic α -NiS. *Journal of the Serbian Chemical Society* **73**, (2008).
48. Ebrahimi Kahrizsang, R., Abbasi, M. H. & Saidi, A. Model-fitting approach to kinetic analysis of non-isothermal oxidation of molybdenite. *Iranian Journal of Chemistry and Chemical Engineering* **26**, (2007).

BIBLIOGRAPHY

49. Granata, S., Faravelli, T. & Ranzi, E. A wide range kinetic modeling study of the pyrolysis and combustion of naphthenes. *Combust Flame* **132**, (2003).
50. Ademe. Validation des méthodes de mesures des Caractéristiques des combustibles bois déchiquetés. *Crittbois-Fibois* (2002).
51. Perry's chemical engineers' handbook. *Choice Reviews Online* **45**, (2008).
52. Andrez, M. Introduction to printed circuit boards (PCB). . <https://pcbtracks.com/printed-circuit-boards/>.
53. Li, J., Duan, H., Yu, K., Liu, L. & Wang, S. Characteristic of low-temperature pyrolysis of printed circuit boards subjected to various atmosphere. *Resour Conserv Recycl* **54**, (2010).
54. Melchiorre, E. Simulazione predittiva della pirolisi dei PCBs tramite Aspen Plus. (University of L'Aquila, 2022).
55. European Commission. *Study on the Critical Raw Materials for the EU*. (2023).
56. Romano, P., Melchiorre, E. & Vegliò, F. ASPEN PLUS Predictive Simulation of Printed Circuit Boards Pyrolysis and Steam Gasification for Organic Fraction Valorization. *Waste* **1**, 281–292 (2023).
57. Korf, N. *et al.* Multi-element chemical analysis of printed circuit boards – challenges and pitfalls. *Waste Management* **92**, (2019).
58. NextPCB. Difference between FR-1, FR-2, FR-3 and FR-4 PCB. <https://www.nextpcb.com/blog/fr-1-pcb>.
59. Romano, P., Ippolito, N. M. & Vegliò, F. Chemical Characterization of an ARDUINO® Board and Its Surface Mount Devices for the Evaluation of Their Intrinsic Economic Value. *Processes* **11**, (2023).
60. Li, J., Shrivastava, P., Gao, Z. & Zhang, H. C. Printed circuit board recycling: A state-of-the-art survey. *IEEE Transactions on Electronics Packaging Manufacturing* **27**, (2004).
61. Lu, Y. & Xu, Z. Precious metals recovery from waste printed circuit boards: A review for current status and perspective. *Resources, Conservation and Recycling* vol. 113 Preprint at <https://doi.org/10.1016/j.resconrec.2016.05.007> (2016).
62. Estrada-Ruiz, R. H., Flores-Campos, R., Gámez-Altamirano, H. A. & Velarde-Sánchez, E. J. Separation of the metallic and non-metallic fraction from printed circuit boards employing green technology. *J Hazard Mater* **311**, (2016).
63. Tansel, B. From electronic consumer products to e-wastes: Global outlook, waste quantities, recycling challenges. *Environment International* vol. 98 Preprint at <https://doi.org/10.1016/j.envint.2016.10.002> (2017).
64. Birloaga, I., Vegliò, F., De Michelis, I. & Ferella, F. Process for the hydrometallurgical treatment of electronic boards. (2018).
65. Birloaga, I. & Vegliò, F. Hydrometallurgical Method For The Recovery Of Base Metals And Precious Metals From A Waste Material. (2019).
66. Ghosh, B., Ghosh, M. K., Parhi, P., Mukherjee, P. S. & Mishra, B. K. Waste Printed Circuit Boards recycling: An extensive assessment of current status. *Journal of Cleaner Production* vol. 94 Preprint at <https://doi.org/10.1016/j.jclepro.2015.02.024> (2015).
67. Luda, M. P. Recycling of Printed Circuit Boards. *Integrated Waste Management* <https://www.intechopen.com/chapters/18491> (2011).
68. Jadhav, U. & Hocheng, H. Hydrometallurgical Recovery of Metals from Large Printed Circuit Board Pieces. *Sci Rep* **5**, (2015).
69. Verma, H. R., Singh, K. K. & Mankhand, T. R. Liberation of metal clads of waste printed circuit boards by removal of halogenated epoxy resin substrate using dimethylacetamide. *Waste Management* **60**, (2017).
70. Gurgul, A., Szczepaniak, W. & Zabłocka-Malicka, M. Incineration and pyrolysis vs. steam gasification of electronic waste. *Science of the Total Environment* **624**, (2018).
71. Arduino S.r.l. <https://store.arduino.cc/products/arduino-mega-2560-rev3>.
72. AspenTechnology, Inc. Aspen Plus Manual: Getting Started Customizing Unit Operation Models. Preprint at (2012).
73. Evangelopoulos, P., Kantarelis, E. & Yang, W. Experimental investigation of the influence of reaction atmosphere on the pyrolysis of printed circuit boards. *Appl Energy* **204**, (2017).

BIBLIOGRAPHY

74. Leuven, K. U. & Gregoir -Principal Author, L. *Metals for Clean Energy: Pathways to solving Europe's raw materials challenge*.
75. Irena. *End-of-Life Management: Solar Photovoltaic Panels*. (2016).
76. Diodati, N. Recupero di argento da pannelli fotovoltaici a fine vita tramite il processo idrometallurgico Gold-REC1: ottimizzazione della lisciviazione attraverso il metodo delle superfici di risposta. (University of L'Aquila, 2023).
77. Levenspiel, O. Chemical reaction engineering. *Industrial and Engineering Chemistry Research* vol. 38 Preprint at <https://doi.org/10.1021/ie990488g> (1999).
78. Faraji, F., Alizadeh, A., Rashchi, F. & Mostoufi, N. Kinetics of leaching: A review. *Reviews in Chemical Engineering* vol. 38 Preprint at <https://doi.org/10.1515/revce-2019-0073> (2022).
79. Clementini, G. Studio della cinetica e dei meccanismi di lisciviazione delle terre rare da magneti permanenti a fine vita in acido citrico. (University of L'Aquila, 2023).
80. Cetrone, V. Recupero di terre rare da magneti permanenti da RAEE e settore automotive. (University of L'Aquila, 2023).
81. Magnet-shop. Aluminum-nickel-cobalt. <https://www.magnet-shop.com/lexikon/aluminum-nickel-cobalt>.
82. Ramprasad, C. *et al.* Strategies and options for the sustainable recovery of rare earth elements from electrical and electronic waste. *Chemical Engineering Journal* vol. 442 Preprint at <https://doi.org/10.1016/j.cej.2022.135992> (2022).
83. Zuffranieri, A. Recupero di terre rare da magneti permanenti a fine vita mediante trattamento idrometallurgico con acido citrico: ottimizzazione della sezione di lisciviazione del processo attraverso la metodologia della superficie di risposta. (University of L'Aquila, 2023).
84. Birloaga, I. & Vegliò, F. Hydrometallurgical method for the treatment of permanent magnets. (2019).

Appendix A

Market Analysis

OIL&GAS CATALYSTS

The global market for industrial catalysts reached a value of approximately 16 billion euros in 2018. Furthermore, the market is expected to reach a value of 23 billion euros by 2024, showing a Compound Annual Growth Rate (CAGR) of 3.9% from 2019-2024. The market's growth is evident both in the Middle East, driven by the growth of oil-related activities, and in Europe, albeit at a slower pace due to economic slowdown in recent years. However, the acceleration in the construction and automotive industries has ensured a balanced growth in the refinery catalyst market.

Favorable regulations approved by major associations and authorities for using catalysts in various refining applications are expected to drive growth. In the United States, shale gas has attracted many markets in North America, leading to numerous exploration and refining projects, which, in turn, have increased the use of catalysts to convert heavy crude oil into lighter fractions. The rapid industrial development of refining and polymer production companies in the Asia-Pacific region is also expected to guide the market. The developments above have increased industrial spending on refining and will continue to stimulate the demand for catalysts. The study concludes that the growing demand for catalysts will persist, increasing the supply of spent catalysts to be treated.

Catalysts are widely used in the petroleum refining industry, and the demand for catalysts is closely related to the petroleum derivatives market. Petroleum derivatives represent almost one-third of global energy demand, mainly gasoline, diesel, aviation fuel, kerosene, and fuel oil. Over 55% of the global demand for petroleum fuels comes from the transportation sector. The increasing demand for petroleum fuels will drive the crude oil refining sector, significantly increasing the demand for refinery catalysts in the forecast period, despite the growing competition from low-carbon footprint fuels. The growing consumption of fuels and other chemicals has led to the rapid growth of the oil industry, further increasing the demand for industrial catalysts. Technological developments, increasing urbanization, and growing automation drive market growth.

The figures below show the trend in global, European, and Italian demand for hydrodesulfurization catalysts and the respective economic market values over the years.

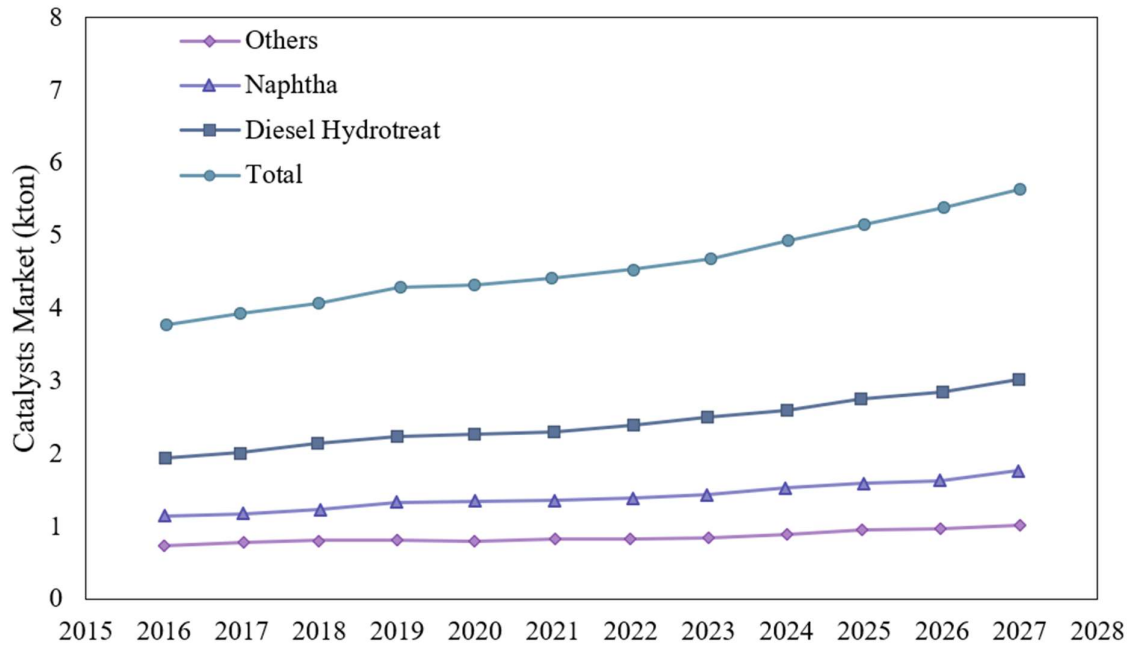


Figure 147. Italy Hydrodesulfurization Catalysts Market, kton by applications.

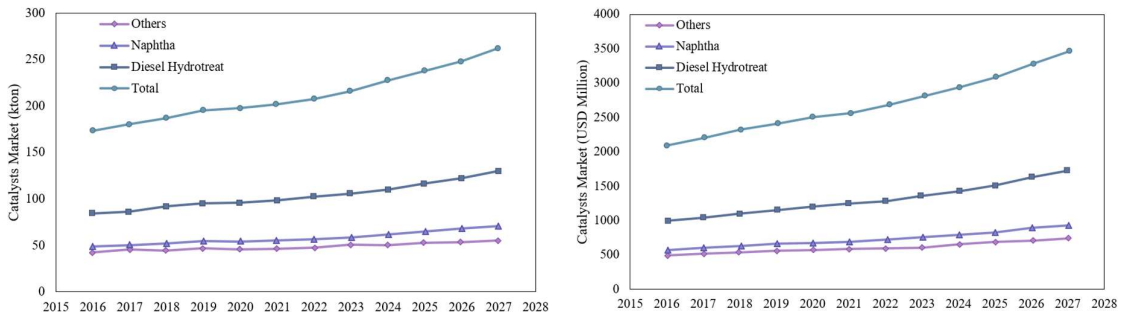


Figure 148. Global Hydrodesulfurization Catalysts Market, by applications.

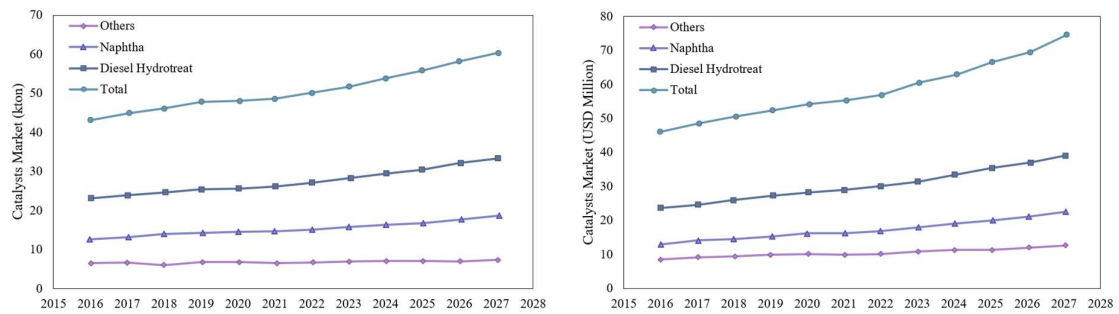


Figure 149. Europe Hydrodesulfurization Catalysts Market, by applications

From the analysis of these Tables, it is possible to summarize the following results:

- Global production of these catalysts will grow from 174,300 ton/year to 262,700 ton/y in the period 2016-2027 with growth of 3.7% per year.
- European production of these catalysts will grow from 43,600 t/y to 60,900 ton/y in the period 2016-2027 with growth of 3.0% per year.

The growth in global catalyst production is inevitably reflected in the amount of waste this market generates in terms of spent catalysts. **Table 99** shows the quantity of spent catalysts produced by various global refineries. From the table it is possible to obtain the graph in **Figure 150**, which shows the subdivision of the spent catalyst market by geographical areas.

Table 99. Estimation of global amount of Oil&Gas spent catalyst in the world.

N°	Refinery	Area	Location	Technology	Design Capacity (BPSO)	Spent catalyst (ton/y)
1	KNPC	Middle-East	Shaalba, Kuwait	H-oil	50000	8824
2	PEMEX	Central America	Tula, Mexico	H-oil	50000	8824
3	PEMEX		Salamanca, Mexico	H-oil	18500	3265
4	BP-Amoco		Texas city, USA	LC-fining	60000	10588
5	Motiva	North-America	Convent, USA	H-oil	43000	7588
6	Syncrude		Mildred Lake, Canada	LC-fining	40000	7059
7	Husky		Lloidminster, Canada	H-oil	35000	6176
8	Shell Scotford (trains 1 and 2)		Scotford, Canada	LC-fining	79000	13941
9	Petro-Canada		Edmonton, Canada	LC-fining	50000	8824
10	Shell Scotford (trains 3)		Alberta, Canada	LC-fining	47000	8294
11	Nothwest		Edmonton, Canada	LC-fining	29000	5118
12	Tonen	Asia	Kawasaki, Japan	H-oil	25000	4412
13	Shenhua		Inner Mongolia, China	T-star	69500	12265
14	ENI	Europe	Milazzo, Italy	LC-fining	25000	4412
15	PKN		Plock, Poland	H-oil	34000	6000
16	Slovnaft		Bratislava, Slovakia	LC-fining	23000	4059
17	Lukoil		Perm, Russia	T-star	70400	12424
18	Neste Oy		Porvoo, Finland	LC-fining	40000	7059
19	Mozyr		Mozyr, Belarus	H-oil	60000	10588
20	Lukoil Burgas		Burgas, Bulgaria	H-oil	n.d.	n.d.

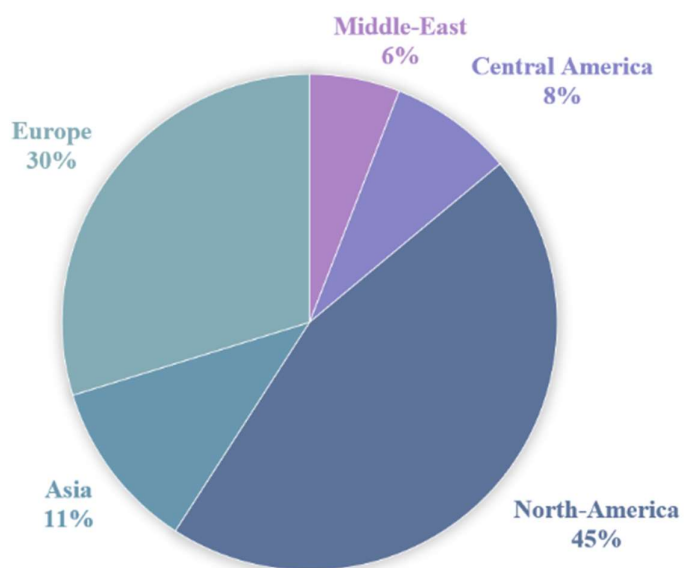


Figure 150. Spent catalysts by geographical area.

References

SIMECO Engineers&Contractors. Feasibility Study for recovery of metals from waste catalysts. ORLEN POLUDNIE S.A. SIMECO Job n. 201211.00. Draft 19/06/2020.

PHOTOVOLTAIC PANELS

A market analysis was conducted to determine the importance of recovering raw materials from end-of-life photovoltaic panels (PVP) within the EU. To do this, we started from the trend of the cumulative PVP capacity in the EU from 2000 to 2050. Through three steps summarized in **Figure 151**, it was determined the impact on the market of the recovery of the raw materials present.

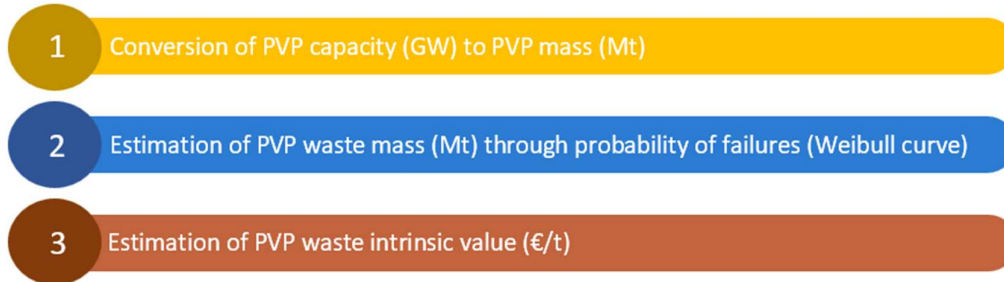


Figure 151. Three-step PV panel waste model

As described in **Figure 151**, the first step of this study was characterized by determining the annual installed capacity in Europe, starting from the data expected for the cumulative capacity expected for photovoltaics. In **Figure 152**, the trend of cumulative capacity in Europe and non-EU countries can be seen.

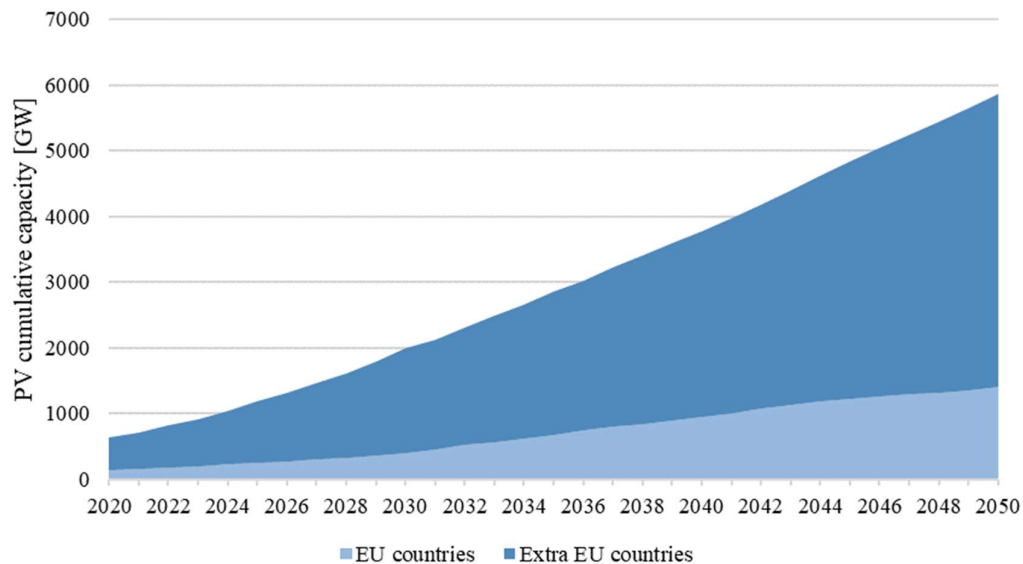


Figure 152. PV cumulative capacity in EU and Extra EU countries from 2020 to 2050.

Starting from this trend, estimating the quantity of panels included as waste flows is possible. Most waste is generally generated during four primary phases of the life cycle of a given PV panel: panel production, panel transportation, panel installation and use, and disposal at the end of the panel's life. The following waste forecasting model covers all life cycle stages except production. This is because production waste is assumed to be easily managed, collected, and treated by waste treatment contractors or manufacturers.

The two main input factors are the conversion of installed capacity (GW) into panel mass (ton) and the probability of losses during the life cycle of the PV panel. The expected capacities (GW) were converted into mass thanks to determining the PV panel weight-to-power ratio trend. To estimate the volumes of installed photovoltaic panel waste (ton).

A regression analysis was performed to estimate the model parameters that describe the trend of the data themselves over time, starting from the literature data. A two-parameter exponential model (α_1, α_2) was hypothesized for the weight-to-power ratio (WPR). Analyzing the arrangement in the graph shown in **Figure 153**. The following equation describes the hypothesized model.

$$WPR = \alpha_1 e^{\alpha_2 t}$$

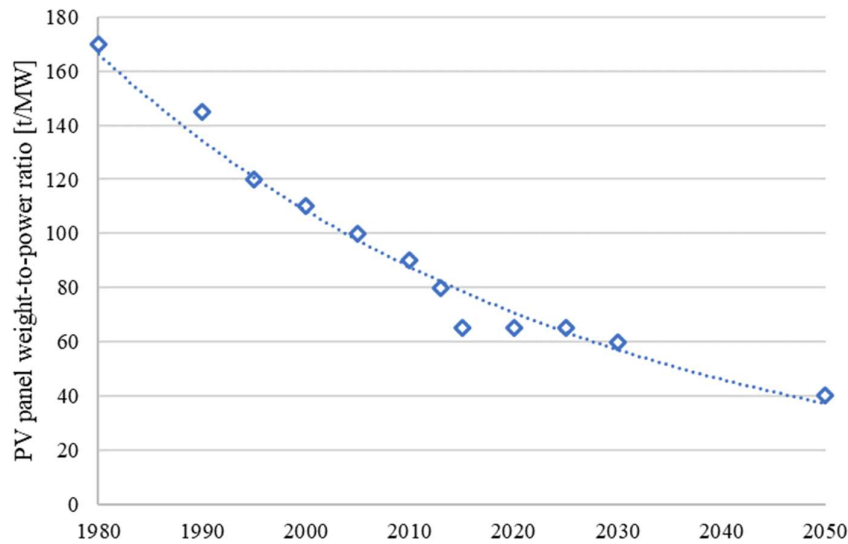


Figure 153. Estimated model for WPR versus years from 1980 to 2050.

Thanks to the model created, it is possible to move from the installed capacity (GW) to the amount of panels placed on the market each year (ton). Multiplying WPR by the installed capacity gives the mass of panels placed on the market.

In order to estimate the quantity of panels that return from the market as waste, some important considerations must be made. The probability of failure is modeled using the Weibull function, reported below.

$$F(x) = 1 - e^{-\left(\frac{x}{\lambda}\right)^k}$$

The Weibull function is a continuous probability distribution used to describe the duration of events that can occur randomly over time. Statistician Wallodi Weibull developed it, and it is often used in reliability analysis and survival modeling.

The Weibull function is characterized by two main parameters: the shape parameter (k) and the scale parameter (λ). The shape parameter determines the shape of the distribution curve. It can describe various shapes, from an exponential distribution (when k is 1) to a normal distribution (when k approaches infinity). The scale parameter affects the time scale or magnitude of the event. In the case in question, λ is the average lifetime of the panel and is assumed to be equal to 30 years. The value of k is

taken from the literature and is equal to 5.376. With these assumptions, the probability of panel failure assumes the trend shown in **Figure 154**.

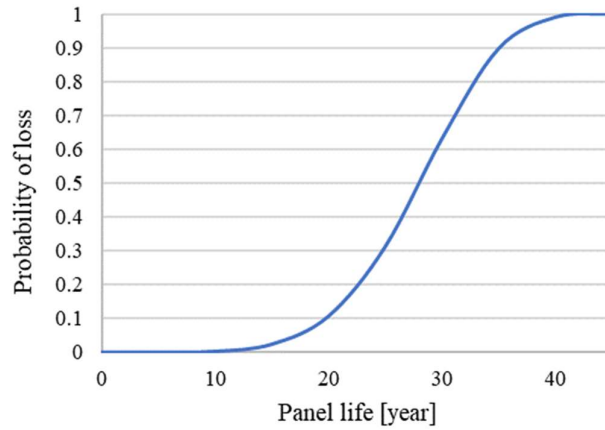


Figure 154. Probability of loss of a panel during its life.

Considering that new panels are placed on the market every year, these will become waste according to a probability function that considers the year of placing on the market. That is, the generalized Weibull function becomes as follows.

$$F(t) = 1 - e^{-\left(\frac{t-t_0}{\lambda}\right)^k} \tag{4.4}$$

Where t_0 represents the year of placing the generic mass of panels on the market. Considering 2000 as the starting point of the calculation (it is assumed that before 2000, the mass of panels installed is negligible), the quantity of waste generated is calculated year by year, starting from the mass introduced in 2001. This procedure will be carried out from 2002 until 2050. By adding the different curves shown in Figure 5, the total mass of waste generated by photovoltaic panels is obtained (the case is reported for EU countries, but the calculation was also carried out globally). The total mass of waste obtained by adding the curves in **Figure 155** is shown in **Figure 156**.

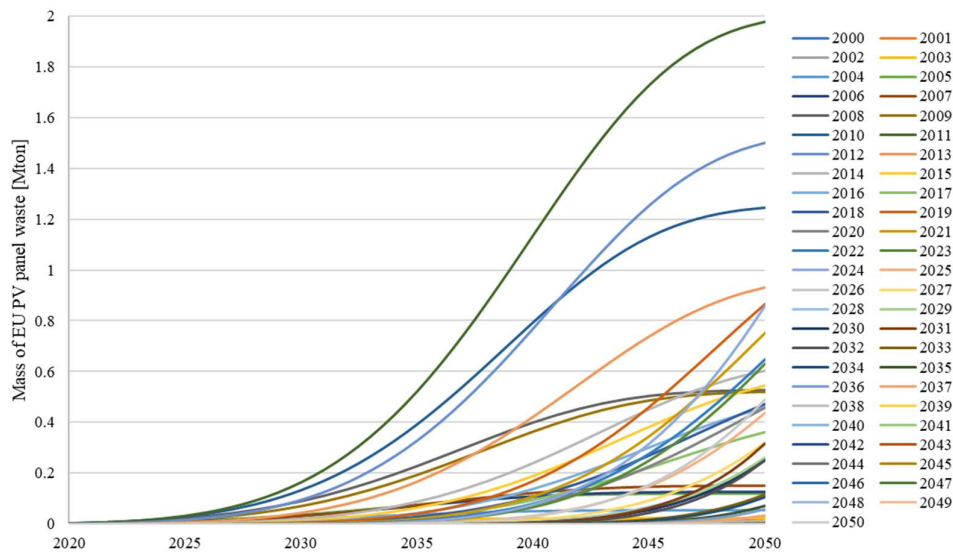


Figure 155. Mass of EU PV panel waste for different years of PV installation from 2020 to 2050.

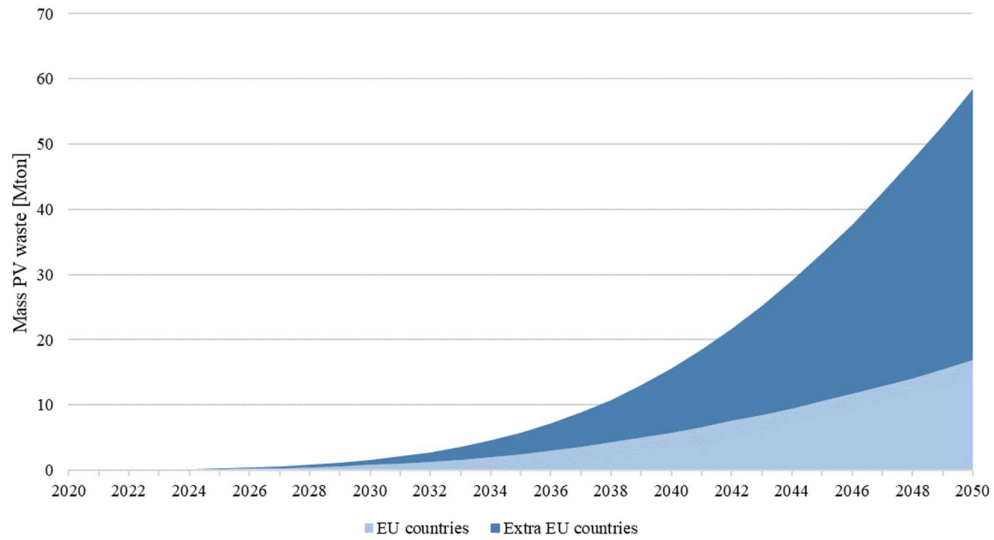


Figure 156. Mass PV panel waste for EU and extra EU countries from 2020 to 2050.

This figure shows an essential graph for estimating the production capacity of any plants to treat end-of-life photovoltaic panels for the recovery and valorization of raw materials.

References

Irena. End-of-Life Management: Solar Photovoltaic Panels. (2016).
 Kuitsche, J. (2010), “Statistical Lifetime Predictions for PV Modules,” presentation www1.eere.energy.gov/solar/pdfs/pvrw2010_kuitsche.pdf
 Revised WEEE Directive (2012/19/EU)
 Solar PV Capacity. Available online: [solar_pv_capacity_bnef.png \(1370×881\) \(wpengine.com\)](#)

PERMANENT MAGNETS

Based on the current recycling levels of end-of-life permanent magnets (around 1%), any activity based on the recovery of REEs could be more economically sustainable. In fact, according to all the reliable sources consulted, this business will become strategic starting in 2030.

However, a market analysis was conducted to evaluate the flows of end-of-life permanent magnets within Europe. The estimated values take into account an average CAGR of 12%.

The numbers obtained are consistent with others in the literature and probably slightly conservative: in 2026, the demand for PM is estimated to be around 25 kton/y, while in 2030, it should rise to about 40 kton/y. The results of the analysis conducted are summarized in **Table 100** and

Table 100. PM Market analysis results.

Year	EU PM required (ton/y) - forecast (a)	PM available x recycling (ton/y) - estimate (b)	PM available for hydromet (ton/y) (c)
2020	n.a.	500	n.a.
2022	16000	725	363
2023	17920	1051	526
2024	20070	1524	762
2025	22479	2210	1105
2026	25176	3205	1602
2027	28197	4647	2324
2028	31581	6738	3369
2029	35371	9770	4885
2030	39615	14167	7084
2031	44369	14900	7450
2032	49694	17135	8568
2033	55657	19705	9853
2034	62336	22661	11331
2035	69816	26060	13030
2036	78194	29969	14985
2037	87577	34465	17232
2038	98086	39634	19817
2039	109857	45579	22790
2040	123039	54099	27050

The quantity of PM available for recovery is estimated very simply using a statistical model (in fact, more complex models could be used, but the results would be similar).

We assumed a moving Gaussian distribution with an average lifetime of PMs equal to 10 years (the value is consistent with the average lifetime of consumer electronics devices, such as HDDs and vehicles that contain PMs). The quantity of PM in the generic year is the integral of the Gaussian from the present moment to the considered moment. This simplified model allows you to have a fast but reasonable estimate of the quantity of EoL PM. To be even more conservative, we assume that only 50% of PM materials will be processed by hydrometallurgical processes while the rest will be reused or recycled in other ways.

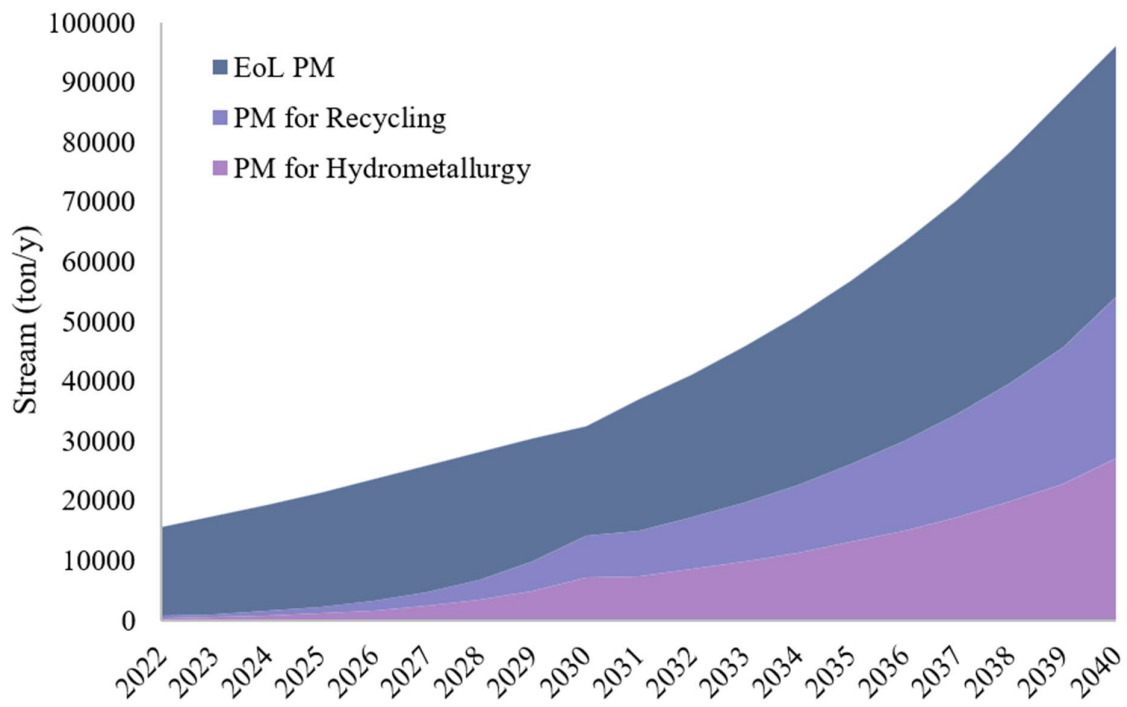


Figure 157. EoL PM Streams trend.

References

Leuven, K. U. & Gregoir -Principal Author, L. *Metals for Clean Energy: Pathways to solving Europe's raw materials challenge.*

Gauß, R. *et al.* Rare Earth Magnets and Motors : A European Call for Action. *A report by the Rare* (2021).

Figures

Figure 1. Criticality assessment results (individual materials and grouped HREEs, LRREs and PGMs). ⁷	15
Figure 2. Main EU suppliers of individual 2023 CRMs. ⁷	15
Figure 3. Photographic aspect of silver and position in the periodic table.	16
Figure 4. Annual average price of silver in the period 2000-2023.	18
Figure 5. Simplified value chain for silver in the EU. ⁸	19
Figure 6. Photographic aspect of PGMs (position as in the periodic table) and position in the periodic table. ...	19
Figure 7. Annual average price of PGMs.	22
Figure 8. Photographic aspect of REEs and position in the periodic table.	23
Figure 9. Annual average price of REEs oxides.	28
Figure 10. Simplified value chain for REE in the EU. ⁸	29
Figure 11. Photographic aspect of Vanadium as a mineral and position in the periodic table.	30
Figure 12. Annual average price of vanadium pentoxide.	31
Figure 13. Simplified value chain for vanadium in the EU. ⁸	31
Figure 14. Aspetto fotografico del molibdeno e posizione nella tavola periodica.....	32
Figure 15. Annual average price of molybdenum between 2000 and 2023.....	33
Figure 16. Simplified value chain for molybdenum in the EU. ⁸	34
Figure 17. Crude oil reserves in million barrels (Gbbbl). ¹⁹	35
Figure 18. Simplified block diagram of the oil refining process. ²⁰	37
Figure 19. Photographic aspect of LCF catalysts.	38
Figure 20. Simplified block diagram of the tests performed for process 1 with the three countercurrent stages highlighted.	43
Figure 21. Simplified block diagram of the tests performed for process 2 with the three countercurrent stages highlighted.	44
Figure 22. Simplified block diagram of the tests performed for process.....	45
Figure 23. CHNS results and removal efficiency for different treatments.	47
Figure 24. Removal mechanism of the organic component by Acetone.	48
Figure 25. Simplified block diagram of ORIM-CAT2 process. ⁴¹	49
Figure 26. Photographic aspect of leaching solution for the four tests.....	52
Figure 27. Photographic aspect of precipitate.	54
Figure 28. Photographic aspect of second precipitate before (a) and after (b) calcination.	55
Figure 29. Elemental composition of second precipitate.....	55
Figure 30. Photographic aspect of the two pre-treated processes.....	55
Figure 31. Photographic aspect of precipitate I before (a) and after (b) drying.	58
Figure 32. Composition of precipitate II.	59
Figure 33. Photographic aspect of the two samples after the thermal pre-treatments.	59
Figure 34. Photographic aspect of the two samples after milling.....	60
Figure 35. V recovery for the 3 tests performed in a single step (15% S/L, 2 h, 85°C).	61
Figure 36. Variation of the height of the solid front and the sedimentation velocity for the three tests.	62
Figure 37. Sedimentation rate for the three tests vs time and sedimentation rate at 30 min.....	63
Figure 38. Average sedimentation speed for the three tests.....	64
Figure 39. Summary of leaching results.....	65

Figure 40. Time trend of the solid front for the sample.....	65
Figure 41. Average speed for the various sedimentation tests.....	65
Figure 42. Summary of the recovery of vanadium and molybdenum for all tests carried out.....	66
Figure 43. Average sedimentation rate for all sedimentation tests carried out.....	66
Figure 44. Weight losses of the drying process (105°C, 24 h) and calcination (600°C, 1 h).....	67
Figure 45. Recovery yields of vanadium and molybdenum.....	68
Figure 46. Photographic aspect of precipitates after filtration.....	68
Figure 47. Composition of solid precipitates in terms of oxides.....	69
Figure 48. Results of the XRD analysis on precipitate 1a relating to vanadium.....	70
Figure 49. Results of the XRD analysis on precipitate 1a relating to molybdenum.....	71
Figure 50. T-xy (left) and partition (right) diagrams of the Acetone - C ₁₄ H ₃₀ system.....	72
Figure 51. Results of sensitivity analysis.....	73
Figure 52. Flowsheet of acetone recovery process.....	73
Figure 53. Catalyst washing diagram with Acetone.....	74
Figure 54. Simplified process diagram of the acetone recovery section.....	75
Figure 55. Flowsheet of simulation.....	76
Figure 56. Mass conversion of Oil as function of Temperature and Air-Oil mass ratio.....	77
Figure 57. Hydrogen produced by 100 kg of Oil as function of Temperature and Air-Oil mass ratio.....	77
Figure 58. Syngas produced for 0.4 (—) and 1 (- -) Air-Oil mass ratio.....	78
Figure 59. Syngas produced with 0.2 Air-Oil mass ratio.....	78
Figure 60. Syngas produced with 1 Air-Oil mass ratio.....	79
Figure 61. Flowsheet of complete gasification process with M&E balance.....	80
Figure 62. Photographic aspect of the catalyst washed and dried in air for 24 h.....	82
Figure 63. Photographic aspect of the sample after two different grindings, following particle size separation.....	82
Figure 64. Particle size distribution of the sample for the two different grindings.....	83
Figure 65. Particle size distribution of the two fractions ground and mixed together.....	83
Figure 66. Significance of factors and their interactions on vanadium and molybdenum leaching.....	85
Figure 67. Effect of major factors on vanadium and molybdenum leaching.....	85
Figure 68. Central Composite Design (CCD) scheme.....	86
Figure 69. Vanadium recovery yield II-order polynomial model.....	89
Figure 70. Molybdenum recovery yield II-order polynomial model.....	89
Figure 71. Simplified diagram of the 2-stage cross-current process.....	90
Figure 72. Extraction yields of vanadium and molybdenum as the solid/liquid ratio varies in the cross-current process Configuration Cross-currents with [H ₂ O ₂]=1.9 mol/L and [NaOH]=1.5 mol/L.....	90
Figure 73. Scheme of tests performed for the countercurrent process.....	91
Figure 74. Vanadium and molybdenum extraction yields as the solid/liquid ratio varies for the countercurrent process Countercurrent configuration with [H ₂ O ₂]=1.9 mol/L and [NaOH]=1.5 mol/L.....	91
Figure 75. Vanadium end molybdenum extraction yields in the cross-current process with [H ₂ O ₂]=1.708 mol/L and [NaOH]=1.635 mol/L, varying the applied pretreatment.....	92
Figure 76. Vanadium and molybdenum extraction yields in the countercurrent process with 15% Solid/Liquid, [H ₂ O ₂]=1.708 mol/L and [NaOH]=1.635 mol/L when varying the H ₂ O ₂ addition method.....	92
Figure 77. Summary of recovery yields and chemicals consumption for different processes.....	94
Figure 78. Rotary kiln scheme.....	95
Figure 79. Rotary kiln section diagram.....	98
Figure 80. Axial thermal profile of the gas and solid phases in the kiln.....	100
Figure 81. Thermal profile of the solid phase in the kiln for different inlet Oil concentrations.....	100
Figure 82. Photographic aspect of the Arduino board, front (left) and back (right).....	106
Figure 83. Photographic aspect of AF81 board, front (left) and back (right).....	107
Figure 84. Total composition of AF81 board.....	107
Figure 85. Block diagram of the developed pyrolysis model. ⁵⁶	110
Figure 86. Flowsheet of the simulation.....	112
Figure 87. Total composition of Arduino Mega 2560.....	115
Figure 88. IEV of Arduino Mega 2560.....	115
Figure 89. Comparison between experimental results and results predicted by the model in the case of an inert environment with nitrogen.....	117
Figure 90. Syngas mass composition.....	117
Figure 91. Syngas composition in case of steam added to the reactor.....	118
Figure 92. Pyrolysis products for different temperatures.....	118
Figure 93. Effect of temperature over organic fraction conversion for different steam streams (feed: 100 kg/h).	119

Figure 94. Potential value creation through PV end-of-life management. ⁷⁵	122
Figure 95. c-Si (monocrystalline) panel, National Renewable Energy Laboratory (NREL). ⁷⁵	124
Figure 96. Thin-film (monolithic integration) panel, NREL. ⁷⁵	124
Figure 97. Evolution to 2030 of materials used for different PV panel technologies as a percentage of total panel mass. ⁷⁵	125
Figure 98. Qualitative comparison between the three major categories of metallurgical processes. ⁵⁹	126
Figure 99. Photographic aspect of solid sample A.	127
Figure 100. The particle size plot of sample B.....	127
Figure 101. Gold-REC1 process diagram for photovoltaic panels.....	128
Figure 102. Rotability properties of a factorial plan.....	130
Figure 103. Overlaying star points with a factorial plane.	130
Figure 104. Representation of concentrations of reactants and products for the reaction $A(g) + bB(s) \rightarrow$ solid product for a particle of unchanging size.	131
Figure 105. Representation of a reacting particle when external diffusion is the controlling resistance.....	132
Figure 106. Representation of a reacting particle when internal diffusion is the controlling resistance.	132
Figure 107. Representation of a reacting particle when chemical reaction is the controlling resistance.....	133
Figure 108. Significance of factors and interactions on silver extraction yields.	135
Figure 109. Response surfaces I-OP for silver recovery yield.	136
Figure 110. Response surfaces II-OP for silver recovery yield.	137
Figure 111. Significance of factors and interactions on silver extraction yields.....	139
Figure 112. Main factors and their interaction effects on silver leaching.....	139
Figure 113. Silver recovery yields vs time for each run of the factorial plan.....	140
Figure 114. Silver recovery yield for different particle size fractions (Temperature: 25 °C, Stirring rate: 60 rpm).	140
Figure 115. Silver recovery yield for different temperatures (Particle size: <53 μm, Stirring rate: 60 rpm).....	141
Figure 116. Silver recovery yield for different stirring rate (Particle size: <53 μm, Temperature: 25 °C).....	141
Figure 117. Graph for estimating Arrhenius parameters (Particle size: <53 μm; Stirring rate: 60 rpm).	142
Figure 118. Correlation matrix between silver and silicon.....	142
Figure 119. Correlation graph between the recovery yields of silver and those of silicon.	143
Figure 120. Hydrometallurgical, pyrometallurgical, and biometallurgical processes for the recovery of REEs. ⁸²	149
Figure 121. Photographic aspect of permanent magnet sample. ⁸³	149
Figure 122. The particle size plot of PM sample.....	150
Figure 123. Simplified block diagram of the Hydro-Nd process.	151
Figure 124. Correlation matrix between the concentrations of the elements in solutions.	154
Figure 125. Correlation graphs between the concentrations of the different elements, in relation to the concentration of neodymium.....	155
Figure 126. Graph of metal recovery yields.	156
Figure 127. Significance of factors and interactions on extraction yields.....	157
Figure 128. Main factors and their interaction effects on leaching.	157
Figure 129. Nd RSM I-order polynomial.	160
Figure 130. Pr RSM I-order polynomial.	160
Figure 131. Dy RSM I-order polynomial.	161
Figure 132. Tb RSM I-order polynomial.....	161
Figure 133. Fe RSM I-order polynomial.....	162
Figure 134. B RSM I-order polynomial.	162
Figure 135. Nd RSM II-order polynomial.....	168
Figure 136. Pr RSM II-order polynomial.	168
Figure 137. Dy RSM II-order polynomial.....	169
Figure 138. Tb RSM II-order polynomial.	169
Figure 139. Fe RSM II-order polynomial.....	170
Figure 140. B RSM II-order polynomial.	170
Figure 141. Scatter diagrams for the I-Order polynomial (S/L=10%).	171
Figure 142. Significance of factors and interactions on REEs extraction yields.....	173
Figure 143. Main factors and their interaction effects on REEs leaching.	173
Figure 144. Extraction yields over time of the metals of interest for each test of the factorial plan.	174
Figure 145. Graphs for estimating Arrhenius parameters.....	177
Figure 146. Design of experiments for Arrhenius parameters estimation.	177
Figure 147. Italy Hydrodesulfurization Catalysts Market, kton by applications.....	187
Figure 148. Global Hydrodesulfurization Catalysts Market, by applications.	187

Figure 149. Europe Hydrodesulfurization Catalysts Market, by applications.....	187
Figure 150. Spent catalysts by geographical area.....	189
Figure 151. Three-step PV panel waste model.....	190
Figure 152. PV cumulative capacity in EU and Extra EU countries from 2020 to 2050.	190
Figure 153. Estimated model for WPR versus years from 1980 to 2050.	191
Figure 154. Probability of loss of a panel during its life.	192
Figure 155. Mass of EU PV panel waste for different years of PV installation from 2020 to 2050.....	192
Figure 156. Mass PV panel waste for EU and extra EU countries from 2020 to 2050.	193
Figure 157. EoL PM Streams trend.	195

Tables

Table 1. Matrix for evaluating the SCP parameter. ⁵	14
Table 2. 2023 Critical Raw Materials (new CRMs in italics). ⁷	14
Table 3. Silver supply and demand in metric ton, 2016-2020 average. ⁸	18
Table 4. PGMs supply and demand in metric ton, 2016-2020 average. ⁸	22
Table 5. REE supply and demand in metric tonnes, 2016-2020 average (in metal content). ⁸	29
Table 6. Vanadium supply and demand in metric tonnes, 2016-2020 average. ⁸	31
Table 7. Molybdenum supply (extraction stage) and demand in metric ton, 2016-2020 average. ⁸	33
Table 8. Main important processes for the recovery of metals from Oil&Gas catalysts.	38
Table 9. Results of chemical composition analysis of LCF sample.....	41
Table 10. Results of CHNS analysis of LCF sample.	41
Table 11. Precipitation tests condition.	44
Table 12. Tests conditions.....	45
Table 13. Conditions of heat treatments.	46
Table 14. Conditions of vanadium precipitation conditions.	46
Table 15. CHNS results of the initial sample and the sample after washing with acetone and water.	48
Table 16. Parameters and levels of the factorial plan.	51
Table 17. Diagram of the tests performed with the 2 levels of the 4 parameters A, B, C, D: high level (+) and low level (-). The 4 replications at the central level (o) are also shown below.	51
Table 18. Results of leaching step for the four tests.	52
Table 19. Concentration and recovery for tests I and II.....	53
Table 20. Concentration and recovery for tests III and IV.....	53
Table 21. Results of first precipitation.....	54
Table 22. Results of second precipitation.	54
Table 23. Results of roasting and calcination steps.	55
Table 24. Concentrations of different elements for all leaching steps and cycles.....	56
Table 25. Vanadium recovery and weight loss for all leaching steps and cycles of process 1.....	56
Table 26. Vanadium recovery and weight loss for all leaching steps and cycles of process 2.....	57
Table 27. Results of vanadium precipitation tests.	57
Table 28. Results of precipitates drying.....	57
Table 29. Composition of precipitates in terms of elements and as V ₂ O ₅	58
Table 30. Results of vanadium precipitation tests for the two different calculation methods.....	58
Table 31. Results of roasting and calcination for the samples.	59
Table 32. Results of leaching steps for the two samples.....	60
Table 33. Weight and moisture losses of solid residues after drying in an oven at 60 °C for 24 h.....	60
Table 34. Results of the four leaching tests.	61
Table 35. Summary of different leaching tests.	61
Table 36. Results of thermal pre-treatments.	64
Table 37. Results of leaching phase.....	64
Table 38. Recovery yields for vanadium and molybdenum.....	64
Table 39. Conditions and results of leaching tests.....	67
Table 40. Recovery yields of vanadium and molybdenum for the various tests.....	67
Table 41. Composition of precipitates determined by analysis of chemical attack solutions.	68
Table 42. Results of citric acid leaching test.	72
Table 43. Material and energy balance results of acetone recovery process.....	74

Table 44. Material balance results of the washing section.....	75
Table 45. Material balance results of acetone recovery section.....	76
Table 46. Syngas components (excluding N ₂ and O ₂).	77
Table 47. Composition of Syngas for 0.1 Air-LCF mass ratio and 400°C.....	79
Table 48. Energy balance of gasification process.	80
Table 49. Comparison between process with acetone and pyrolysis.	81
Table 50. Results of washing with acetone and water.	82
Table 51. Results in terms of V and Mo concentration.....	84
Table 52. results of the factorial plan for leaching.....	84
Table 53. Central Composite Design for the investigated process.....	87
Table 54. Summary of recovery yields, chemicals consumption and costs for different processes.....	93
Table 55. Main RK reactions and related kinetic data.	97
Table 56. Relations for the specific heats at constant pressure of the substances present in the system.	99
Table 57. Kiln parameters used in the calculation code.....	99
Table 58. Materials and main characteristics of various FRs. ⁵⁹	105
Table 59. Characterization of PCBs powders.	109
Table 60. Characterization of back panels.....	110
Table 61. PCBs proximate analysis.	111
Table 62. PCBs ultimate analysis.	111
Table 63. Components removed from the Arduino board and chemical attack methods.....	112
Table 64. Results of qualitative analysis.....	114
Table 65. Results of quantitative analysis.....	114
Table 66. Extraction yields for different AF81 powders.....	116
Table 67. Extraction yields for AF81 back panels.....	116
Table 68. Market share of PV panels by technology groups (2014-2030). ⁷⁵	123
Table 69. Composition of solid sample.	127
Table 70. Factors and levels of factorial plan.	129
Table 71. Factorial plan for PV panels kinetic analysis.	134
Table 72. New factorial plan with silver extraction yields (without Thiourea).	135
Table 73. Parameters of the I-OP surfaces with the related coefficients of determination.	136
Table 74. Parameters of the II-OP surfaces with the related coefficients of determination.	137
Table 75. Optimal leaching conditions (10 g/L).	137
Table 76. Chemical composition of different size fractions.	138
Table 77. Silver kinetic constants (min ⁻¹) and determination coefficients at different run.....	141
Table 78. Mass composition of the PM sample.	150
Table 79. Factors and levels of factorial plan.	152
Table 80. Factorial plan for kinetic analysis.	153
Table 81. Concentration of metals in solutions after leaching.....	153
Table 82. Metals recovery yields.	156
Table 83. RSM I-order polynomial (S/L=10%).	158
Table 84. RSM I-order polynomial (S/L=20%).	158
Table 85. Regression analysis results for RSM I-Order polynomial in terms of R ² and SS (S/L=10%).	163
Table 86. Regression analysis results for RSM I-Order polynomial in terms of R ² and SS (S/L=20%).	163
Table 87. Full factorial plan with star points.	163
Table 88. Results in terms of concentrations for star points.	164
Table 89. Results in terms of recovery yields for star points.....	164
Table 90. RSM II-order polynomial (S/L=10%).	165
Table 91. RSM II-order polynomial (S/L=10%).	166
Table 92. Regression analysis results for II-Order polynomial in terms of R ² and SS (S/L=10%).	167
Table 93. Regression analysis results for II-Order polynomial in terms of R ² and SS (S/L=20%).	167
Table 94. Optimal leaching conditions.	172
Table 95. Recovery yields in optimal leaching conditions.	172
Table 96. Chemical composition of different size fractions.	172
Table 97. Kinetic constants (min ⁻¹) and determination coefficients at different run.	175
Table 98. Arrhenius parameters for different conditions.	178
Table 99. Estimation of global amount of Oil&Gas spent catalyst in the world.....	188
Table 100. PM Market analysis results.....	194

Projects & Companies



PEACOC

(Available online: [PEACOC Project \(peacoc-h2020.eu\)](http://peacoc-h2020.eu))



TREASURE

(Available online: [Home - Treasure \(treasureproject.eu\)](http://treasureproject.eu))



PASSENGER

(Available online: [For sustainable rare-earth-free permanent magnets - Passenger \(passenger-project.eu\)](http://passenger-project.eu))



NEW-RE

(Available online: [Project New-RE - Erion](http://erion.eu))

INSPIREE

n.a.



Orim S.p.a

(Available online: [Orim | recupero metalli, smaltimento rifiuti industriali - Orim](http://orim.it))



Itelyum S.p.a.

(Available online: [Itelyum](http://itelyum.com))



Simgreen S.r.l.

(Available online: [SimGreen](http://simgreen.com))

Lorusso
Estrazione S.r.l.

n.a.